ASD-TDR-63-745

INVESTIGATION OF STORED ENERGY ROTORS FOR RECOVERY

TECHNICAL DOCUMENTARY REPORT No. ASD-TDR-63-745

DECEMBER 1963

FLIGHT DYNAMICS LABORATORY
RESEARCH AND TECHNOLOGY DIVISION
AIR FORCE SYSTEMS COMMAND
WRIGHT-PATTERSON AIR FORCE BASE, OHIO

Project No. 6065, Task No. 606501

(Prepared under Contract No. AF 33(616)-7544 by
Kaman Aircraft Corporation, Bloomfield, Connecticut)

NOTICES

When Government drawings, specifications, or other data are used for any purpose other than in connection with a definitely related Government procurement operation, the United States Government thereby incurs no responsibility nor any obligation whatsoever; and the fact that the Government may have formulated, furnished, or in any way supplied the said drawings, specifications, or other data, is not to be regarded by implication or otherwise as in any manner licensing the holder or any other person or corporation, or conveying any rights or permission to manufacture, use, or sell any patented invention that may in any way be related thereto.

Qualified requesters may obtain copies of this report from the Defense Documentation Center (DDC), (formerly ASTIA), Cameron Station, Bldg. 5, 5010 Duke Street, Alexandria 4, Virginia

This report has been released to the Office of Technical Services, U.S. Department of Commerce, Washington 25, D.C., in stock quantities for sale to the general public.

Copies of this report should not be returned to the Aeronautical Systems Division unless return is required by security considerations, contractual obligations, or notice on a specific document.

400 - January 1964 - 162-24-447

FOREWORD

This final Technical Documentary Report, Kaman Report No. R-467, was prepared by Kaman Aircraft Corporation, Bloomfield, Connecticut, in compliance with requirements of Contract No. AF33(616)-7544 and Supplemental Agreements 1 through 6. The report covers analytical studies and experimental tests performed from 13 June 1960 through the completion of the program.

Work by Kaman Aircraft was conducted under Project No. 6065, Task 606501, sponsored by the Air Force Flight Dynamics Laboratory, Research and Technology Division. Messrs. Robert Tyndall, Clint Eckstrom, and James H. DeWeese served as the Air Force Project Officers.

Acknowledgement is made of the technical assistance, support, and co-operation provided by the personnel at the Propulsion Wind Tunnel, USAF Arnold Engineering Development Center, Tullahoma, Tennessee, during the wind tunnel testing phase, and the USAF 6511th Test Group (Parachutes), El Centro, California, in performing air drop tests. Messrs. Dean Herron and Larry Galigher were assigned Project Engineer responsibilities for the wind tunnel facility. Mr. James Waite was Project Engineer for the 6511th Test Group.

The program at Kaman Aircraft was under the cognizance of Mr. D. W. Robinson, Jr., Chief Research Engineer. Messrs. B. A. Goodale and J. J. Barzda were Project Engineers. Staff members who contributed significantly to the program included:

Mr. D. Goodridge	-	Avionics Engineer
Mr. N. Ham	-	Senior Staff Engineer, Aerodynamics
Mr. R. Hollrock	-	Design Specialist
Mr. D. LaBarre	-	Avionics Specialist
Mr. R. Mack	-	Chief, Automatic Controls
Mr. H. McIntyre	-	Dynamics Specialist
Mr. E. Schultz	-	Supervisor, Advance Research
Mr. M. Smith	-	Dynamics Analyst
Mr. W. Storer	-	Stress Engineer Specialist

ABSTRACT

Analytical studies on the performance, stability, and control characteristics of rotary-wing decelerators in axial descent, controlled glide flight, and flared landings were performed to investigate the potential capabilities of stored energy rotor systems for the retardation and controlled recovery of payloads. Rotor parameters such as diameter, solidity, disc loading, mass, etc., were considered. Theoretical predictions are compared with experimental test results.

Wind tunnel tests simulating typical re-entry trajectory altitude and dynamic conditions were performed on a rotary-wing decelerator system, similar in configuration and construction to the free-flight test rotor system, at speeds from Mach 0.5 to 3.0 to demonstrate feasibility of deploying and operating such systems at supersonic speeds in axial flow and to determine the rotor and governor characteristics for such an operation.

Free-flight drop tests with remotely-controlled rotary-wing test vehicles launched at subsonic speeds were performed to demonstrate the feasibility of controlled recovery, study stability and response to control, explore the performance potential, and determine problem areas requiring additional research or investigation.

Potential applications for rotary-wing decelerator systems were studied. System characteristics are related to mission requirements.

Conclusions formed on the basis of the analytical studies and experimental tests are presented and recommendations are made relative to additional research and applications.

This technical documentary report has been reviewed and is approved.

THERON J. BAKER
Vehicle Equipment Division
AF Flight Dynamics Laboratory

TABLE OF CONTENTS

TABLE OF CONTENTS (Cont'd)

TABLE OF CONTENTS (Cont'd)

LIST OF ILLUSTRATIONS

LIST OF ILLUSTRATIONS (Cont'd)

LIST OF ILLUSTRATIONS (Cont'd)

LIST OF ILLUSTRATIONS (Cont'd)

LIST OF ILLUSTRATIONS (Cont'd)

LIST OF ILLUSTRATIONS (Cont'd)

LIST OF ILLUSTRATIONS (Cont'd)

LIST OF TABLES

LIST OF SYMBOLS

A,B,C, etc.	Coefficients in lift and torque force expressions; suffixed 1, 2, and 3 is an integrated variation of these coefficients
A	Rotor disc area, drag area; sq ft
$\bar{A}$	Surface area, sq ft
A_{1Z}	Lateral tilt of no-feather axis with respect to the X-Z plane, positive tilted right; radians or degrees
a	Acceleration or deceleration, ft/sec^2
a'	Angle between the projection of the rotor force vector in the plane of symmetry and the no-feather axis, positive force vector tilted back; radians or degrees
b	Number of blades
b'	Angle between the projection of the rotor force vector on the Y-Z plane and the no-feather axis, positive vector tilted right; radians or degrees
b_1	Lateral tilt of tip path plane with respect to no-feather axis, positive rotor tilted to right; radians or degrees
B_{1Z}	Longitudinal tilt of no-feather axis with respect to the Y-Z plane, positive tilted forward; radians or degrees
c	Blade chord
C_D	Total drag-force coefficient
C_{D_R}	Rotor thrust or drag-force coefficient
C_f	Skin friction coefficient
C_L	Lift-force coefficient
C_N	Blade section normal-force coefficient

C_{N_o}	Constant portion of C_N
C_n	Rotor yawing-moment coefficient
C_T	Rotor thrust-force coefficient, $T/\rho(\Omega R)^2\pi R^2$
C_y	Rotor side-force coefficient
C/C_c	Critical damping ratio
D	Drag force
D_f	Parasite drag of non-rotor components
e	Blade flapping hinge offset, ft; natural logarithm
E_y	$1/2\ (e\ b\ S_b\ \Omega^2)$
F	Skin friction parameter
f	Equivalent flat plate area, ft^2
F_c	Blade centrifugal force, lbs
F_s	Governor spring force, lbs
G, g	Gravitational acceleration
H	Component of R perpendicular to the no-feather axis along the X-axis, positive lateral force at hub right; lbs
$\dot{H}$	Energy/area/time
$\dot{H}$	Heat transfer per unit area
h	Heat transfer coefficient; distance beween center of gravity and hub; ft
H_o	Energy/area/length distance along trajectory
I_p	Rotor polar moment of inertia, slug-ft^2

I_x, I_y, I_z	Moment of inertia about the X, Y, and Z axes respectively, slug-ft^2
K_E	Kinetic energy
L	Lift force
ℓ	Rotor blade span; distance between center of gravity and body aerodynamic center; ft
ℓ_s	Rotor blade length behind shock wave, ft
M	Mach number; rotor figure of merit
m	Mass, slug-ft^2
m_b	Rotor total blade mass, slug-ft^2
M_f	Aerodynamic pitching moment of fuselage about the center of gravity, positive nose-up; ft-lbs
M_{h_1}	Longitudinal moment at rotor hub, positive nose-up moment; ft-lbs
M_{h_2}	Lateral moment at rotor hub, positive clockwise moment about X-axis; ft-lbs
M_x	Moment about X-axis, ft-lbs
N,n	Load factor, T/W
n	Vehicle motion perpendicular
n_o	Initial load factor
N_2	Nitrogen molecule
O_2	Oxygen molecule
P	Rotor power, HP
PNF	Plane of no-feathering
p,q,r	Incremental change in angular velocities around X, Y, and Z axes respectively, positive according to right-hand rule; radians/second

LIST OF SYMBOLS (Cont'd)

Q	Over-all heat transfer, BTU's; torque at rotor shaft; ft-lbs
R	Blade radius; resultant rotor force; lbs
RPM	Rotor speed, revolutions/minute
r, r_n	Radius; blade span station; ft
$\bar{r}$	Non-dimensional radius, recovery factor
R_G	Glide rotor radius, ft
R_v	Vertical descent rotor radius, ft
S_b	Blade area, ft^2
S_t	Tail distance from body center of gravity, horizontal; ft
T	Rotor thrust, lbs; temperature; component of R parallel to the no-feather axis; lbs
t	Time, seconds; blade airfoil thickness, ft
T_{aw}	Adiabatic wall temperature
t_f	Time required for flare, seconds
T_w	Surface wall temperature
U	Total airspeed, ft/sec or mph
u,v,w	Component of total airspeed along the X, Y, and Z axes, respectively; ft/sec
U_p	Velocity perpendicular to PNF
U_t	Velocity in PNF
V	Velocity
V_E	Re-entry velocity
V^o	Free-stream velocity

LIST OF SYMBOLS (Cont'd)

V_R	Rotational component of velocity
V_v	Vertical rate of descent, ft/sec
W	Weight, lbs
W_b	Total blade weight, lbs
W_{b_G}	Total blade weight, glide descent rotor
W_{b_V}	Total blade weight, vertical descent rotor
W_{R_G}	Total blade weight, glide descent rotor
W_{R_V}	Total blade weight, vertical descent rotor
X, Y, Z	Principal body axes, a right-handed orthogonal axes system with the X, Y, and Z axes aligned with the body principal axes. The origin of the axes frame is the center of gravity of the ROTOCHUTE. The X-axis is positive forward, the Y-axis is positive to the right, and the Z-axis is positive downward. Forces directed along the X, Y, and Z axes are considered positive. Moments are positive clockwise about the X, Y, and Z axes when viewed along the positive direction of the axis.
X_p	Distance from blade hinge to point of action of resultant blade axial force
X_{c_g}	Distance from blade hinge to blade center of gravity
Y	Altitude, ft
Y_E	Re-entry altitude, ft
α	Angle between free stream velocity vector and rotor tip path plane
α_f	Fuselage angle of attack, angle between the projection of the relative wind on the plane of symmetry and the ROTOCHUTE X-axis, positive nose-up; radians or degrees

α_r	Rotor angle of attack, angle between the flight path and the plane perpendicular to axis of no-feathering, positive no-feather axis tilted back; radians or degrees
α_x	Pitch angle, positive nose-up, radians
α_y	Roll angle, positive blade tip down, radians
β	Blade flapping or coning angle, angle between blade and plane perpendicular to rotor axis of rotation; density-altitude relation constant
β_f	Fuselage angle of sideslip, angle between the relative wind and the X-Z plane, positive nose left, radians or degrees
γ	Flight path angle from horizon; Ratio of specific heats for air, c_p/c_v
δ_t	Tail angle of attack, radians
ζ	Non-dimensional offset
θ	Fuselage attitude angle, angle between the X-axis and the horizontal plane, positive nose-up; radians or degrees
Θ	Collective pitch, constant term in Fourier series expressing blade pitch angle; radians or degrees
Θ_E	Re-entry angle between flight path and horizon; degrees
λ, λ_r	Blade local inflow angle, U_p
λ_d	Axial descent advance ratio, $(U/\Omega R)$
μ	Glide advance ratio, $(U \cos \alpha/\Omega R)$
ρ	Standard air density, slugs/ft^2
σ	Rotor solidity, ratio of blade area to rotor disc area

τ_1	Differentiation lag constant
τ_2	Selectric actuator lag
Φ	Fuselage roll angle, angle between the Y-axis and the horizontal line, the Y-Z plane, positive right roll; radians or degrees
ϕ	Inflow angle at blade element in plane perpendicular blade span axis, radians
Ψ	Rotor blade azimuth angle, zero aft
Ω, w	Rotor rotational speed, radians/sec
ζ	Vehicle motion about rotor blade direction

SUBSCRIPTS

b	Blade
c	Servo-command signal
e	Servo error signal
f	Fuselage; final condition
L	Response with first-order time lag
t	Vertical tail
o	Steady-state or initial condition
r	Rotor

1. INTRODUCTION

Accomplishments in aerospace endeavors within the past few years have made possible launchings of manned and instrumented aerospace vehicles to high altitudes and earth orbits. Interplanetary exploration and travel is imminent. Accurate control, staging, and guidance is possible throughout the launch, ascent, and orbiting phase of the mission. Re-entry may be initiated at any desired point in space. From then on, however, limitations of present-day recovery systems preclude precise flight path control of the returning aerospace vehicle during re-entry and at touchdown.

To achieve the desired degree of control over re-entry sequences and guidance during the terminal phase of space missions, much interest and effort is being expended in investigating and developing recovery systems that will provide safer, more precise and more economical recovery.

Preliminary evaluation of rotary-wing decelerator and recovery systems reveals potential characteristics and performance capabilities very appropriate for the recovery function. The stored energy rotor recovery system combines in one unit the features for initial retardation and stabilization, drag modulation, useful L/D glide, maneuverability, and terminal flare for near-zero velocity touchdown.

Recognizing the importance of this potential, the Aeronautical Systems Division established and sponsored the research program documented herein to demonstrate the feasibility of using stored energy rotor systems for the retardation and recovery of payloads and investigate capabilities. The program compared analytically derived performance with experimental test results.

The experimental test phases of the program involved extensive use of Kaman Aircraft's demonstrated and proven ROTOCHUTE* concept, one of the more successful rotary-wing

* Registered Trade Mark

Manuscript released by the author 22 July 1963 for publication as an ASD Technical Documentary Report

decelerator systems. The ROTOCHUTE is a multi-bladed helicopter type rotor system providing controlled aerodynamic retardation in autorotative descent.

Development of the system for aerial delivery of supply containers from aircraft flying at high speeds and low altitudes began in late 1952 under Office of Naval Research Contract NOnr 901(00). The result was the ROTOCHUTE decelerator system incorporating a governing mechanism which precludes rotor overspeed throughout deployment, retardation, and descent. With governing, a lightweight rotor system provides retardation and stable descent over a wide spectrum of operational speeds.

Numerous configurations involving fixed and telescoping span blades have since been demonstrated for other applications. Rotor diameters have ranged from 1 foot to 24 feet, payloads from 6 pounds to 900 pounds. Prior to the ASD program, deployment had been performed from aircraft at speeds up to 545 knots and 1100 feet altitude, at Mach 0.98 from a missile, and at Mach 1.2 on a 6"-47 caliber, cannon-fired flare shell.

Under U.S. Navy sponsorship, Kaman Aircraft also developed remote control systems for flying unmanned drone helicopters, and in 1952 successfully demonstrated the feasibility of controlling a helicopter by radio commands from a remote control station. Further effort, sponsored by Bureau of Naval Weapons, improved system performance, accuracy, reliability, and ease of control.

Capabilities in the above technological areas provided the natural combination of knowledge and skills required to develop the remotely-controlled flight test vehicle for the ASD program experimental tests.

Section 2 of this report summarizes the analytical investigations performed during the program. The analyses were directed toward establishing design criteria to derive optimum performance from a stored energy rotor recovery system and to provide guidance in the design of the test systems. The effects of rotor diameter, solidity, disc loading, and other parameters on performance, stability, and control were investigated. Glide flight studies were limited to subsonic speeds. Axial flow operation at supersonic speeds was studied and early results were encouraging enough to initiate the wind tunnel tests.

Section 3 covers the program wind tunnel test phase. The wind tunnel test objectives are delineated and the KRC-6M test rotor system and pre-tunnel test checkout are described. Test procedures, data, and results from the runs in the Transonic Circuit (Mach 0.5 to Mach 1.5) and Supersonic Circuit (Mach 1.6 to Mach 3.0) in Arnold Engineering Development Center's Propulsion Wind Tunnel Facility, Tullahoma, Tennessee, are presented. Test data are compared with performance predicted analytically.

Section 4 deals with the free-flight air drops conducted at the U.S. Air Force 6511th Test Group (Parachutes) Facility at El Centro, California. The KRC-6 test vehicle and preflight ground testing are described. The individual drops are discussed and results analyzed.

Preliminary design considerations, requirements, and capabilities of rotary-wing decelerator systems relative to potential applications in various types of recovery missions are discussed in Section 5.

Conclusions based on the analytical investigations and experimental test results are presented in Section 6. Also included in the section are recommendations for follow-on research and development to realize the full potential of stored energy rotor systems for recovery.

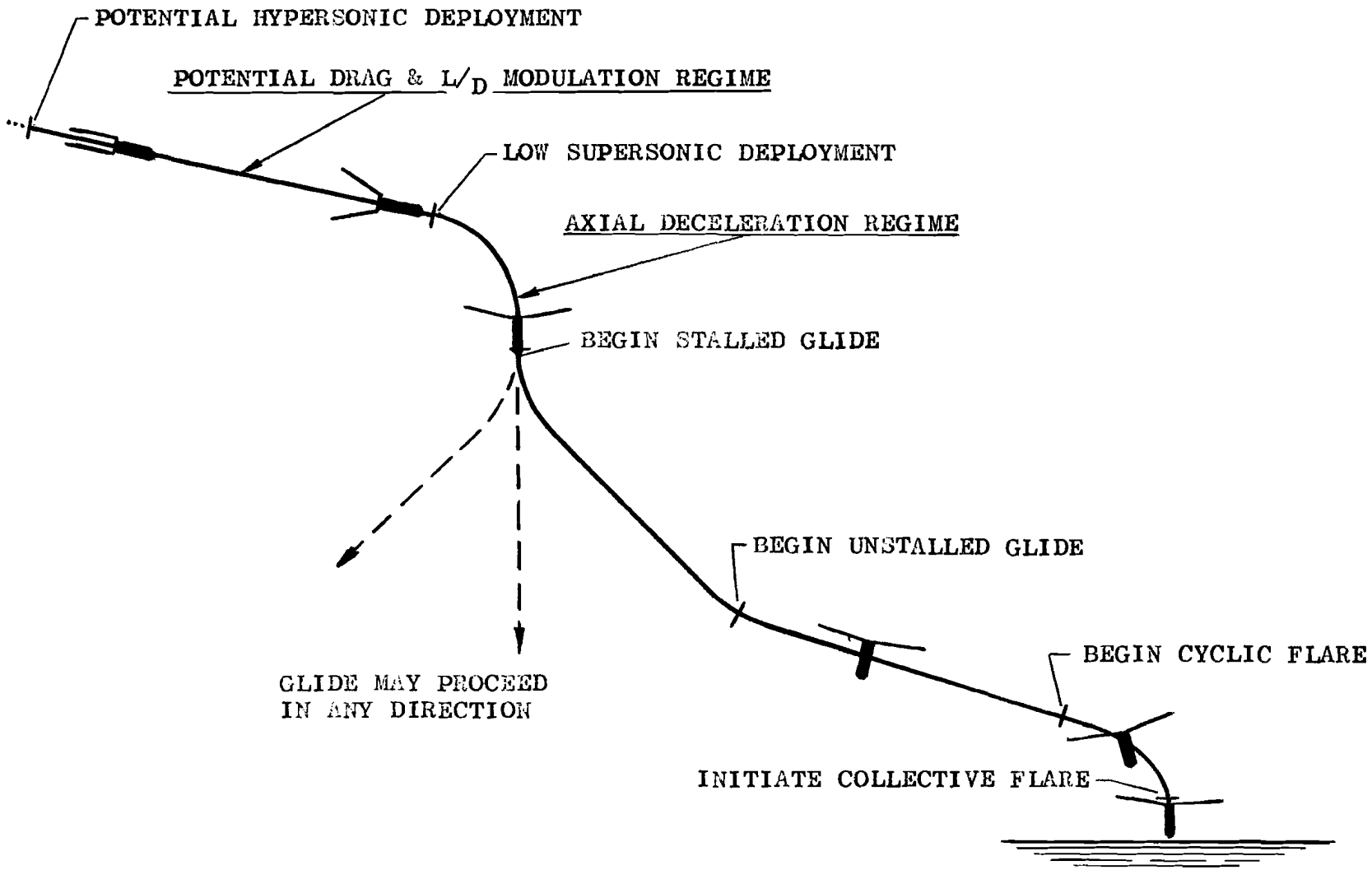

PHASES OF OPERATION DURING RECOVERY
FIGURE 1

2. ANALYTICAL INVESTIGATIONS

Application of rotary-wing decelerators to the recovery of space vehicles involves consideration of a variety of flight conditions and design compromises. A typical recovery flight profile is presented in Figure 1. Two possible initial conditions are indicated. One involves deployment at hypersonic speeds shortly after re-entry into the earth's atmosphere, and subsequent variation of the rotor drag and L/D ratio to achieve an optimum trajectory with respect to deceleration, heating, and guidance. More detailed studies are needed to accurately estimate the aerodynamics and heat protection requirements of such a rotor. Recovery for immediate applications is based on deployment at supersonic speeds involving limited heating.

Deployment of a ROTOCHUTE system is initiated by applying coning, pitch, and sweep to the rotor blades by means of the deployment mechanism to generate an acceleration torque about the rotor axis of rotation. Deployment time is a function of the above parameters.

The phase following deployment involves axial deceleration of the vehicle until it assumes a near-vertical attitude descent. During this time, the rotor accelerates to the equilibrium rotational speed prescribed by the governor. Rotational speed control is obtained by varying blade pitch angle to maintain equilibrium autorotational torque for any flight condition.

At high inflow velocities, the rotor blades are completely stalled over the entire span and act as drag plates. In this condition, the rotor drag or retardation force is largely dependent on the rotor blade area. Limited glide during this phase may be initiated by tilting the rotor disc relative to the vehicle to generate a horizontal component of the rotor drag force. A terminal glide condition at a given altitude results when a balance is attained between the vehicle vertical aerodynamic forces and vehicle weight, and between the vehicle horizontal rotor forces and vehicle drag. Gliding velocities are largely dependent upon the vehicle system equivalent flat plate drag area and rotor disc loading.

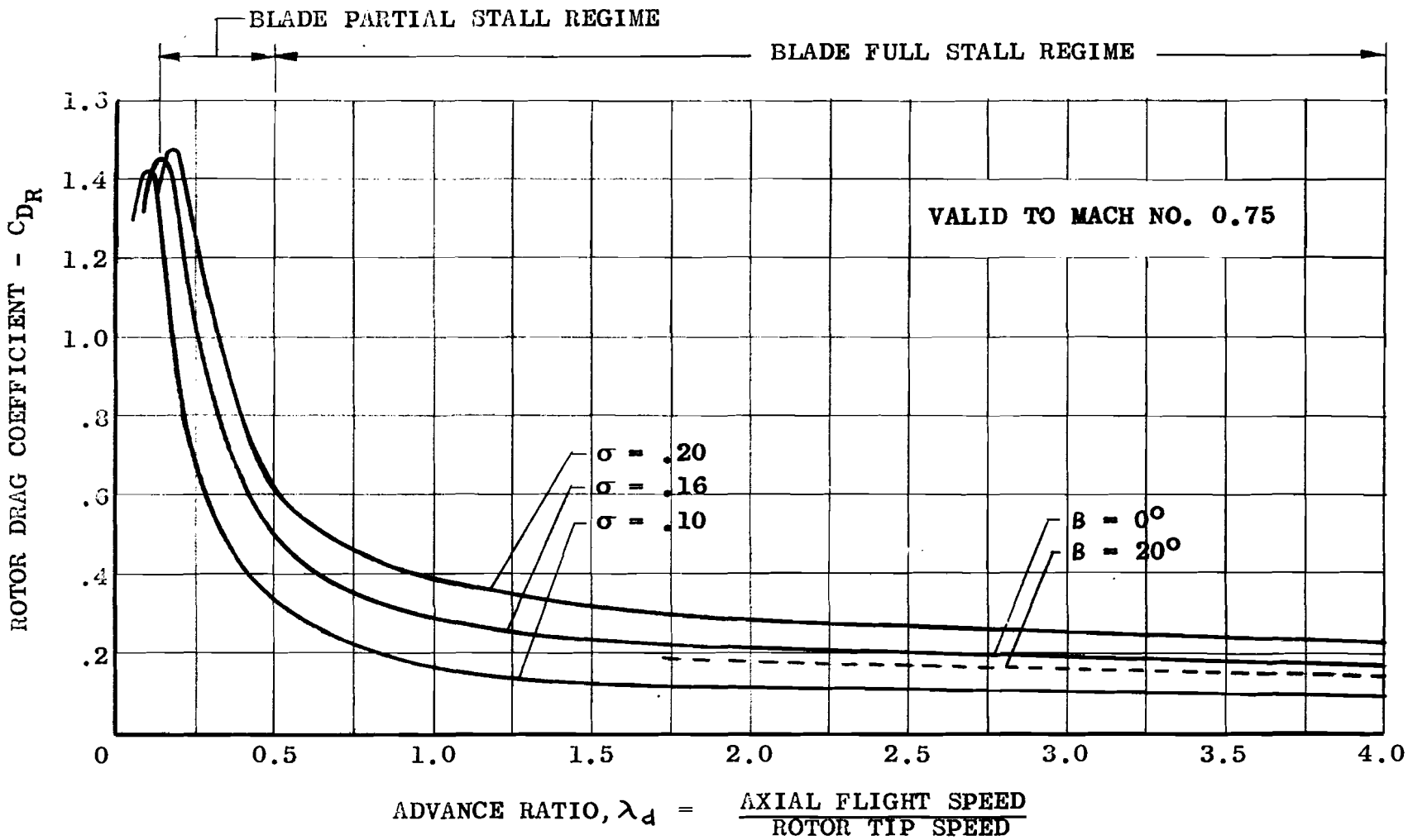

ROTOR DRAG COEFFICIENT VARIATION WITH ADVANCE RATIO

FIGURE 2

Rotor blades become "unstalled" over the major portion of the span when the inflow velocity becomes low relative to blade tip speed. The altitude at which this transition occurs is influenced by the rotor blade loading and tip speed. A much shallower glide is now possible from this altitude down to the landing area. The rotor is operating in a condition comparable to that of a helicopter with power off.

For landing, the horizontal velocity of the vehicle may be reduced to near-zero by tilting the rotor disc aft relative to its equilibrium glide attitude by a specified amount and at a specified rate. This maneuver is called the "cyclic flare". The vehicle will now be sinking at a rate dependent upon the rotor disc loading.

The final flight phase prior to ground contact uses the rotational energy of the rotor to decelerate the vehicle to near-zero impact velocity. "Collective flare" is performed by rapidly increasing blade pitch collectively to near-stall values to generate maximum lift. The rotor RPM will drop off during the "flare". The amount of rotor rotational energy is a function of the sinking speed subsequent to the cyclic flare.

Typical ROTOCHUTE drag characteristics in axial flight are shown in Figure 2 as a function of the advance ratio (λ_d), the ratio of axial descent speed to rotor tip speed. For a selected rotor tip speed, the maximum drag coefficient is realized at lower descent speeds with lower rotor solidities. At higher axial descent speeds, the drag coefficient increases with the rotor solidity. Therefore, a compromise is required in the choice of blade solidity for a particular application, including the consideration that blade weight generally increases with increasing solidity. Coning of the blades, dependent upon blade inertia characteristics and tip speed, influences the resultant drag at high advance ratios.

Terminal descent velocity of a ROTOCHUTE may be expressed by:

$$V_v = \sqrt{\frac{W/A}{1/2 \quad \rho \quad C_{D_R}}}$$

For sea level conditions and $C_{D_R} = 1.4$

$$V_v = 25 \sqrt{W/A}$$

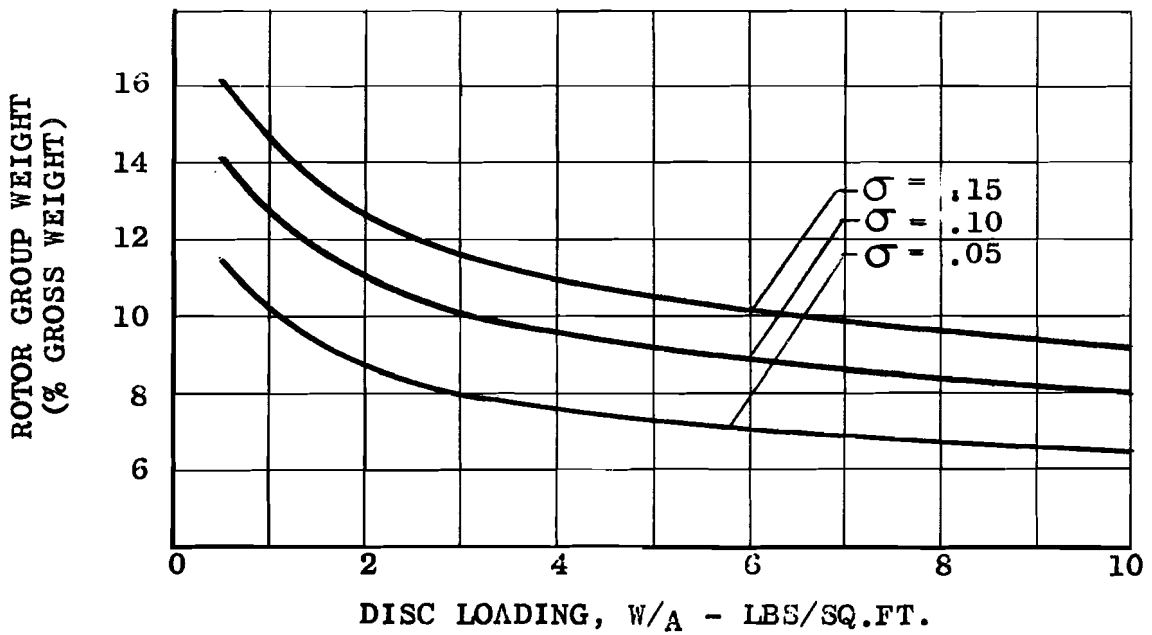

VARIATION OF ROTOR GROUP WEIGHT AS A FUNCTION OF ROTOR DISC LOADING & SOLIDITY

FIGURE 3

Choice of the rotor disc loading is, therefore, determined by the desired descent velocity, rotor size consideration, and weight limitation.

Approximate rotor group weight variation with disc loading and rotor solidity is presented in Figure 3 for gross weights in the 6,000- to 12,000-pound range. The curves were determined from the helicopter weight formula of Reference 1, reduced by 20 per cent to account for advances in the state-of-the-art and the fact that a ROTOCHUTE rotor is not shaft-driven. The approximation includes the weight of rotor blades, retention fittings, hub assembly, and control linkages.

The successful operation of the rotary-wing decelerator is predicated on its ability to operate in new environments and high velocity inflow. The following paragraphs discuss the analytical studies performed to determine the aerodynamic performance and stability of rotary-wing decelerators in the various flight modes.

SUMMARY OF ANALYSES

The analyses indicated that controlled recovery of payloads with rotary-wing decelerators is feasible. No basic technical problem areas were encountered.

The analyses indicate that rigid blade rotors, at least, may be deployed and operated at supersonic speeds early in the re-entry for retardation and stabilization. As an example, a rotor for a Mercury-type capsule would develop up to 10,000 pounds drag force at Mach 2.0 speed and 100,000 feet altitude. The drag force could be modulated to lower values for trajectory control by controlling rotor tip speeds which, in turn, control blade coning. For example, coning the blades to 45^{o} would change the drag force to approximately 5,000 pounds.

Rotor systems alone have potential glide L/D ratios of five or better, depending on the blade profile and rotor system parasite drag characteristics. The addition of a payload body decreases the glide capability, but glides at L/D ratios 2.5 to 3.0 are very feasible. Glide at L/D ratio of 3.0 from 25,000 feet altitude would provide approximately 15 miles range in still air.

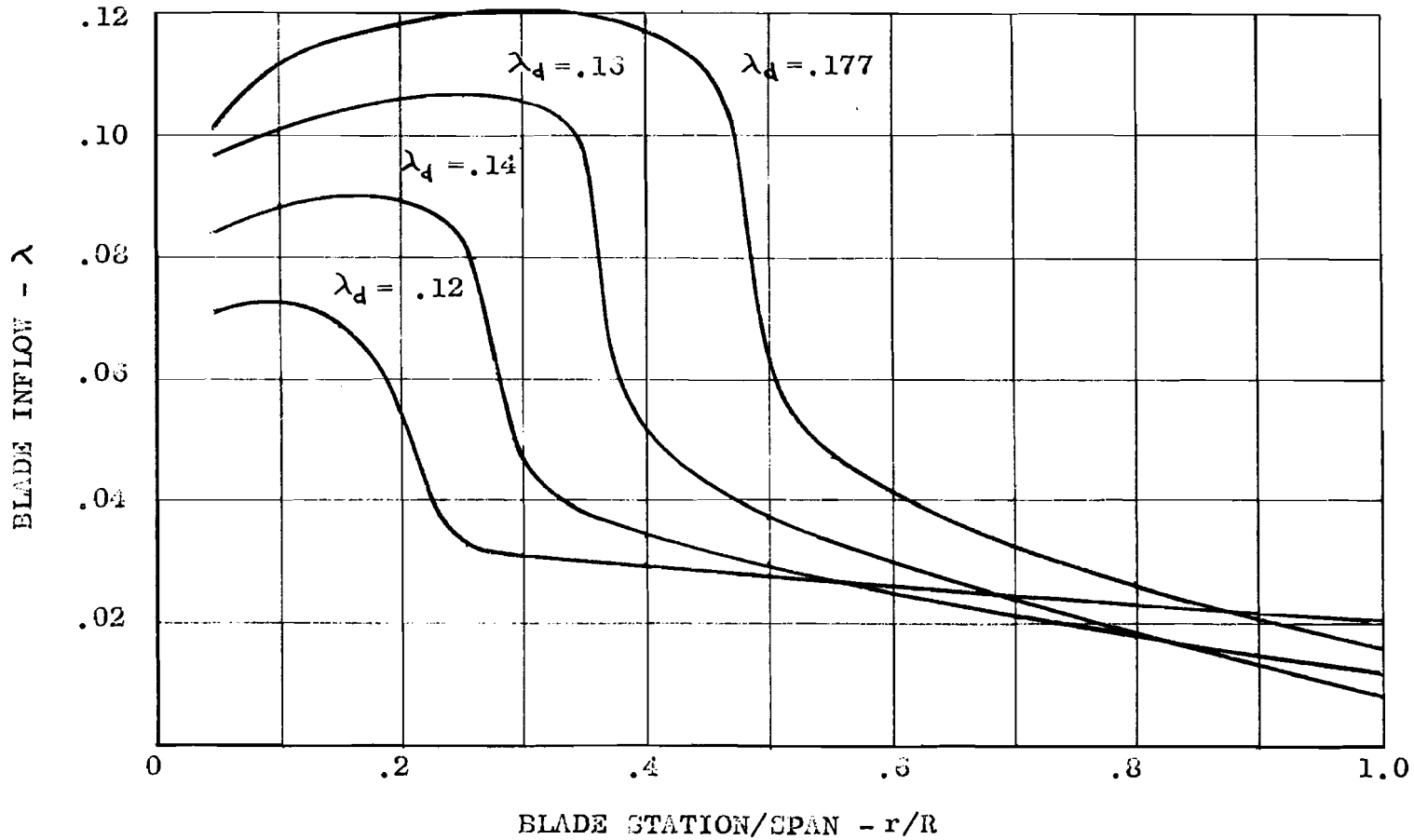

VARIATION OF BLADE INFLOW AS A FUNCTION OF BLADE STATION

FIGURE 4

Although rotor systems may not always be inherently stable, they are controllable manually or with automatic stabilization systems. Guidance control may be manual or remote. Programming a mission is feasible. Additional studies for a better understanding of inherent stability and parametric effects are required.

Although it is best to design for rates of descent approximately 50 to 60 feet per second from the rotor size and weight consideration, lower descent rates are possible with larger diameter rotors.

Impact velocities, in the order of five feet per second or less, are feasible through cyclic and collective flare retardation. It is recognized that pilot proficiency is an important factor during the maneuver; but control requirement characteristics for the maneuver may be determined through tests and used for programmed automatic landings.

A. AERODYNAMIC STUDIES

1. Axial Flight Model

a. Unstalled Regime

In this regime, near-terminal or steady-state descent, only the inboard portion of rotor blades is stalled. In the usual helicopter notation, this mode of operation borders the windmill brake and vortex ring states. Induced velocity in this regime is greater than or equal to half the descent velocity.

The lack of uniform inflow along the rotor blade span precludes the use of standard helicopter theory in predicting the rotor performance. Instead, a "strip analysis" must be performed.

A number of stations along the blade span are analyzed. Since the net shaft torque in autorotation is zero, inflow at the various stations may be determined by iteration for particular value of axial flow velocity and assumed blade pitch. Then, rotor thrust may be calculated. Details regarding the "strip analysis" and analytical steps are presented in Appendix 1.

Results of analyses for the KRC-6 rotor system have been plotted. Figure 4 indicates the variation of inflow along the blade span for various advance ratios. Lack of uniformity of the inflow is very evident for all advance ratios studied. Figures 5 and 6 show the near-linear variation of blade pitch and thrust with descent velocity. Blade pitch is thus a suitable parameter for positive governing in axial flight. Figure 7 presents the calculated drag-force coefficient at various descent velocities in the "unstalled" regime under study.

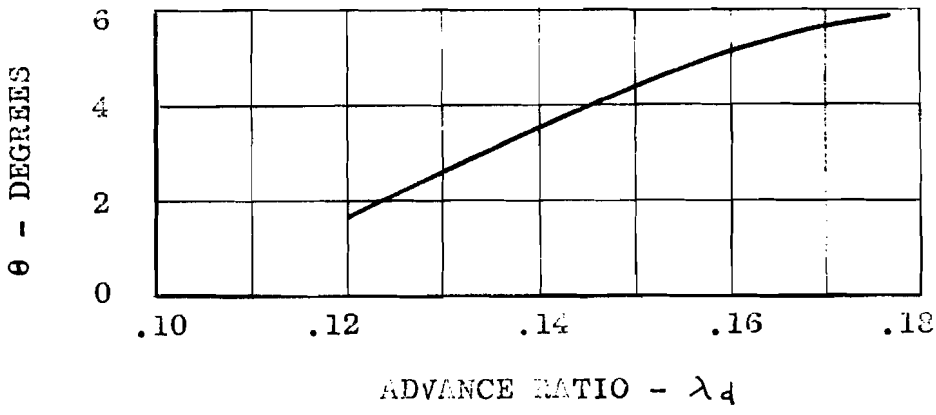

FIGURE 5

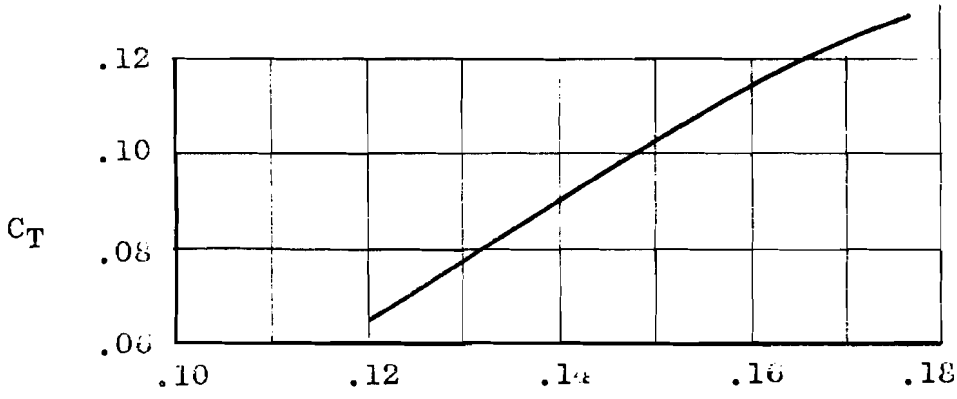

FIGURE 6

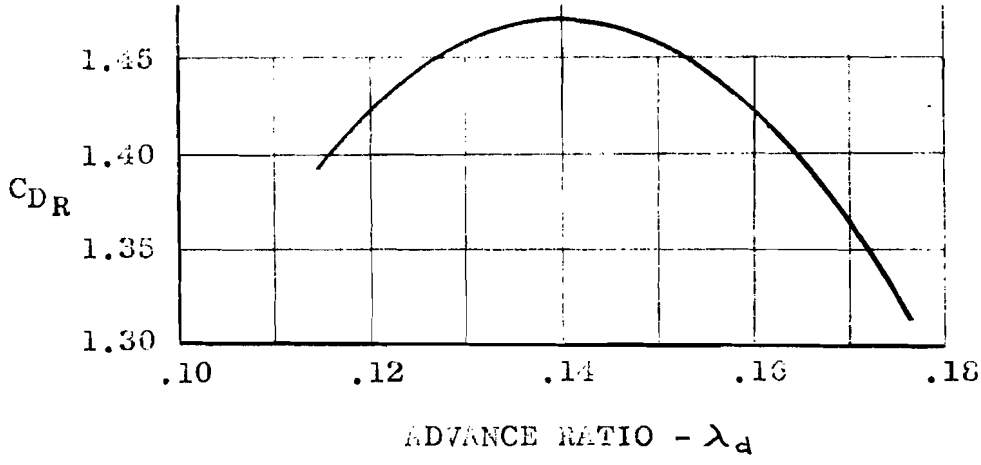

FIGURE 7

b. Stalled Regime

At higher advance ratios and inflow, the rotor blades become completely stalled. A different analytical approach is used for this regime. Blade section characteristics, expressed as a function of local angle of attack, are used. The analysis, discussed in detail in Appendix 1, covers operation of a rotor with offset flapping hinges from subsonic to hypersonic speeds. Governor operation and requirements for rotor rotational equilibrium are included.

In the stalled regime, rotor drag is more a variable of blade frontal area, i.e. solidity and coning, rather than rotor rotational speed.

Caclulated performance is presented and compared with experimental test results in Section 3, Wind Tunnel Tests.

2. Glide Flight

a. Low Subsonic Speed Glide

Analytical studies of glide were restricted to glide at low advance ratios because the regime represented the program's prime area of interest. The performance and trim calculations for glide at low advance ratios are based on conventional equations of equilibrium and data from Reference 2. Details of the analysis are found in Appendix 1.

Because the charts in Reference 2 did not yield desired accuracy for the range of parameters investigated, the relevant equations were programmed on an IBM digital computer and new charts were developed. The equilibrium equations were written with three degrees of freedom, with and without the effects of a horizontal trim surface.

Trim data was calculated for various equivalent flat plate areas for eight-foot and ten-foot diameter rotors.

Vehicle glide path angle (γ) variation is shown in Figure 8. It will be noted that the glide path angle with respect to the horizon is better with the larger rotor. The glide angle is also affected by the vehicle equivalent flat plate area. The glide becomes steeper with increasing equivalent flat plate area. For a given rotor, optimum glide occurs at lower advance ratios with increasing flat plate area.

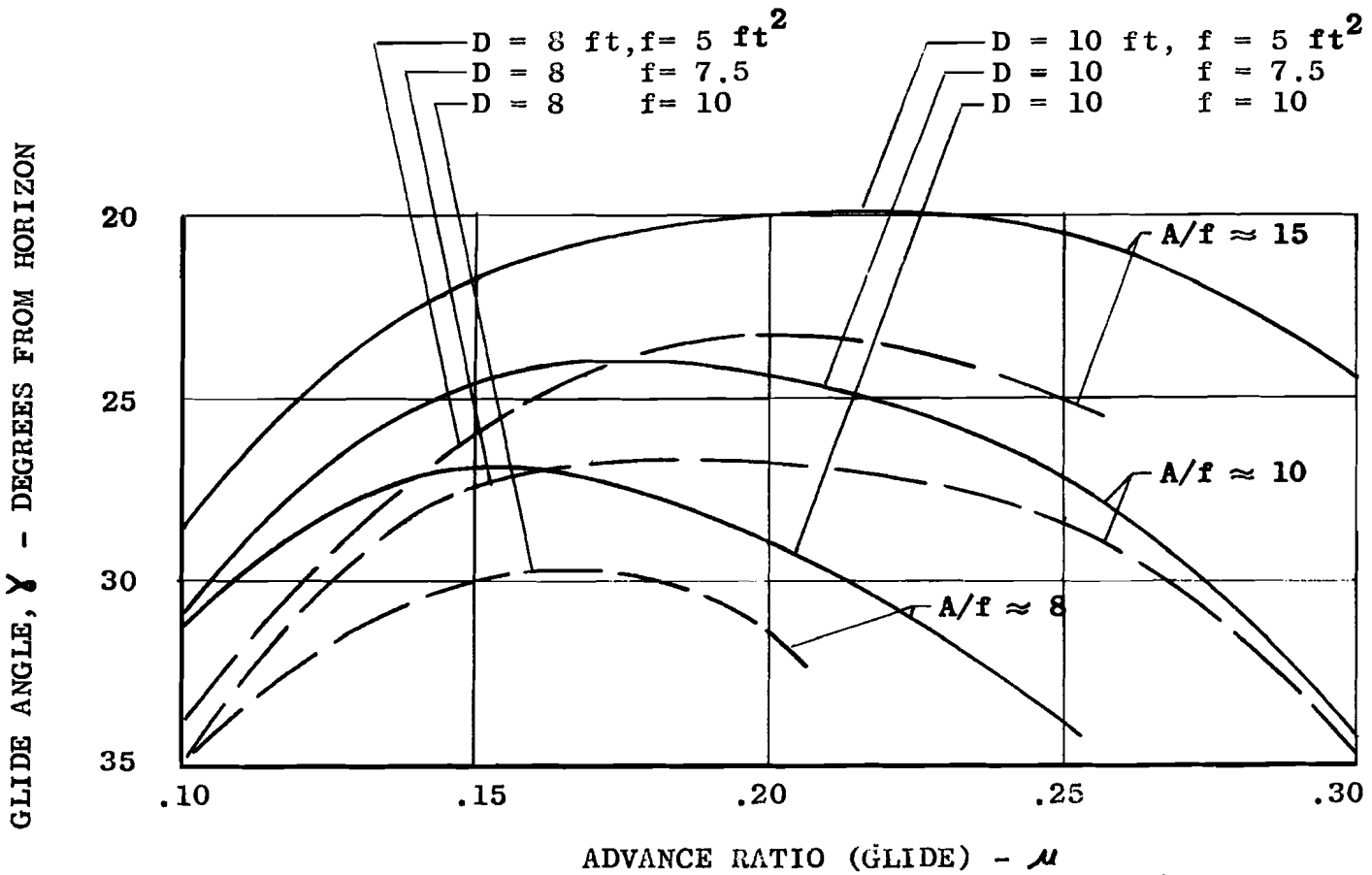

VARIATION OF GLIDE PATH ANGLE WITH GLIDE SPEED FOR 8 & 10 FOOT DIAMETER ROTORS AND VARIOUS EQUIVALENT FLAT PLATE AREAS, f

FIGURE 8

Figure 9 presents the test vehicle pitch attitude variation with advance ratios. An almost linear variation is noted at advance ratios greater than 0.15 and is significant from a stability viewpoint. Its relevance is discussed under Stability and Control.

Rotor hub tilt requirements are indicated in Figure 10. In general, the control requirement is less with the larger rotor or at higher body drag for the flight test vehicle configuration studied.

b. Supersonic Glide Flight

The capability for supersonic glide is a desirable means of extending the glide range of rotary-wing recovery systems. If feasible, supersonic glide could be initiated at high altitude during a re-entry trajectory. A typical glide trajectory could be characterized by three flight regimes.

1. High supersonic glide where the rotational tip speeds are small compared to flight speeds.

2. Transonic glide where the rotational tip speeds and flight speeds are approximately of the same order. Flow conditions in this regime are complex.

3. Subsonic glide where rotational tip speeds are high compared with the flight speeds. Flow conditions generally are subsonic or near subsonic.

A rotor designed for optimum operation in Condition "1" must also operate efficiently in Condition "3", and be capable of at least passing through the transient Condition "2".

The supersonic analysis performed during the present investigation has concentrated on the axial flight condition, with the glide maneuver being treated in a qualitative manner. Certain general conclusions have been formed relative to supersonic glide. First, from an aerodynamic heating standpoint, the supersonic gliding rotor is more critical than the rotor operating at the same stagnation temperature in axial flow. In axial flow, the free stream is approaching the blade in a nearly perpendicular direction, and the blade is equivalent to

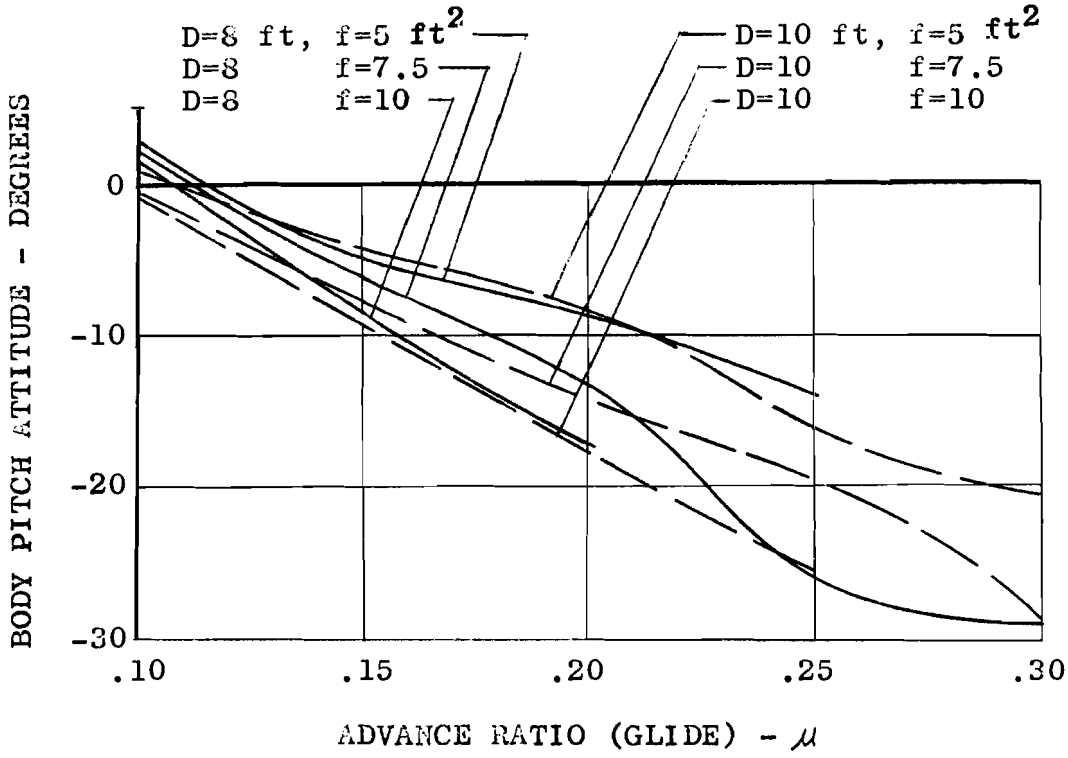

FIGURE 9

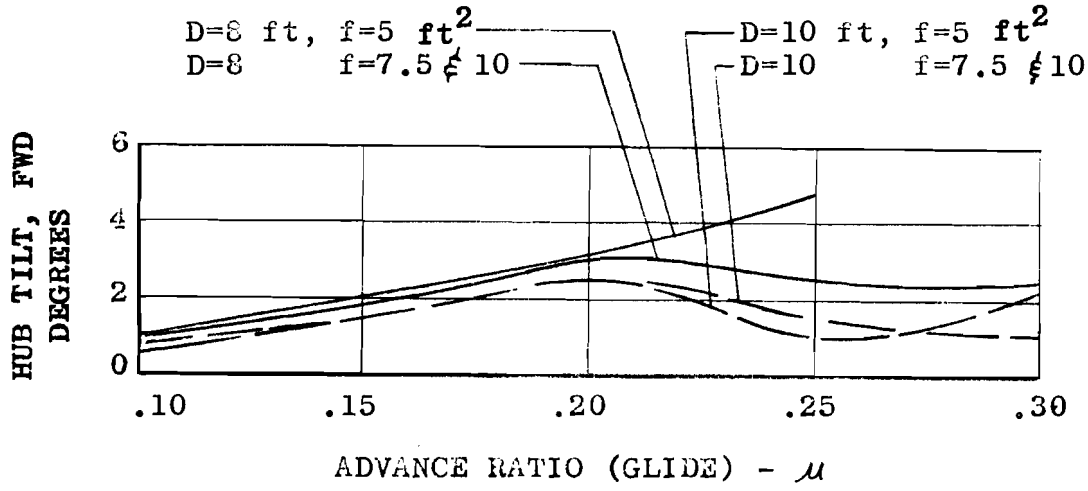

FIGURE 10

a very blunt body. The boundary layer velocity gradient near the blunt body is low, hence heat transfer is low. Also, there is considerable material to conduct and distribute the heat. These beneficial considerations are lost in the gliding rotor. In the gliding rotor, the stagnation point is located on the relatively sharp leading and trailing edges. For extended glide, it is estimated that the blade skin temperature would approach 85-88 per cent of the stagnation temperature.

Second, the use of higher harmonic cyclic pitch control appears to have considerable merit. At high supersonic speeds, the retreating blade is in a completely reversed flow field. Second harmonic cyclic control can be phased to result in negative blade pitch angles on the retreating blade at an azimuth angle of 270 degrees. Hence, the retreating blade can be used to generate lift in the reversed flow region. With second harmonic control, means must be provided for removing the higher harmonic control for advance ratios less than one.

Four-bladed rotors would have to be used to minimize "two-per-rev" vertical vibration. The vibration generated with two-bladed rotors would most likely be unacceptable.

Third, during the experimental wind tunnel program, the 8-foot rotor was tested at Mach numbers of from 0.5 to 3.0. During this program, the rotor angle of attack was varied up to 9.5 degrees from pure axial flight. Side forces were measured at the supersonic speeds which corresponded to low L/D glide. At Mach numbers up to 3.0, there was no indication of any problems with low L/D glide. However, it should be emphasized that the variation in rotor angle of attack was very restricted and results should not be generalized.

3. Landing

The stored energy of the ROTOCHUTE is composed of the potential energy due to altitude and the kinetic energy due to velocity of the mass, plus the rotational energy in the rotor. Use can be made of this energy in arresting the horizontal and vertical velocity just prior to touchdown. The kinetic energy of translation is used for the cyclic flare, while the rotational energy in the rotor is the energy source for the collective flare.

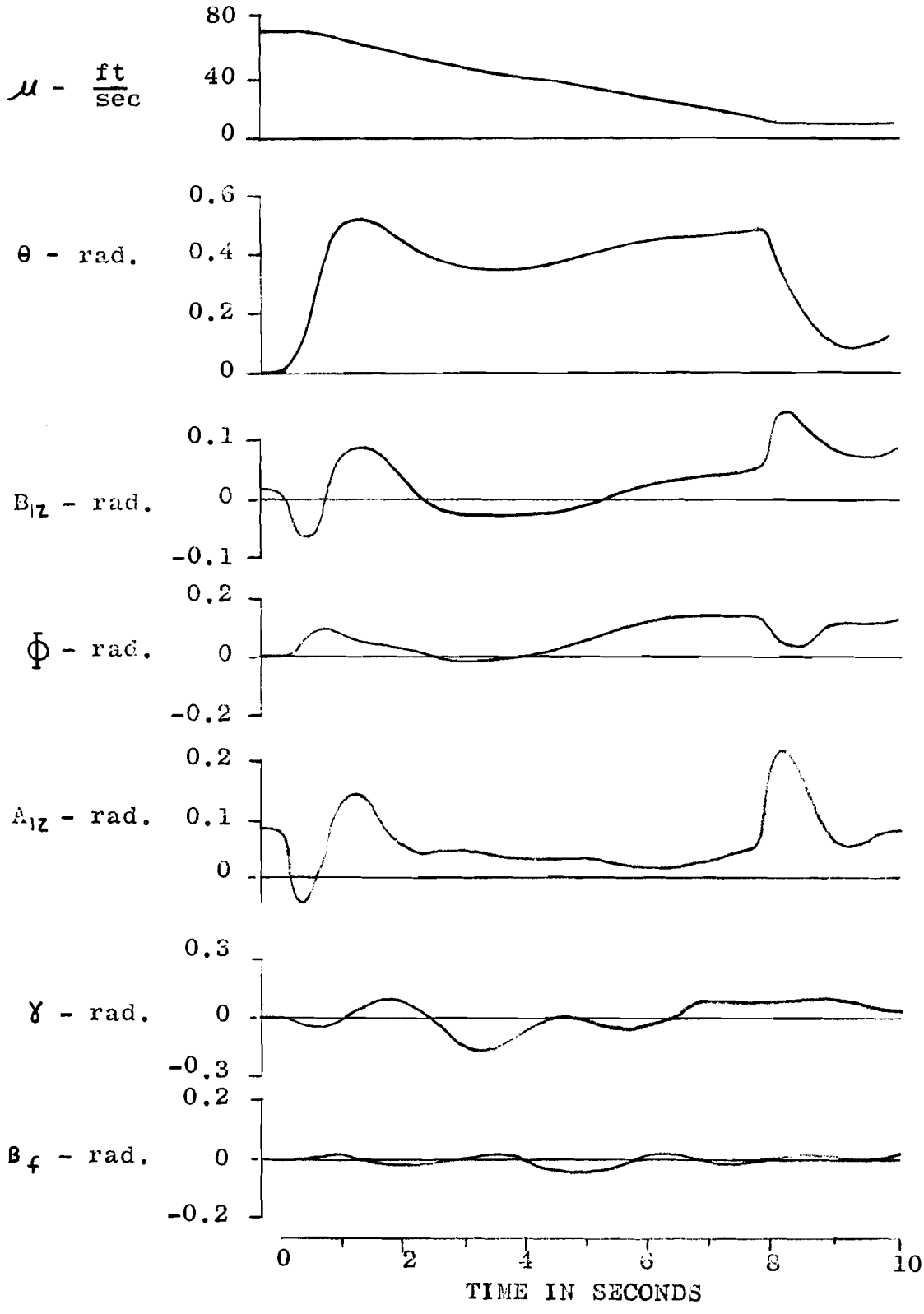

NON-LINEAR RESPONSE TO A 23° Θ_c COMMAND-FLARE SIMULATION

FIGURE 11

a. Cyclic Flare

The glide regime analysis was extended to a "cyclic flare" maneuver. It was deemed best to study the maneuver by simulation on a PACE Analog Computer. During the non-linear cyclic flare simulation of the ROTOCHUTE, derivatives varying significantly with advance ratio were programmed on function multipliers. The servo-motors associated with the function multipliers were driven by the advance ratio (μ) voltage. With this setup, it was possible to simulate cyclic flare maneuvers where large speed variations were encountered.

Figure 11 presents a simulated cyclic flare maneuver. The initial trim forward speed was 76 feet per second (μ = 0.16). The technique used in performing the flare was to command a 23-degree nose-up pitch attitude command. Following this command, the forward speed dropped off in a linear manner. At a forward speed of about 8 feet per second, the attitude command was removed. At this point, collective pitch was increased prior to touchdown. The complete maneuver was performed in about 9 seconds. The lateral ASE appeared capable of satisfactorily controlling roll attitude and heading during this maneuver. Lateral commands could be applied, if desired, to further reduce the roll excursion.

Figure 12 presents a plot of the trajectory profile during the flare maneuver. The divergence in flight path angle is apparent for $t > 6$ seconds. The flare maneuver was initiated at an altitude of 85 feet and required a ground distance of 330 feet to arrest forward speed. The attitude command was for a 23-degree nose-up pitch attitude.

b. Collective Flare

The "collective flare" maneuver may be employed to retard the vertical rate of descent. Stored rotational energy of the rotor is used to generate increased rotor drag or lift just prior to impact by powering the rotor momentarily with the blades set at an optimum high pitch.

If the maneuver is performed after glide and cyclic flare, the vertical descent will already have been partially retarded, leaving less work to be performed by the rotor. However, "collective flare" from vertical axial descent may be desirable in certain applications. Comparative studies of the two modes, presented in Appendix I, were performed. Results indicate that,

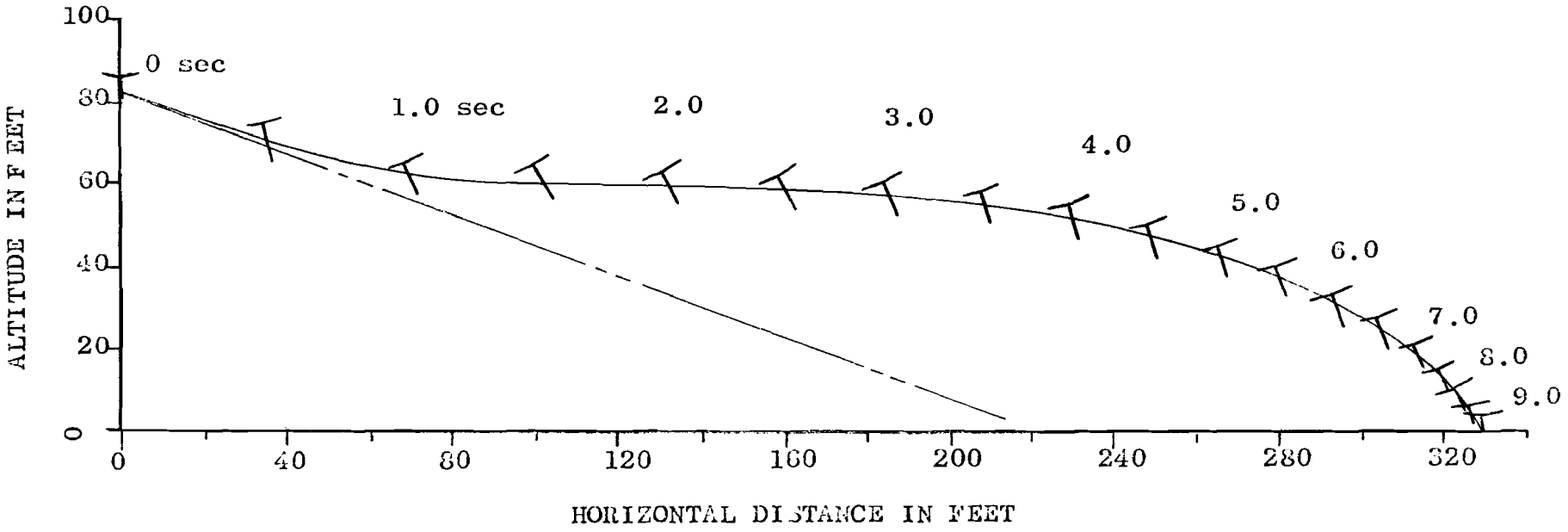

TRAJECTORY PROFILE DURING FLARE MANEUVER

FIGURE 12

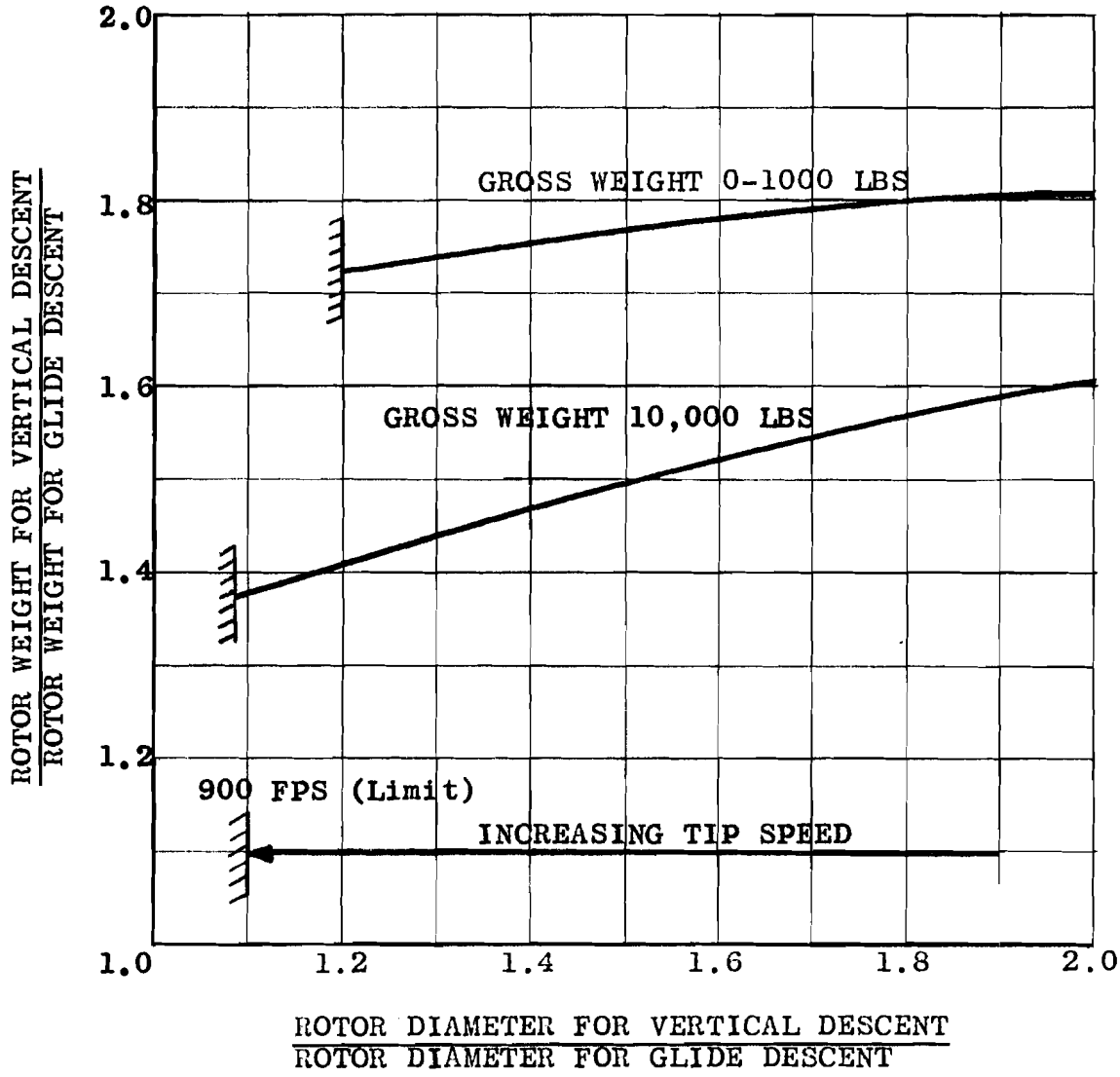

COMPARISON OF REQUIRED ROTOR SIZE AND WEIGHT FOR VERTICAL AND GLIDING AUTOROTATIVE DESCENTS

FIGURE 13

if collective flare is performed after a vertical descent, rather than after glide and cyclic flare, the rotor must be larger and heavier than a gliding rotor.

The results of the analyses are plotted in Figure 13. For gross weights up to 1000 pounds, a rotor to be flared from vertical descent will be at least 1.2 larger in diameter and 1.73 times heavier than a rotor flared from glide. For the 10,000-pound range, the vertical descent rotor will be approximately 1.08 larger and 1.38 heavier. If the diameters are reduced, tip speeds increase above the 900 feet per second limit.

The use of auxiliary rotor power devices would improve the comparison considerably at the expense of increased complexity and probably some penalty in rotor weight and/or size.

B. STABILITY AND CONTROL

1. Subsonic Axial Flight

Actual tests have shown that flight instabilities of ROTOCHUTES in axial flight may be of two modes: "spiral mode", corresponding to the phugoid (long-period, lightly damped) mode in conventional aircraft terminology, in which the flight path is a helix and the body axes remain essentially aligned; and a "wobble mode" in which the body axes wobble but the flight path is linear. It is, of course, possible for both types of instability to occur simultaneously.

Analytical methods have now been developed which identify these modes for a particular configuration. These methods were used to produce Figure 14 which indicates stability trends for the test vehicle with an 8-foot diameter rotor.

Each curve of the figure represents the variation of a root of the perturbation characteristic equation. If any-one of these roots indicates a negative damping ratio, an instability is indicated. If the root frequency is high, the instability is a wobble mode; if low, it is a spiral mode.

D = 8 Ft.
W = 280 Lbs.
I_y = 52 Slug-Ft.

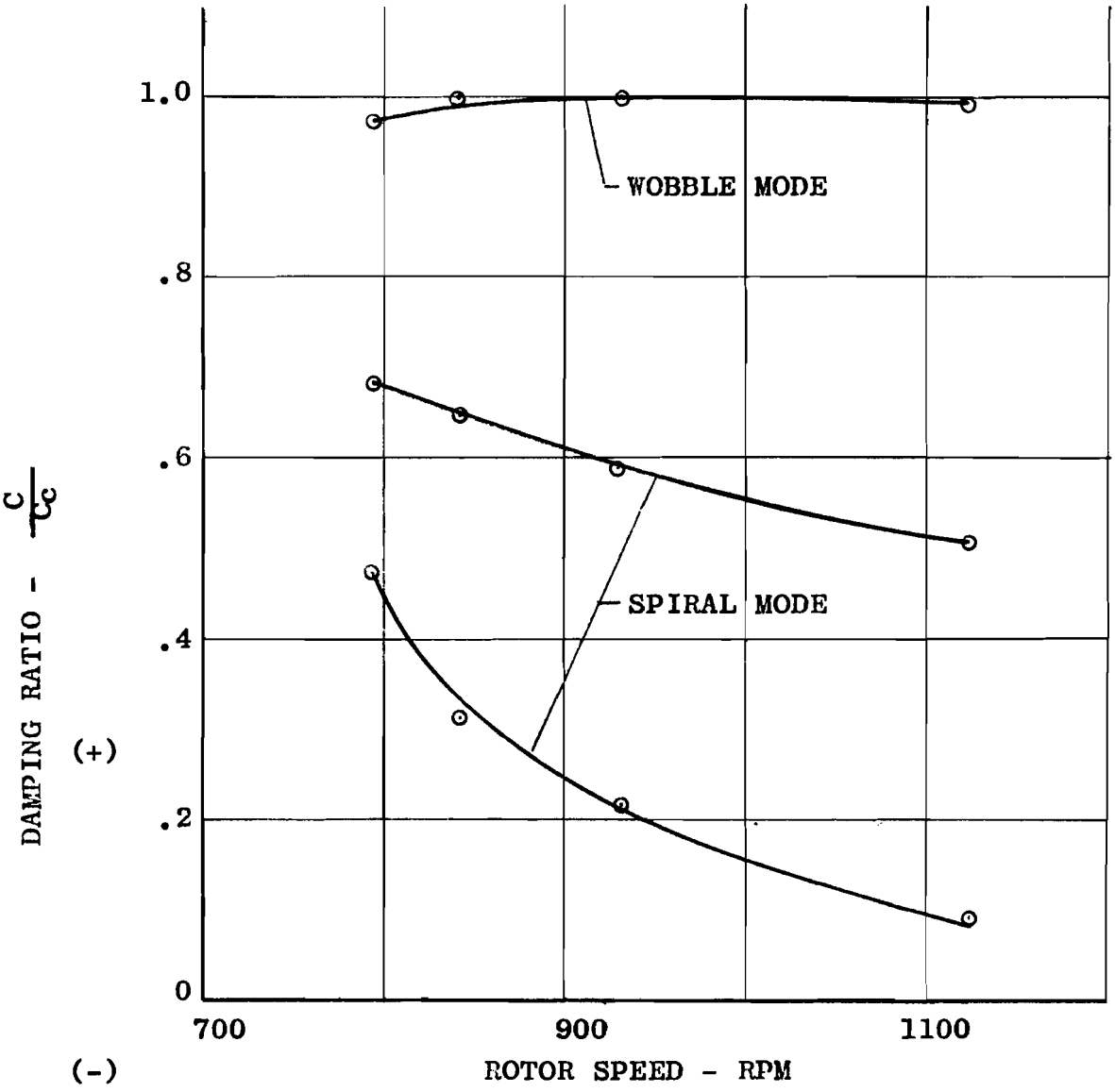

STABILITY AS A FUNCTION OF ROTOR SPEED

FIGURE 14

Figure 14 indicates that, between 800 and 1100 RPM, the ROTOCHUTE will be free from both spiral and wobble instability. Above 1100 RPM, a tendency toward spiral is indicated by the lower curve which is approaching the negative region. It is not yet clearly understood to what extent each parameter affects stability, and additional study effort in this area is required. During the experimental tests, it was demonstrated that an unstable configuration can be stabilized with automatic stabilization equipment. Also, configurations have been built which are inherently stable.

Analytical methods used for determining axial flight stability are presented in detail in Appendix I. Standard helicopter procedure is not applicable because of lack of uniform inflow to the rotor. The analysis uses the "Strip Analysis" previously discussed.

2. Gliding Flight

Since inflow in forward flight beyond a certain minimum advance ratio may be considered uniform, standard heliocpter theory is applied. Such an application has been used in Appendix II, where the force and moment derivatives required in the equations of motion are listed in terms of flapping derivatives. Appendix II also includes the equations of motion based on the Automatic Stabilization Equipment (ASE) used in the flight test vehicle. Trimmed perturbation equations and the ASE equations were programmed onto the computer.

Flight was simulated by giving the vehicle an initial (trim) value of glide velocity (μ) and then a command attitude signal (θ) through the ASE. The ASE then commands the hub tilt angle (B_{1Z}) necessary for stable flight. Investigations were performed for a vehicle with and without a horizontal trim tail surface.

The results are shown in Figures 15 and 16 and indicate that, with and without a horizontal tail, the ROTOCHUTE is stable in axial flight with ASE. In this flight mode, the pilot command (θ) and B_{1Z} are zero when there is no tail. With a tail, the ASE automatically sets B_{1Z} at a negative value to counteract the tail effect.

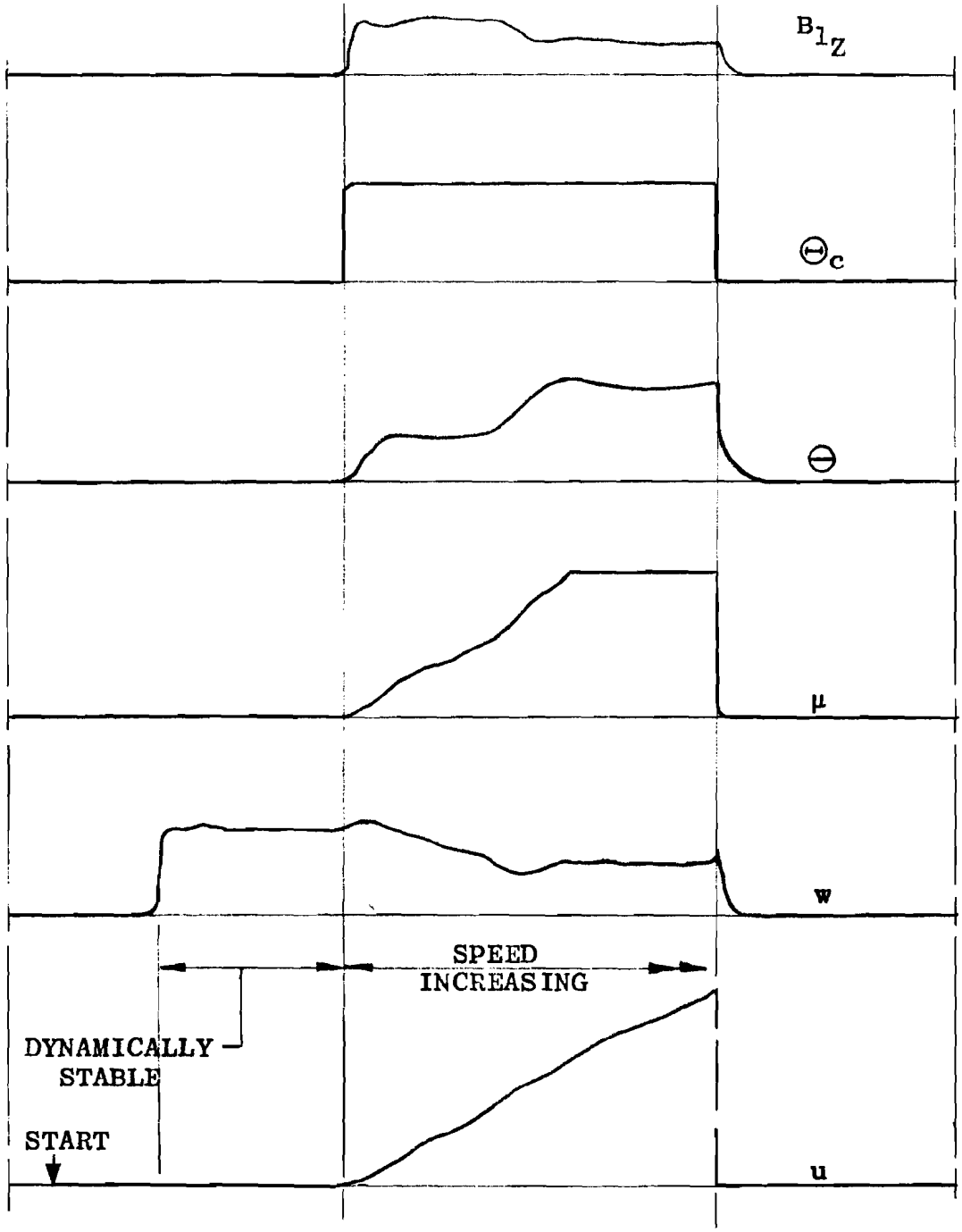

ANALOG FLIGHT SIMULATION OF A ROTOCHUTE

(WITH A.S.E. AND NO HORIZONTAL TAIL)

FIGURE 15

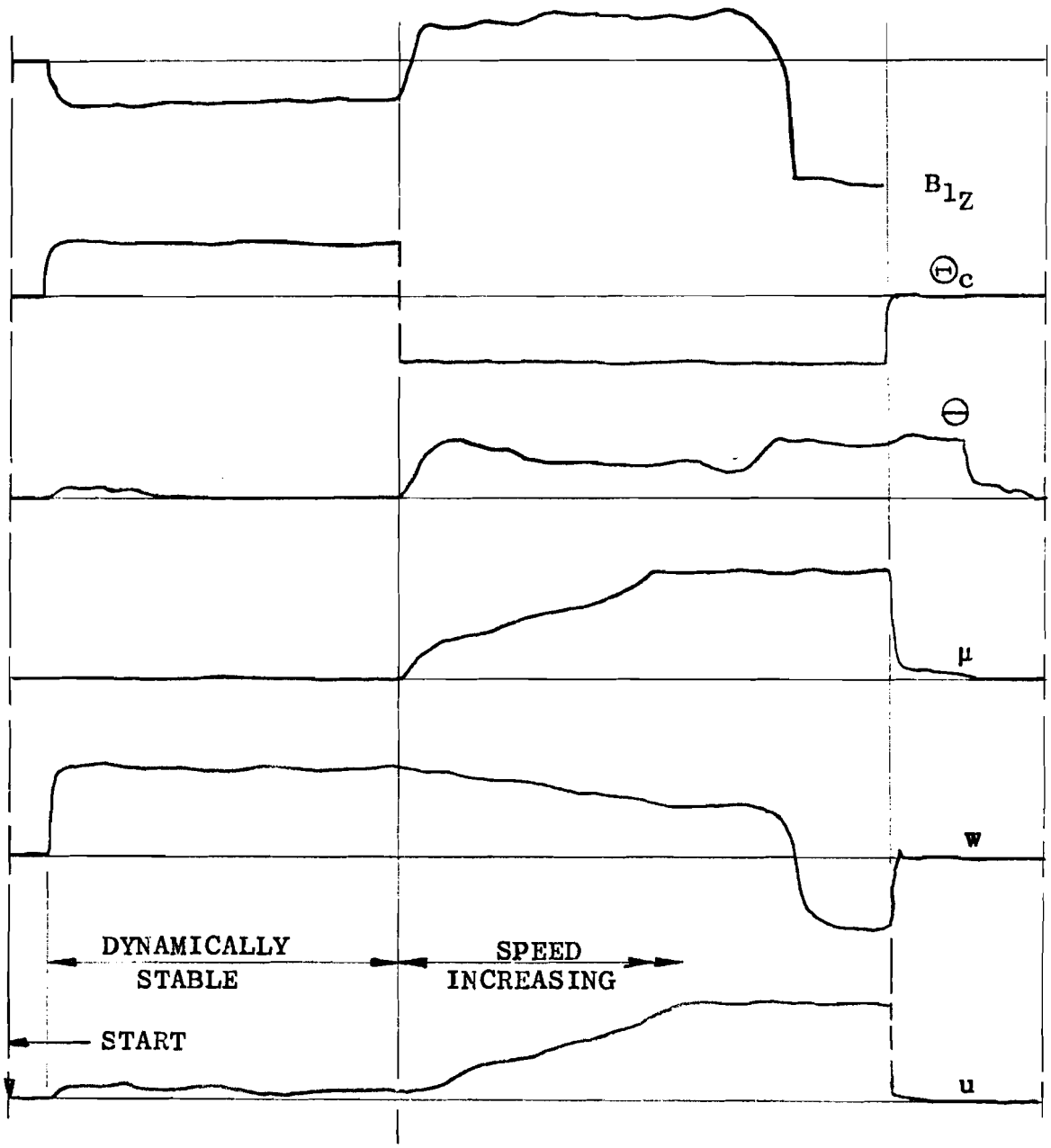

ANALOG FLIGHT SIMULATION OF A ROTOCHUTE

(WITH A.S.E. AND HORIZONTAL TAIL)

FIGURE 16

After a short period in axial flight, the system was put into forward flight by a pilot command (θ), the minimum necessary. Although the total B_{1Z} is approximately the same for both cases because of the initial negative B_{1Z} required with a tail, the net forward B_{1Z} required is less than that without a tail. Both with and without the tail, the velocities (u and w), and the advance ratio, μ, increase continuously, but do not oscillate. The lack of oscillation indicates stability, but the continuous velocity increase indicates a static speed unbalance.

3. ASE Feedback

Of special interest is the fact that pitch attitude is used as a feedback signal to the ASE. Plotted as a function of advanced ratio (μ), the pitch attitude, (θ), is shown in Figure 17 for configurations with and without a tail. Between μ_1 and μ_2, pitch attitude is not a good indication of speed. At these moderate values of advance ratio, the system, controlled by an ASE which has this unstable attitude signal for feedback, will be speed unstable. The unstable range of μ is approximately from 0.025 to 0.15 for both configurations.

It was pointed out in the glide flight discussion that above $\mu = 0.15$, the pitch attitude is a single-value function of μ. Thus the system will be speed stable for $\mu > 0.15$.

C. RE-ENTRY AND AERODYNAMIC HEATING

1. Trajectories

The re-entry phase was investigated as a prelude to the study of aerodynamic heating that a rotor would be subjected to in such a mode of operation. The rotor was used in axial flight as a constant and variable area drag device to retard a re-entry vehicle until a relatively low speed is reached and glide operation may begin.

Two distinctive types of entry were considered: the modulated and the non-modulated type entry. In the case of the non-modulated entry, the rotor was held fully open for the duration of the entry. This is equivalent to a constant area drag device. At high supersonic speed, the drag coefficient remains essentially constant, therefore, the system has a constant equivalent flat plate drag area, C_DA.

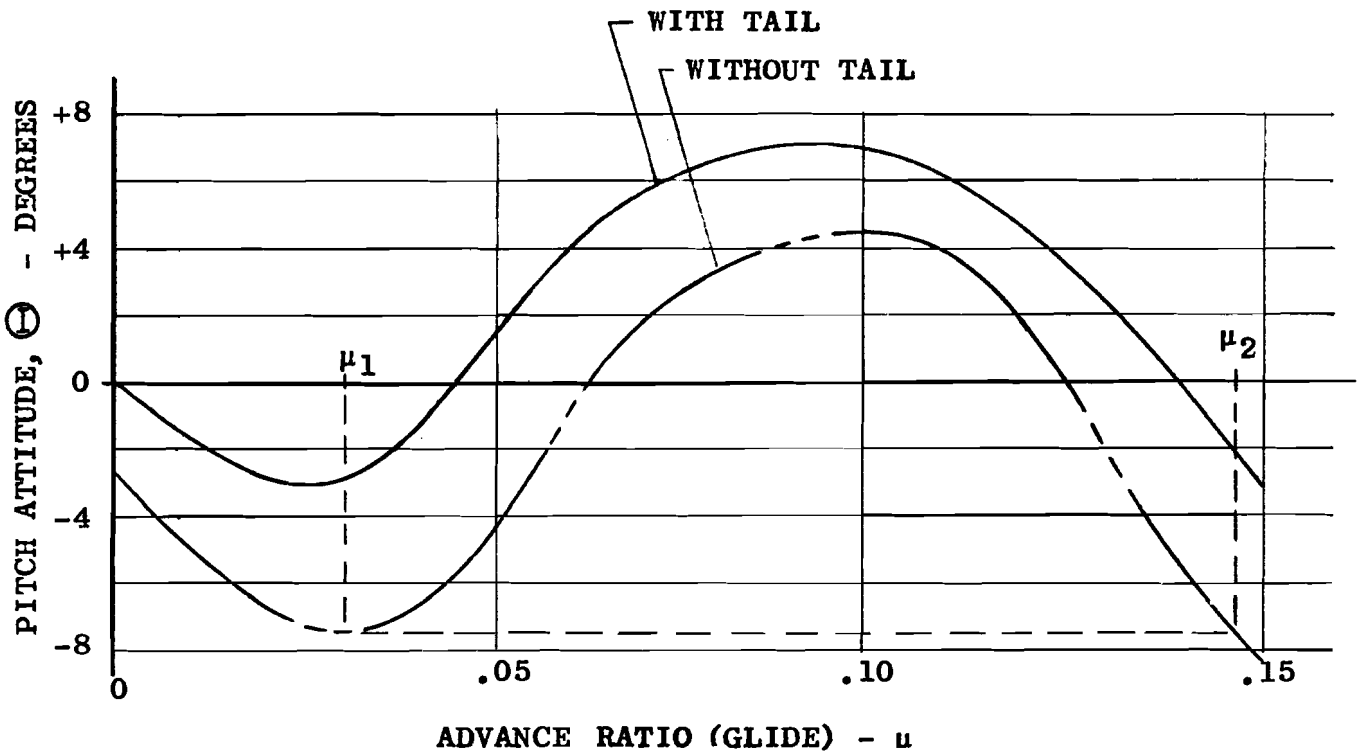

VARIATION OF PITCH ATTITUDE WITH GLIDE SPEED

FIGURE 17

For the modulated entry, the rotor area was varied by coning the blades back so as to control the deceleration. The vehicle was permitted to enter the atmosphere with the rotor fully open until a predetermined deceleration was reached. At that point, the rotor was coned in a manner to produce constant deceleration.

The altitude-time, velocity-time and deceleration data was calculated using the motion analysis of Reference 3. The assumptions are that (1) the force of gravity and centrifugal acceleration are negligible as compared to the aerodynamic drag force, and therefore the trajectory is assumed to be a straight line; and that (2) the atmospheric air density varies exponentially with altitude. For assumption (1) to hold, the entry angle has to be greater than 5^{o} (Reference 4).

The air density was assumed to vary exponentially with altitude. The relationship is given in Reference 3 as:

$$\rho = \rho_{o} e^{-\beta Y} = .0034\, e^{-\frac{Y}{22000}}$$

Figure 18 shows density versus altitude for the above equation. The air density of the ARDC model atmosphere is shown for comparison.

All trajectory calculations assume that the earth's atmosphere ends at 250,000 feet altitude, i.e. air density above that altitude is negligible. Consequently, the initial entry conditions are established at this altitude.

2. Unmodulated Entry

The pertinent equations for unmodulated entry are given in Reference 3 and presented in Appendix IV. The following expression for deceleration in unmodulated entry is the final derivation.

$$\frac{n}{V_E^2 \sin \theta_E} = \frac{\beta}{g} \left(\frac{V}{V_E}\right)^2 \ln \frac{V}{V_E}$$

The equation shows that for unmodulated entry the deceleration is a function only of speed and flight path angle. Figure 19 shows the results of solving the equation for

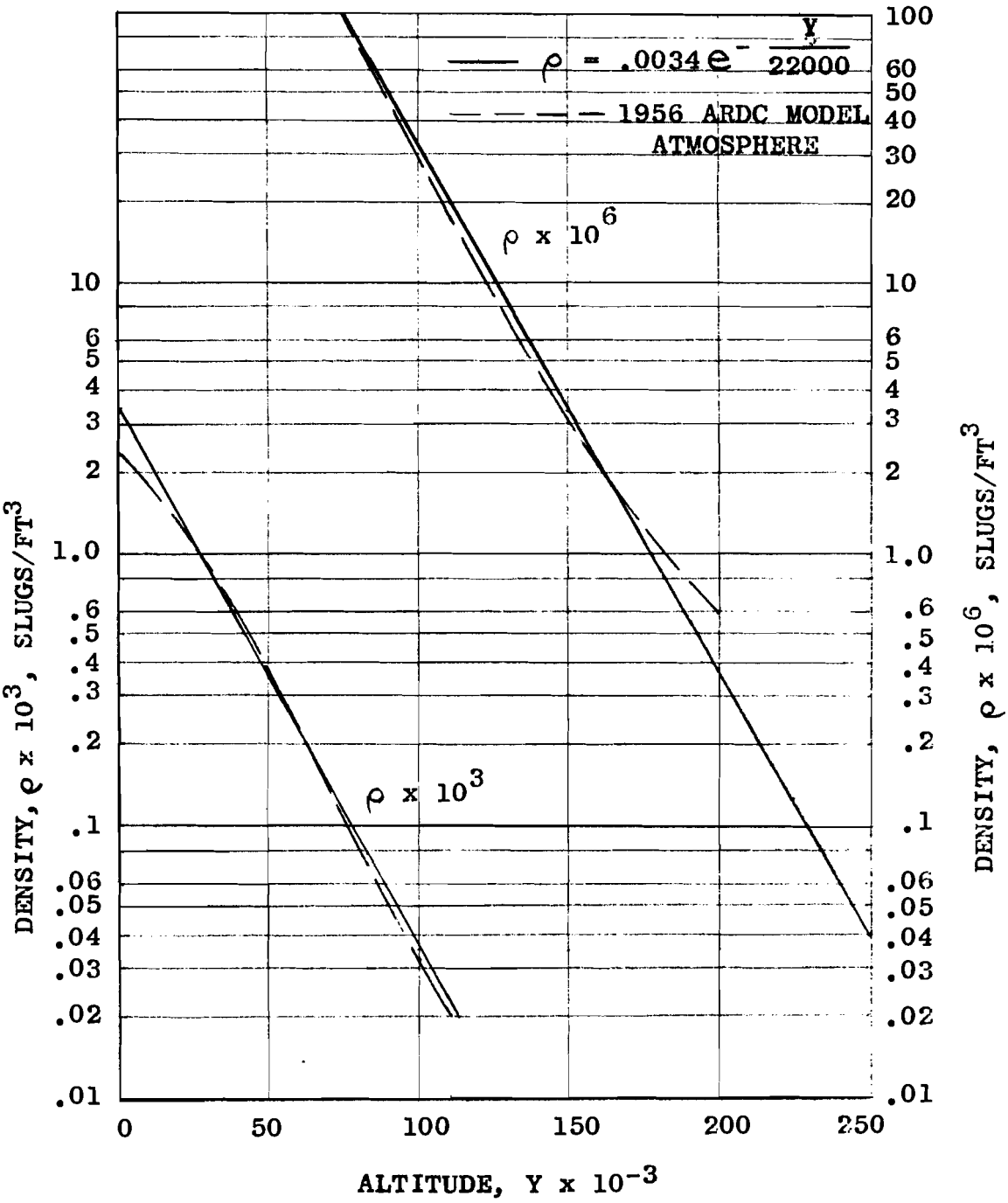

VARIATION OF ATMOSPHERIC DENSITY WITH ALTITUDE

FIGURE 18

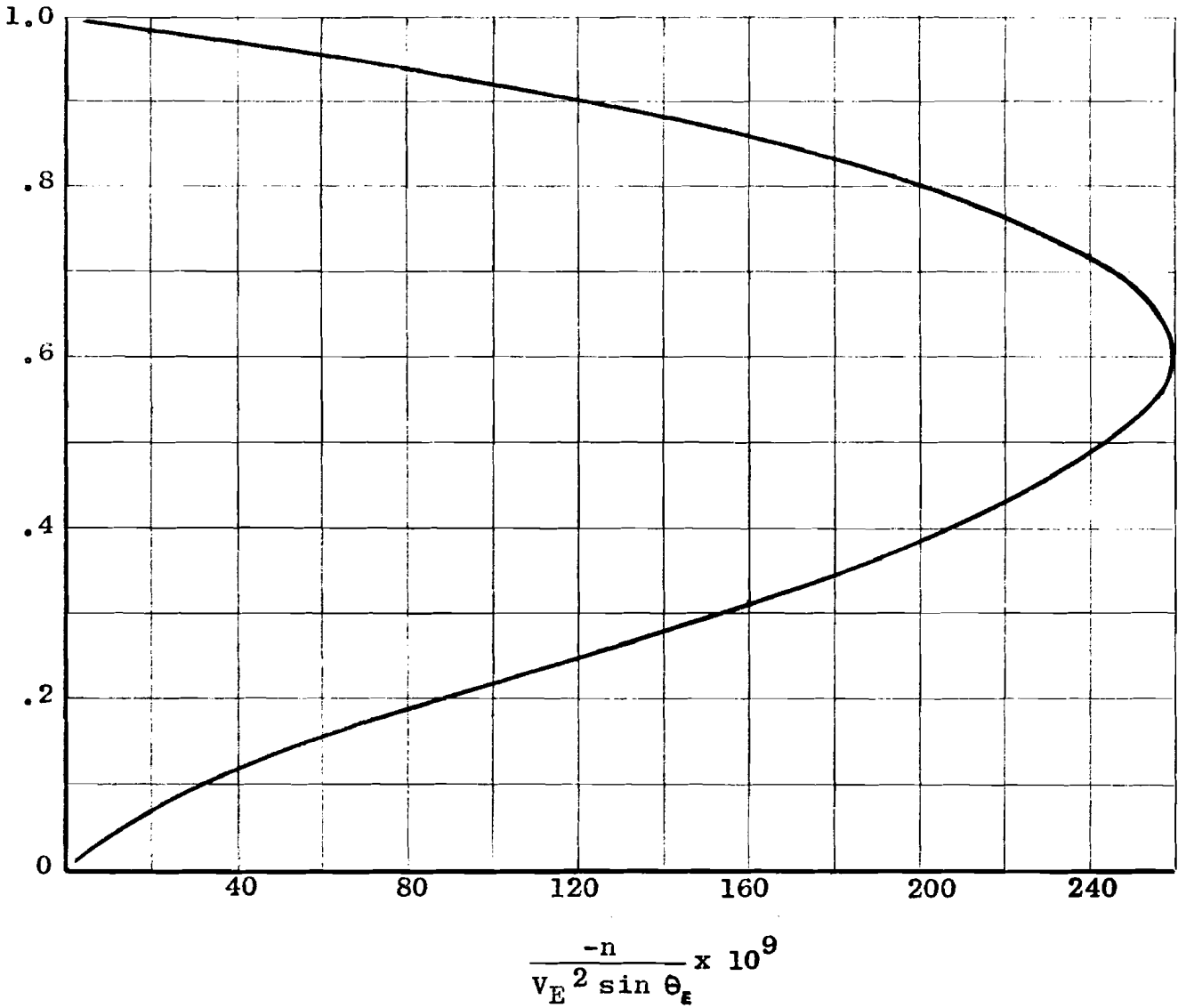

ROTOCHUTE DECELERATION AT CONSTANT C_D INDEPENDENT OF W/C_DA

FIGURE 19

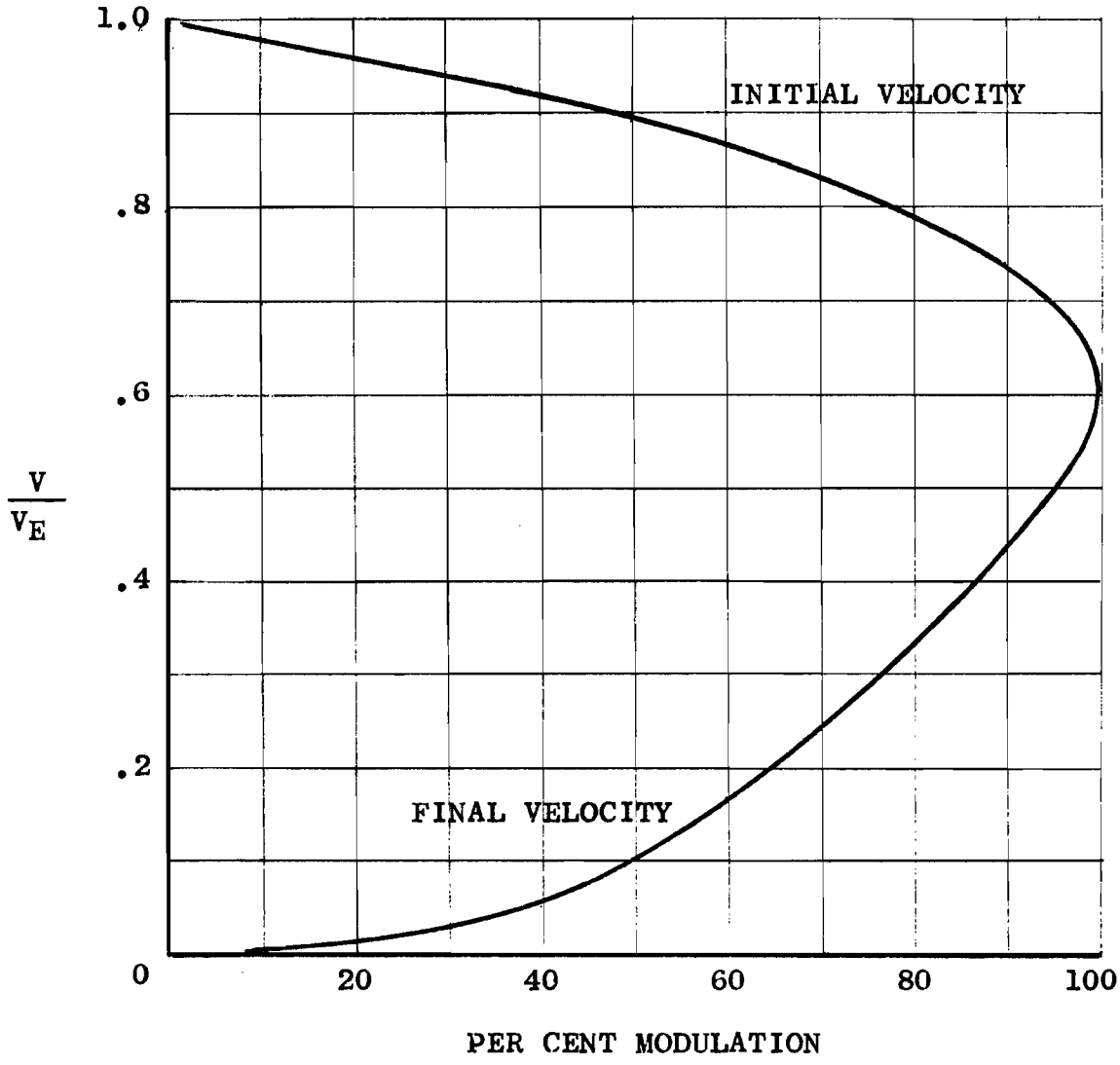

VELOCITY BOUNDARIES FOR MODULATED FLIGHT

FIGURE 20

various V/V_E ratios. The plot shows that the maximum deceleration is $-n/V_E^2 \sin \theta_E = .259 \times 10^{-6}$ and that it occurs at $V/V_E = .606$.

3. Modulated Entry

The initial phase of this entry is identical to the unmodulated case up to the point where a desired maximum deceleration is reached. The velocity where this occurs is defined by Figure 19.

In the modulated phase of flight, the rotor disc area, A, is varied so as to yield constant deceleration at an arbitrarily chosen value. Initially, the disc area is decreased as the dynamic pressure increases with density until maximum dynamic pressure is reached. From there on, the disc area is increased until the rotor is fully opened. At this point, the vehicle continues along an unmodulated trajectory, decelerating at levels below maximum.

Figure 20 shows initial and final velocities of modulated flight in terms of per cent modulation where per cent modulation is defined as the ratio of constant deceleration of modulated flight to the maximum deceleration of non-modulated flight for the same vehicles:

$$\% \text{ modulation} = \frac{\frac{n}{V_E^2 \sin\theta_E}}{.259 \times 10^{-6}}$$

The modulation of deceleration is achieved by changing the drag of the system. As the rotor blades are coned back, the equivalent flat plate drag area of the rotor disc, C_DA, is reduced, thereby reducing drag and deceleration. C_D is the total drag coefficient of the body and the ROTOCHUTE, referred to the fully-opened rotor disc area. From this definition it follows that C_D remains constant for the unmodulated entry, while for the modulated case, C_D entry is started at its maximum value and varied as a function of dynamic pressure once the maximum desired deceleration is reached. The modulation capability is limited only by the body drag itself, i.e. the C_DA of the body with the rotor fully coned back. Greater percentages of modulation may be achieved with streamlined bodies. Therefore, the C_D may be reduced by factors of anywhere from 2:1 for Mercury type capsule to 4:1 for Eggers body capsules.

4. Typical Trajectories

Sample trajectories for modulated and unmodulated flight were calculated for axial flight entries. For all cases, the ballistic parameter W/C_DA was chosen for a reasonable configuration. If a reasonable disc loading W/A is taken as 5 pounds per square foot, and rotor solidity $\sigma = .18$, then for a $C_N = 1.84$ (Reference 5), $C_D = (1.84) \times (.18) = .333$ and $W/C_DA = 5/.333 = 15$ for a fully-opened rotor. This value falls in the mid-range of presently considered ROTOCHUTE applications.

Figures 21 and 22 show trajectories for two combinations of entrance velocity and entrance angle. The entrance angles 90^o and 10^o represent the extremes for flight path angles for which the developed equations are applicable. The trajectories are shown for the unmodulated flight and flight-modulated for maximum deceleration equal to 25, 50, and 75 per cent of the unmodulated peak deceleration. In both cases, calculations were based on assumptions and equations as discussed previously.

Figures 23 and 24 show the required C_D and variation of coning angle with time to provide modulation for the previous sample cases. The previously assumed $W/A = 5$ pounds per square foot was used. The coning angles were calculated with the assumption that total body C_D equals the rotor C_{DR}. In effect, the body drag was considered negligible as compared to the rotor drag. C_N and σ values of 1.84 and .18 respectively were used. These values give negligible coning for unmodulated flight.

Figure 25 demonstrates the use of rotor coning angle to limit the peak deceleration during a typical re-entry. The peak deceleration is independent of the ballistic coefficient, as long as the ballistic coefficient remains constant. However, the magnitude of the ballistic coefficient may be varied within certain limits by controlling the rotor blade coning angle. With the rotor deployed, the initial deceleration occurs at a higher altitude than for the capsule alone. This allows a longer deceleration period during re-entry before ground impact. The load factor limit during the modulated re-entry must be sufficiently high to insure desired terminal velocity at ground contact.

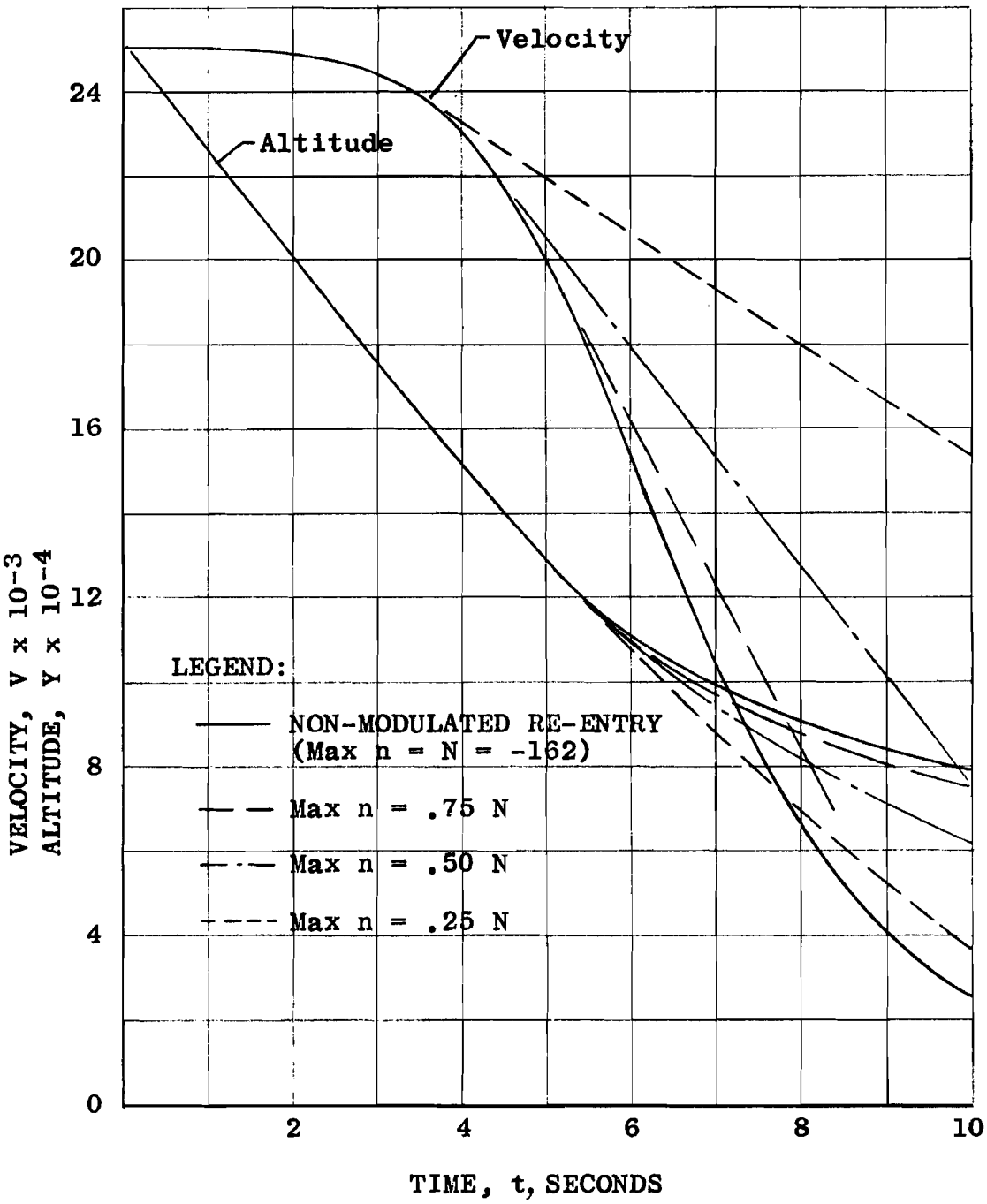

ROTOCHUTE TRAJECTORY, $\theta_E = 90^\circ$

W/C_DA = 15 (Min) V_E = 25,000 FPS

θ_E = 90° Y_E = 250,000 FT

FIGURE 21

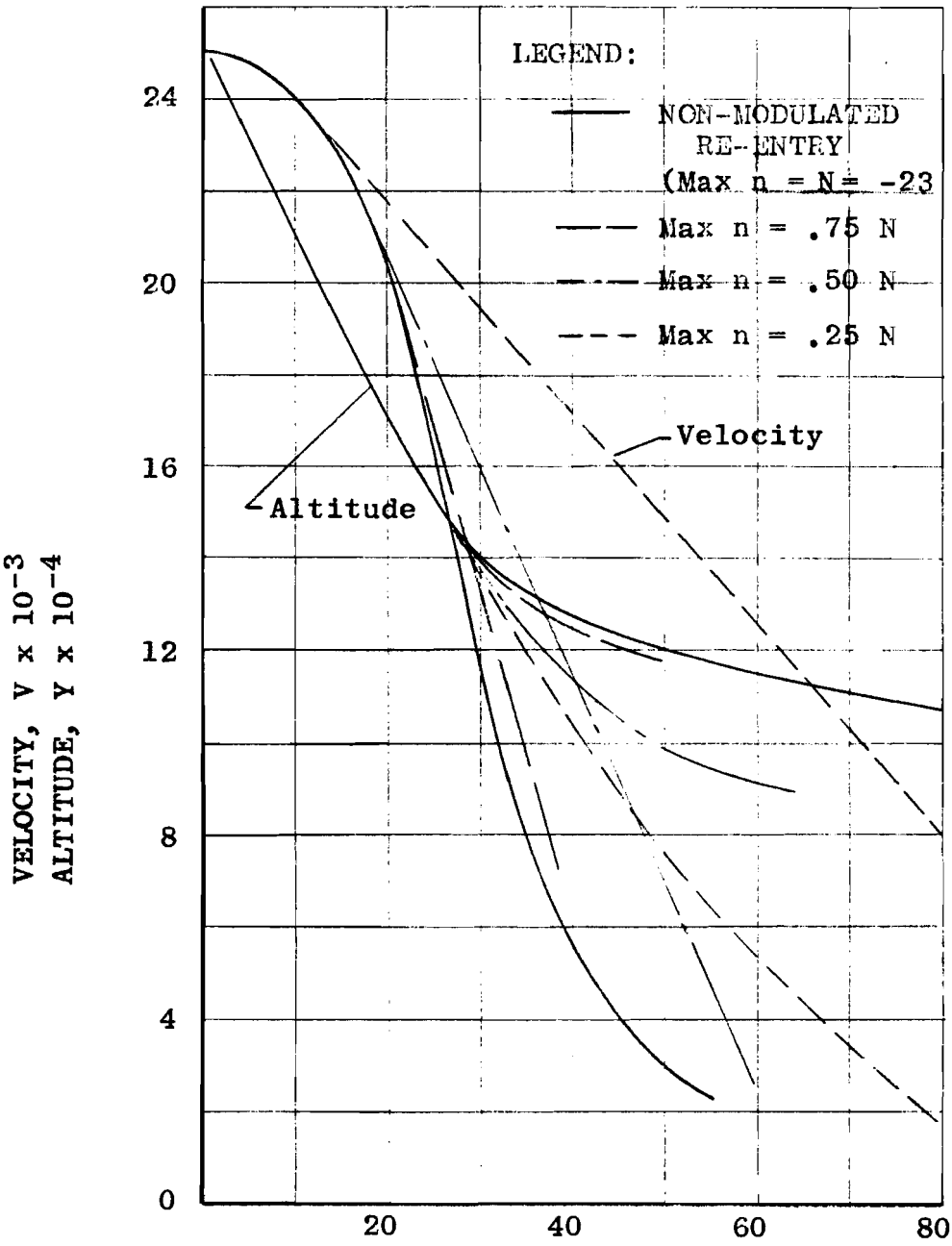

ROTOCHUTE TRAJECTORY, $\theta_\epsilon = 10^\circ$

W/C_DA = 15 (Min.) V_E = 25,000 FPS

θ_E = 10° Y_E = 250,000 Ft

FIGURE 22

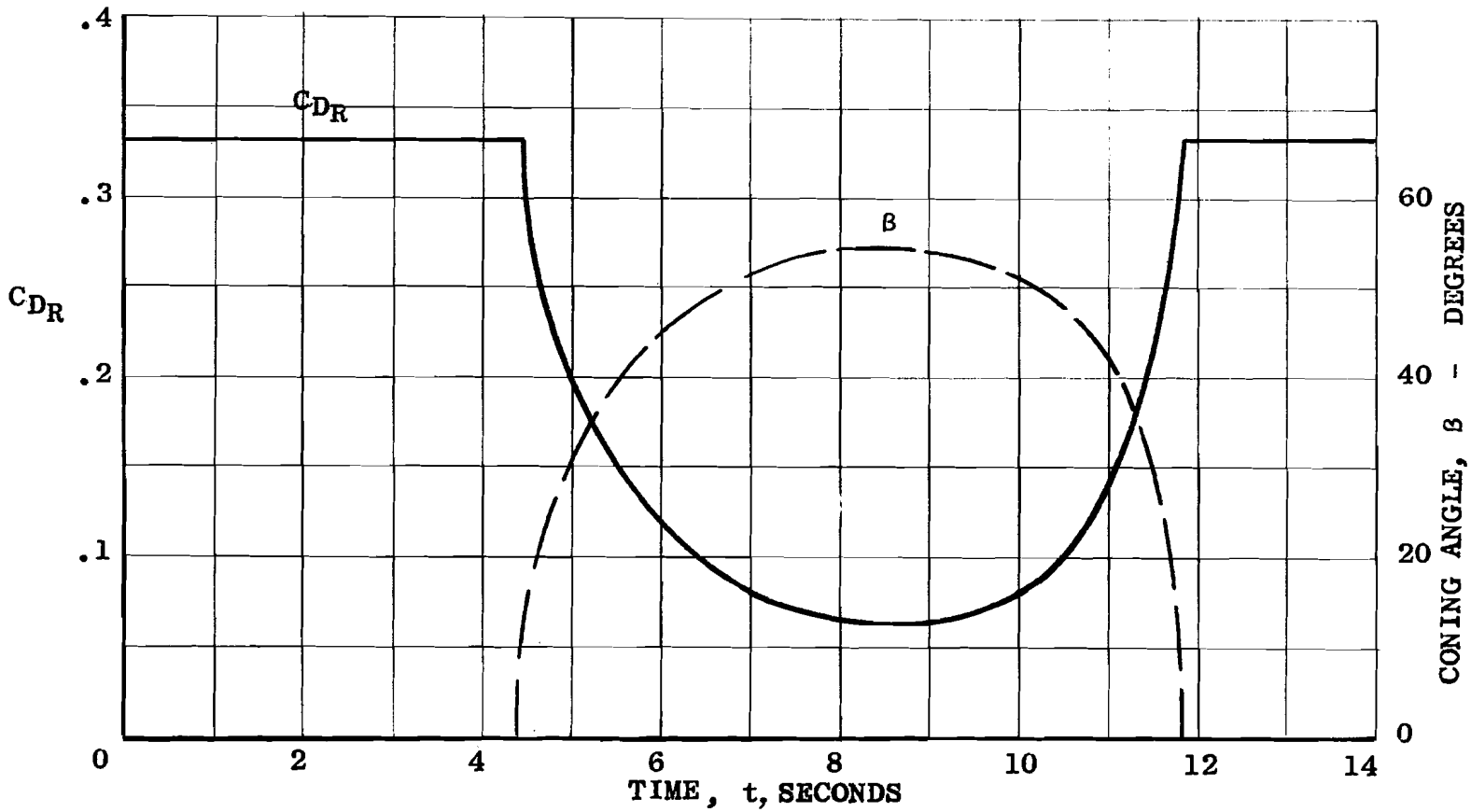

DRAG COEFFICIENT AND CONING ANGLE VERSUS TIME, $\Theta_E = 90^\circ$

W/A = 5 PSF $\Theta_E = 90^\circ$ V_E = 25000 FPS Y_E = 250000 Ft

FIGURE 23

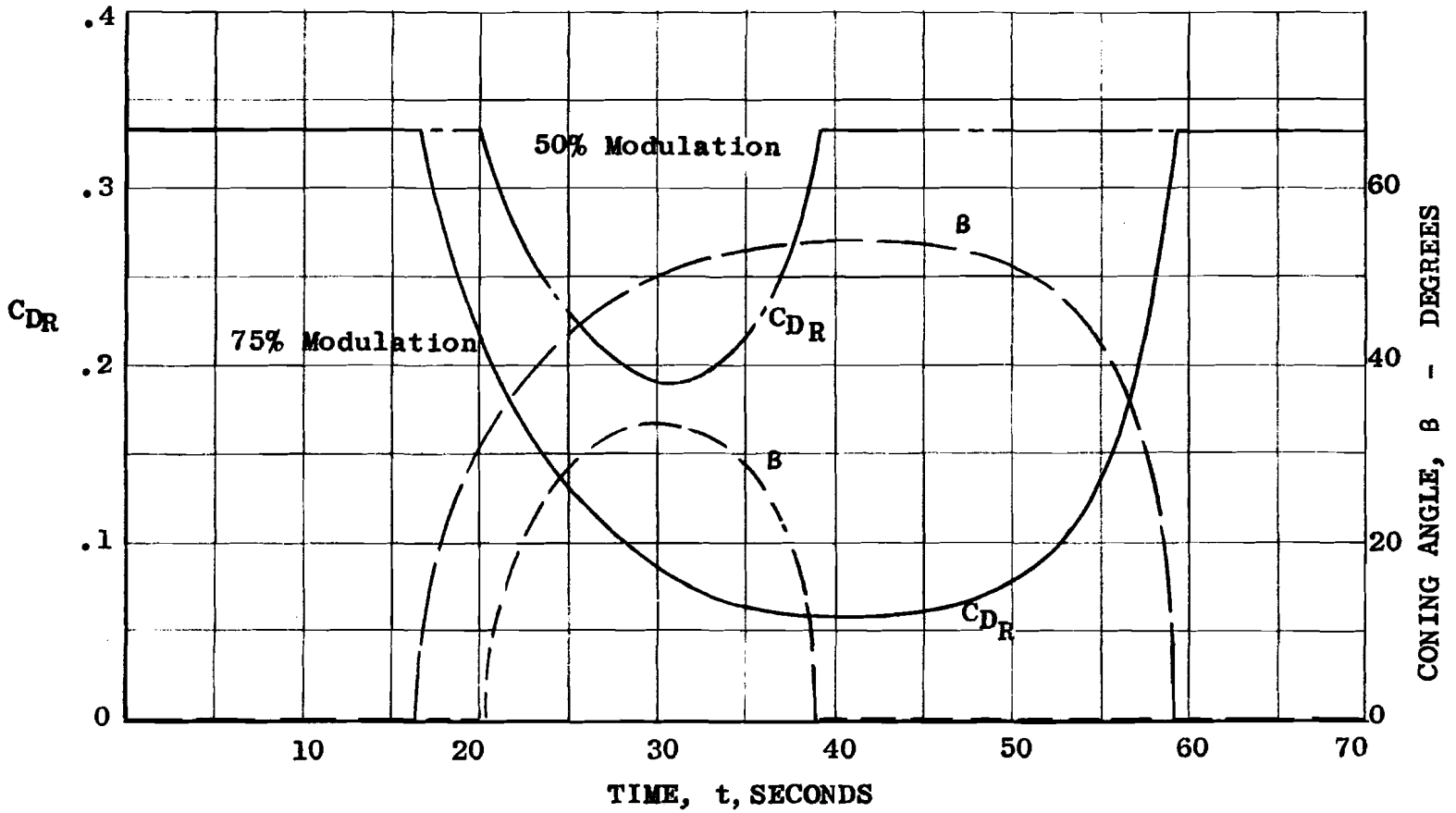

DRAG COEFFICIENT AND CONING ANGLE VERSUS TIME, $\theta_E = 10^\circ$

W/A = 5 PSF $\theta_E = 10^\circ$ V_E = 25000 FPS Y_E = 250000 FT.

FIGURE 24

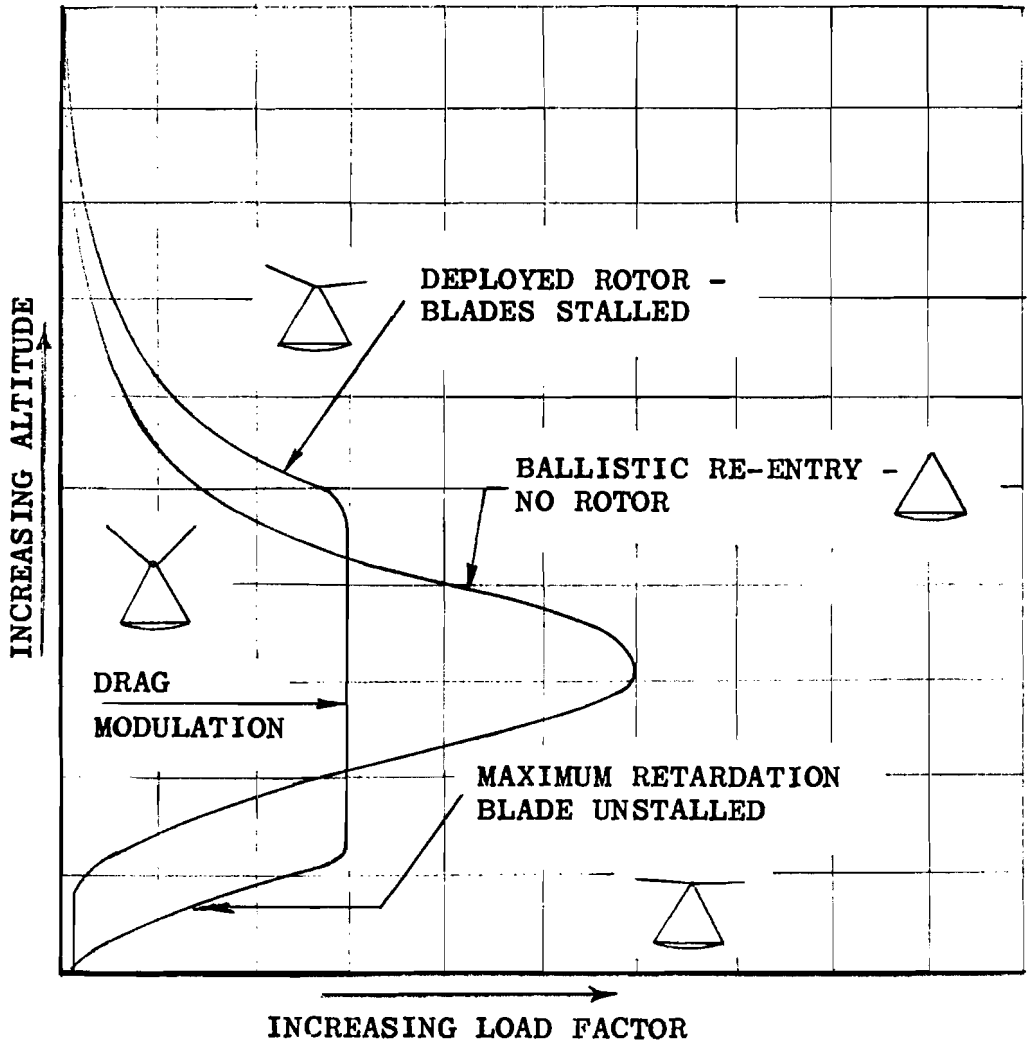

CONTROL OF RE-ENTRY LOAD FACTOR BY MEANS OF DRAG MODULATION

FIGURE 25

5. Aerodynamic Heating

The thermal effects involved in the descent of a rotor configuration along "re-entry" trajectories were studied on a limited basis. Specifically, for such configurations, the temperature distribution on the blade surface, the heat transfer rate to which the blade is exposed, necessary cooling schemes, and weight penalties are pertinent areas of inquiry.

The discussion in Appendix IV is concerned with preliminary evaluation of the thermal problem in order to indicate appropriate parameters, assumptions, relation to re-entry dynamics, and some limitations.

In summary, the energy exchange represents the change in kinetic energy of the vehicle from entry to impact. Peak heating occurs at high altitudes in the disassociated gas region. Heat protection appears more favorable for a rotor in axial flow operation. Stagnation occurs against the broad surface of the rotor blade, presenting a larger effective "nose" radius and more exposed surface to transfer the heat for ablation or conductance.

3. WIND TUNNEL TESTS

A. INTRODUCTION

Wind tunnel investigations with the KRC-6M model of the ROTOCHUTE rotor system were performed in the Transonic and Supersonic Circuits of the 16-Foot Propulsion Wind Tunnel Facility at Arnold Engineering Development Center, Tullahoma, Tennessee. Arrangements for testing at the Government-furnished facility were made by the Aeronautical Systems Division, Wright-Patterson Air Force Base, Ohio.

Tests from Mach 0.5 through Mach 1.5 were performed in the Transonic Circuit. Runs up to Mach 3.0 were completed in the Supersonic Circuit. Successful deployment, governing, and operation of the ROTOCHUTE were achieved throughout the regimes investigated. Experimental results correlated closely with predicted theoretical performance. Details of this phase of the program are presented in this section.

B. OBJECTIVE

Prime objective of the testing was to determine the feasibility of employing rotary-wing systems for aerodynamic deceleration at supersonic free-stream velocities. Deployment, retardation, and over-all operation of the rotor system in axial flow stream were to be investigated and performance characteristics determined. Yawed operation was to be investigated within the limits permitted by the tunnel mounting provisions.

C. CONCLUSIONS

As a result of successful deployment, governing, and operation of the KRC-6M rotor system at speeds up to Mach 3.0 (tunnel limit) and evaluation of test data, it is concluded that:

1. The feasibility of aerodynamic deceleration with a rotary-wing system in axial flow at speeds up to Mach 3.0 was demonstrated.

2. Deployment, governing, and operation in axial flow at speeds up to Mach 3.0 presented no problem.

3. Drag modulation or control of the retardation force during re-entry is feasible with control of rotor coning angle through control of rotor tip speed.

4. Agreement between theoretical performance and experimental results is excellent, excepting the Mach 1.0 regime, where prediction becomes complicated as a result of unpredictable flows.

5. The rotor governing action was positive at all test conditions. No tendency for the rotor to overspeed or to oscillate about the governed speed was noted.

6. At constant Mach number, a large change in dynamic pressure is required to change rotational speed a significant amount.

7. The drag-force coefficient is proportional to rotor solidity in the blade fully-stalled regime.

8. Angle of attack up to 9^{o} yaw had little effect on the model drag-force coefficient.

9. The side-force and yawing-moment coefficients at angle of attack up to 9^{o} were small.

D. WIND TUNNEL TEST MODEL

The KRC-6M wind tunnel model installation in the Transonic Circuit is shown in Figure 26. Internal details of the model are presented in Figure 27. The tunnel model rotor system basic configuration (4-bladed, 8-foot diameter) was very similar to the original rotor system of the flight test vehicle. Blade rotation was counterclockwise, looking upstream.

Basic elements of the rotor system are the rotor blades, hub assembly, governor mechanism, synchronizer system, and deployment or release pin. The rotor assembly was attached to a steel rotating shaft mounted on the steel stationary shaft through a set of ball bearings. The stationary shaft mounted to the tunnel sting support through the 2.5-inch diameter balance system which measured the rotor moments, drag, and side forces. A multi-channel slip ring served as the rotary electrical connector between the rotating and stationary elements of the rotor assembly for the model data sensor signals.

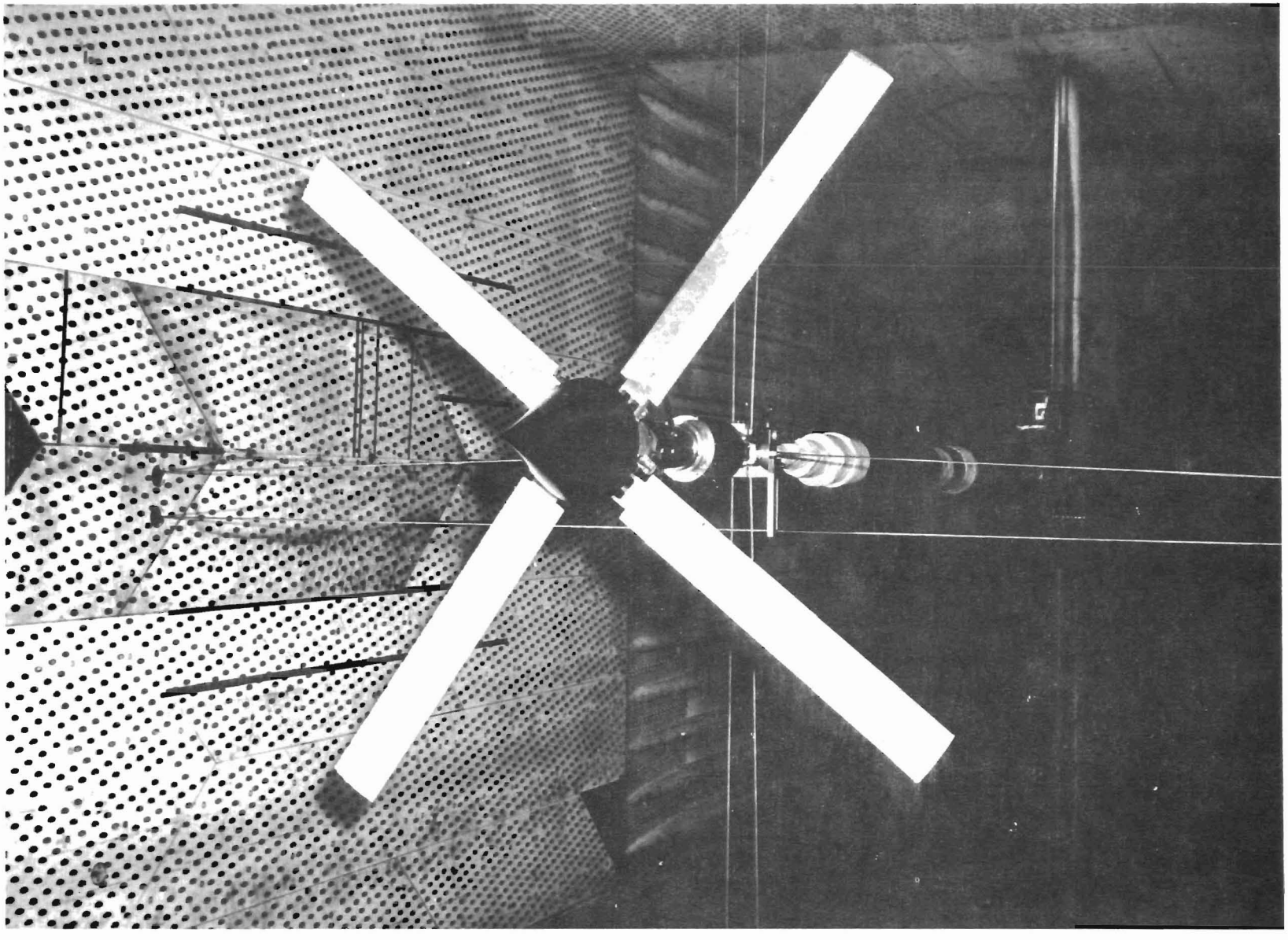

FIGURE 26 KRC-6M MODEL INSTALLATION IN AEDC WIND TUNNEL

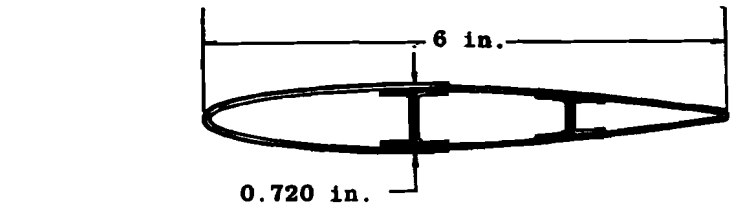

Blade Section - NACA 0012-64

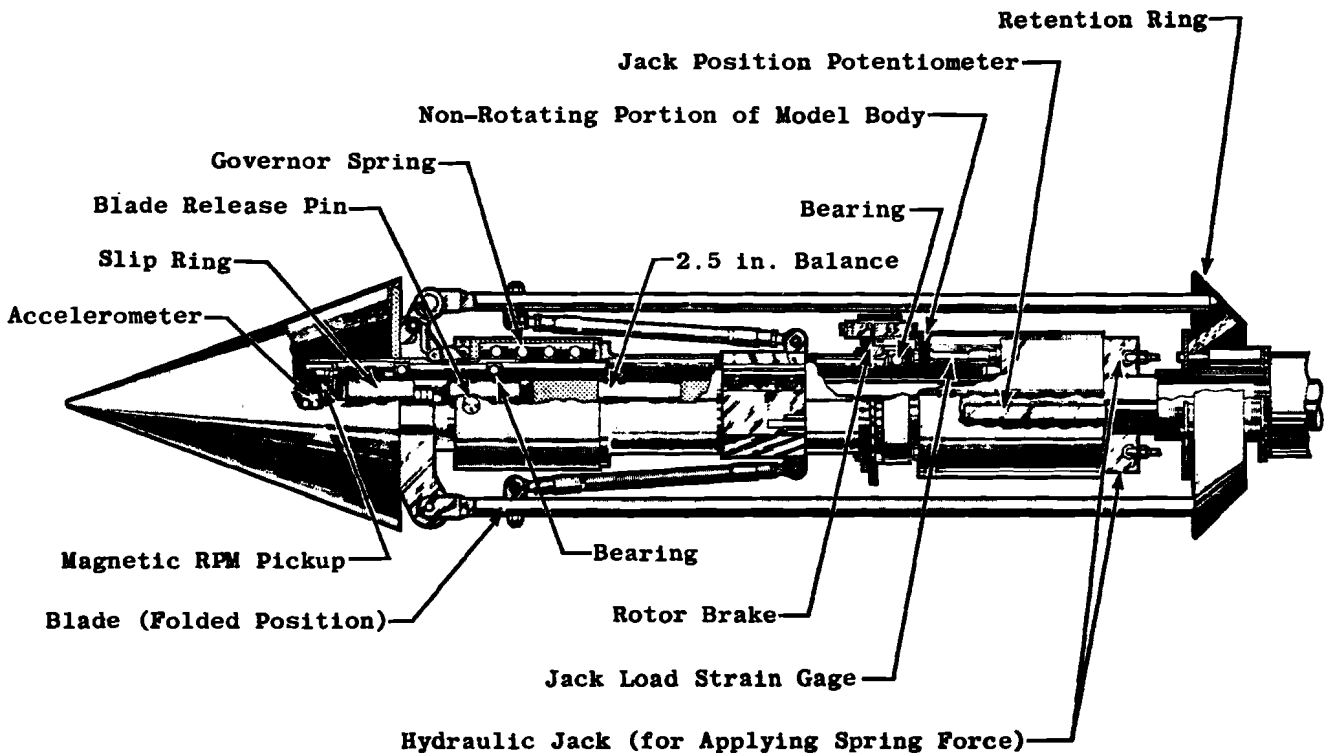

Internal Details of the Model

FIGURE 27

Rotor blades were lightweight and of simple construction. Aluminum alloy spars, skins, and inboard grip fitting were bonded together with an epoxy resin. The two-point blade attachment to the cast steel hub permitted flapping and pitch freedom. The blade could flap or cone from 5^{o} in the direction of flight to 90^{o} aft (blade stowed position - parallel to axis of rotation). The blade pitch was -10^{o} to $+12^{o}$ (at 0^{o} coning). The forward attachment to the hub was through a self-aligning spherical-type bearing. The rear attachment picked up the governor mechanism crank.

All blades were positioned at uniform coning or flapping by the synchronizer system. Synchronizer rods, attached at the blade inboard area, picked up the synchronizer slide, which traversed along the rotating shaft as blades coned in unison.

The governor mechanism controlled rotor RPM through collective pitch change of the blades in response to blade centrifugal forces. Selected governed speed was established by preloading the governing spring to balance the sensed blade centrifugal force at the rotor equilibrium blade pitch setting. Increasing the preload increased governed RPM. On the model, spring preload was controlled by compressing the downstream end of the spring with a sliding pressure member actuated by the two hydraulic jacks. The two rod members connecting the jacks to the slide were strain-gaged to measure the compressive load. When the hydraulic pressure on the jacks was relieved, the spring resumed essentially a "no-load" position for minimum RPM. Jack positioning was sensed with a coupled potentiometer.

Two "overspeed" accelerometers, installed on the model in parallel circuits, sensed centrifugal forces to limit the rotor speed to 1250 RPM maximum, a limit dictated by the tunnel facility safety factor requirements. Either accelerometer could signal the "reflief" of the jack hydraulic pressure.

Once governed speed was selected, rotor speeds higher than that selected would produce higher centrifugal forces. The governor spring in turn would, through the linkage, be compressed to a higher balancing load. During the balancing process, the blades were controlled collectively to a pitch setting greater than that for equilibrium, thus slowing the rotor. If rotor RPM had dropped below the selected speed, blade pitch would have been reduced and rotor speed would increase. A magnetic pick-up sensor provided rotor RPM data.

Prior to deployment, the spring housing was positioned such that the blades folded parallel to the axis of rotation. The housing was retained in this position and the rotor was restrained from turning by the internal deployment pin mechanism. When the pin was pulled by nitrogen gas pressure to disengage from the housing and rotating shaft, the rotor deployment cycle was initiated. The rotor assembly became free to rotate and the housing was forced against the hub by the spring pressure and positioned the blade attachment points through the governor mechanism such that blades were positioned in a "precone" and "presweep" attitude. In essence, the blades were forced into the air stream. Resulting forces generated a torque about the rotor axis of rotation and induced rotor rotation. As RPM increased, centrifugal forces on the blades opened the blade to an equilibrium operating cone position where the centrifugal force moments about the blade flapping axis were balanced by thrust load moments.

A conical shape was selected for the model nose for ease in predicting flow properties about it. The cone structure was molded fiberglass.

During the interval between testing in the Transonic and Supersonic Circuits, a rotor brake and a conical device to restrain blades in the folded position were added to the model to minimize potential problems during changes in operating conditions. Transient shock waves were expected during the change. Both the brake and cone were actuated hydraulically. Potentiometers for sensing the spring housing position (to determine blade pitch in a more direct manner) and blade flapping or coning were also added.

E. FUNCTIONAL CHECK OF THE MODEL

Prior to wind tunnel testing, the KRC-6M rotor system tunnel model was mounted on a truck as shown in Figure 28. Runs at speeds up to 55 miles per hour were made along a taxi strip at a local airport to perform functional checks of the model systems, calibrate and check the overspeed cut-out, and obtain performance and governing characteristics data at speeds simulating the terminal descent regime.

Instrumentation measured airspeed, rotor RPM spring deflection, and spring preload. The data obtained, more a qualitative measurement, were sufficiently accurate to determine proper functioning of the model and establish initial operational governor preload settings.

FIGURE 28 GROUND TEST OF KRC-6M MODEL

The low speed drag force data as determined by these truck runs are presented in Figure 29 for relative airspeeds up to 70 feet per second.

F. WIND TUNNEL FACILITY

The Transonic and Supersonic Circuits of the AEDC Propulsion Wind Tunnel are closed, single-return tunnels with 16-foot square test sections. Tunnel conditions are controlled by a water exchange air cooler and a scavenging and make-up air system. Subsonic Mach numbers are generated in the Transonic Circuit with a sonic nozzle contour and compressor stator blade control. Supersonic Mach numbers are generated by contouring the nozzle together with stator blade adjustment. Detailed descriptions of the circuits, operating characteristics, and related equipment will be found in Reference 6.

G. TEST PROCEDURE

Data were taken for two types of model operation. The first was a slow, controlled rotor deployment, and the second was a rapid rotor deployment.

In the first case, the rotor was permitted to reach its equilibrium speed without any preload on the governor spring. When tunnel test conditions had stabilized, data were recorded at this equilibrium speed. The governor spring preload was then applied and increased until the next desired test rotational speed was reached. Data were taken at each stabilized test rotational speed until the desired range of tip speeds was investigated. The spring preload was then reduced to zero, the tunnel operation changed to the next test condition, and the procedure repeated. Tunnel operating temperatures were limited to 220°F maximum.

In rapid deployments, simulating flight deployment, the blades were folded and the deployment pin was in "lock" position. The governor spring was preloaded. After the desired tunnel test operating conditions were established, the deployment pin was pulled, and the rotor deployed. The transient and steady-state data were recorded.

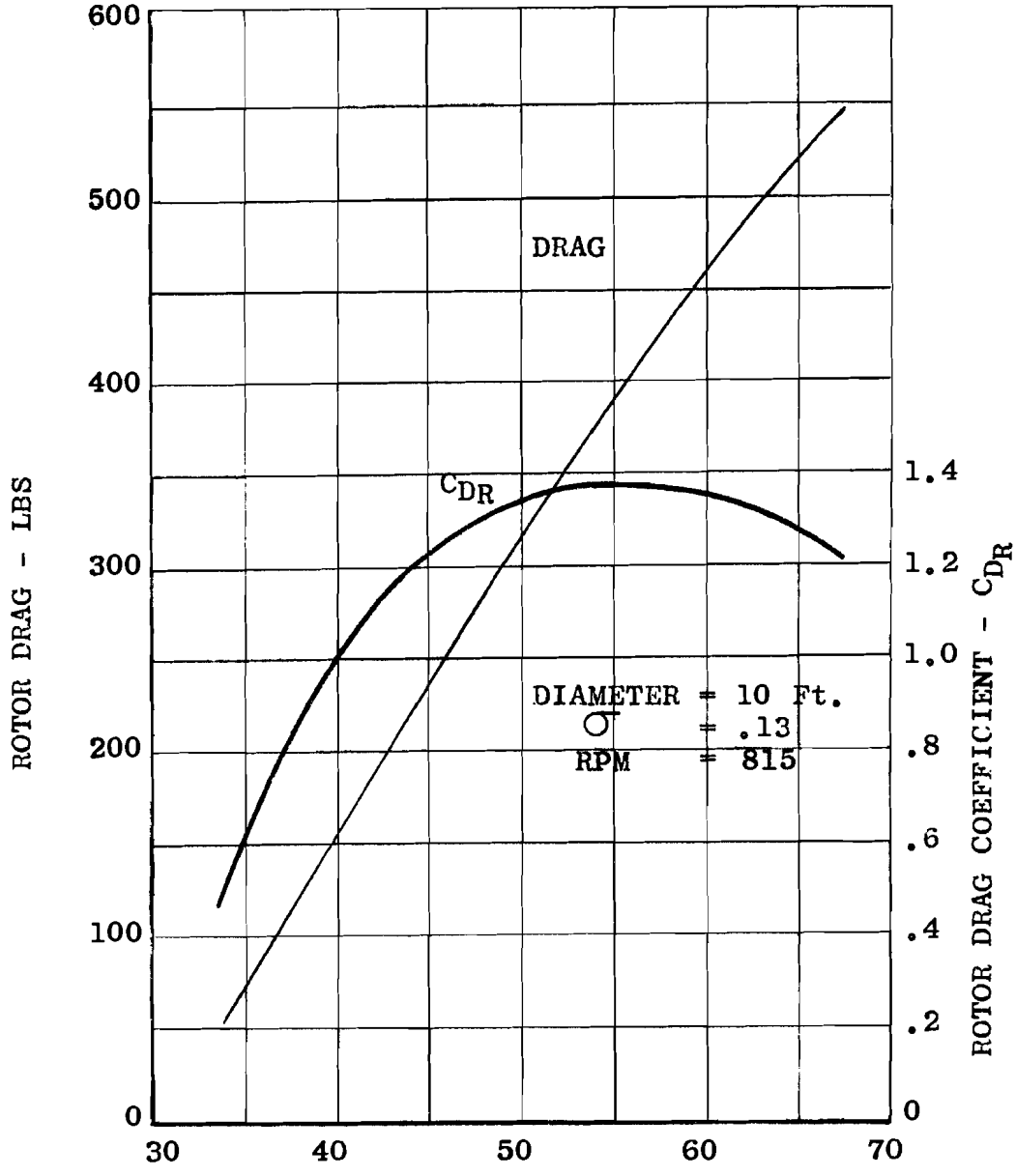

ROTOR TEST DATA

FIGURE 29

TABLE 1

SUMMARY OF TEST CONDITIONS

TRANSONIC TUNNEL TESTS

CONFIGURATION	SPRING RATE LBS/IN	M	ALTITUDE FEET x 10^{-3}	α, DEGREES	ΩR FT/SEC	p, PSFA	T, °F	VARIABLE ITEM	VALUE	*PART NUMBER
4 Blades, 8-Ft Rotor	500	0.50	54.0	0	Variable	200.5	91	ΩR	360, 439, 523	001
			54.0	3	450	200.5	91	--		001
			62.2	0	Variable	135.4	92	ΩR	170, 255, 350, 420	002
			73.0			80.6	88		139, 294, 347, 408	003
		0.75	77.1			66.0	60		141, 250, 350, 438	004
		0.75	77.2	3	440	65.9	60	--		005
		1.00	85.0	0	Variable	44.8	15	ΩR	160, 264, 353, 436	007
		1.00	85.0	3	428	44.8	15	--		008
		1.22	88.9	0	Variable	37.6	-10	ΩR	168, 282, 351, 456	009
		1.22	89.3	3	458	36.8	-12	--		010
		1.43	92.4	0	Variable	31.9	-49	ΩR	172, 237, 349, 426	011
		1.42	92.0	3	428	32.6	-47	--		012
		1.38	93.7	0	Variable	30.1	-42	ΩR	Fast Deployment 0-252	013
	1000	0.50	49.4	0	Variable	249.8	70	ΩR	152, 255, 352, 457, 822	014
			54.1			199.4	84		144, 248, 351, 449, 526	015
			64.6			119.8	85		125, 254, 352, 445, 452 499	016
	1250		49.4			249.8	70		142, 250, 349, 452, 527	017
			54.1			199.4	85		124, 254, 351, 448, 483	018
			64.6			120.1	88		149, 253, 350, 455, 478	019
		0.51	54.1	Variable	448	198.9	62	α	5, 7.7	020
		0.76	77.3		446	65.4	41		5, 7.7	021
		1.01	85.1		447	44.7	9		5, 7.7	022
		1.20	88.8		448	37.8	-13		5, 7.7	023
		1.42	91.7		449	33.1	-47		5, 7.7	024
2 Blades, 8-Ft Rotor		0.50	39.6	Variable	450	398.9	89		0, 3, 5	025, 026
		0.75	62.7		448	132.1	57		0, 3, 5	025, 027
		1.01	70.7		455	89.5	19		0, 3, 5	025, 028
		1.26	75.7		447	70.4	-18		0, 3, 5	025, 029
		1.50	79.7	5	448	58.0	-60	--		025
4 Blades, 7-Ft Rotor		0.50	54.1	0	Variable	199.4	75	ΩR	122, 262, 354, 451	030
		1.46	88.8	0	Variable	37.7	-56	ΩR	157, 254, 354, 449	031
Blades Removed	---	0.50	4.5	Variable	---	159.7	92	α	0, 3, 5, 7.6	033
		0.75	33.8			528.8	61		0, 3, 5, 7.6	034
		1.00	41.9			359.4	23		0, 3, 5, 7.7	035
		1.25	46.6			284.6	-16		0, 3, 5, 7.7	036
		1.50	50.9			232.7	-58		0, 3, 5, 7.7	037

* Test Reference Number

TABLE 2

SUMMARY OF TEST CONDITIONS

SUPERSONIC TUNNEL TESTS

CONFIGURATION	PRING RATE LBS/IN	M	ALTITUDE $\frac{}{3}$ FEET x 10^{-3}	α, DEGREES	ΩR FT/SEC	p, PSFA	T °F	VARIABLE ITEM	VALUES	*PART NUMBER
4 Blades, 8-Ft. Rotor	930	1.85	89.1	0	Variable	37.70	174	ΩR	211,255,296,348,413,448, 497	033
		1.88	89.1	5	Variable	37.70	175	ΩR	212,448	034
		1.88	89.1	9.5	Variable	37.70	175	ΩR	213,340	034
		2.13	96.0	0	Variable	27.45	124	ΩR	201,250,297,355,400,450, 500	031
		2.13	96.0	5	Variable	27.50	126	ΩR	207,451	032
		2.13	96.0	9.5	Variable	27.84	126	ΩR	208,452	032
		2.55	100.0	0	Variable	23.24	174	ΩR	239,302,350,401,462,494,	005
		2.55	100.0	5	Variable	23.24	174	ΩR	236,297,349,400,450,504	006
		2.55	100.0	9.5	Variable	23.14	178	ΩR	234,451	007
		2.58	104.6	0	Variable	18.90	185	ΩR	217,352,453,502	008
		2.91	118.0	0	Variable	10.65	166	ΩR	205,304,350,399,451,500	009
		2.91	118.0	5	Variable	10.65	163	ΩR	209,451	010
		2.91	118.0	9.5	Variable	10.65	163	ΩR	208,420	010
	1500	2.89	118.8	0	Variable	10.33	180	ΩR	194,441	023
	1500	2.89	118.8	5	Variable	10.30	179	ΩR	195,452	023
	1500	2.89	118.8	9.5	Variable	10.30	175	ΩR	193,452	023
	1500	2.69	111.5	0	Variable	14.01	177	ΩR	233,252,304,355,400,455, 500	024
	1500	2.92	105.4	0	Variable	18.25	180	ΩR	246,267,302,353,403,455, 504	025
2 Blades, 8-Ft. Rotor	930	1.88	89.2	0	Variable	37.80	171	ΩR	216,253,321,347,419,446, 502	037
	930	2.14	96.3	0	Variable	27.30	182.2	ΩR	208,252,287,345,390,423, 452,496	039
	1500	2.51	99.2	0	Variable	23.97	196	ΩR	240,248,305,354,408,449, 497	027
4 Blades, 7-Ft. Rotor	930	1.85	89.9	0	Variable	37.90	174	ΩR	194,253,296,345,400, 449	060
	930	2.15	97.1	0	Variable	26.30	158	ΩR	194,249,309,352,397, 451	057
	930	2.15	89.1	0	Variable	37.90	172	ΩR	224,253,300,360,395, 452	059
		2.51	99.2	0	Variable	24.10	191	ΩR	211,244,299,347,396,452	045
		2.89	118.3	0	Variable	10.55	183	ΩR	161,194,246,301,348,405,453	050
		2.89	116.4	0	Variable	11.40	172	ΩR	172,195,254,310,352,400,448	047
		2.89	110.8	0	Variable	14.42	186	ΩR	187,246,306,357,412,450	052
		2.91	106.4	0	Variable	17.50	188	ΩR	206,254,300,355,401,452	054
Blades Removed		1.88	89.2	Variable	-----	38.00	178	α	0,5,9.5	043
		2.12	95.9	Variable	-----	27.60	172	α	0,5,9.5	042
		2.55	99.9	Variable	-----	23.10	187	α	0,5,9.5	014
		2.92	118.3	Variable	-----	10.58	159	α	0,5,9.5	018

* Test Reference Number

H. TEST PROGRAM

The test program was established to investigate operation of the rotor system in axial flow for the range of speeds attained in the Transonic and Supersonic Circuits; namely, Mach 0.5 to Mach 3.0. Test conditions simulated a typical re-entry flight trajectory.

The following rotor configurations were tested to determine the effects of rotor geometry on the performance. The 4-bladed, 8-foot diameter rotor was the basic configuration and most similar to the flight test rotor system.

Number of Blades	Rotor Diameter	σ
4	8 Feet	.159
2	8 Feet	.079
4	7 Feet	.182

To determine the effect of governor spring rate upon governing characteristics, investigations were performed with governor springs having 500, 930, 1000, and 1250 pounds per inch spring rate.

Although the investigations were primarily for axial flow operation, the tunnel model support system permitted yawing the rotor axis up to 9.5^{o} with respect to the air stream. Runs were made at various small yaw angles up to the limit permitted.

The test conditions and variables for the Transonic and Supersonic Circuits are summarized in Tables 1 and 2, respectively.

I. TEST RESULTS

The variation of rotor drag and drag-force coefficient (C_{D_R}) with Mach number at various rotor tip speeds is presented in Figures 30 and 31. The rotor axial drag force varies with the air flow dynamic pressure when blades are stalled. At constant values of Mach number, the drag-force coefficient (C_{D_R}) is shown to decrease with lower rotor tip speeds, indicating that the drag-force coefficient is a function of the blade coning angle, or, in turn, the blade projected flat plate area. The feasibility of using a ROTOCHUTE for drag modulation or control of the retardation force is thus confirmed from this plot. In this particular ROTOCHUTE system, the limitations of the governing mechanism linkage, not

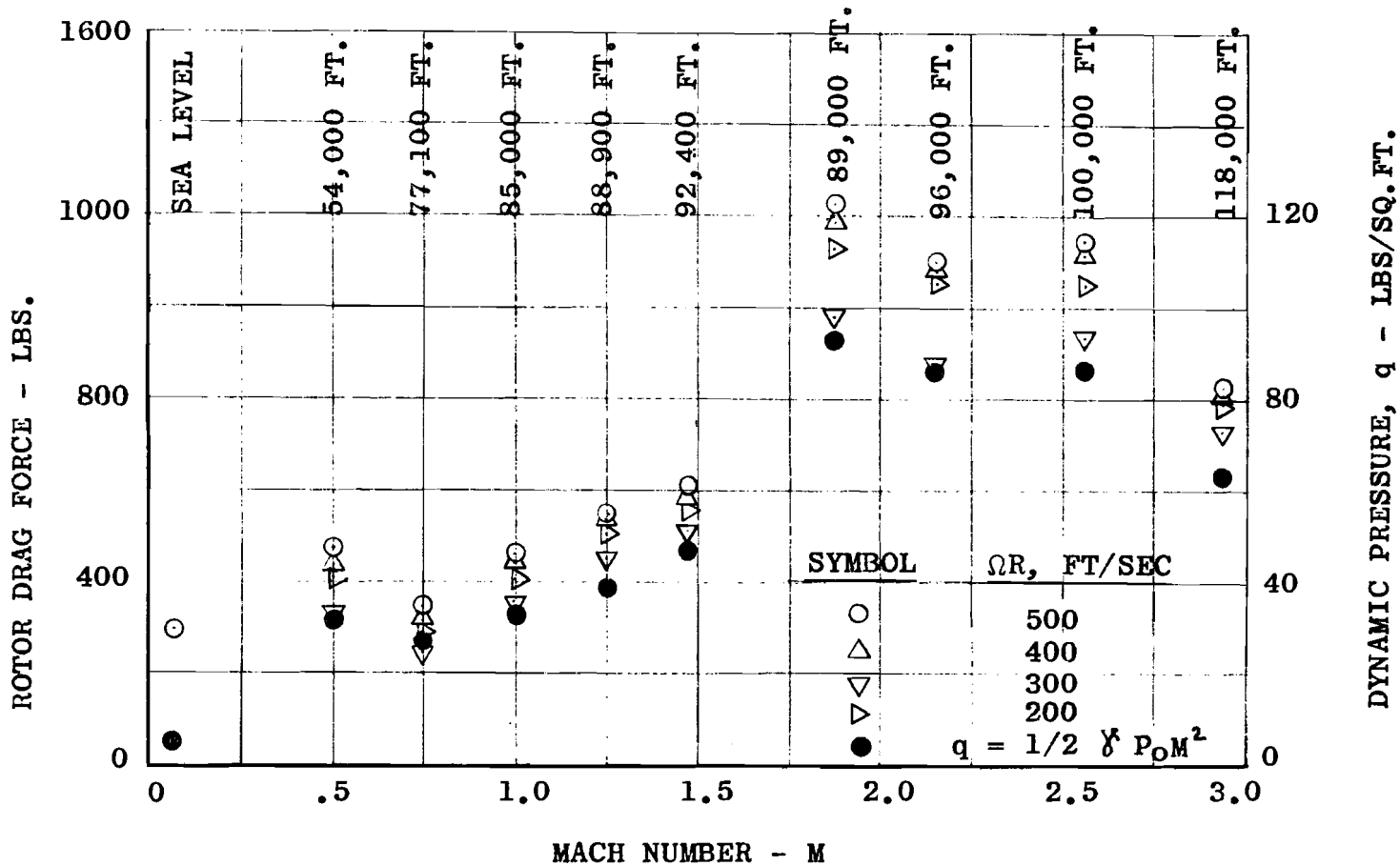

MODEL WIND TUNNEL TEST DRAG FORCE DATA

FIGURE 30

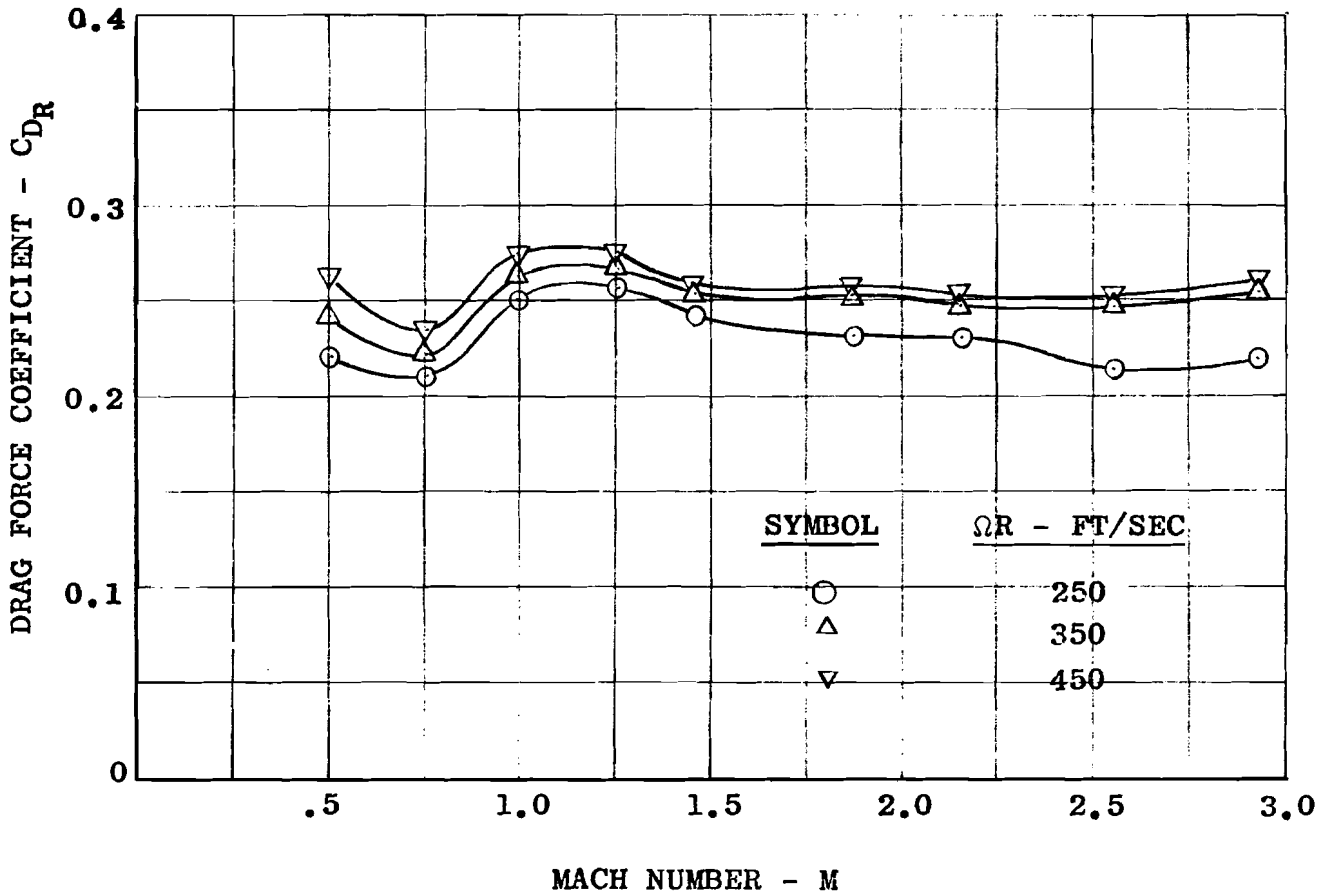

VARIATION OF DRAG-FORCE COEFFICIENT WITH TRAJECTORY MACH NUMBERS

FIGURE 31

designed specifically for the drag modulation function, limited governing the rotor speed below 200 feet per second. The drag-force coefficient could be modulated to lower values by designing the governing linkage system to govern to lower rotor speeds.

C_{D_R} as a function of the tip velocity ratio is plotted in Figure 32. The data for each Mach number at the highest ratio of $V/\Omega R$ were taken at the rotational speed that the rotor reached without any governor spring preload. Data for the three altitudes at Mach 0.5 show the small effect of altitude on C_{D_R}.

The model blade coning as a function of blade centrifugal force to blade axial force is plotted in Figure 33. Theoretical coning, derived from the simple relationship $\beta = \text{arc cot } (Fc/F_{A_b})$, closely approximates the measured data and indicates that the resultant blade axial force acts at or near the blade center of gravity. By assuming the blade is an element of a right circular cone, a simple analysis of the coning angle is made by summing the moments about the flapping hinge due to blade centrifugal and axial forces.

$$F_c \cdot X_{cg} \cdot \sin \beta = F_{A_b} \cdot X_b \cdot \cos \beta$$

$$\beta = \text{arc cot } \frac{X_{cg}}{X_b} \cdot \frac{F_c}{F_{A_b}}$$

When the ratio (X_{cg}/X_b) approaches a value equal to one, indicating that the axial-force action is near or through the blade center of gravity station, the relation becomes similar to the one plotted.

Figure 34 indicates the effect of small angles of attack on aerodynamic force coefficients. Angle of attack affects the drag-force coefficient little or none. The side force and yawing moment data show some scatter from inaccuracy in measuring the very small quantities. An instrumentation shift, occurring at 0^o and 3^o angle of attack, caused the shift in measured data. No appreciable effect of Mach number on the side-force and yawing-moment coefficients is indicated.

SYMBOL	M	ALTITUDE - FT	SYMBOL	M	ALTITUDE - FT
○	.50	54,000	◺	1.43	92,000
○	.50	62,000	▼	1.88	89,000
○	.50	73,000	▲	2.13	96,000
□	.75	77,000	●	2.55	100,000
◇	1.00	85,000	▶	2.88	118,000
△	1.22	88,900			

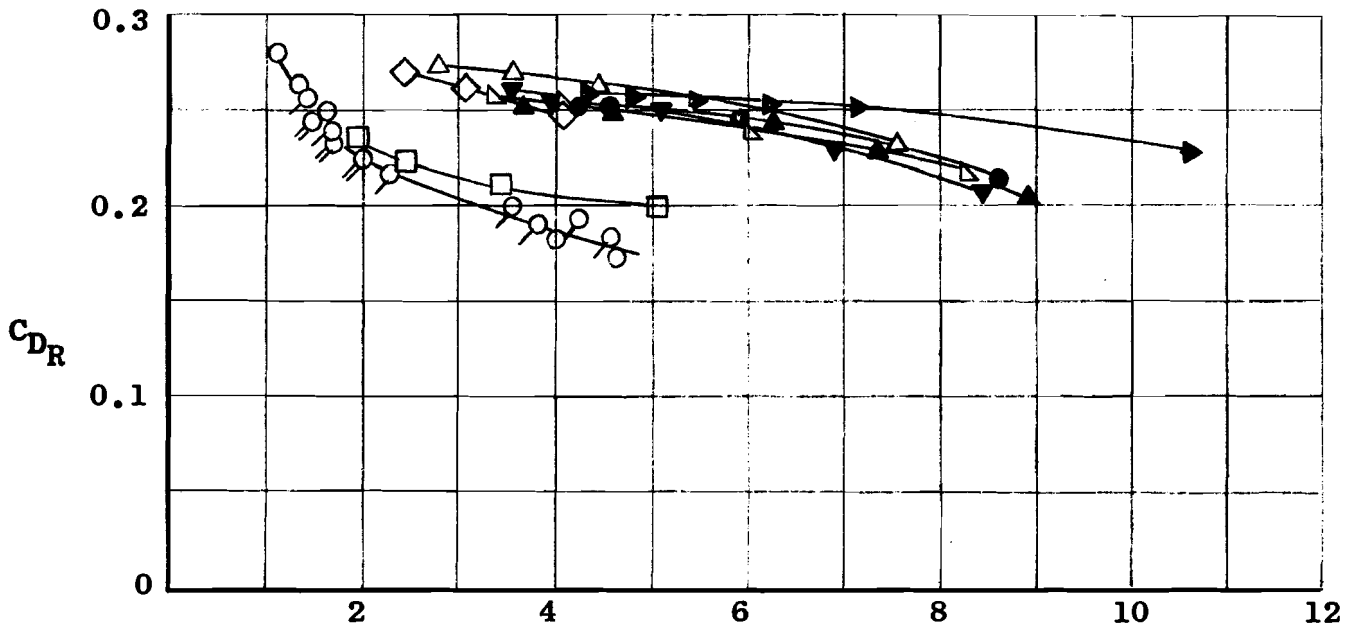

VARIATION OF DRAG-FORCE COEFFICIENT WITH ADVANCE RATIO

FIGURE 32

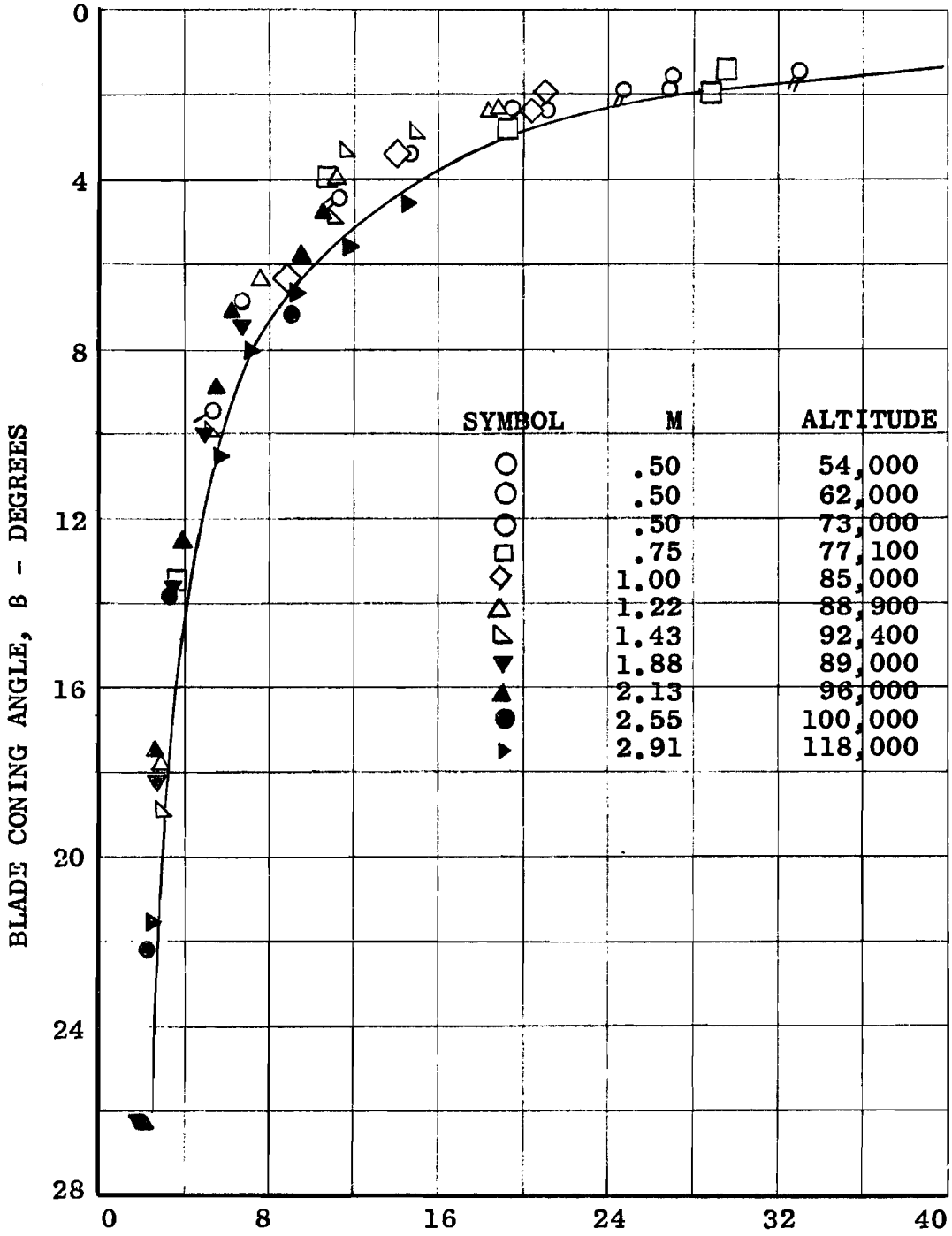

VARIATION OF BLADE CONING ANGLE WITH F_c/F_{A_b} RATIO

FIGURE 33

SYMBOL	M	ALTITUDE
▽	1.88	89,000
△	2.13	96,000
○	2.55	100,000
▷	2.91	118,000

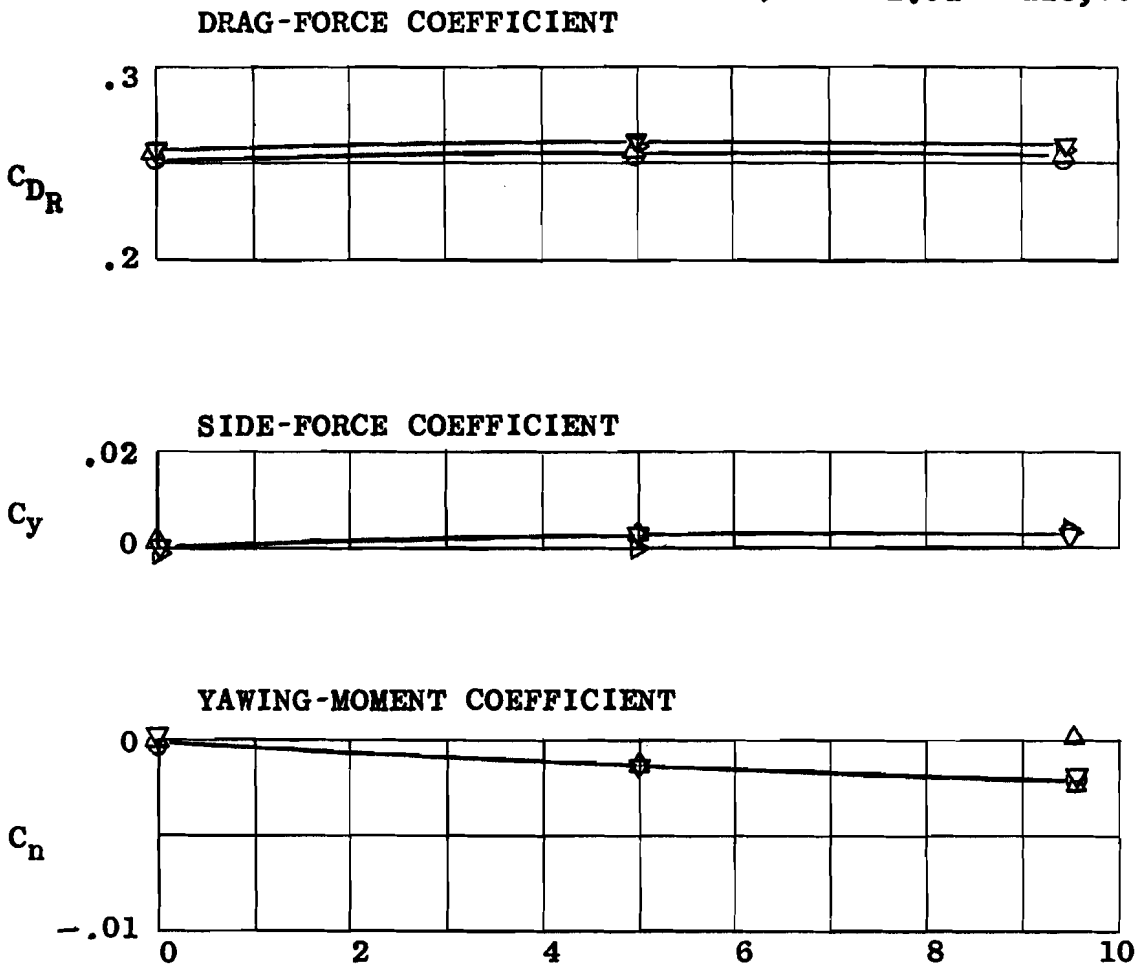

VARIATION OF C_{D_R}, C_y, AND C_n WITH YAW ANGLE

FIGURE 34

One of the test objectives was to determine governor spring preload for desired rotor speeds. The spring load variation with λ_d for trajectory conditions is shown in Figure 35. Since the spring reacts a portion of the centrifugal force through the governor linkage, the spring preload increases with rotational speeds. The spring preload to maintain a constant rotor speed along the trajectory is indicated by the dotted lines.

The effect of free-stream dynamic pressure on the spring load for constant tip velocity is presented in Figure 36. The spring force decreases slightly as the dynamic pressure increases, because aerodynamic moments, aiding spring-load moments to balance constant centrifugal moments at constant tip speed, are increased. However, if the spring preload is held constant, a large change in dynamic pressure is required to change rotational speed by a significant amount.

To evaluate the effect of rotor solidity on the drag-force coefficient, data were obtained with the 2-bladed, 8-foot diameter rotor and the 4-bladed, 7-foot diameter configuration. Figure 37 shows the effect of solidity on the drag-force coefficient for the Mach number range tested. C_{D_R} has been divided by rotor solidity. In essence, the coefficient is proportional to the solidity for the configurations tested. An increase of C_{D_R}/σ for the smaller drag-force rotors is noted at supersonic Mach numbers. Part of the increase is attributed to the fact that the model tare drag becomes a greater percentage of the drag force for these configurations at supersonic speeds. Drag-force tares presented in Figure 38 were obtained with blades removed and the model shaft stationary.

Tunnel blockage effects may be considered negligible since the drag coefficients for rotors of widely varying solidity correlated to a very close degree.

The time history of axial force, spring load, and rotor tip velocity during a rapid deployment of the basic configuration at Mach 1.375 and 3.0 are presented in Figures 39 and 40. At Mach 1.375, the rotor reached equilibrium rotational speed, and axial drag force in approximately 2.5 seconds after blade release. Inflection points on the tip velocity and drag-force curves are noted at approximately 1.5 seconds as the governing action begins. Governing action during deployment was very smooth, and no tendency for the rotor to overspeed or oscillate about the governed

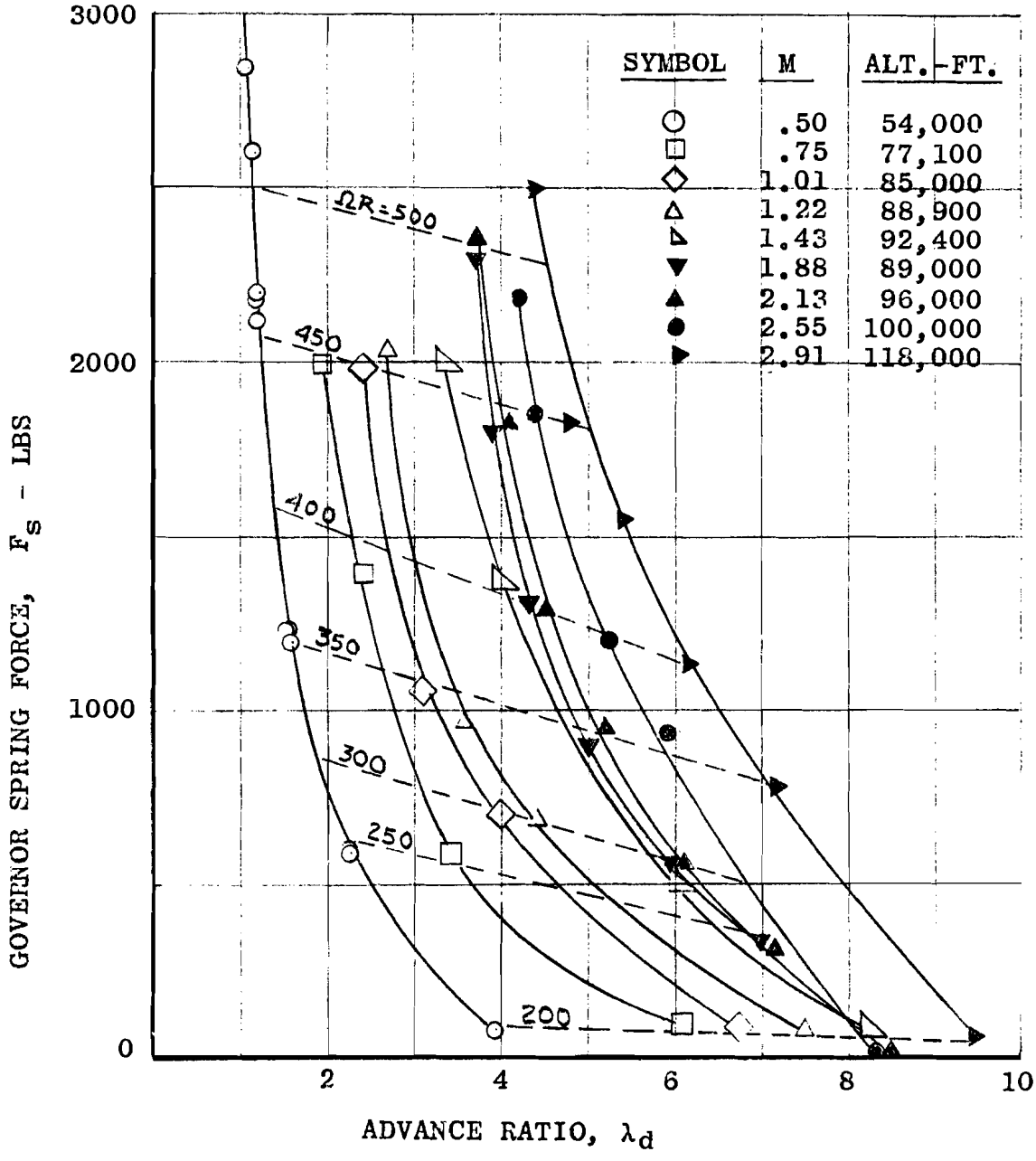

VARIATION OF GOVERNOR SPRING FORCE WITH ADVANCE RATIO

FIGURE 35

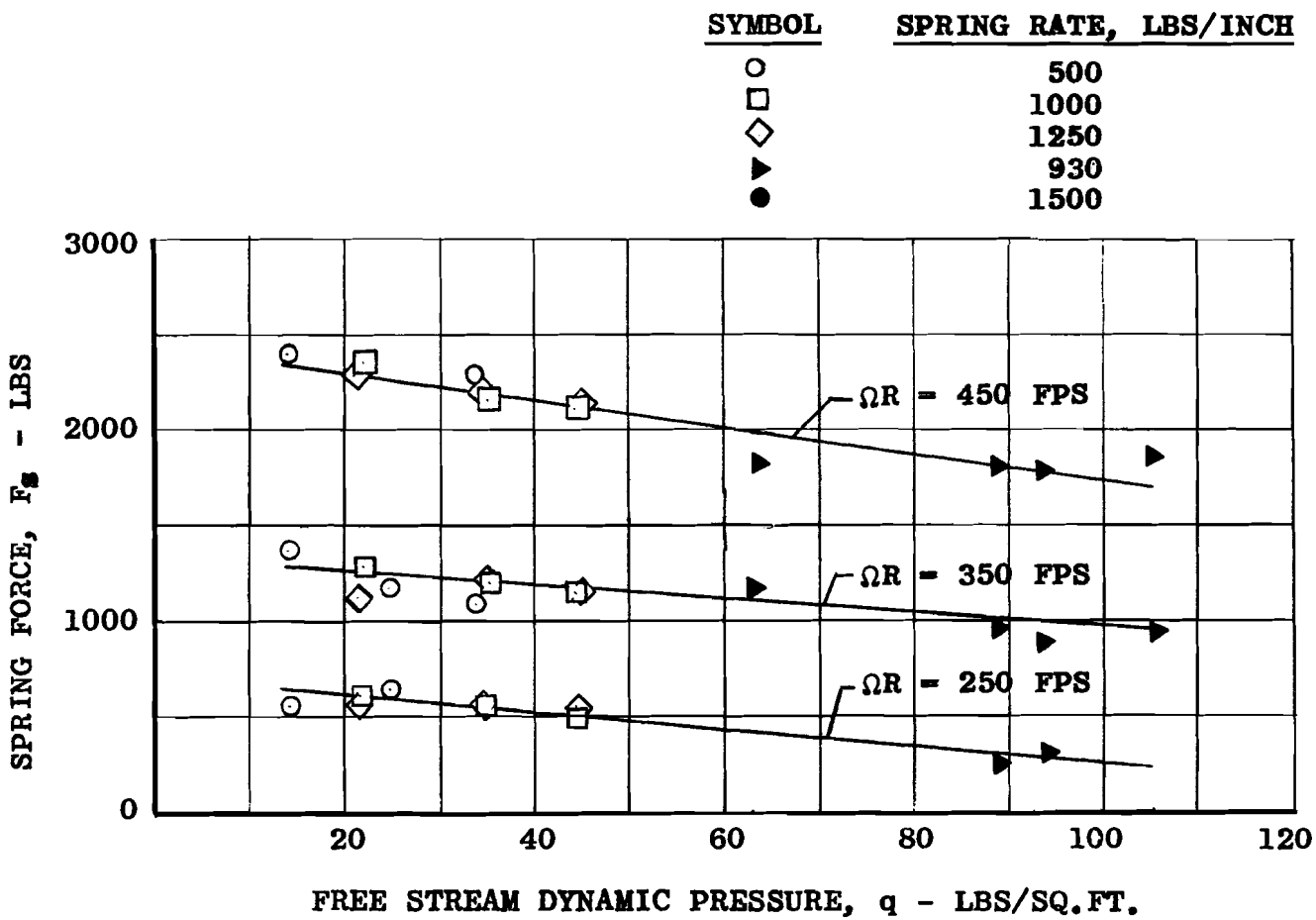

EFFECT OF DYNAMIC PRESSURE ON GOVERNOR SPRING FORCE

(FOR CONSTANT TIP VELOCITY)

FIGURE 36

SYMBOL	CONFIGURATION
○	4 Blade, 8-Foot Dia. Rotor
□	2 Blade, 8-Foot Dia. Rotor
△	4 Blade, 7-Foot Dia. Rotor

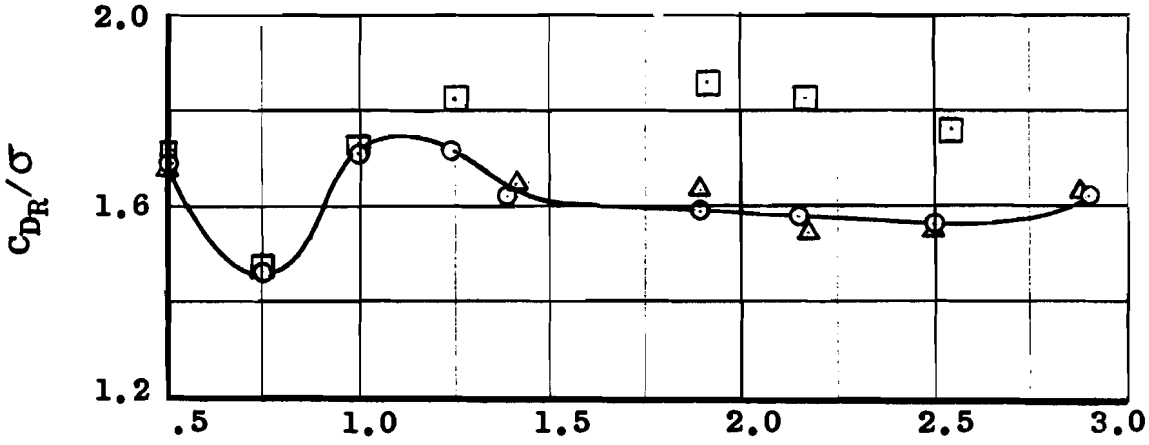

EFFECT OF ROTOR SOLIDITY ON DRAG COEFFICIENT

(ΩR = 450 FPS)

FIGURE 37

○ Based On 8-Ft. Diameter Rotor Disc Area

□ Based On 7-Ft. Diameter Rotor Disc Area

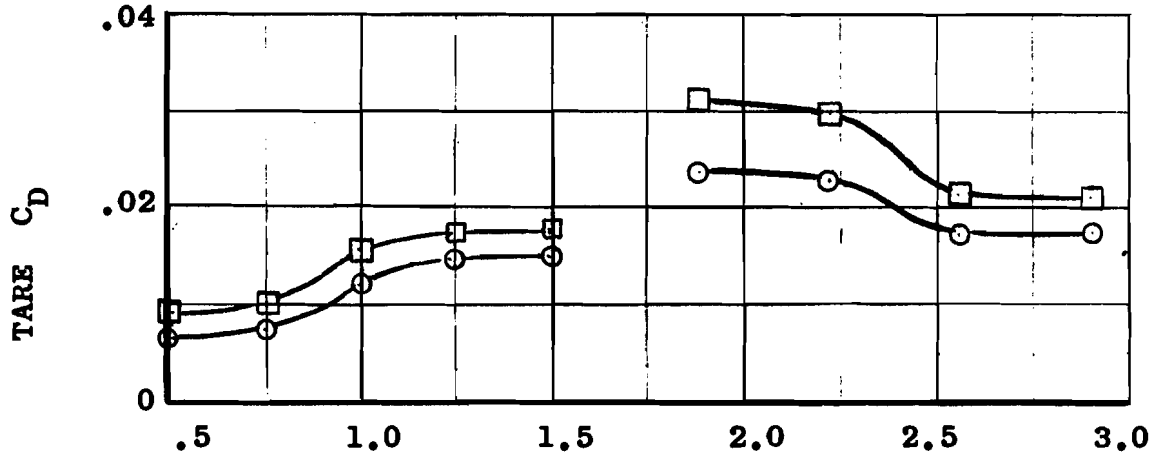

MODEL TARE DRAG COEFFICIENTS

FIGURE 38

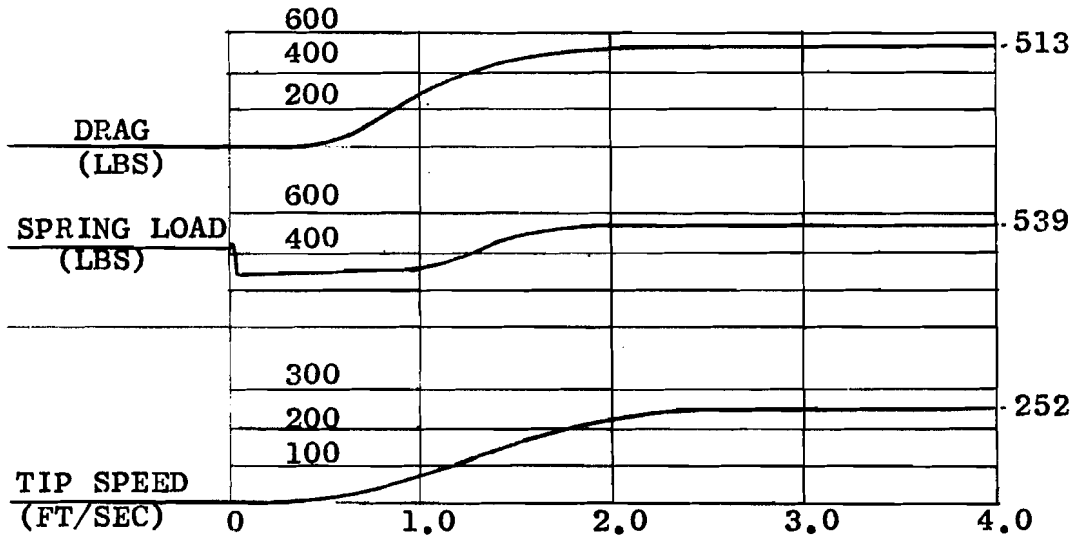

TIME HISTORY: RAPID DEPLOYMENT AT M - 1.38, 93000 FT.

FIGURE 39

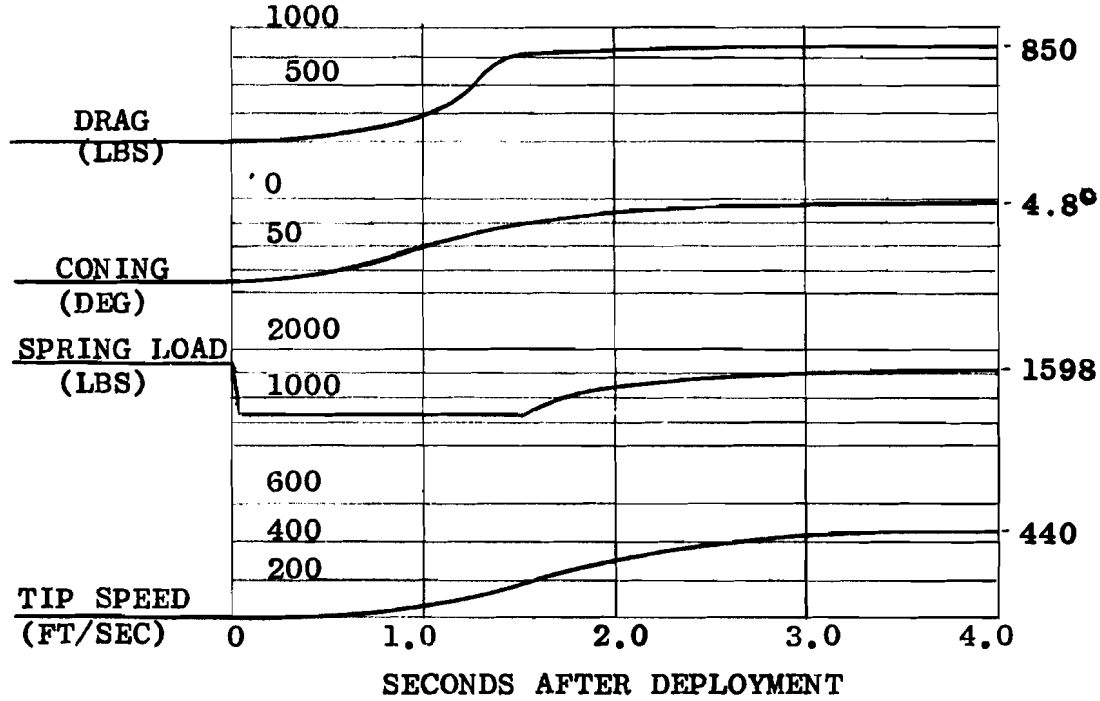

TIME HISTORY: RAPID DEPLOYMENT AT M - 3.0, 118000 FT.

FIGURE 40

value was noted. The stable operation on reaching equilibrium was typical of the ROTOCHUTE operation at all test conditions. At Mach 3.0, equilibrium thrust or drag was developed in approximately 1.5 seconds, and the force build-up is related to coning.

Rotor blade failure occurred during a shutdown from Mach 2.93 operation. During the shutdown phase, shock waves travel upstream through the tunnel test section. Normally, the rotor was braked to a standstill for operation when the shock waves passed through. In this instance, however, the rotor was operating at an RPM exceeding the rotor brake stopping capability. The governor spring preload system had jammed, and the spring load could not be relieved. The shock wave pressures were severe enough to cause blade failure.

The model and installation sustained little damage. The preload system was modified, a new set of blades installed, and the system was put into operation again with minimum delay. No further trouble was experienced.

J. COMPARISON OF THEORY AND EXPERIMENTAL DATA

Figures 41 and 42 compare calculated axial-force coefficients with corresponding experimental results for the basic rotor configuration. Agreement between theoretical and experimental data is close at the subsonic Mach numbers. A discrepancy between predicted and experimental values is noted at the Mach 1.0 regime, but becomes smaller and more negligible as the Mach number increases. The discrepancy is attributed to interference between the nose cone shock wave and the rotor, an effect not included in theoretical predictions.

Rotational speed of the rotor as a function of governor spring preload is presented in Figure 43. The minimal scatter of data for the test range of Mach numbers, dynamic pressures, and governor spring rates indicates that the effect of these parameters on governing characteristics is negligible.

Rotor moments and lateral forces at the small rotor axis angles of yaw (limited by the tunnel support system) were generally too low in magnitude with respect to the balance sensitivity to permit accurate measurements.

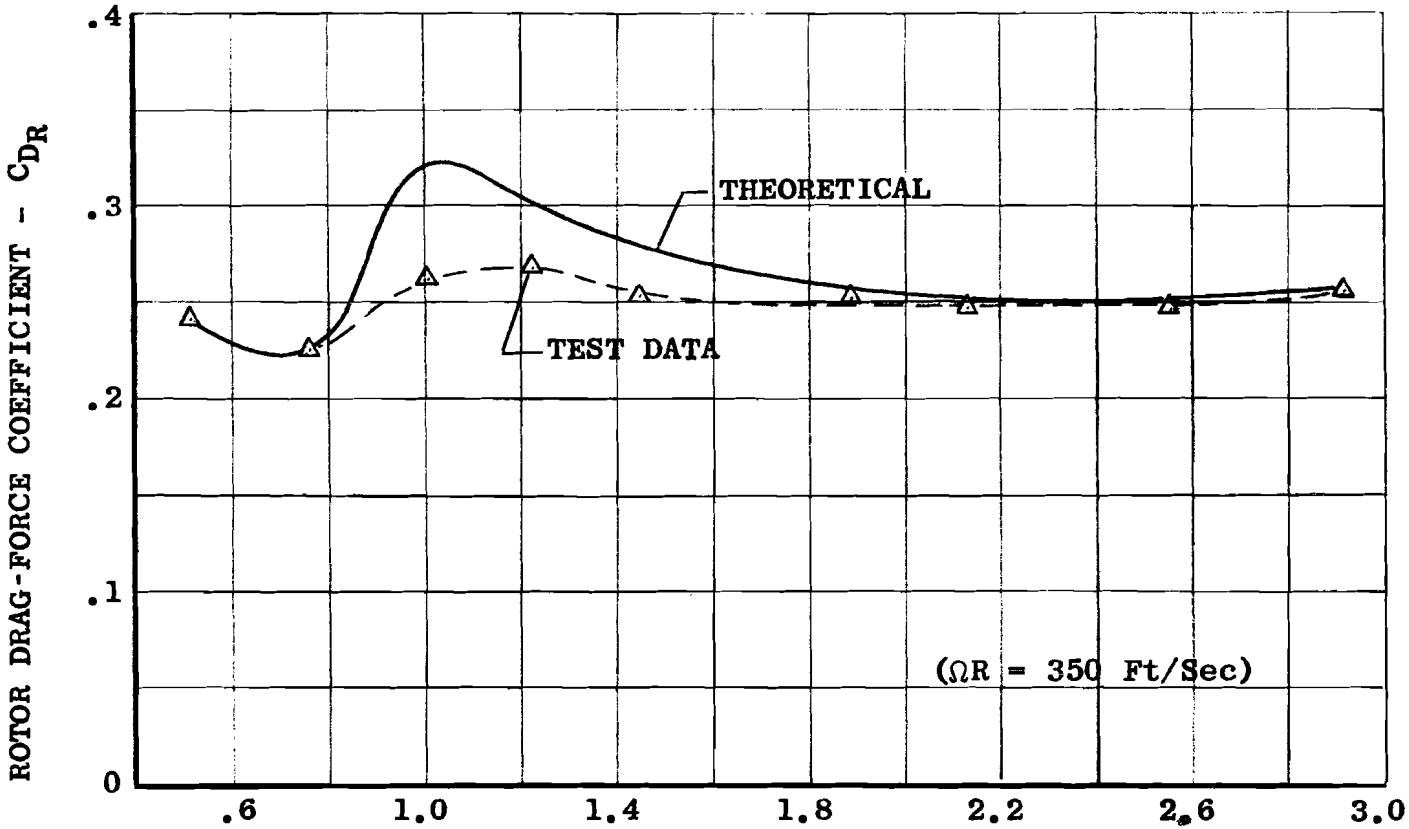

COMPARISON OF THEORETICAL AND EXPERIMENTAL C_{D_R} AT VARIOUS MACH NUMBERS

FIGURE 41

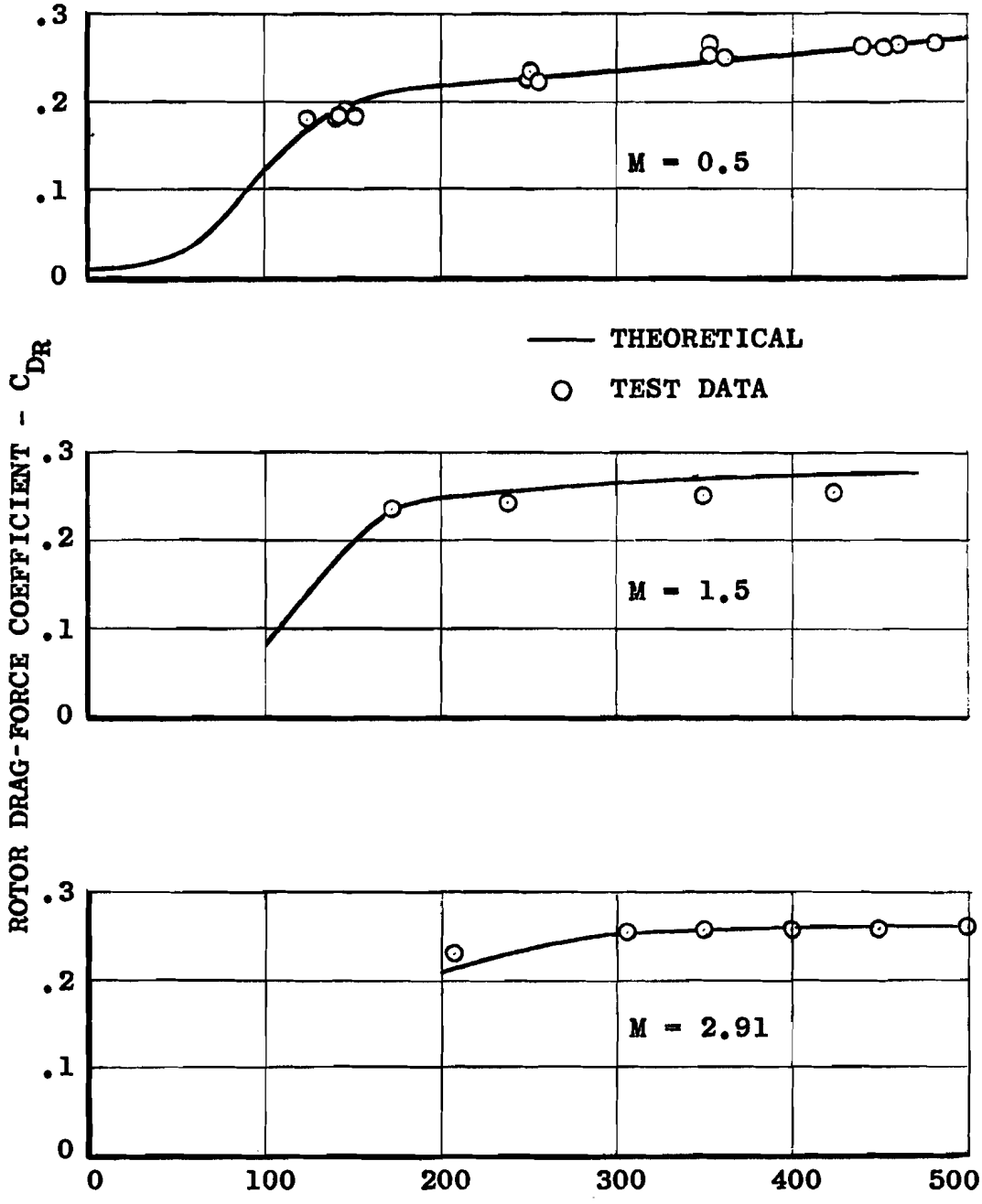

COMPARISON OF THEORETICAL AND EXPERIMENTAL C_{D_R} AT VARIOUS TIP SPEEDS AND MACH NUMBERS

FIGURE 42

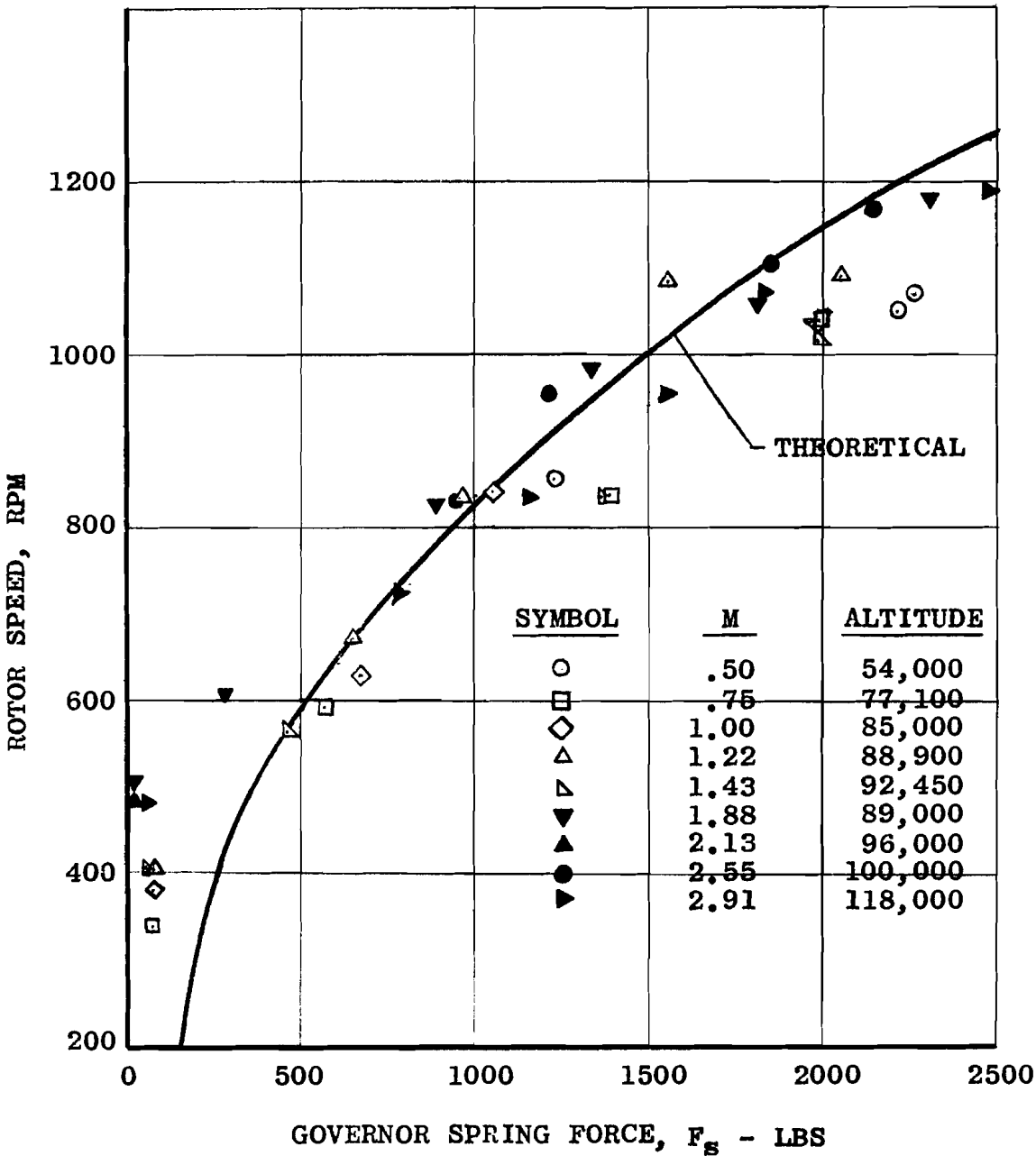

COMPARISON OF THEORETICAL AND EXPERIMENTAL GOVERNING CHARACTERISTICS

FIGURE 43

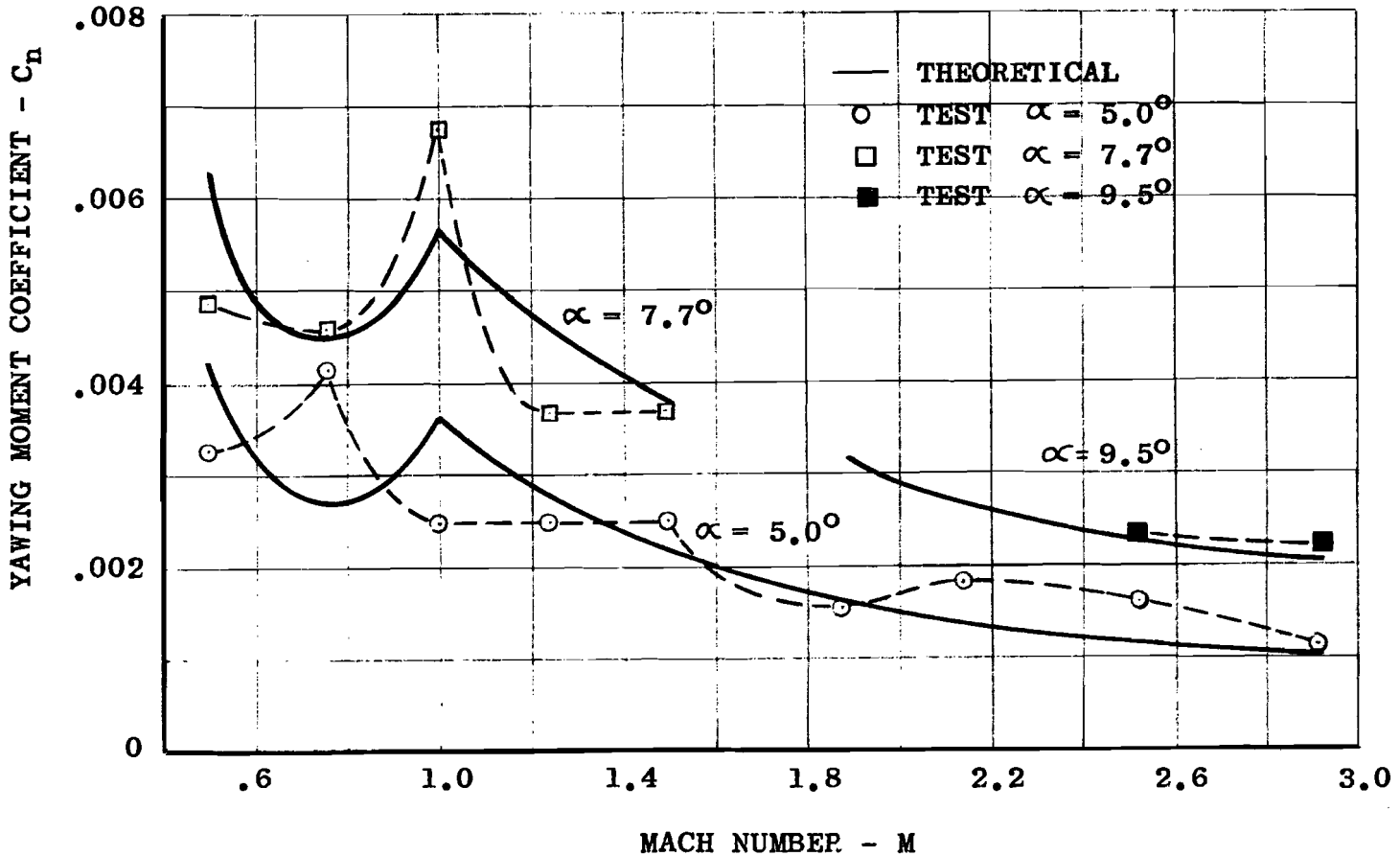

COMPARISON OF THEORETICAL AND EXPERIMENTAL YAWING-MOMENT COEFFICIENTS

FIGURE 44

Yawing-moment coefficients for various yaw angles are presented in Figure 44 at various test Mach numbers. Agreement between theoretical and experimental results is reasonable in view of the insensitive measurements of the small forces involved. Discrepancies are believed due, in part, to insufficient data on blade section characteristics at high angles of attack, as discussed previously; and at lower Mach numbers, to the inadequate expression of the blade section normal force coefficient characteristic by its equation at advance ratios approaching unity.

Agreement improves with increasing Mach number, as might be expected, for the following reason. Reference 7 indicates that, theoretically, $C_N \rightarrow \overline{C}_N \sin^2 \alpha_x$ as $M \rightarrow \infty$, that is, $C_{N_o} \rightarrow 0$. Hence, the expression for the blade normal force coefficient becomes an increasingly better representation as Mach number increases. Data at the higher Mach numbers confirm this prediction. Accurate calculation of rotor moments and lateral forces may have to be performed by numerical integration, using accurate, yet to be obtained, blade section data at high angles of attack.

4. EXPLORATORY AIR DROP TESTS

A. INTRODUCTION

Exploratory air drop tests were conducted with remotely-controlled KRC-6 ROTOCHUTE flight test vehicles at the Joint Navy-Air Force Parachute Test Facility, El Centro, California. The U. S. Air Force 6511th Test Group (Parachute) provided the drop aircraft and other necessary support services. Testing at the Government-furnished facility was arranged by the Aeronautical Systems Division.

The air drop tests demonstrated the capabilities and performance potential of the ROTOCHUTE-type decelerator concept and defined areas wherein additional research and experimenting would prove valuable in realizing the full potential of rotary-wing decelerators. Details and results pertaining to the air drop tests are presented in this section.

B. OBJECTIVE

The prime objective of the exploratory air drop testing was to demonstrate the feasibility of utilizing a rotary-wing decelerator for retardation at subsonic speed, controlled glide descent, and near-zero velocity landing. The tests were defined to explore the test vehicle glide capability, maneuverability, response to control, and touchdown performance.

C. CONCLUSIONS

As a result of successfully deploying the rotor system, gliding, and maneuvering the KRC-6 ROTOCHUTE during descent, demonstrating the "flared" landing functions, and evaluating test results and data, it is concluded that:

1. It is feasible to retard and recover payloads with remotely-controlled, rotary-wing decelerator systems.

2. The behavior and performance in flight can be reasonably predicted.

3. Transition into glide from axial descent is smooth and stable.

4. Rotary-wing decelerator systems will provide useful glide L/D ratios for many applications.

5. Parasite drag of the recoverable unit has an important effect on the glide ratio. The higher the drag, the steeper the descent.

6. Horizontal and vertical touchdown velocities can be substantially reduced by means of the "cyclic" and "collective" flare maneuver.

7. Spiral instability of the ROTOCHUTE induced by operation of the rotor at RPM's above the stable range can be controlled and eliminated by automatic stabilization.

8. The horizontal stabilizer is not an essential element to the concept for trim if sufficient trim control is provided in the rotor system design.

9. The collective pitch should be controllable for co-ordination with cyclic control during the landing flare maneuver.

10. More effective lateral control is required during cyclic flare to prevent roll and eventual spiral.

11. Rotor forces, performance, aerodynamic and stability characteristics of a recoverable unit as an entity should be determined as accurately as possible in wind tunnel and other tests to provide the data and knowledge for more accurate analytical prediction of the behavior and performance and a minimum development period.

12. Additional study and flight testing of the cyclic and collective flare landing maneuver is required for a better demonstration of the performance potential in this regime.

D. FLIGHT TEST VEHICLE

To demonstrate feasibility of controlled recovery and provide experimental flight test data on rotary-wing decelerator system performance and behavior during controlled glide descent and maneuvers, a remotely-controlled KRC-6 ROTOCHUTE flight test vehicle was designed and fabricated. Existing available hardware and components were used to the maximum extent possible. Systems were incorporated for rotor deployment, remote control

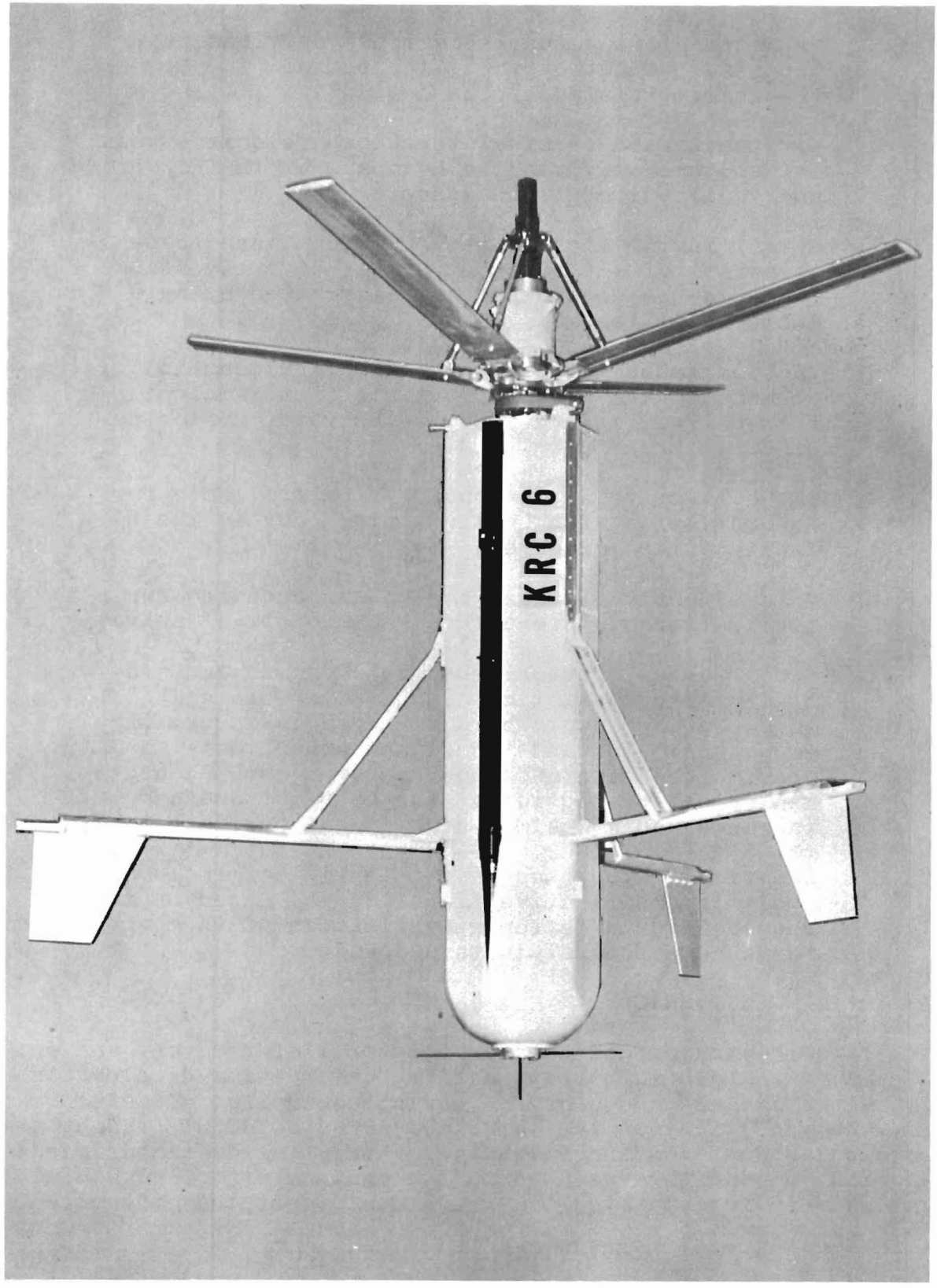

FIGURE 45 KRC-6 TEST VEHICLE (Original Configuration)

and guidance, stabilization, telemetry and flare functions. Instrumentation was provided to record vehicle attitude and behavior, rotor system data, and flight performance. The original configuration, prior to modifications during tests, is shown in Figure 45.

The KRC-6 rotor system was adapted from the proven KRC-4 ROTOCHUTE rotor system. The four-bladed rotor was initially eight feet in diameter. Basic elements of the rotor system are essentially those described for the wind tunnel model in Section 3. However, the synchronizer system was modified and a collective "flare" control system was added. Also, the rotor hub was cast of aluminum alloy for weight reduction. Figure 46 and Figure 47 show the rotor system (final configuration) in the deployed and stowed state respectively.

Rotor deployment is initiated at launch or release when the firing pin of the T-33 Delay Initiator (a U.S. Army Ordnance unit used extensively in aircraft ejection seat installations) is pulled by a static line attached to the launch aircraft. A short delay ensues (2 and 3 second delays were used) before the main charge is fired to generate the gas pressure pulling for the rotor deployment pin. A short length of high temperature hydraulic hose transmits the gas pressure from the initiator unit mounted on the body to the deployment pin chamber.

The synchronizer system was modified to permit limited differential flapping of blades, thus reducing rotor aft pitching moments, hence servo control loads, during glide. The synchronizer rods, instead of attaching directly to the synchronizing slide element, couple to the slide through limited-travel cranks which allow approximately $\pm 10^{o}$ blade flapping from nominal operation coning position.

The "one-shot" collective flare system positions all blades at a selected "high" pitch or angle of attack simultaneously on a command signal. The electrical signal ignites the T14E2 Ignition Element of the M1A1 Thruster Actuator mounted within the upper section of the rotor assembly. The two pyrotechnic units are U.S. Army Ordnance Frankford Arsenal items. The ignition element fires the thruster. Generated internal gas pressure powers the thruster piston which, through connecting linkage, pulls "up" on the governor housing to compress the governor spring. This upward motion of the housing positions the blades at the selected pitch setting through the governor mechanism linkage. The "flare" pitch setting is established by adjustment of the collective flare rod assembly length. The shorter the length, the higher the pitch. During normal governing action, relative motion between

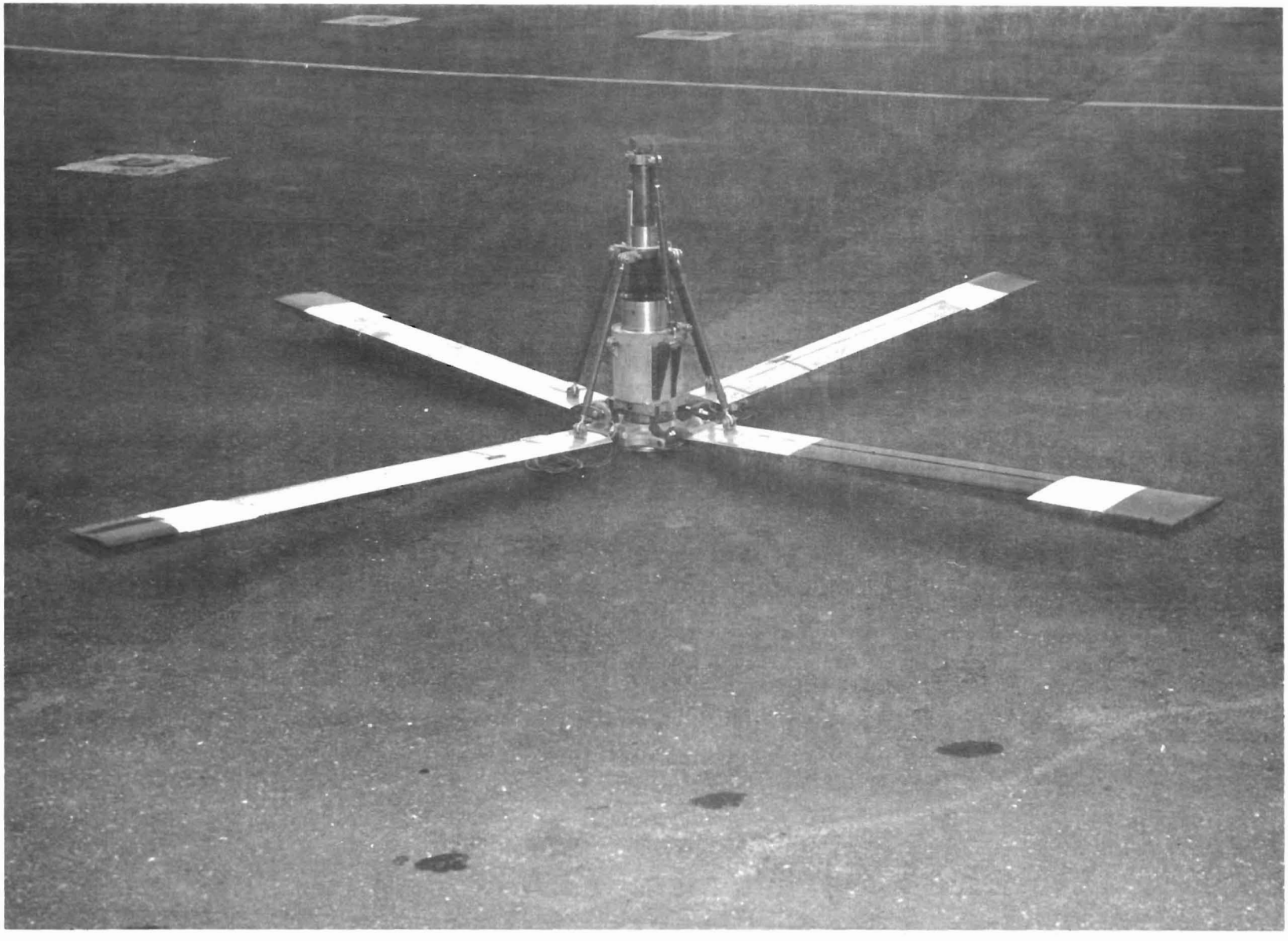

FIGURE 46 KRC-6 ROTOR ASSEMBLY (Deployed)

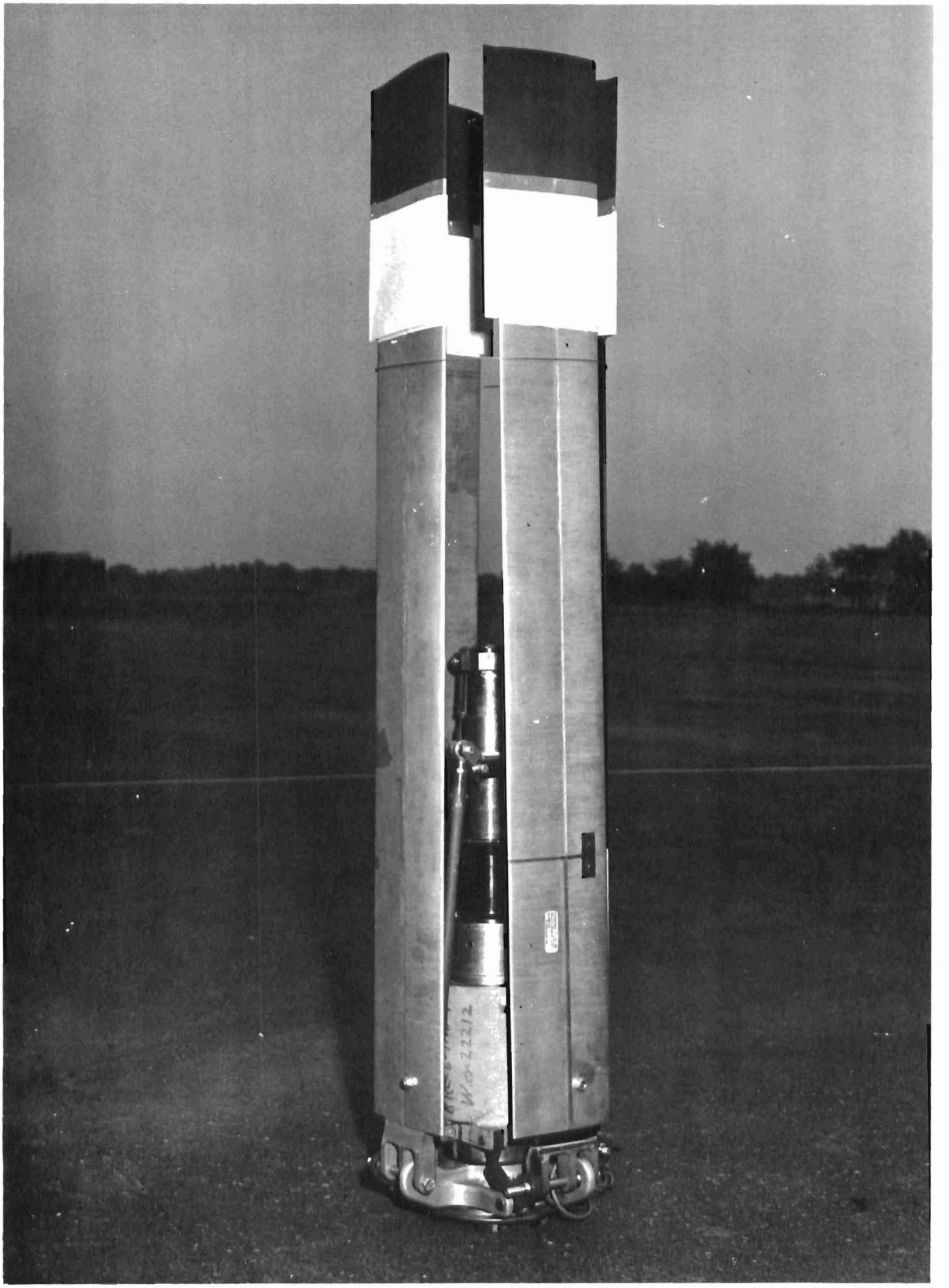

FIGURE 47 KRC-6 ROTOR ASSEMBLY (Pre-Deployment)

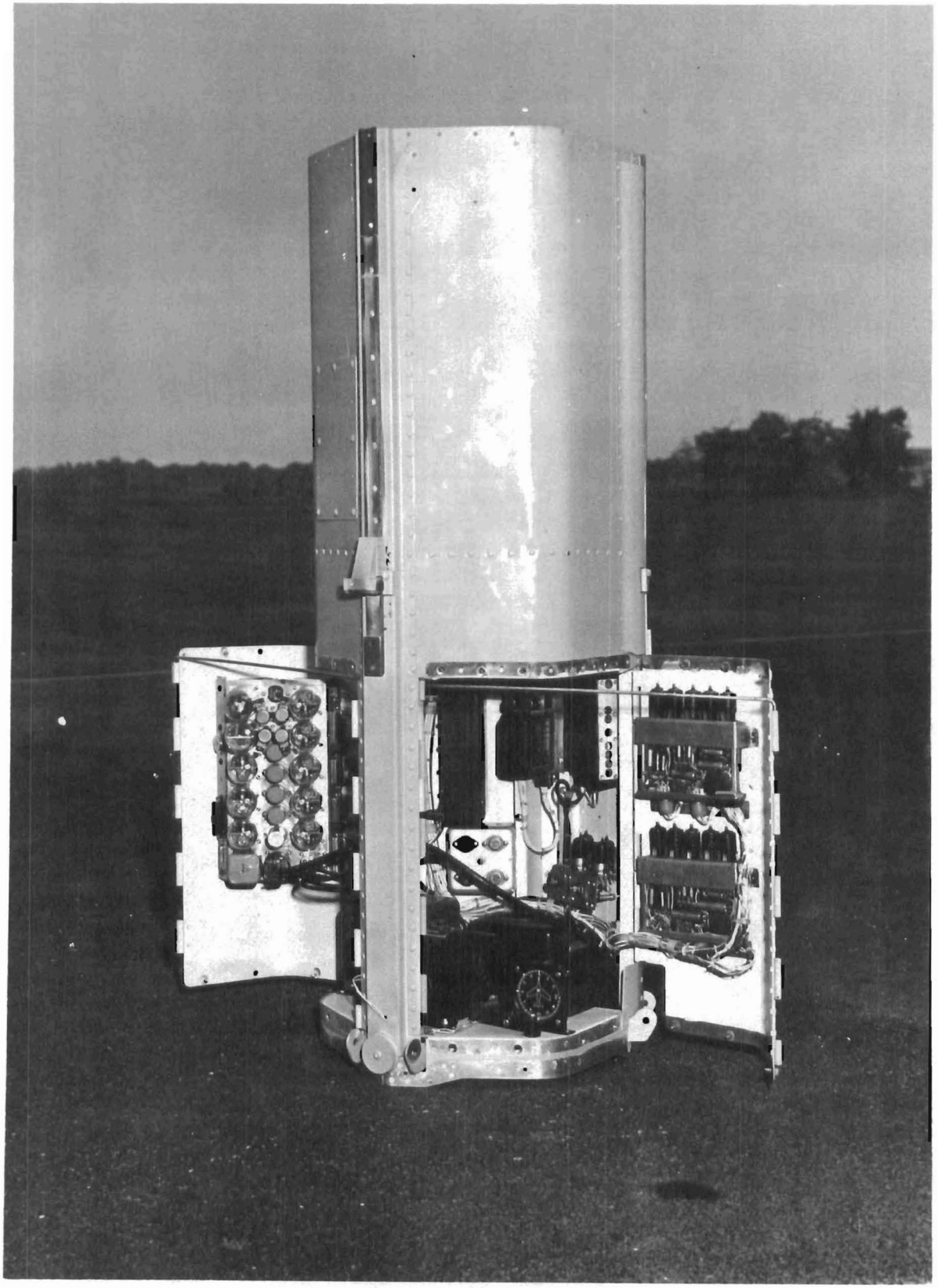

FIGURE 48 KRC-6 BODY UNIT

the "flare" rod assemblies and actuating cross arm (attached to the thruster piston output terminal) is allowed by slots in the rod assembly upper terminal fitting.

A multiple-channel slip ring serves as the electrical coupling between the stationary and rotating portions of the rotor assembly for the rotor instrumentation sensor and collective "flare" signals. Rotor parameters such as housing position, blade coning, and blade bending stresses (flatwise and chordwise) and rotor rpm may be recorded. RPM signals from the magnetic pickup do not pass through the slip ring, since the pickup is mounted on the stationary control spider.

The stationary shaft supporting the rotor assembly picks up the control spider, which is mounted atop the body unit through an automotive-type universal assembly. The universal allows tilt freedom of the rotor assembly in all directions with respect to the body. The pitch and roll control rods pick up the control spider and position the rotor as commanded.

The body unit, Figure 48, houses the remote control and guidance, stabilization, and telemetry systems. The body (hexagonal in cross-section, 16 inches across the flats) is fabricated of aluminum alloy skins, bulkheads, and appropriate stringers. Two hinged doors with quick-release fasteners provide access to the lower compartment wherein the avionics and telemetry components are installed. The rotor attachment-servo pedestal and electromechanical control servos are located in the upper compartment. The upper bulkhead, pedestal, servos and spider assemble as a removable unit, Figure 49 and Figure 50. A hand-hole in the side of the body provides limited access to the servos. Standard lugs on 14-inch centers are provided for aircraft bomb rack support and launch. Figure 51 shows the major body assembly units.

Fins at the aft end of the body stabilize the vehicle longitudinally during the launch phase prior to rotor deployment. The stabilizing fins are mounted on retractable legs or tubes held against the body by solenoid-operated locking pins. After rotor deployment, as the test vehicle approaches vertical descent, the legs are deployed. Shock chords pull the leg struts past track latches to lock the legs in a plane perpendicular to the body longitudinal axis. The two forward fins are free to swivel and weathercock during the glide for minimum drag. The aft fin is fixed on its leg and acts as a directional fin in glide to establish body heading. At touchdown, the tripod leg system was to serve as a rudimentary alighting gear. Figure 52 shows the legs in various stages of deployment.

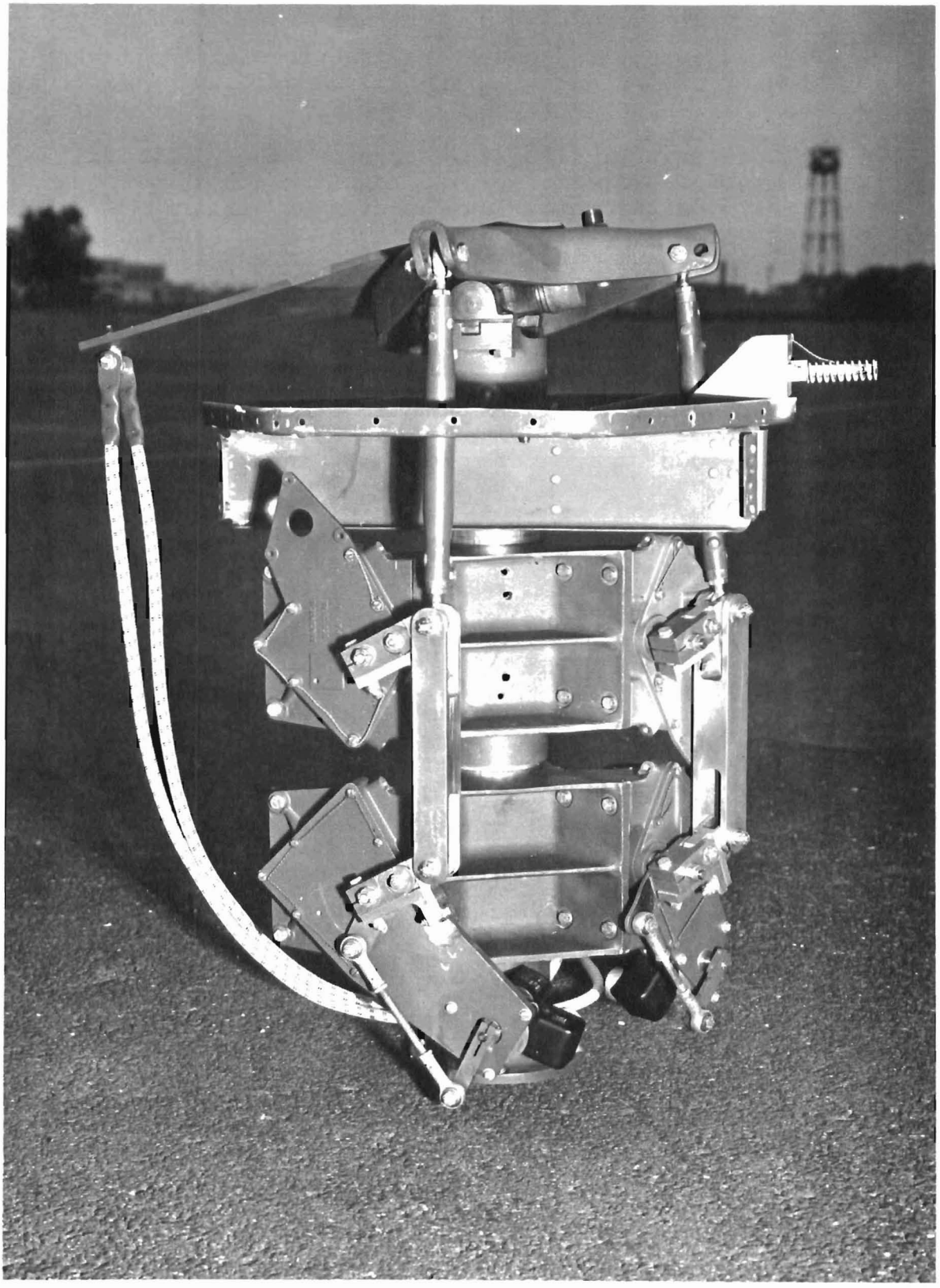

FIGURE 49 KRC-6 ROTOR CONTROL SYSTEM

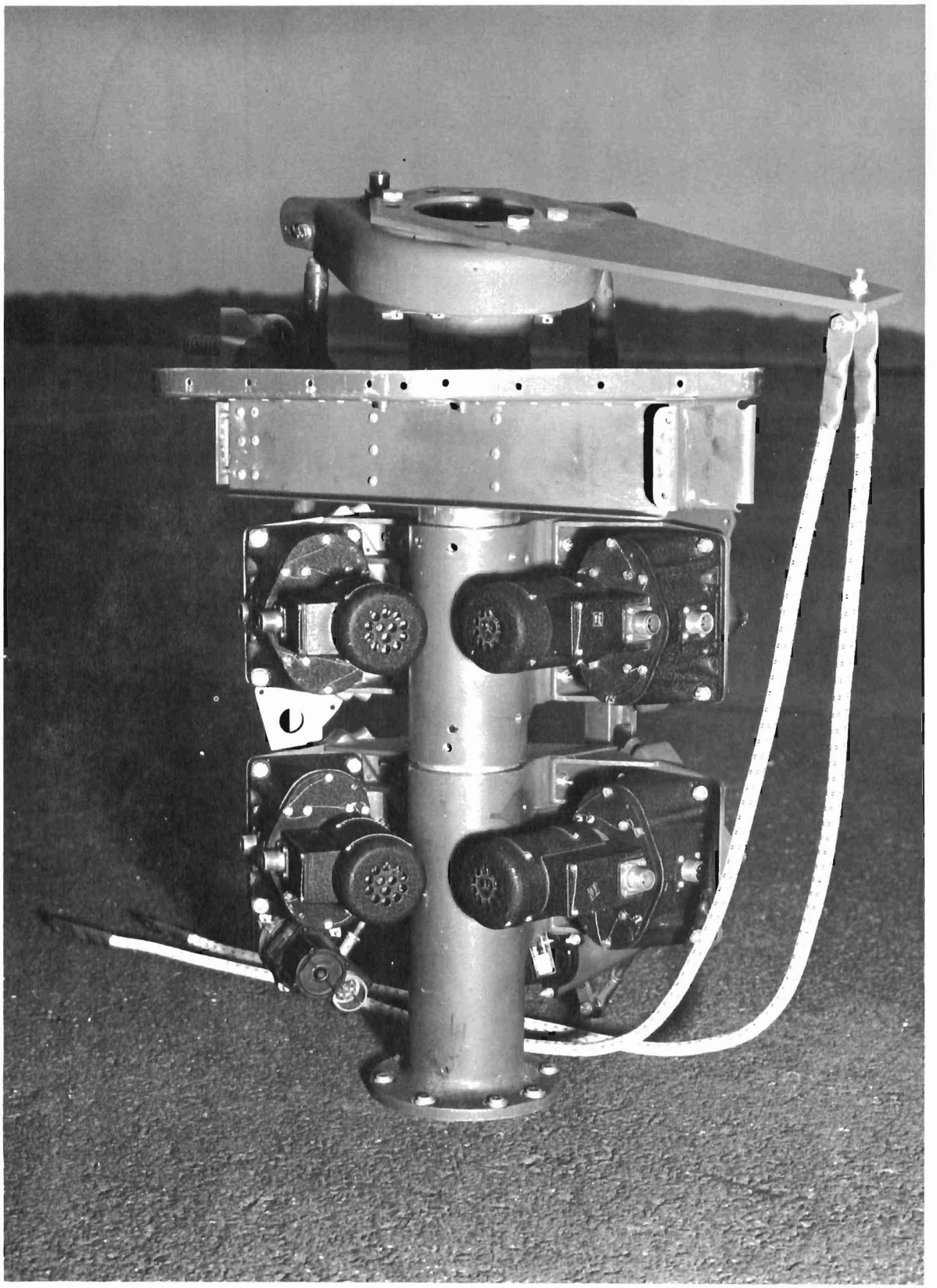

FIGURE 50 KRC-6 ROTOR CONTROL SERVO INSTALLATION

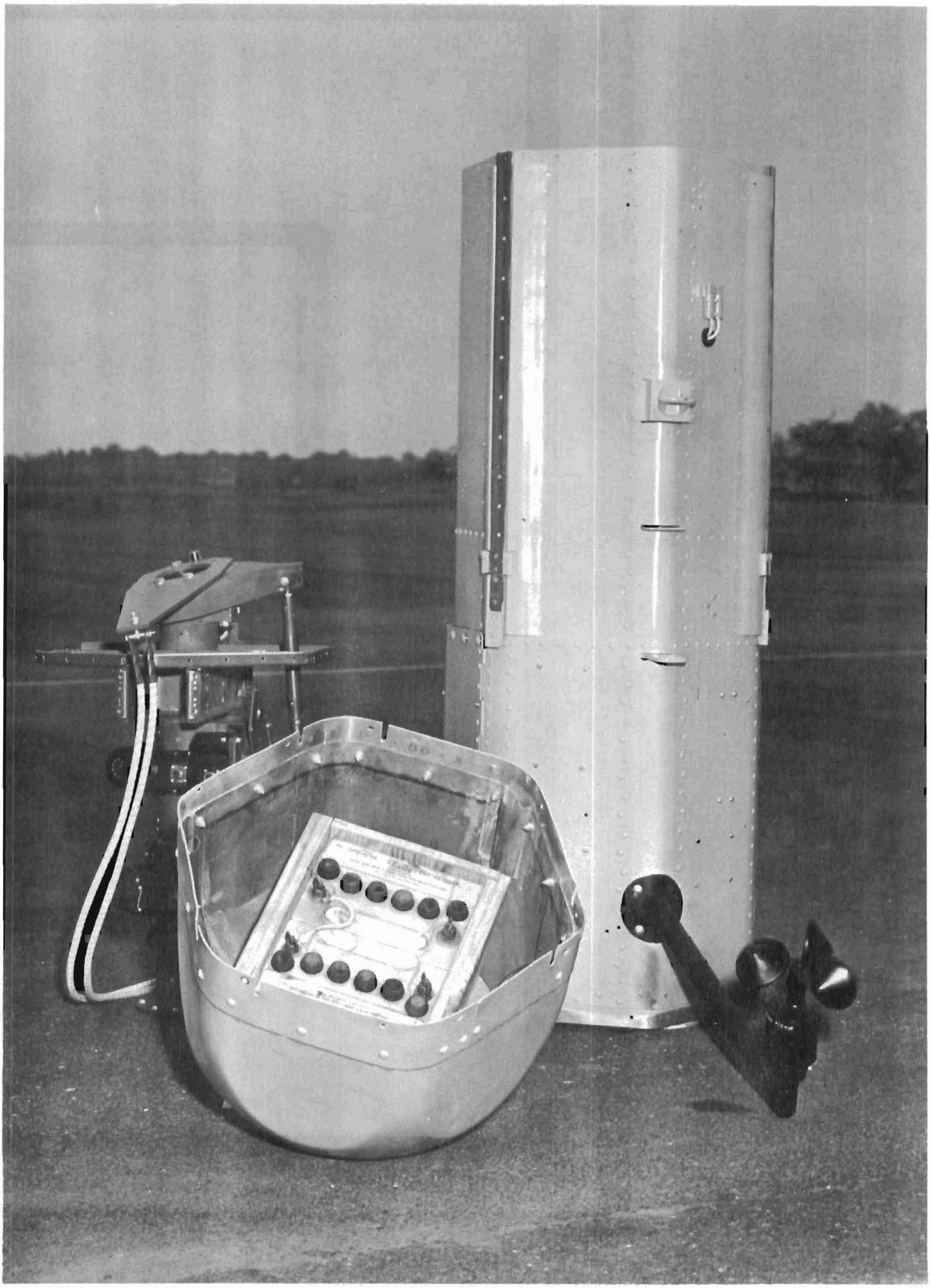

FIGURE 51 KRC-6 BODY UNITS

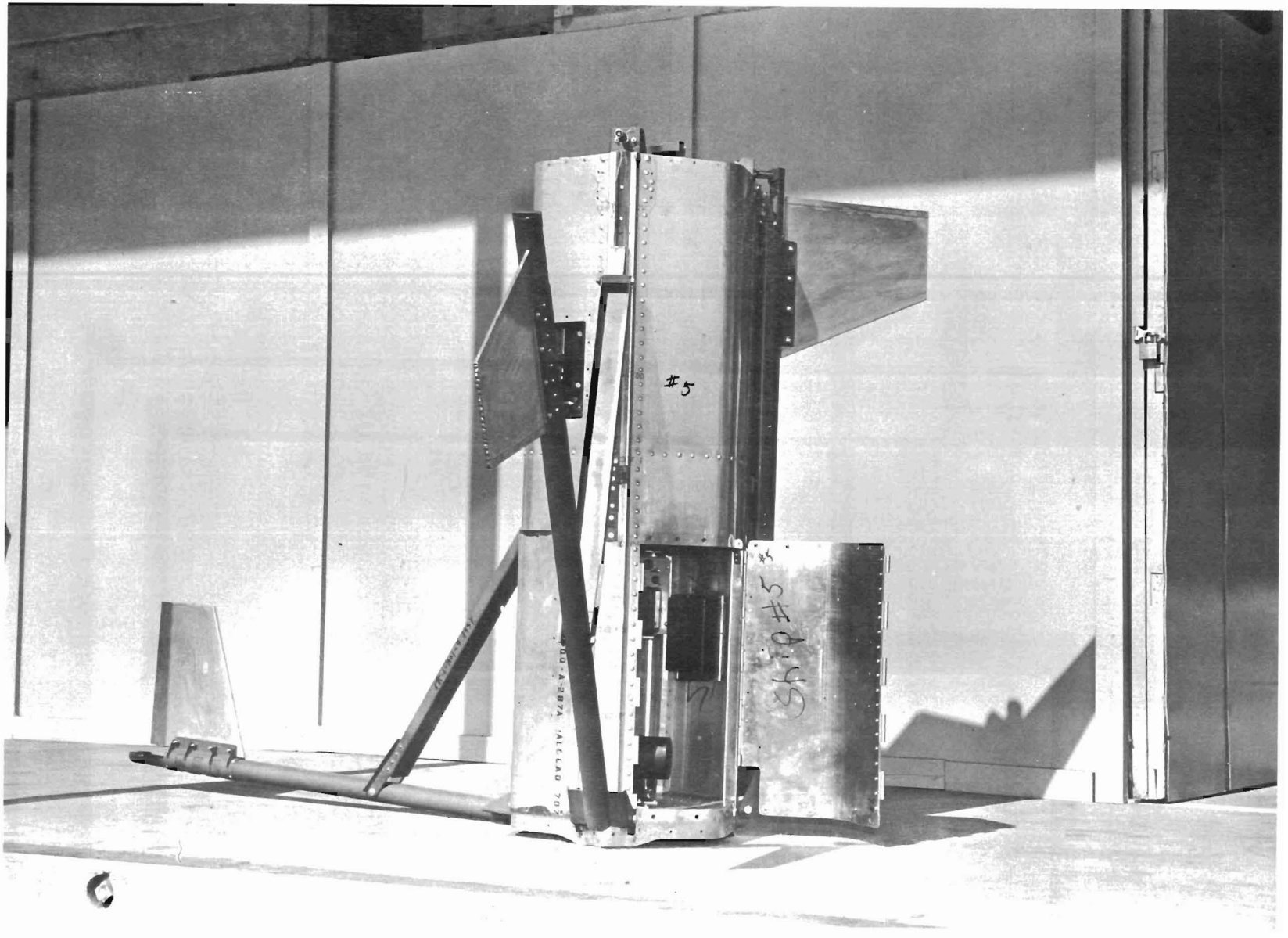

FIGURE 52 STAGES OF FIN DEPLOYMENT

The primary electrical power system, wet-cell batteries supplying up to 30 amperes, 24-volt DC current, is housed in the nose cone, a molded re-inforced fiberglass shell. This forward location of batteries is favorable for locating the vehicle center of gravity as far forward as possible and attenuating impact shock forces. The airborne receiving and transmitting antennae are mounted on the forward end of the cone.

The KRC-6 avionic system, consisting of the ground station and airborne installation, was designed to provide the following capabilities:

1. Programming and initiation of deployment and flight functions.

2. Remote control during descent.

3. Automatic stabilization during descent.

4. Telemetry of vehicle test data.

The remote control is a compass-oriented system, i.e. the vehicle will fly in the heading in which the operator positions the control stick, regardless of the instantaneous body heading. Vehicle control is effected by pitch and/or lateral tilt of the rotor with respect to the body. The vehicle will glide in the direction of rotor tilt. Body heading is controlled by the fixed directional fin which weathercocks the body in the flight direction during glide. The vertical gyro provides spatial reference for automatic stabilization of the pitch and roll attitude. This reference can be biased by control commands to establish and maintain body tilt up to 45^{o} from the vertical.

Six remote control channels for ground-to-air control are provided. Two are proportional control channels for transmitting North-South, East-West components of heading commands. The remaining channels are "on-off" switching commands. Two switching channels are used to "arm" and "fire" the collective flare thruster. The third switching channel initiates the telemetry calibration sequencing. The fourth channel is a spare.

The air-to-ground telemetry system provides fourteen proportional channels for transmitting test data or information. Present test vehicles are instrumented to include body heading and attitude information, control response, accelerations, and rotor data.

The ground station includes the operator's control console with the control stick and the ground portion of the communications system.

The control console, Figure 53, tripod-mounted for operator convenience, incorporates the push-button switches for switching command signals to initiate flight functions; read-out instruments for rotor RPM, body attitude, and airspeeds; and the control stick. The stick is gimbal-mounted to swivel approximately 30^{o} from the vertical in all directions and generates proportional North-South and East-West command signals as a function of its tilt by means of potentiometers attached at the base of the stick. A centering spring positions the stick in "neutral", hands-off.

Control commands and data telemetry signals are transmitted on FM telemetry bands by a two-way radio link, shown in Figure 54. Ground-to-air commands are broadcast on a carrier frequency of 410 mc., with a Babcock T-450 transmitter. Its rated maximum output power is 35 watts. The airborne receiver is an R.S. Electronics Model 2611 unit. Air-to-ground telemetry information is relayed on an FM carrier frequency of 232.9 mc. The airborne transmitter, a Tele-Dynamics Model 1001A unit, rated at 3.5 to 4.5 watts output, feeds a gamma-matched halo antenna mounted on the vehicle nose cone. The ground station receiver is a Nems-Clark Model 1673 receiver. It is shown in Figure 55 as an asembly with the coder-decoder unit.

Transmission of multiple channels of ground-to-air command signals and air-to-ground telemetry data information is achieved by the use of a two-way multiplexing or "time sharing" coding-decoding system manufactured by Sierra Research Corporation. This two-way data link, Model DL101, provides two time-divided composite signals consisting of the two proportional four "on-off" channels in the ground-to-air link and the fourteen proportional telemetry channels in the air-to-ground link.

The composite pulse train output of the ground-to-air coder amplitude modulates a 20 KC subcarrier which frequency modulates the 410 mc transmitter. The output of the air-to-ground coder is similarly used with a 70 KC subcarrier modulator to modulate the 232.9 mc airborne transmitter. The receiver output signal of each link is demodulated and applied to a decoder input which separates the composite signal into the original number of individual channels. The discrete samples of information thus entering each output channel are stored in an emitter follower to provide an essentially continuous output.

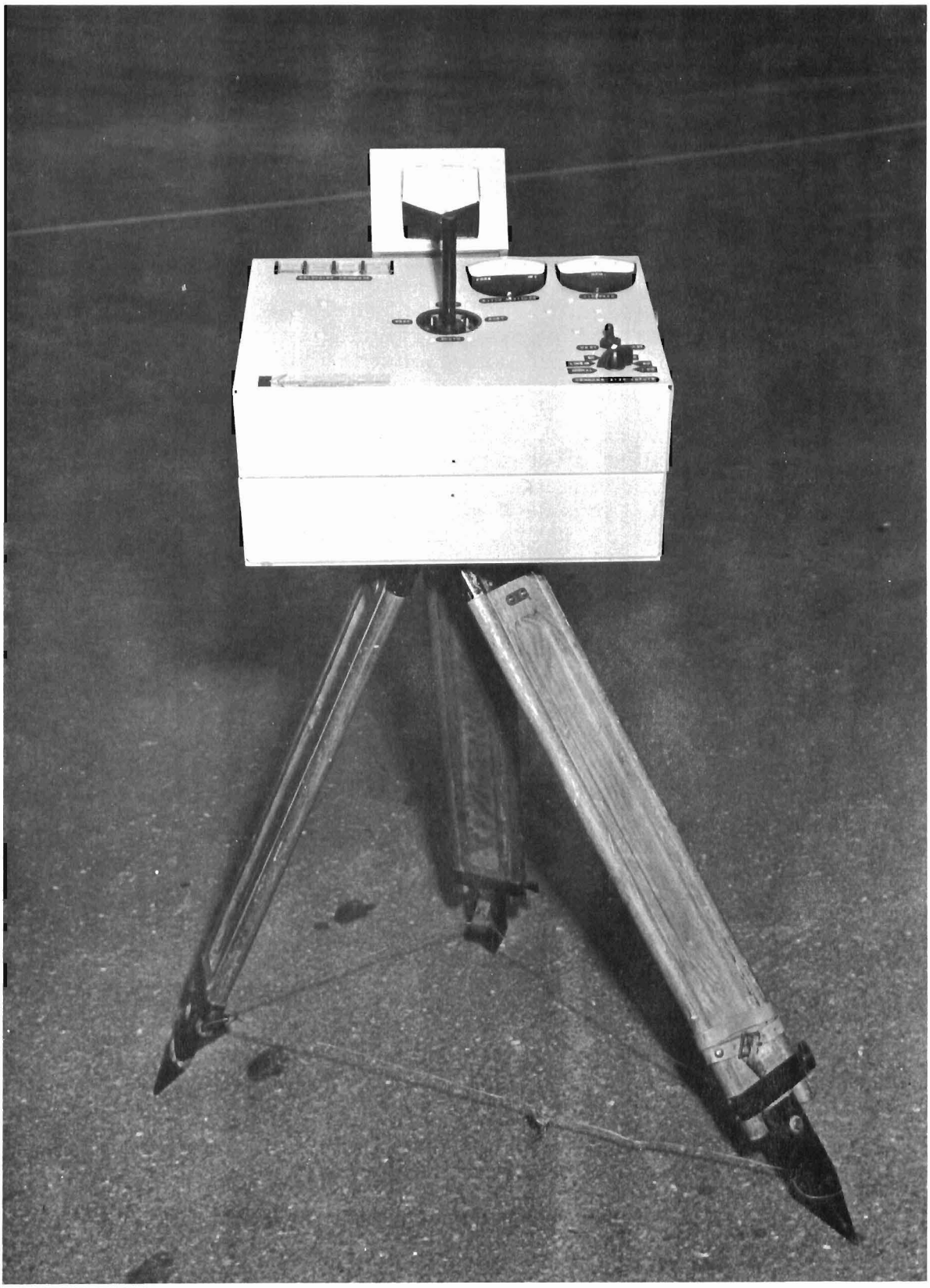

FIGURE 53 GROUND CONTROL UNIT

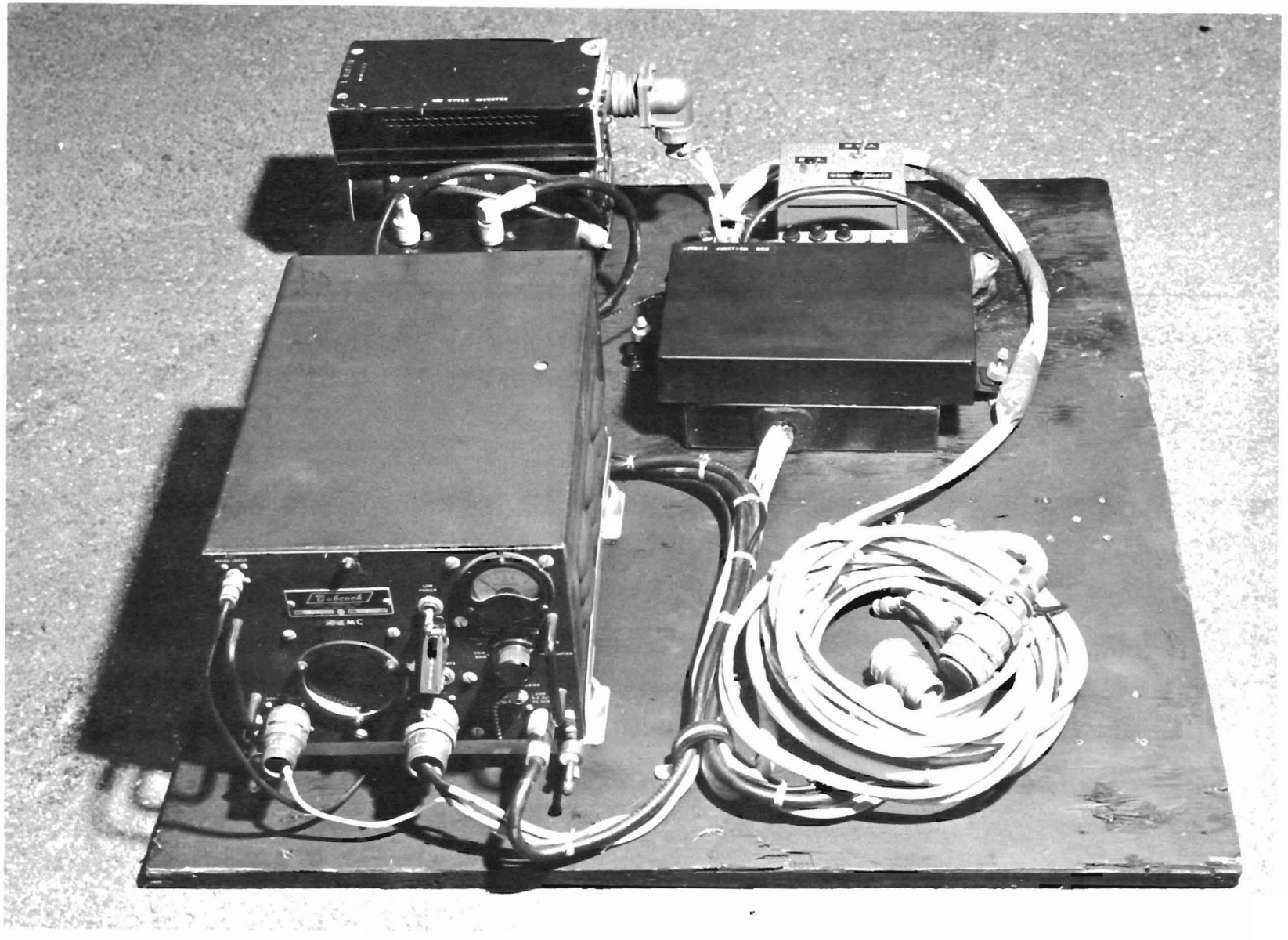

FIGURE 54 GROUND STATION TRANSMITTER AND POWER SUPPLY

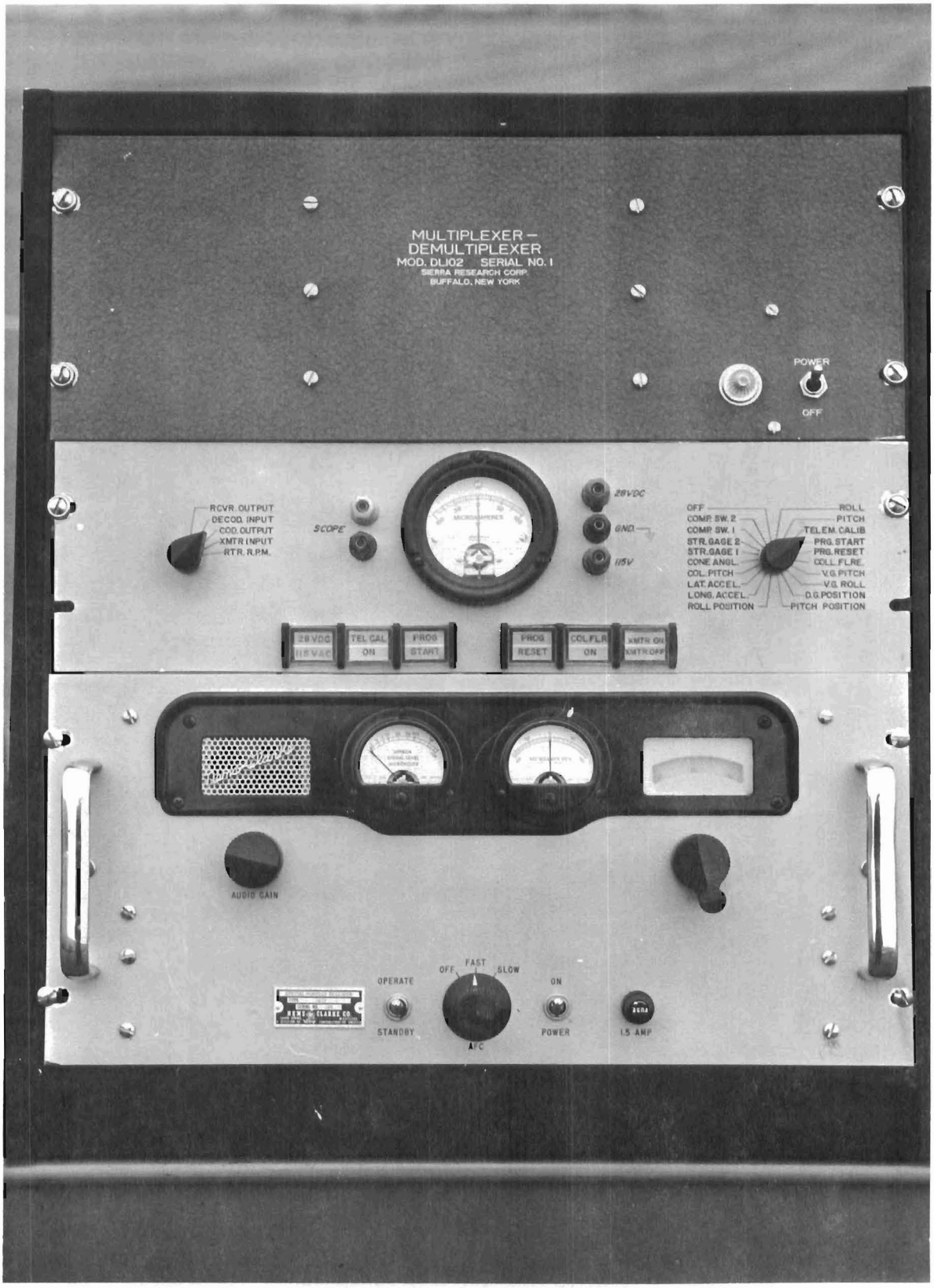

FIGURE 55 GROUND STATION RECEIVER AND CODER-DECODER UNIT

Due to the finite speed of R.F. energy propagation, the above system is limited to a range of approximately 30 miles (unless modified). All radio frequency modulators and demodulators used in the system were manufactured by Kaman Aircraft Corporation.

The fourteen proportional telemetry channels designed to transmit direct current signals have a cut-off frequency of approximately 20 cps; consequently, all 400 cps data signals must be demodulated prior to data system processing. Table 3 presents a summary of telemetry data provided in the ROTOCHUTE air drop tests. The telemetered data carrier signal is decoded by a Sierra decoder unit into channel signals appropriate for recording by oscillograph for permanent synchronized record of command control signals and telemetered information.

The airborne system comprises the airborne units of the communications link, attitude sensors, switching and sequencing circuits, control servos, and data sensors.

The command carrier signal from the ground station is detected by the airborne command receiver, and decoded by a Sierra Research CD-101 decoder unit into proper proportional control signals and switching outputs.

The proportional control signals are channeled to the command modulator which generates outputs, as a function of the control signals, for exciting the North-South and East-West stator windings of a resolver in the General Electric Model KD-6 Directional Gyro. The gyro provides the heading reference for properly routing the command inputs. The resolver rotor, which remains aligned at the initial compass heading, couples command inputs as a function of instantaneous vehicle heading into the pitch and roll servo channels to tilt the rotor in the commanded direction regardless of the vehicle heading.

Automatic stabilization of the vehicle is achieved by means of vertical gyro error voltages inserted into pitch and roll hub control servo loops. The Lear Model 1080H vertical gyro provides pitch and roll attitude voltages to the summing bridges of the corresponding servo amplifiers. Each amplifier provides proportional plus derivative amplification of the gyro error signal. The amplified signals are then summed in the output stage to provide differential clutch current for the Lear Model 118AB actuator. Lear 14501D1 follow-ups provide actuator position and velocity feedback signals to the amplifier inputs, completing

TABLE 3

TELEMETRY DATA PROVISIONS

OPERATIONAL PARAMETER	TEST DROP NUMBER	REMARKS
Pitch Servo Position	4,5,6,9,10,11,12,13	Demodulated Signal
Roll Servo Position	4,5,6,9,10,11,12,13	Demodulated Signal
Pitch Attitude	4,5,6,9,10,11,12,13	Demodulated Signal
Roll Attitude	4,5,6,9,10,11,12,13	Demodulated Signal
Directional Gyro Heading	4,5,6,9,10,11,12,13	Demodulated Signal, 2 Channels
Rotor Speed	4,5,6,9,10,11,12,13	Special Pulse Circuit Operation
Rotor Housing Position	6,9,10,11,12	
Blade Cone Angle	6,9,10	
Blade Bending	10	Demodulated Signal
Chord Bending	10	Demodulated Signal
Pitch Rod Force	6,11,12	Demodulated Signal
Roll Rod Force	6,11,12	Demodulated Signal
Collective Flare Arming	10,11,12,13	
Lateral Accelerometer	4,5,6,9,10	

the position servo loop. A derivation analysis of servo loop characteristics and transfer functions is presented in Appendix C.

The flight program command control comprises the circuits, switching, relays, and time delays to:

1. Uncage the directional gyro

2. Deploy the alighting gear and directional fin

3. Unground servo command signals

4. Arm and initiate the collective flare control

5. Implement other desired functions

Data sensors such as magnetic pickups, accelerometers, potentiometers, strain gages, etc. provide electrical signals of test data such as rotor RPM, axial and lateral accelerations, heading, pitch and roll attitude, blade pitch and coning, and blade stresses. The telemetry signal control amplifies or modifies the data sensor signals into the form suitable for telemetering. The Sierra decoder unit converts and codes data sensor information into a telemetered carrier signal for transmission to the ground station by the airborne transmitter.

During flight, up to 30 amperes, 24-volt DC electrical power is supplied for the airborne system by two Exide AC-54 batteries connected in series. Portions of this power are converted to 250-volt DC current by a Universal Transistor Power Supply Dynamotor, Model 6075-10, and to 115-volt, 400 cps AC current by an Eicor Inverter to fulfill the power needs of various subsystems.

The ground control station operates on 28-volt DC primary power. A Bendix Aviation Type MG54C Inverter supplies 115-volt, 400 cps AC current for the ground station receiver and coder-decoder.

A more detailed discussion of the avionic system is presented in Appendix III.

E. FUNCTIONAL TESTS OF THE FLIGHT TEST VEHICLE

Ground truck tests were performed on the flight test vehicle to check systems function, obtain preliminary qualitative performance data, and establish governor spring setting for flight. A KRC-6 test vehicle without fins and alighting gear was mounted, as shown in Figure 56, in a double-gimbal rig aboard a truck for the checkout.

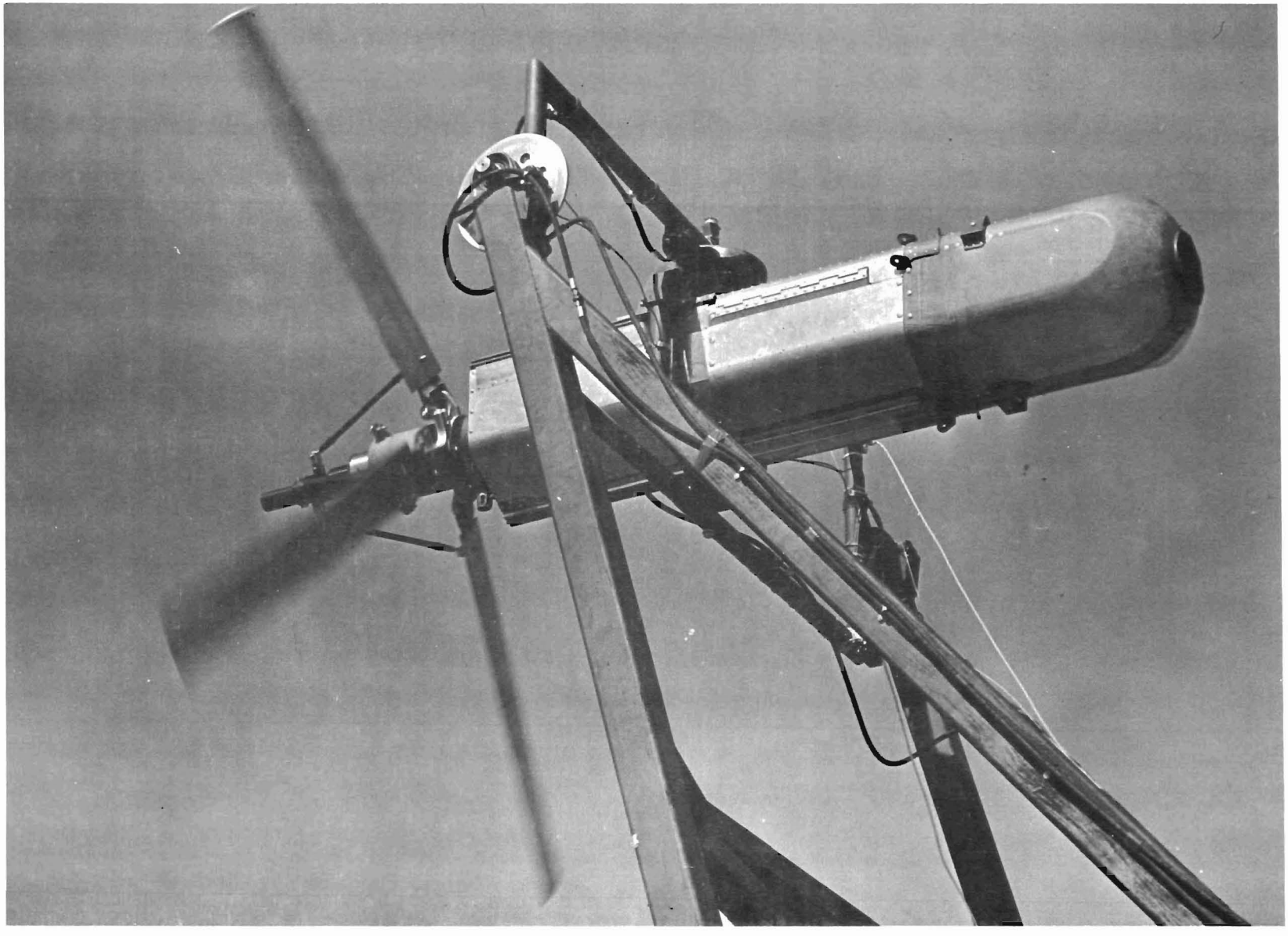

FIGURE 56 GROUND TEST RIG (Truck-Mounted)

The small inner gimbal permitted angular displacement of the vehicle about its lateral axis. The outer rectangular gimbal permitted pitch attitude variation. Aircraft-type disc brakes locked the gimbals in any selected attitude when hydraulic pressure was applied. The pitch gimbal was strain-gaged to provide rotor thrust data.

Runs were made at speeds 35 to 55 miles per hour (ground speed) along an airport taxi strip and a half-mile oval speedway track. Measurements were taken of rotor pitching moment in the glide attitude, rotor RPM, and thrust. Response to control commands was observed.

Thrusts as high as 565 pounds were measured in axial operation. Thrust data indicated that a one "G" axial rate of descent was 55 to 60 feet per second. In glide, thrusts of 535 pounds were obtained at 86 feet per second airspeed, 1130 rpm, and 24° rotor angle of attack. The rotor was "speed stable" throughout all attitudes tested.

The rotor pitching moment was continuous "nose-up" for the speed regime investigated. However, moments were running higher than predicted. It was necessary to increase the rotor tilt nearly 50 per cent to $\pm 7^{\circ}$ for adequate control during flight.

Systems functions were checked during the testing. No major deficiencies were found. Transport for several hundred miles over various road conditions proved the ruggedness and reliability of the avionic equipment and installation. Valuable handling and operating experience was gained.

F. TEST FACILITY

Launch aircraft, chase aircraft, and other support services were provided by the U.S. Air Force 6511th Test Group (Parachute) at the Joint Parachute Test Facility, El Centro, California. The Facility was established and is equipped to perform development, testing, and evaluation of parachute systems and other retardation devices. Detailed information concerning the Facility may be found in Reference 8. The ROTOCHUTE drops were carried out at the desert TATU range.

G. TEST PROCEDURE

Each KRC-6 test vehicle was readied with the necessary provisions to demonstrate its test objectives. On the scheduled drop day, the ROTOCHUTE was attached to the launch aircraft release system at the station air field. The drop zone was approximately 30 minutes distant (by automobile travel). Test vehicle systems were activated prior to take-off or in-flight. Flight personnel were indoctrinated and co-ordinated for the required in-flight activation and operation. The period between activation of systems and release was kept to the minimum possible whenever battery operation was involved, since useful battery life was considered to be 30 to 40 minutes on a full charge.

When all support operations were in readiness, the drop zone range control guided the launch aircraft by radar to the launch point at the established test release altitude and airspeed. The TATU drop controller counted down the release.

High speed, 16mm color motion pictures, taken from the launch aircraft, chase plane, and two ground cameras at the drop site, monitored the drop test from launch to impact. Time from release to impact was clocked with stop watches. Trajectory and other flight performance were determined from cinetheodolite film taken during the drop from the five stations located around the drop zone. The cinetheodolite data were read, reduced, and tabulzted by the 6511th Group and supporting personnel.

Telemetered data were recorded on the oscillograph which was part of the Kaman-operated ground control station. As back-up the telemetry carrier-signal was taped by the 6511th Test Group Instrumentation Operations.

H. TEST PROGRAM

The air drop tests were established to provide step-by-step knowledge and experience on the behavior and performance of the remotely-controlled ROTOCHUTE system from release to impact and to explore the systems capability for glide, control, and touchdown.

According to plan, initial drops were made with "bare model" test vehicles (without control, stabilization or telemetry equipment) to explore launching procedures and problems, to check rotor deployment and performance, governor spring preload, vehicle stability in descent, and to check the vehicle and mechanical systems airworthiness, functioning, and reliability.

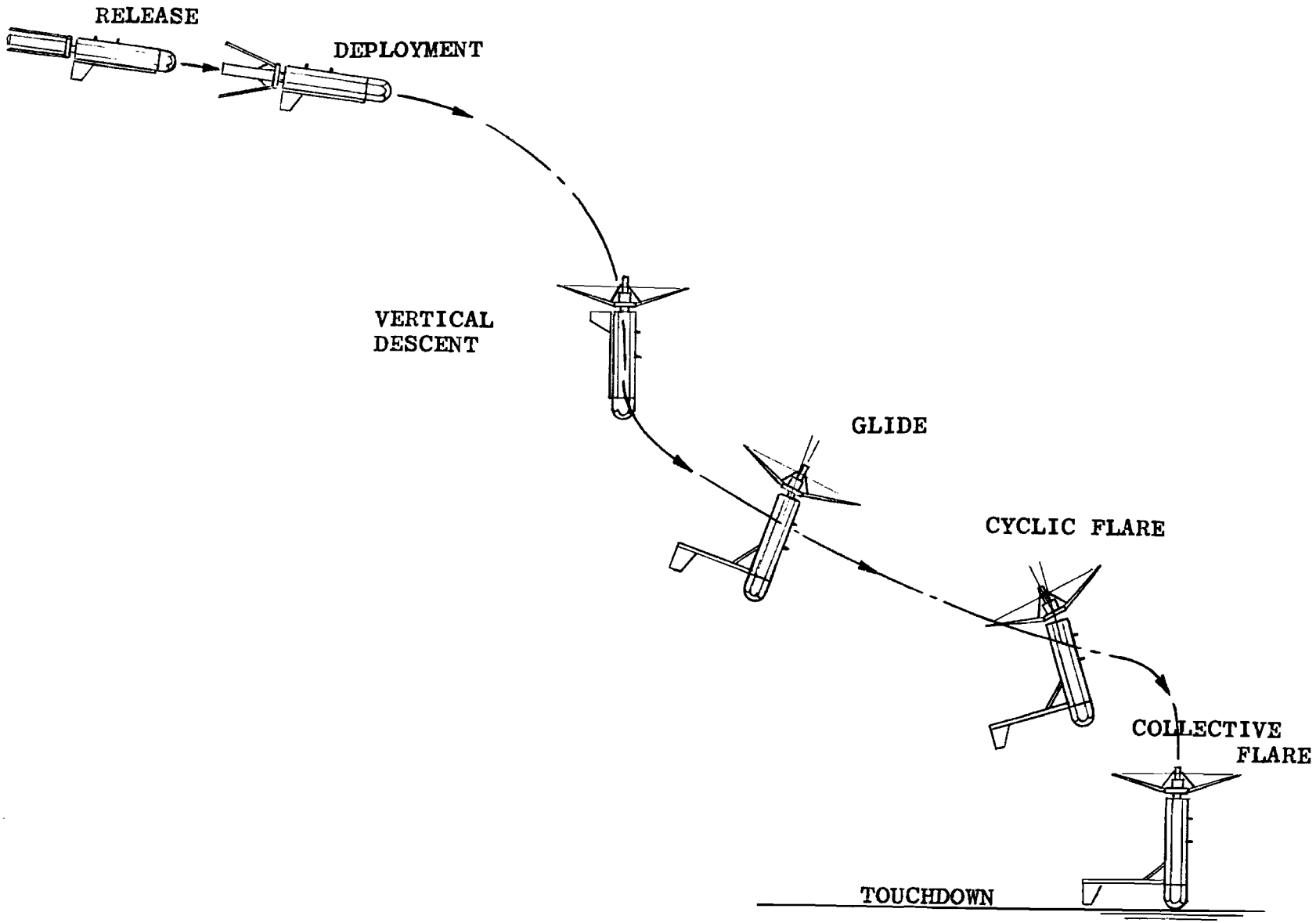

TEST FLIGHT PROFILE

FIGURE 57

Once the vehicle and mechanical systems were deemed to be airworthy and functioning properly, the remote control models with automatic stabilization, instrumentation, and telemetry were air-dropped, with specific objectives planned for each particular flight. The planned flight profile may be seen in Figure 57.

Data and results were analyzed after each test to determine what, if any, modifications were to be incorporated in the next test vehicle. Objectives for the follow-on test were revised in accordance with those achieved from drops already performed.

The air drops performed during the test series are tabulated in Table 4. Launch and chase aircraft, launch conditions, and other information pertinent to the drop are summarized in the table.

I. AIR DROP TESTS

Thirteen air drop tests were performed. Three KRC-6 "bare" models, two "dummy" models (to check launch procedures from the H-21 helicopter), and eight KRC-6 controlled models were dropped. Modifications to improve behavior and/or performance were incorporated whenever visual observation or recorded data indicated a need.

A "bare" model KRC-6 ROTOCHUTE was readied for the first test. It was ballasted to simulate the weight and inertia of controlled models with a full complement of equipment. The governor was set for 1140 RPM rotor speed. Fin deployment was timed to occur 16 seconds after release.

ROTOCHUTE No. 1 was released from a B-66 aircraft at 254 knots and 1870 feet altitude. A relatively low release altitude was selected to insure better visual observation and camera coverage of the release and deployment events. The aircraft was in a 10^{o} dive attitude at release, simulating the launch attitude planned for controlled models to minimize any possibility for tumbling the attitude gyros.

The gyro gimbals are limited in their displacement. As mounted in the test vehicle, if the body approached horizontal and rolled 180^{o}, the gyro limitations are reached and the gyro may tumble.

The test vehicle separated cleanly from the aircraft, maintaining a stable attitude to approximately 12 feet below the bomb bay door. It then pitched up sharply and climbed relative to the aircraft, passing close to the horizontal stabilizer. Two seconds after release, the rotor deployed while the vehicle was

TABLE 4

SUMMARY OF AIR DROP TESTS

ROTOCHUTE NO.	1	2	3	4	5	6	7	8	9	10	11	12	13
USAF TEST NO.	1229 F62	1354 F62	1358 F62	1359 F62	1386 F62	1410 F62	1385 F62	1411 F62	1470 F62	2021 F62	2052 F62	0407 F63	0464 F63
DATE	7-16-62	7-20-62	7-24-62	7-26-62	8-1-62	8-7-62	8-16-62	8-17-62	8-22-62	12-3-62	1-8-63	4-4-63	4-11-63
TIME (PST)	08:21	07:57	10:06	06:10	06:26	06:16	10:29	06:57	08:10	12:25	08:39	09:39	09:22
GROUND TEMP (^{o}F)	89	99	104	86	87	90	109	94	95	70	75	70	66
SURFACE WIND (KTS)	S-5	W-4	E-5	NW-7	NW-7	NW-8	N-7	0	SW-9	0	0	W-4	N-6
LAUNCH AIRCRAFT	B-66	C-130	C-130	C-130	C-130	C-130	H-21	H-21	H-21	H-21	H-21	H-21	H-21
LAUNCH SPEED (KTS)	254	120	140	166	154	170	19	20	9	42	46	60	44
LAUNCH ALTITUDE, MSL (FT)	1870	3230	3165	5345	5740	8265	5715	5400	5420	6530	5485	5300	5880
LAUNCH ATTITUDE (DEG)	-10^{o}	+30^{o}	-7^{o}	-12^{o}	-16^{o}	-16^{o}	-90^{o}	-90^{o}	-90^{o}	-90^{o}	-90^{o}	-90^{o}	-90^{o}
CONFIGURATION	BARE	BARE	BARE	GUIDED	GUIDED	GUIDED	DUMMY	DUMMY	GUIDED	GUIDED	GUIDED	GUIDED	GUIDED
WEIGHT (LBS)	272	275	273	275	274	274	266	264	270	275	295	279	305
ROTOR DIA. (FT)	8	8	8	8	8	8	8	8	8	8	8	10	10
GOVERNED RPM	1140	1000	1000	1000	1000	1000	0	0	1000	1000	1060	820	820
TIME TO IMPACT (SEC)	23.2	38.0	36.8	32.9	79.6	51.5	26.4	26.8	73.6	97.0	70.0	49.2	108.5
AV. R/D (FT/SEC)	80.5	85.0	86.0	162.5	72.2	160.5	216.5	202.0	73.7	67.3	78.3	107.6	54.1
MIN R/D (FT/SEC)	70.0	69.4	69.2	---	66.4	---	---	---	62.4	54.2	61.4	---	26.8
MAX GLIDE RATIO L/D	0.55	0.64	0.40	---	0.26	---	---	---	0.59	0.94	1.07	---	2.38

in a 45° nose-high attitude and began to decelerate the vehicle. As descent reached vertical, a 4- to 5-second period spiral developed. The fins and alighting gear deployed as programmed. The spiraling continued until impact, at which instant the body longitudinal axis was approximately 55° from vertical. The nose cone, alighting gear and rotor assembly were damaged. The body was relatively intact and reusable.

The following results were indicated by this first test. The mechanical systems functioned properly and were airworthy. Longitudinal stability prior to rotor deployment must be improved to preclude gyro tumbling in controlled models from the pitch-up. Rate of descent was higher than predicted because of rotor tilt during spiral and above standard air temperature. The spiral, while not excessive or unexpected, occurred sooner than desired after rotor deployment.

Spiral instability of ROTOCHUTE systems often occurs when rotor tip speeds are high. Although spiral of the KRC-6 vehicle was expected at rotor speeds of 900 rpm or greater, the rotor was governed at 1140 rpm to provide increased rotor stored (kinetic) energy for the collective flare mode. Automatic stabilization was expected to overcome the spiral if not too severe. It was deemed prudent, however, that descent be stable until automatic stabilization can assume control.

In consideration of the above results, the following modifications were incorporated on Test Vehicle No. 2, also a "bare" model. The rotor governed speed was reduced to 1000 RPM to delay onset of the spiral. Since, on controlled vehicles, automatic stabilization becomes operative when the fin and alighting gear deploy, this sequence timing was reduced to 10 seconds, thus reducing the required period for uncontrolled stable descent. To improve longitudinal stability, the nose cone was shortened 10.5 inches and the fins were moved aft 3.5 inches. In effect, the vehicle density was increased, reducing any tendency to "float" or "fly", and effective fin tail arm was improved since the body center of gravity was now further forward in relation to the fin surfaces. The modified version is shown in Figure 58.

Until launch behavior could be demonstrated as being satisfactory, the 6511th Group Flight Operations preferred to launch from a C-130 aircraft at lower airspeeds. A launch device used by the 6511th Group in a previous program was adapted for release of the KRC-6 ROTOCHUTE from the aft end of the C-130 aircraft.

FIGURE 58 KRC-6 WITH MODIFIED NOSE CONE

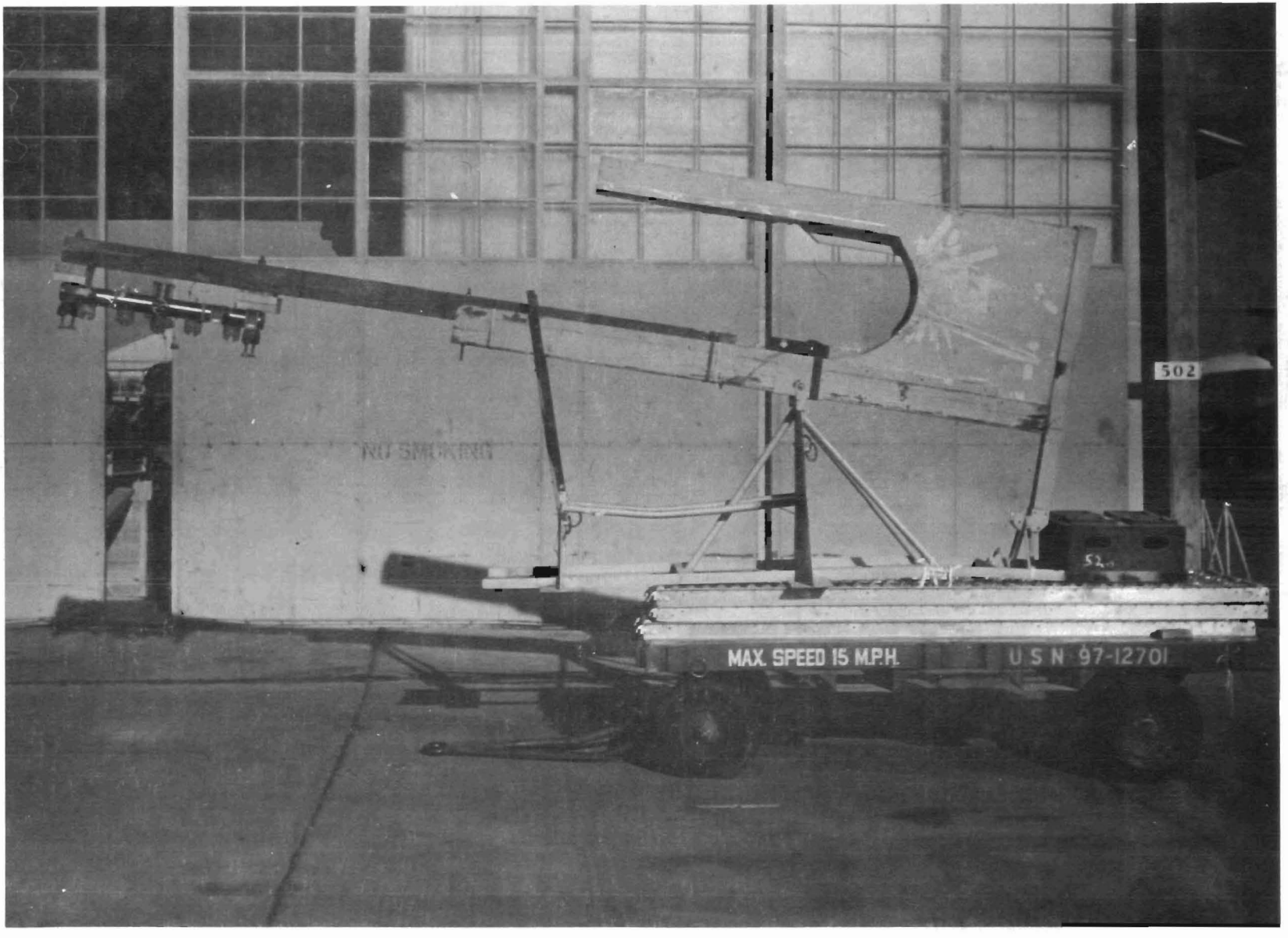

FIGURE 59 LAUNCHER DEVICE

ROTOCHUTE No. 2 was released in a 30° nose-high attitude from the C-130 aircraft, sliding aft, tail first, off the launcher on a wooden carriage. This launch method was an expedient used to check the vehicle stability and descent performance with a minimum of delay while hardware for the launcher was being readied to release the vehicles in an attitude compatible with gyro requirements for controlled models. Release was at 120 knots airspeed and 3230 feet altitude.

The ROTOCHUTE pitched nose-down immediately upon release. The rotor deployed 3 seconds later (a 3-second delay initiator was used). The vehicle achieved a retarded stable vertical descent which continued until deployment of the fins after launch. A spiral then developed and continued to impact.

Behavior and performance of ROTOCHUTE No. 2 compared to that of ROTOCHUTE No. 1 was improved. Initial descent was stable for a longer period, spiral was at a slower rate, and the average rate of descent was comparable, 85 feet per second compared to 81 feet per second. Mechanical system functions, vehicle stability, and performance were now considered satisfactory for dropping the controlled models.

However, to demonstrate repeatability of performance and to test the launch technique planned for controlled models, a third "bare" model was dropped. The launcher, Figure 59, by now was fitted with a B-66 type ejection rack to support the test vehicle in a 7° nose-down attitude. Vehicle No. 3 was similar to ROTOCHUTE No. 2 in configuration and timing of functions. The fins and alighting gear were, however, non-deployable. Since spiral during the No. 2 test began simultaneously with gear deployment, it was of interest to determine whether the spiral was induced by the extended gear or whether the occurrence was merely coincidental.

ROTOCHUTE No. 3 was released from the C-130 aircraft at 140 knots airspeed and 3165 feet altitude. It nosed-down, pitched up, and then aligned itself with the relative wind at rotor deployment. Vertical descent was stable for about 10 seconds. The spiral developed and descent was similar to that of ROTOCHUTE No. 2. Rate of descent again averaged 86 feet per second.

Similar behavior of the No. 2 and No. 3 test vehicles demonstrated the repeatability of flight performance. Onset of spiral was delayed sufficiently to enable the automatic stabilization systems to assume control. Spiral rate was considered slow enough to be controlled. Alighting gear position appeared to have little effect on spiral behavior.

Acceptable aircraft separation (ground tests indicated that a momentary pitch-up with simultaneous roll did not readily tumble the gyros), rotor deployment, system functions, and performance having been satisfactorily demonstrated, drops of controlled vehicles were initiated.

The primary objective of the first controlled flight was to determine vehicle response to commands, validate control system gains and ratios, and otherwise become familiar with the vehicle characteristics in controlled glide descent. As a safeguard to assure achievement of test objectives, the collective "flare" thruster was left out until the remote control, stabilization, and telemetry networks were proven to be satisfactory and reliable. A possibility existed that a random signal emanating from the circuits could inadvertently "fire" the collective flare thruster. An "arming" circuit was eventually provided as a safeguard.

ROTOCHUTE No. 4 free-fell after release from the aircraft when rotor deployment was not initiated. A deployment initiator with no charge had been inadvertently installed. The free-fall theodolite data provided useful vehicle drag and longitudinal stability characteristics.

Test No. 4 objectives were adopted for Test No. 5. ROTOCHUTE No. 5, similar in configuration to No. 4, was released from the C-130 aircraft at 154 knots and 5740 feet altitude. The aircraft was in a 10^{o} dive attitude at release. This attitude was requested to minimize a pitching tendency noted in motion pictures of Drop No. 4 by improving the test vehicle alignment with the relative wind at release.

After the rotor deployed, the vehicle decelerated into a stable vertical descent. The fins and alighting gear deployed at the programmed time. The automatic stabilization systems and remote guidance systems became operative. The descent continued stable and vertical. When commands were signalled by the controller from the ground station, the vehicle responded. Limited glide was achieved and the flight direction was changed. Theodolite data indicated flight against reported wind. Average rate of descent was 72 feet per second, substantiating predicted rotor performance. Much of the avionic equipment sustained no damage and electrical power had to be switched "off" at retrieval. The batteries were still intact. The sensitivie gyros were damaged, however. ROTOCHUTE No. 5 after impact is shown in Figure 60.

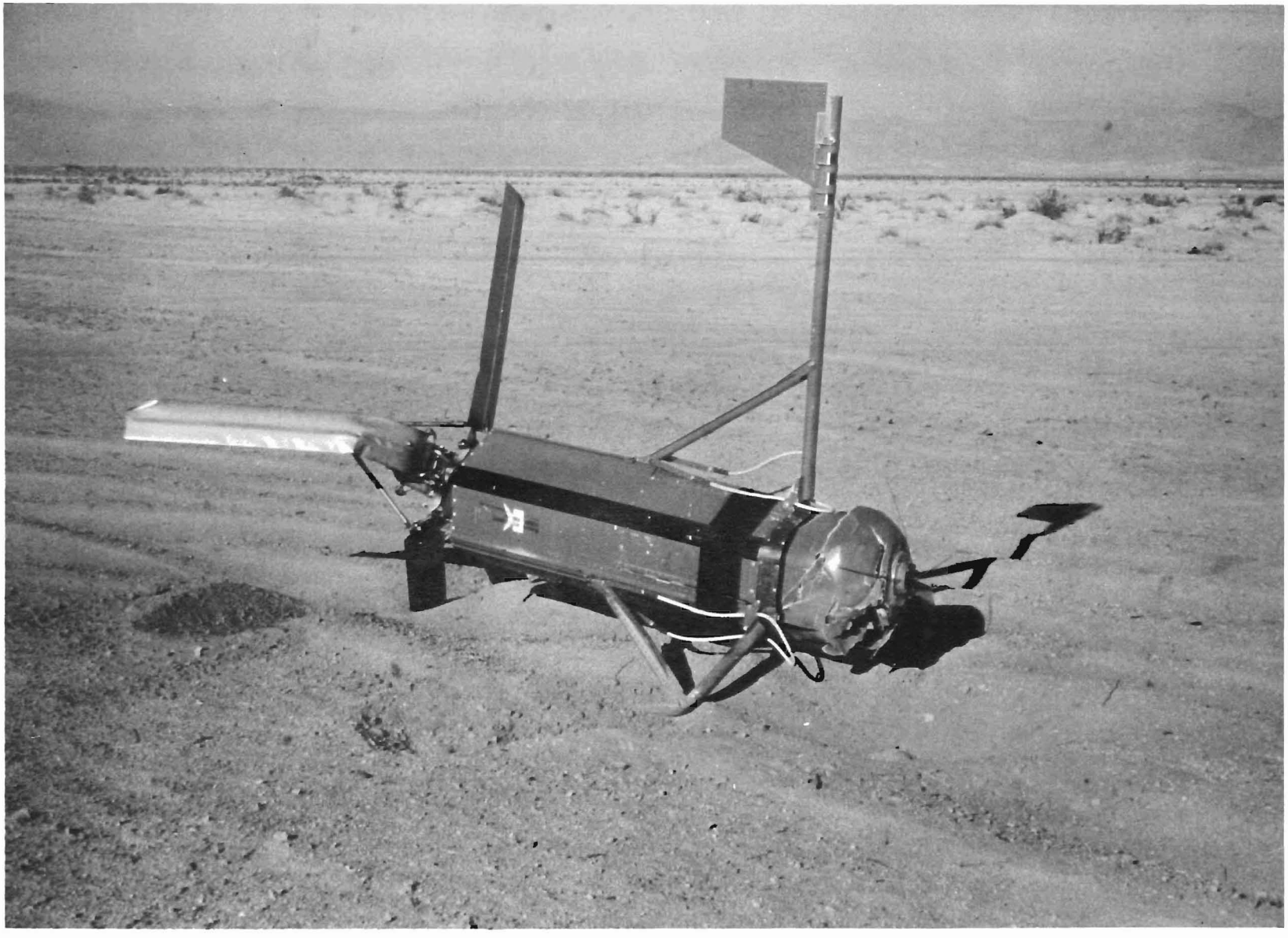

FIGURE 60 NO. 5 TEST VEHICLE AFTER TOUCHDOWN

Even though the vehicle responded to commands and glide was attained, the response was sluggish and the glide fell short of expectations. Since the test vehicle was being flown for the first time without previous experience to serve as a guide, the controller may have signalled commands too rapidly for effective control. In the next flight, the commands were to be signalled more gradually and for longer periods to allow the vehicle a better opportunity of establishing glide. Rotor tilt was increased 50 per cent on all subsequent vehicles for additional control power.

ROTOCHUTE No. 6 was launched under conditions similar to Drop No. 5, except that release speed was 170 knots and altitude was 8265 feet. The vehicle began to tumble during rotor deployment, and rotor blade failures occurred approximately 11 seconds after release. Plane-to-air motion pictures indicated that events up to rotor deployment were normal. Approximately one second after deployment, the hub was tilted hard-over. This minimized any stability the rotor was providing at the moment and allowed the vehicle to yaw broadside to the flight path. The adverse attitude prevented attainment of operational rotor speed and induced excessive flapping of the blades to the extent that several synchronizer rods buckled. With this flapping freedom and low RPM, the blades were damaged against the shaft hardware. They also hit the retracted fins, aggravating the tumbling.

Pictures and data did not establish whether excessive loads displaced the servo to its hard-over position or whether the servo lost its stiffness as a result of an electrical or mechanical malfunction. Since the attitude at the instant of rotor deployment appeared as favorable as that of Vehicle No. 5 at the same instant, it is probable that airloads were no more severe. Random failure of the servo or servo system electrically or mechanically is believed to be the most logical explanation.

Accordingly, the servo circuits and power supply were reviewed for potential problem points. Rotor blade synchronizer rods were strengthened. In addition, since turbulence behind the C-130 launch area may have been a contributing factor in the failure, remaining drops were performed from an H-21 helicopter at or near hover. The ROTOCHUTE could be suspended vertically from the personnel hoist, as in Figure 61, and released from a cartridge-fired, quick-release hook.

To check the handling and release procedure and investigate the effect of rotor downwash on the drop-away, two "dummy" vehicles with non-deployable rotor assemblies, built up from salvaged bodies and hardware, were dropped prior to controlled vehicles. Drop Tests No. 7 and No. 8 proved that drop-away was stable and satisfactory.

FIGURE 61 HELICOPTER LAUNCHING POSITION

The flight plan for Test No. 6 was adopted for Test No. 9. ROTOCHUTE No. 9, a controlled model, was released at 5420 feet altitude from hover. The rotor and alighting gear were inadvertently deployed prior to release of the ROTOCHUTE. Upon release, however, the rotor accelerated to operating speed and the initial descent was stable - the stabilization system was already operative. Glide and response to control were improved over that of ROTOCHUTE No. 5. Glide into wind and several changes in flight direction were effected. The vehicle's collective flare system - now installed with a safety arming circuit to preclude inadvertent initiation - was "armed" and signalled to "fire" just prior to impact. However, the "flare" failed to respond to the command.

Examination of the flare circuit and hardware disclosed that the failure to "fire" resulted from intermittent discontinuity of the ground lead at the thruster igniter electrical connector. Ground attachment to the igniter mating connector is unconventional. The circuit had checked out satisfactorily in all functional tests. A more positive connection was provided in subsequent installations.

Although response to commands was improved and snappier, it still was less than satisfactory. Glide performance fell short of the expected potential. When the rotor tilt was increased, control system "gains" were left unchanged. As a result, full "command" signals could now override "stabilization feedback" signals which reached a limit at vertical gyro "saturation" - at approximately a 50^{o} pitch attitude. The control system response to large "command" signals became open-loop, making the control system "direct" control rather than one of "attitude" control. Body attitude must, therefore, be controlled visually by the operator. This was thought to be feasible. However, the rapid attitude changes and visual distance involved rendered such control difficult. Recorded data indicated that the behavior and non-phased corrections by the operator produced a flight with a series of dives and pull-ups that prevented establishing proper glide.

Accordingly, control system gains were revised on subsequent installations to provide a closed-loop system for all control stick commands. Commanded body tilt was limited to 45^{o}. Visual indicators for roll and pitch attitude were added to the control console for the operator's reference. Timed, planned commands to establish glide as a function of control stick displacement were planned for the next test. As an aid, a switch-operated control was added to the console. With the new control, stepped commands simulating 20 per cent to 100 per cent stick displacement

could be signalled for East or West flight. An "option" switch permitted changeover to manual control with the stick.

ROTOCHUTE No. 10 was launched from the H-21 at 42 knots airspeed and 6530 feet altitude. The rotor was already deployed, alighting gear down, and stabilization system engaged at release. In accordance with the flight program, free axial descent was permitted for the initial 10 seconds. Next, a series of commands tilting the rotor from 20 per cent up to 100 per cent tilt in the West direction was signalled during the next 35 seconds. Remaining descent and landing was controlled manually with the "stick". The ROTOCHUTE had been launched approximately 1.5 miles from ground control, and was not visible to the operator at touchdown. Consequently, collective flare was never initiated before impact.

Oscillograph data indicated that the vehicle responded satisfactorily to control commands. Body pitch attitude and hub tilt relative to the ground indicated that the vehicle was in glide, but oscillated about the pitch axis. Hub tilt was less than commanded because of servo droop. Theodolite data indicated that 0.6 to 1.0 ratio glide was achieved during the 80 per cent to 100 per cent tilt command period.

Flight data also indicated that approximately 200 foot-pounds rotor pitching moments at higher glide speeds exceeded trim moments available through rotor tilt. The moments drooped the pitch servo and reduced available control.

Rotor blade stresses were recorded during this flight. Stresses throughout the flight were well below design allowable and steady.

Vehicle No. 11, Figure 62, was fitted with a horizontal stabilizer to provide an estimated 100 foot-pounds forward (negative) pitching moment, reducing required trim control within available limits. The horizontal tail was attached to the aft alighting gear leg. Dual pitch servos were installed in tandem. Thus, droop was reduced by lessening the load at which each servo operated. Servo loads were further relieved with a bungee system attached to the hub. The bungee, attached to the hub and body, counterbalanced 60 foot-pounds of the hub moment.

ROTOCHUTE No. 11 was launched from the helicopter at 46 knots airspeed and 5485 feet altitude. Since alighting gear deployment in flight was dictated by the horizontal tail installation, the rotor was deployed after release. Otherwise, if the tail were "down" before the rotor reached operational speed, tumbling could be induced by the pitching moment. The release was performed approximately 1/4 mile from the ground control.

FIGURE 62 KRC-6 WITH HORIZONTAL TAIL

The flight plan used in Test No. 10 was again followed. The vehicle responded well to commands and a definite glide was noted. The collective flare was initiated approximately 150 feet above the ground to insure coverage by theodolite cameras. A peak 2.5 "G" deceleration force was recorded. Rotor RPM decayed to zero RPM in approximately 0.58 seconds, and the vehicle free-fell to impact.

Flight data, Figure 63, indicates that the vehicle closely followed the commands and commanded direction. An approximate 90° change in flight direction was performed. Directional instability during glide was encountered. Because available lateral rotor tilt was less than in forward pitch, yaw displacement reduced the rotor tilt and the vehicle tended to porpoise pitchwise in the direction of flight. Since the glide attitude was not steady, glide performance was adversely affected.

Although a peak 2.5 "G" retardation was recorded, full benefit for vertical retardation was not realized, because the body was pitched forward nearly 42°. Total deceleration along the longitudinal axis was 1 "G" - second. It is estimated that the resultant vertical retardation was 13 feet per second, too small to be reflected in the "smoothed" theodolite data showing a "dive" high rate of descent.

To minimize or eliminate heading instability, two vertical fins were mounted at the tips of the horizontal tail on the remaining test vehicles. This reduced any "blanketing" of the fins by the body in forward flight. Operation of the increased vertical tail area in improved air flow was expected to improve the directional stability. Also, the two forward alighting gear tubes and fins were left off. In yaw, one leg exposed its full length to air flow while the other foreshortened. The unequal drag results in a turning moment. Removal of the legs also reduced vehicle parasite drag, a factor favorable for improving glide performance.

To increase the rotor rpm decay period and improve the flare performance, rotor inertia was increased with tip weights. Rotor diameter was increased to 10 feet from 8 feet to lower the rotor disc loading. The vehicle gross weight had increased to nearly 300 pounds as a result of modifications. The lower disc loading would reduce the axial rate of descent and improve glide performance. The modified rotor is shown in Figures 46 and 47.

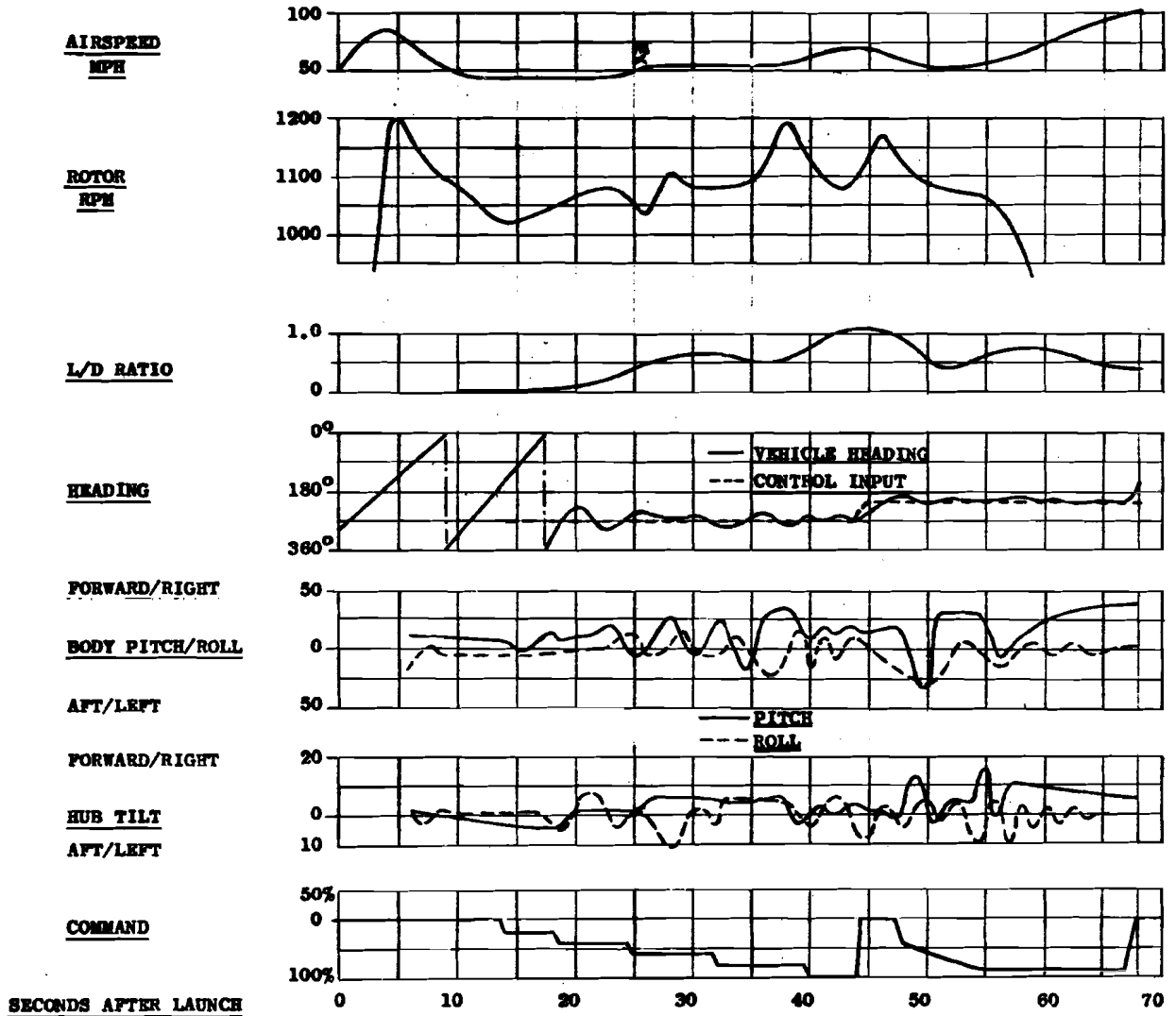

TIME HISTORY TEST NO. 11

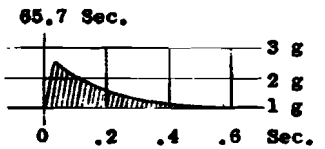

COLLECTIVE FLARE

FIGURE 63

TIME HISTORY TEST NO. 11
Figure 63

An anemometer type airspeed unit, seen clearly in Figure 51, was mounted from the front of the body to provide flight airspeed information to the operator for controlling the glide and attitude. To minimize nose-over pitching during the collective flare phase, the horizontal tail was mounted to pivot freely automatically when collective flare was "fired".

ROTOCHUTE No. 12, Figure 64, incorporating the above modifications, was released from 5300 feet altitude and 60 knots airspeed. Because it was released at a higher than normal forward speed, the test vehicle, being aerodynamically stable, nosed up sharply to 10° above the horizontal and rolled simultaneously. This change in attitude exceeded the vertical gyro design limitations and was sufficient to tumble the gyro and lose control of spatial reference. The lack of reference resulted in loss of stability and control after the automatic stabilization became operative.

Finding no indication of other malfunctions, it was concluded that the severe pitch-up was a random event brought on by the particular launch conditions. No change was made to Vehicle No. 13, except to increase its pitching inertia. Twenty pounds of ballast were added in the nose section. Drop procedures were reviewed with the helicopter flight officer.

The final test vehicle, ROTOCHUTE No. 13, was released at 44 knots airspeed and 5880 feet altitude. Rotor deployment and other programmed functions were normal.

Control stick commands were signalled for gradual tilt of the rotor to the West until indicated airspeed stabilized at approximately 70 miles per hour. Airspeed, pitch attitude, and rotor rpm were monitored from the control console indicators, Figure 65. The command was then gradually changed from West to East until glide was re-established in the opposite direction. Besides being a change in flight direction, the maneuver represented a "slow" cyclic flare.

A rapid cyclic flare was performed at 1100 feet altitude. The vehicle tilted aft and slowed. It then rolled off to the right into a tight spiral. A command was signalled for glide, but the vehicle did not appear to respond immediately. Since little altitude remained, the stick was put at neutral for vertical descent to initiate collective "flare" in as nearly a vertical attitude as possible. The flare thruster was "fired" two seconds before impact.

FIGURE 64 KRC-6 TEST VEHICLE (Final Configuration)

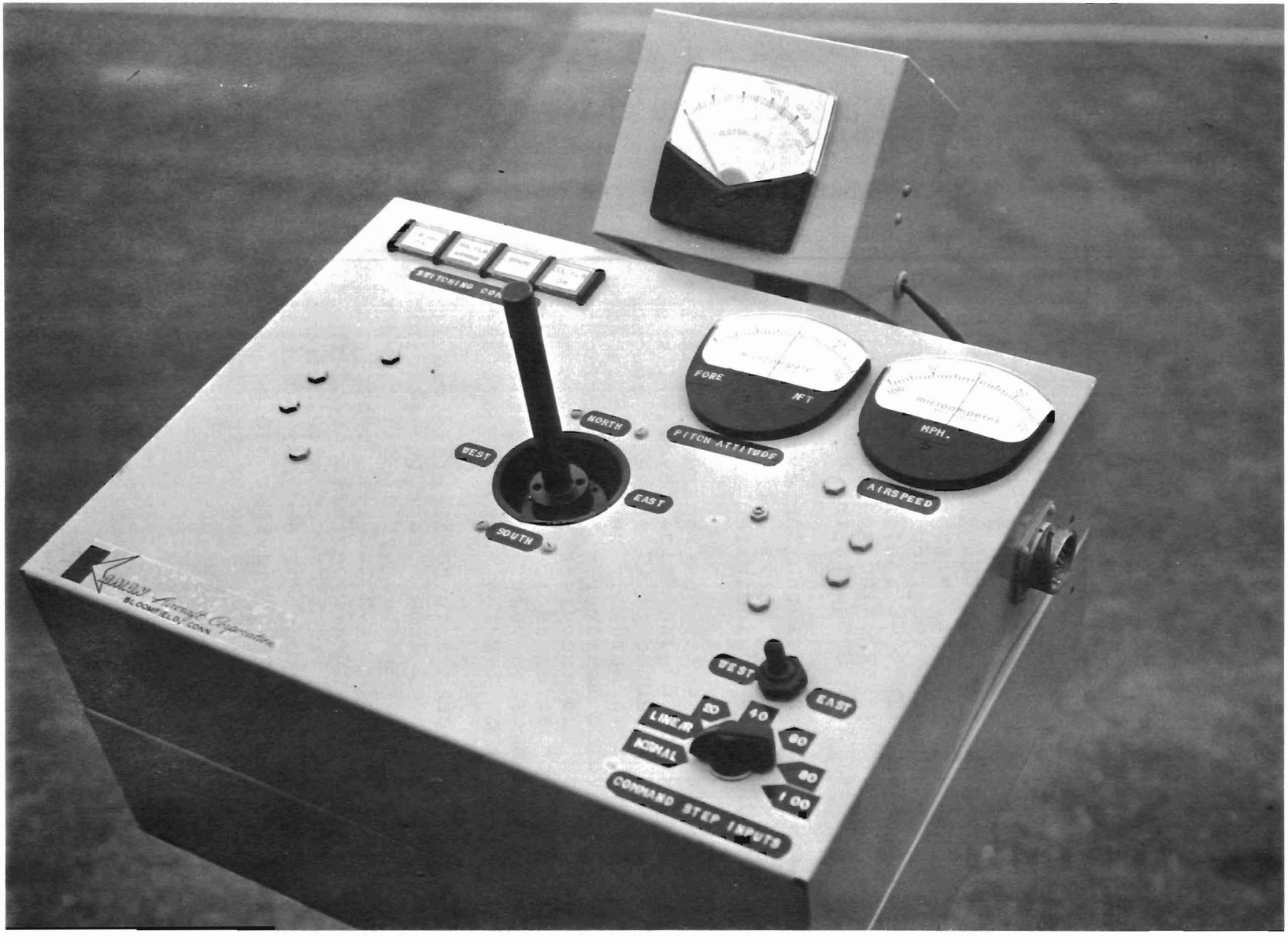

FIGURE 65 GROUND CONTROL UNIT (Final Configuration)

Telemetry signals were recieved at the control station after impact. On arriving at the touchdown site, the vehicle body was found to be relatively intact, except for the nose cone which had sheared off laterally. Avionic systems were still operating electrically and were switched "off". Subsequent bench tests indicated that the avionic equipment was still operable and undamaged. Even the sensitive gyros were not damaged.

The final drop was the most successful of the series in regards to performing desired flight functions and maneuvers, flight performance, and recovery of sensitive equipment. Nominal rate of descent was 54 feet per second.

Flight direction was changed 180°. This is shown by a plot of the x and y co-ordinates as recorded by theodolite, Figure 66, and in flight data as recorded by oscillograph, Figure 67. The small arrows in Figure 66 indicate the relative wind at the various altitudes. Average wind velocity multiplied by the flight time from Point A to B equals the drift distance from A to B.

Glide at L/D ratios ranging from 1.6 to 2.0 was maintained for extended duration. Maximum L/D of 2.38 was achieved for a short period. This is indicated in Figure 67.

Horizontal velocity was retarded to 12 feet per second from 84 feet per second during "slow" cyclic flare. Vertical rate of descent was retarded to 27 feet per second. With respect to ground, the vehicle actually reversed direction of flight. The "rapid" cyclic maneuver retarded horizontal velocity to 4 feet per second and increased rotor speed to 910 from 810 RPM. Rate of descent decreased to 46.5 feet per second. Figure 68 indicates the changes in velocity as obtained from theodolite data. Respective commands for the maneuvers are also indicated.

The large decrease in horizontal velocity with attendant increase in rotor speed demonstrate the feasibility and value of cyclic flare. Co-ordinated cyclic flare and collective pitch control (not feasible with the test vehicle hardware) would undoubtedly improve over-all performance of the landing maneuver. Spiral during the cyclic flare is attributed to softness of the lateral control. The control did not effectively overcome the rolling tendency induced by gyroscopic coupling of the rotor. Gyroscopic moments are generated by the longitudinal pitch rate of the rotor.

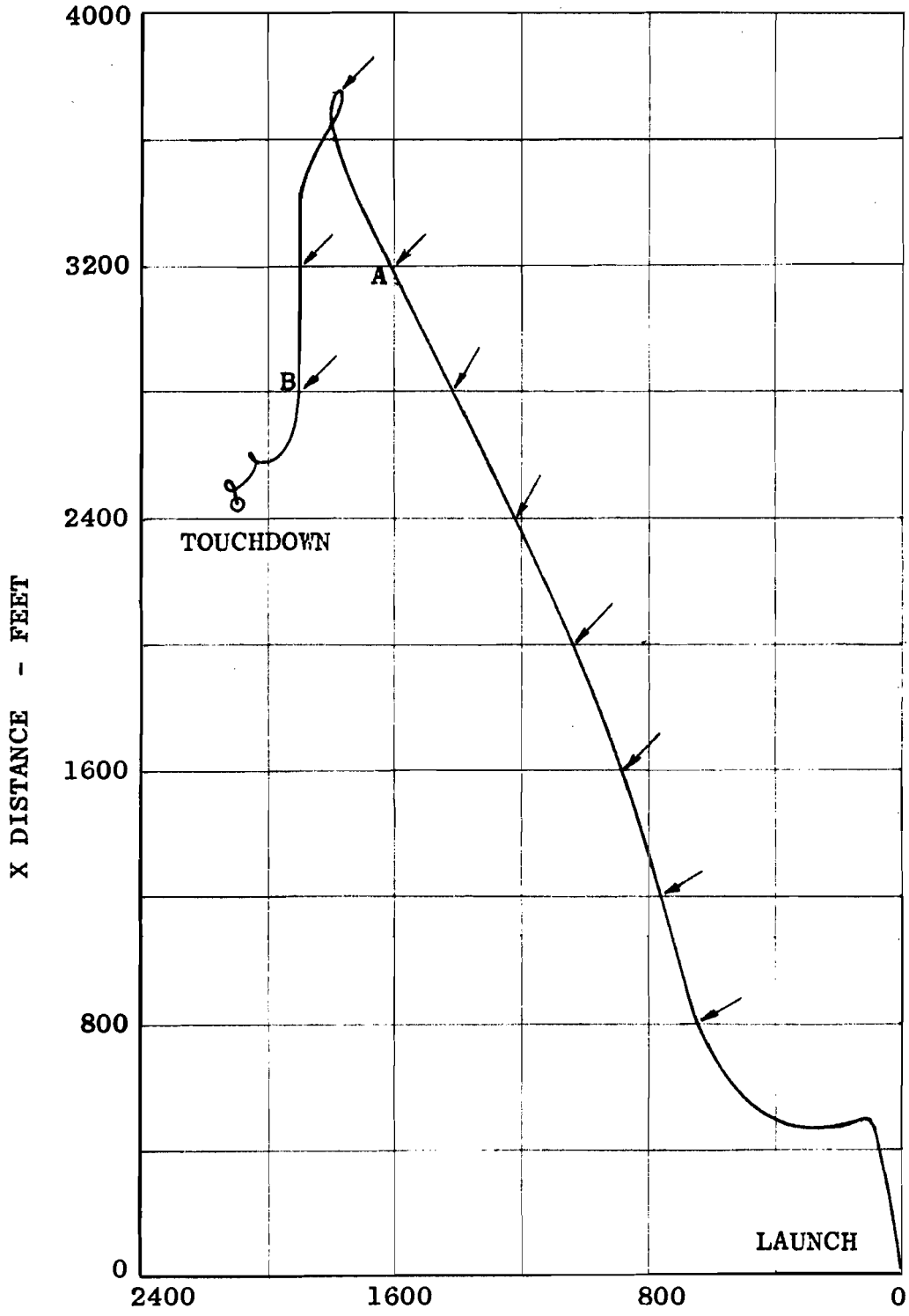

GROUND FLIGHT PATH, TEST No. 13

FIGURE 66

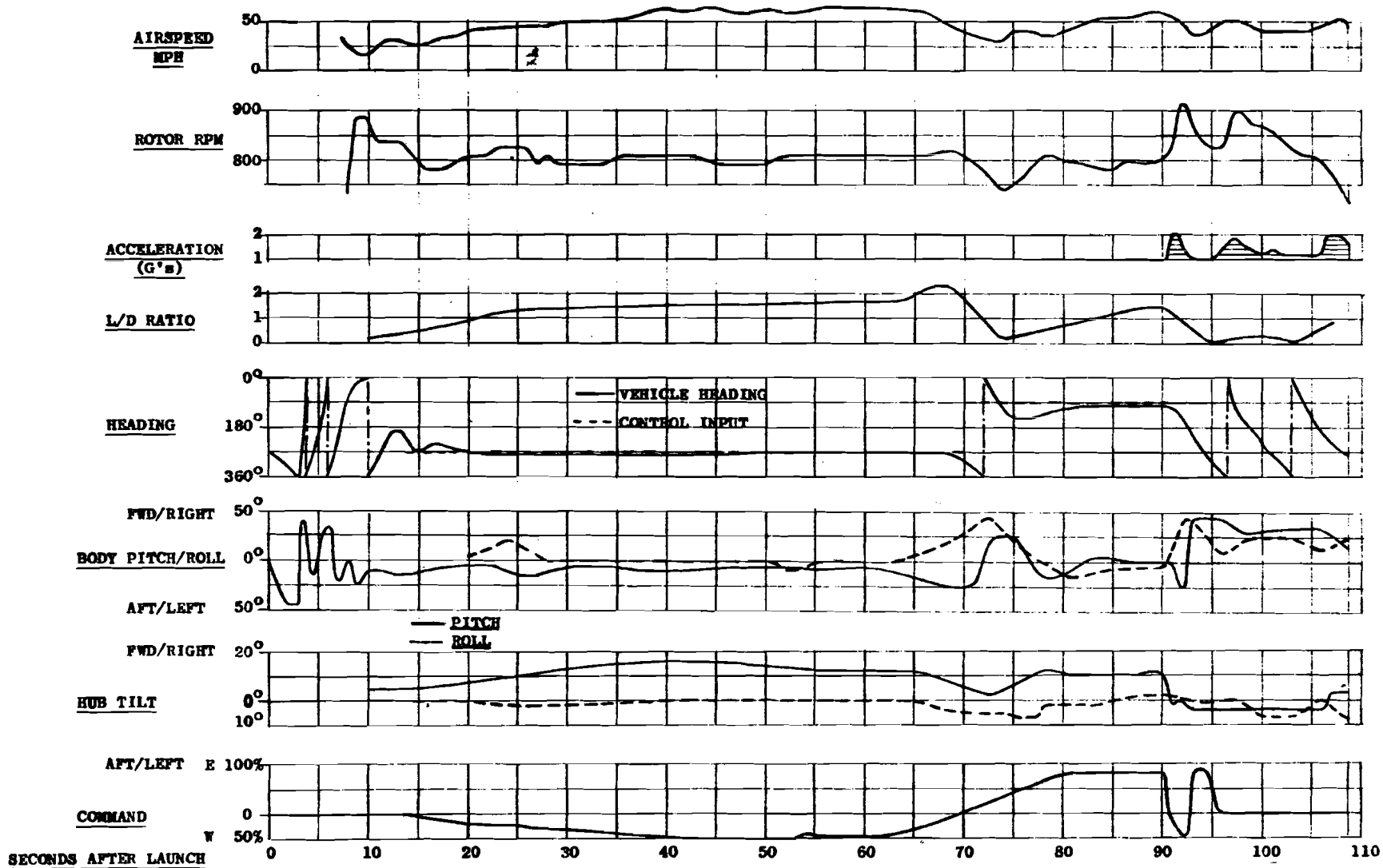

TIME HISTORY TEST NO. 13

FIGURE 67

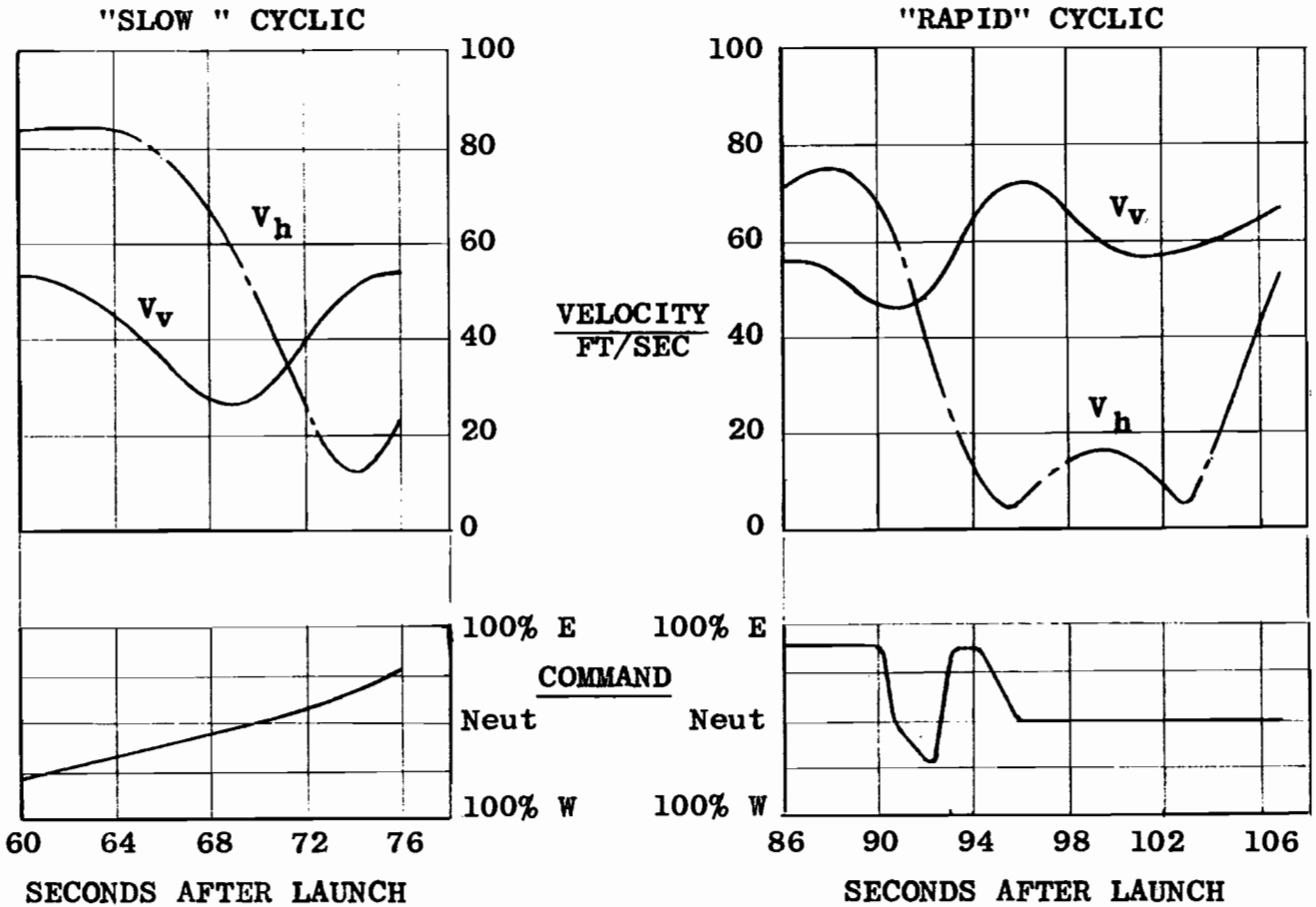

VARIATION OF VELOCITIES DURING CYCLIC FLARE

FIGURE 68

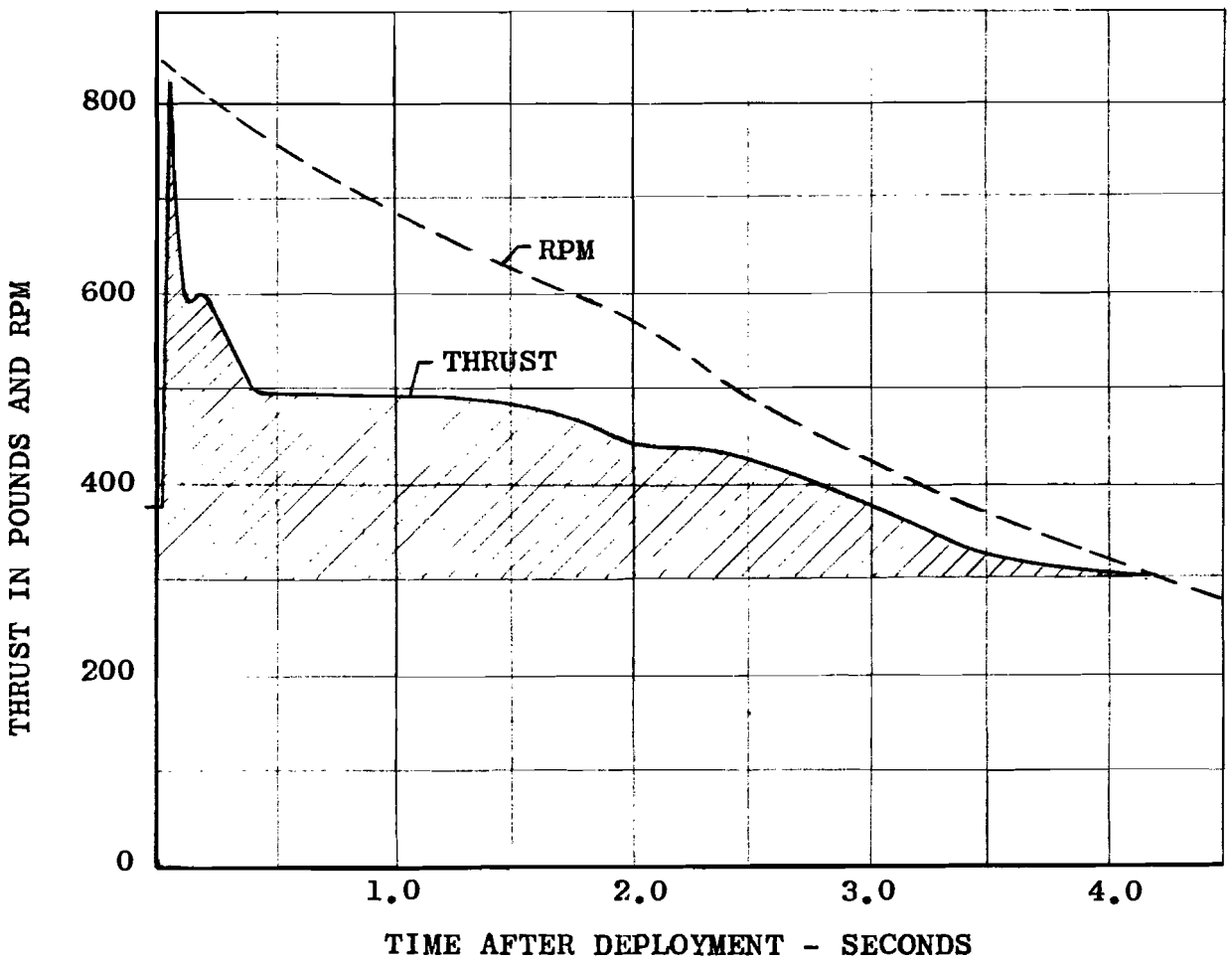

ROTOR PERFORMANCE DURING COLLECTIVE FLARE (TRUCK TEST DATA)

FIGURE 69

Data on collective flare performance did not corroborate one another fully. The operable condition of the avionic equipment and gyros after impact indicates a soft touchdown. A 1.4 "G"-second deceleration was recorded by the vehicle accelerometer. Taking into account the 35° tilt of the vehicle at the instant vertical descent should have been retarded by 37 feet per second. Yet, recorded vehicle airspeed indicated little retardation. Airspeed anemometer rotor inertia may not have reflected the rapid deceleration. Theodolite data stopped a fraction of a second after initiation of the flare.

A structural failure in the collective flare control system prevented attainment of the retardation potential recorded during truck tests, Figure 69. The fitting attaching a "flare" control rod to the rotor spring housing broke upon initiation of the flare. As a result, the housing was not positioned for optimum blade pitch setting, and maximum thrust was not developed.

J. RESULTS

The air drop tests demonstrated that a rotary-wing decelerator system, and in particular the ROTOCHUTE concept, can:

1. Be deployed at various launch speeds and attitudes.
2. Be guided from axial descent into glide flight.
3. Be kept stable in all flight regimes.
4. Be maneuvered during descent and controlled in heading.
5. Glide at L/D ratios of 2.0 or better.
6. Retard impact velocities through cyclic and collective flare.
7. Recover payloads intact and in an operable condition.

The following performances were achieved with the KRC-6 ROTOCHUTE flight test system during the air drops:

Rotor Drag Coefficient, C_{D_R}	-	1.2
Terminal Rate of Descent (Axial)	-	52 ft/sec
Maximum Glide (From Horizontal)	-	23^{o}
Extended Glide (From Horizontal)	-	30^{o}
Cyclic Flare Retardation		
Horizontal Velocity	-	to 4 from 77 ft/sec
Vertical Velocity	-	to 27 from 77 ft/sec
Collective Flare Deceleration		
Peak	-	2.5 "G"
Average	-	1.4 "G" seconds

Although the KRC-6 ROTOCHUTE vehicle was a newly created flight system and was flown for the first time in the air drop tests, all systems performed their intended functions in most instances, even during adverse conditions.

The rotor system deployed satisfactorily and reliably, even in adverse yaw attitudes. Although stable flight prior to deployment is desirable, deployments during the test demonstrated that oscillations as high as 45^{o} yaw can be tolerated.

Spiral tendency of the ROTOCHUTE induced by operating the rotor at speeds above the stable range to provide maximum rotor stored energy for the flare phase was satisfactorily curtailed and controlled by the Automatic Stabilization System.

Axial descent performance closely agreed with the performance predicted analytically. The performance in glide was predicted qualitatively. Quantitatively, actual glide results failed to agree more closely because accurate detail data of the vehicle characteristics were lacking. The program permitted only limited investigation and testing prior to flight.

The vehicles were maneuvered during descent and flight headings changed. With proper system "gains", adequate servo stiffness, and stable directional control, the vehicle responded to commands and flew in the heading commanded, neglecting wind drift, even into reported winds. Vehicle response lagged commands by approximately one second.

Vehicle drag prevented glide at L/D ratios much higher than 2.0. The test vehicle body equivalent flat plate area was large relative to the rotor disc area, the rotor hub assembly was disproportionately large to the rotor size (in comparison to rotors for larger payloads), and modifications to the rotor (increasing the diameter by adding blade tip extensions) resulted in higher blade drag. When body drag was reduced by removal of the legs and other minor modifications, the glide range improved. The test vehicle configuration in actuality simulated a missile booster recovery configuration. Capsules would be smaller in relation to the rotor.

Although a horizontal stabilizer was ultimately added because the rotor tilt on the test vehicle could not be increased to produce enough trim control to counterbalance rotor aft pitching moments being encountered, the surface is not necessarily essential in other applications. Providing adequate trim control by designing insufficient rotor tilt at the outset or reducing the rotor pitching moment by using cyclic pitch of blades to tilt the rotor plane would eliminate the need for a horizontal stabilizer for trim.

Touchdown velocities were higher than predicted because the vehicle rolled and spiralled during the cyclic flare and collective pitch control was not co-ordinated with cyclic control during the landing. This was not feasible with the existing test vehicle control provisions. The lateral control must be made more effective to prevent roll, and ensuing spiral, during the cyclic flare mode. Servo control of collective pitch would permit co-ordination during the landing maneuver. The servo could also be "slaved" to rotor RPM for governing, eliminating the governing spring.

Just as with any other experimental aircraft or aerospace system, each test provided data, knowledge, and experience to make the succeeding flight a better one.

5. APPLICATION STUDIES

INTRODUCTION

Limited preliminary studies were performed for the use of rotary-wing systems in recovery of missile boosters, data capsules, manned capsules, and other payloads. While basic requirements are similar for most of the applications, enough differences exist to conclude that use of rotary-wing decelerators, although feasible technically, in all applications, are more practical in certain ones than others.

The stored energy rotor recovery system combines in one system all elements for initial retardation and stabilization, drag modulation, useful L/D ratio glide, guidance capability, and touchdown at near-zero velocities.

In the present state-of-the-art, cost, stowage, and weight may be unfavorable for simple recovery missions. However, when control during descent, glide capability, soft touchdown, or accuracy of delivery is an important consideration, rotary-wing decelerator systems are competitive.

APPLICATIONS

In addition to many features of rotary-wing decelerators already mentioned, advantageous use may be made of the following inherent or design ROTOCHUTE concept characteristics in applications:

1. Low drag profile prior to deployment.
2. Controlled deployment forces without shock loads.
3. Rapid deployment openings which are repetitive within close tolerance from system to system.
4. Programmed launch and deployment cycles.
5. Wide range of speed and altitude deployment.

Broadly speaking, applications for rotary-wing decelerators may be classified in the following categories:

A. Recovery - Guided delivery of payload to a selected site. Recovery of boosters, data capsules, manned capsules, instrument packages typify applications in this category.

B. Delivery - Free-fall aerial delivery of items such as supplies weapons, instrument packages, and remote operating stations for meteorology and guidance.

C. Retardation - Initial deceleration to provide maximum separation between launch vehicle and payload; or descent where terminal delivery is not a consideration. Retardation of tactical and anti-personnel weapons, flares, and meteorological sondes fall in this category.

A. RECOVERY APPLICATIONS

Figure 70 depicts the wide variation in size, shape, and weight of present-day missile boosters, manned capsules, and nose cones. The variation makes nearly each application an individual design task. However, recovery requirements for each group may be categorized to some extent.

1. Boosters

Since missile boosters or separable first stages, presently expendable, involve expensive rocket motors and related hardware, recovery of such units becomes an important economic consideration, especially as the number of launchings for a system increase. Savings effected through such recovery could reduce a program over-all cost or permit more systems for a given budget.

For practical recovery of missile boosters, a recovery system must delivery the booster to a convenient site down range, since this will affect transportation and other refurbishing costs. Return to the reconditioning facility must be a relatively simple matter and involve a small number of personnel. Damage of expensive engine and control systems by contamination from salt water or earth must be limited or minimized. Glide range of a recovery system will establish the extent of choices of recovery areas.

Recovery touchdown must be at low enough velocities to prevent major damage to relatively fragile shell structures of most boosters in the recoverable state.

Recovery of boosters with rotors, although technically feasible, does not represent the best field for immediate application. Limiting the rotor disc to a maximum loading of 6 pounds per square foot for collective flare performance considerations, a 100-foot diameter rotor would retard 47,000 pounds

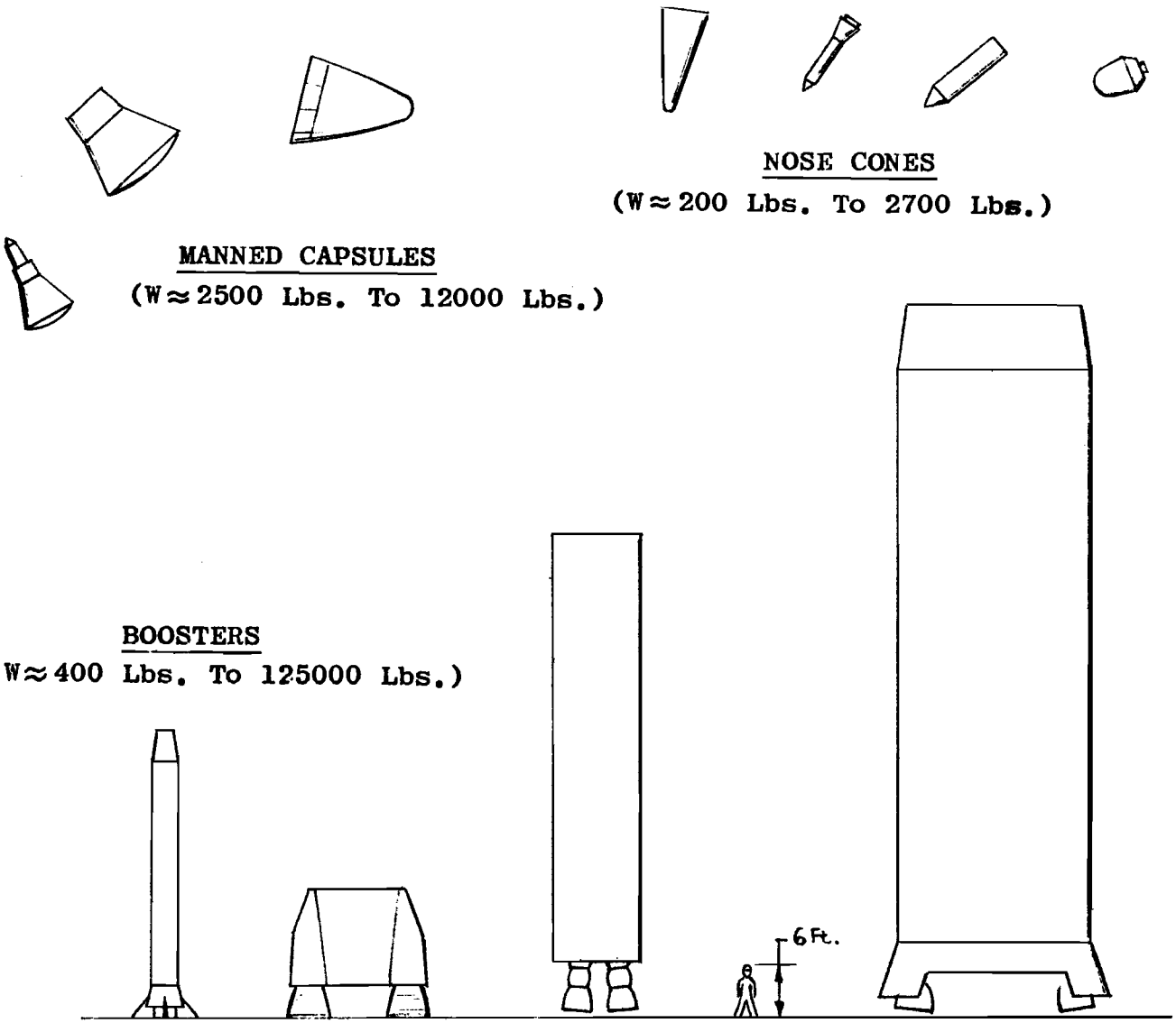

REPRESENTATIVE RECOVERABLE SYSTEMS

FIGURE 70

gross weight to 65 f.p.s. terminal descent. In general, for a given descent rate, the required rotor diameter will be the same as that of the projected diameter of a parachute.

Stowage of rigid or telescoping blades may be a problem, especially since the blades should not be attached directly to the shell. If attached directly, energy of rotation of the booster at impact can be as detrimental as a high impact velocity. Figure 71 shows a proposed system for a typical booster.

Development of stowable, flexible blade rotor systems can change the picture, since larger rotor diameters may become more practical and stowage becomes less of a problem.

2. Manned Capsules

The prime requisite for manned capsule recovery systems is, of course, to return personnel safely and unharmed even under emergency circumstances. Other requisites may be summarized as follows:

Reliability - The recovery system should be at least as reliable as present-day parachute systems. If this requirement is not met, remaining requirements become academic.

Low Deployment Shock Forces - Retardation systems may be deployed during a period of high "q". Resulting deployment shock forces should not be so large as to transmit objectionably high loads to the capsule. Both the physical "G" tolerance of the astronaut and the strength of the capsule (with its influence on weight) must be considered in determining what constitutes objectionally high loads.

Stabilization - During re-entry, many capsules must be stabilized to prevent tumbling and align the heat shield. It is desirable that the recovery system assume this function as soon as feasible to reduce the operating time of reaction control jets.

Drag Modulation - To reduce peak values of deceleration during re-entry, drag modulation by the recovery system becomes a desirable function.

Glide Capability - Glide capability is desirable to compensate to the extent possible for errors and tolerances in the retro-rocket firing and re-entry events. This is especially so for proposed land recovery operations where the vehicle must touchdown at the prepared area.

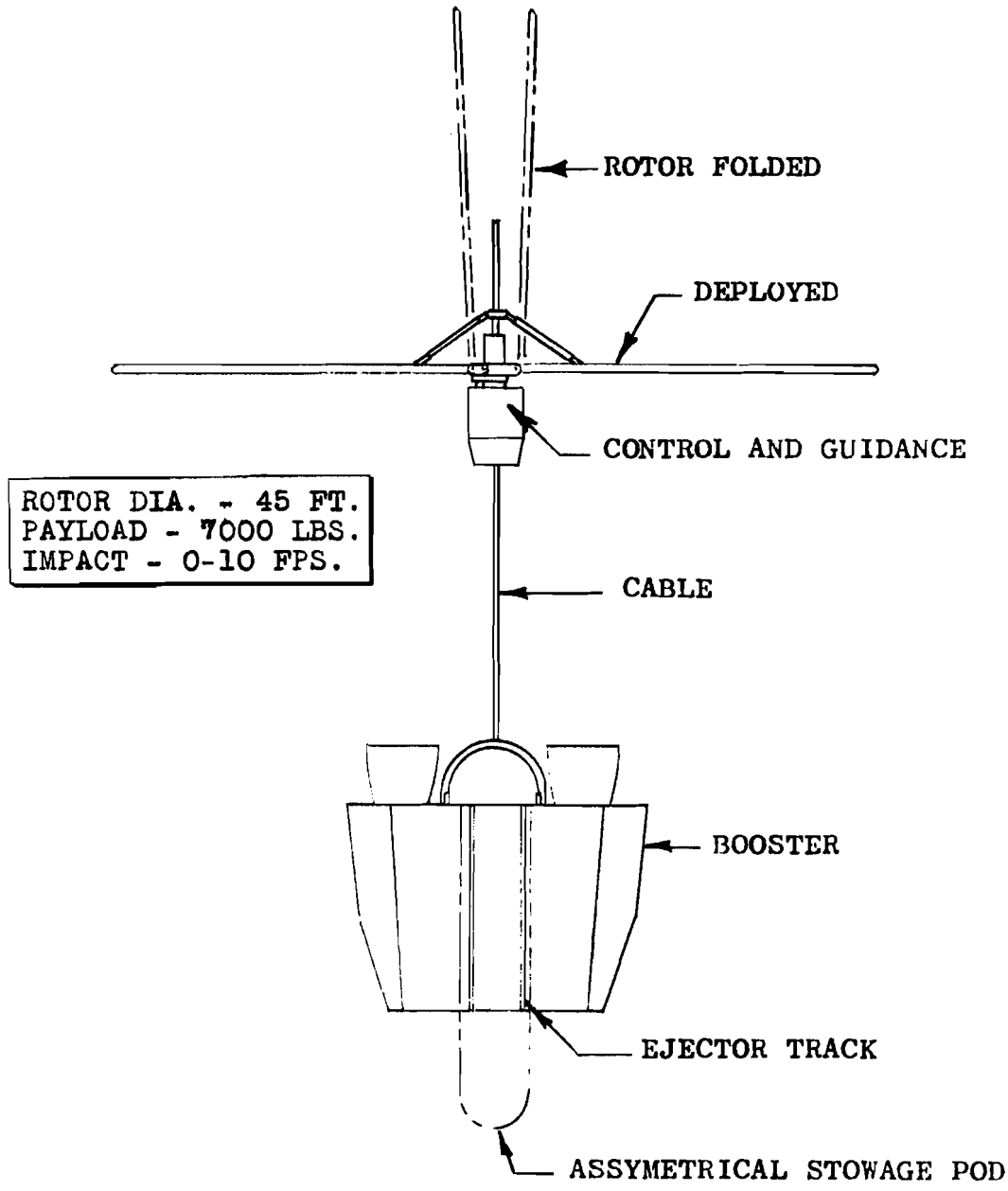

ROTOCHUTE INSTALLATION FOR AN ATLAS-TYPE BOOSTER

FIGURE 71

Maneuverability - The recovery system must be capable of being guided to the selected landing site. In addition, it must be sufficiently responsive to control commands in avoiding local obstacles or hazards, especially if an emergency recovery at an unprepared site was being performed.

Handling Qualities - A capsule and recovery system must exhibit good handling qualities during the glide descent and landing phase. The physical and mental conditions of astronauts returning from a space mission must be considered in evaluating "good handling qualities" characteristics.

Zero Velocity Touchdown - The unpredictable tolerances and errors during re-entry deem it probable that a percentage of the recoveries will not reach the prepared recovery area. The recovery system should, therefore, be capable of providing zero horizontal translation and near-zero vertical velocity at touchdown.

Remote Guidance - Remote guidance and control of returning space vehicles is not only desirable, but essential, if astronauts are disabled or incapable of control for any reason.

Simplicity - The above functions should be capable of being carried out with rugged, durable hardware and a minimum of components, subsystems, and sequences to provide optimum reliability, minimum weight, and minimum expense.

Compactness - The recovery system should be lightweight and of a configuration that is readily stowable on the recovery vehicle system.

Without a doubt, other recovery systems may be optimum in providing one or more of the above requirements. But rotary-wing decelerators have the potential in providing a majority of the above requirements.

In particular, such systems are capable of providing initial retardation and stabilization as well as terminal descent retardation. Only one deployment sequence is involved. Deployment may be initiated at high speeds and altitudes.

Figure 72 shows one stowed configuration.

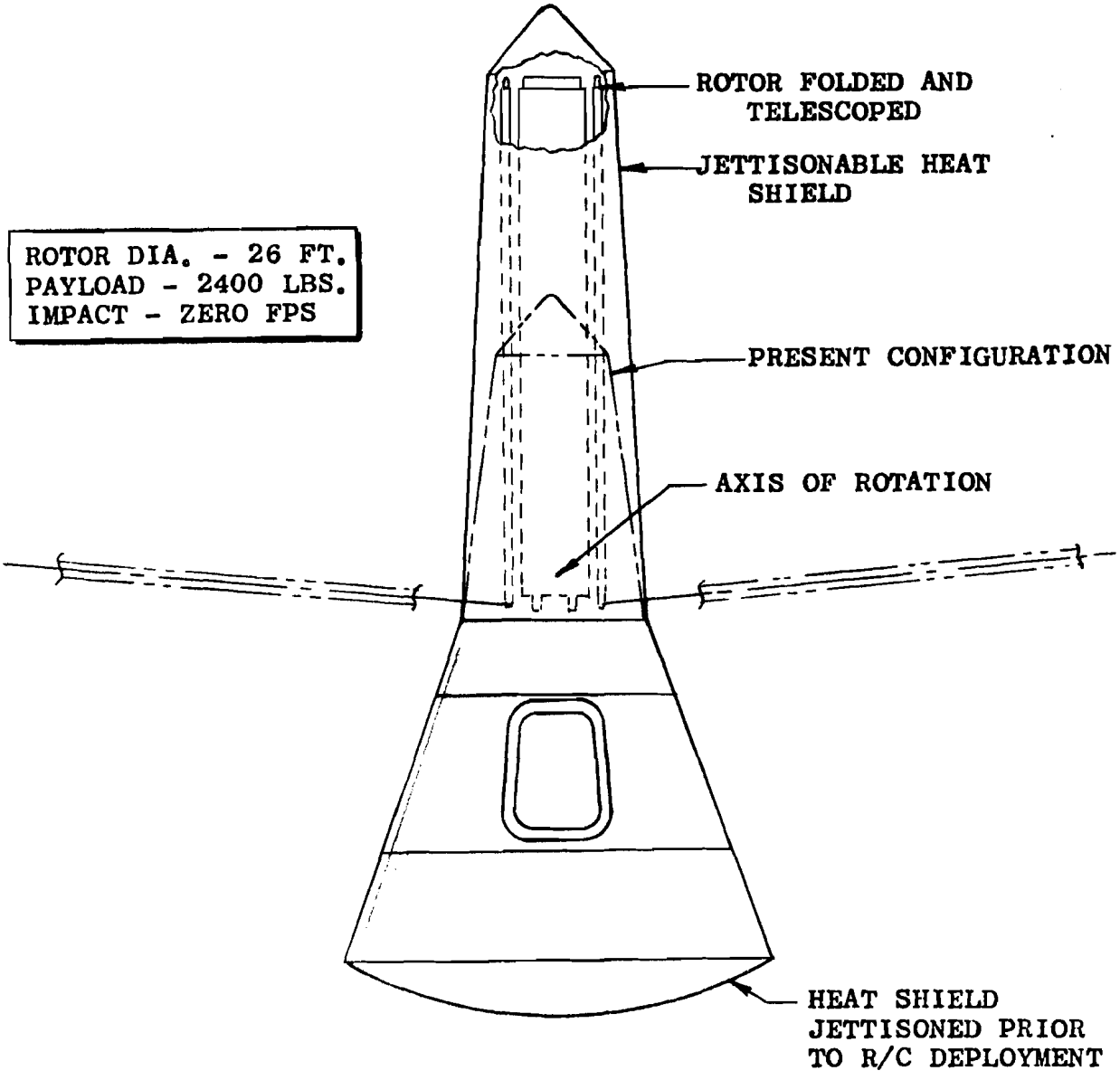

ROTOCHUTE INSTALLATION FOR A MERCURY-TYPE CAPSULE

FIGURE 72

The ability of rotary-wing decelerators to provide recovery at near-zero horizontal and vertical speeds is considered to be the most important attribute. This means that a relatively small recovery site need be provided. But more important, the system provides a potential for safe recovery away from a prepared site. Emergencies in orbit or errors during re-entry could necessitate such touchdown. A rotary-wing system provides the maneuverability to avoid local hazards during the approach.

In the Contractor's opinion, recovery of manned capsules represents the best potential application for sophisticated remotely-controlled rotary-wing decelerator systems. Safe return of personnel warrants consideration of the features and performance such systems are potentially capable of providing.

3. Data Capsules

Many space programs involve the gathering of important scientific data with relatively expensive instrumentation. Recovery of such packages becomes costly because a number of teams must patrol a broad recovery zone. Guided recovery with drag modulation could reduce the recovery zone target by compensating for errors such as wind drift.

Meteorological sonde packages are often lofted almost vertically to high altitudes by rockets and drift down at established rates of descent. The rates at the higher altitudes are such that the recovery system will give very low rates of descent at lower altitudes. Such systems are subject to excessive wind drift and eventual loss. Recovery could be enhanced by jettisoning the initial retarding system and using a rotary-wing decelerator at the lower altitudes. This category of operation essentially involves a launch, retardation, and unguided vertical descent. Performance of the rotor at the initial and terminal phases is an important design consideration. This arrangement could provide higher rates of descent with less wind drift and recovery at the launch area with return guidance by a homing beacon system.

Figure 73 illustrates a typical data capsule modified with a rotary-wing decelerator.

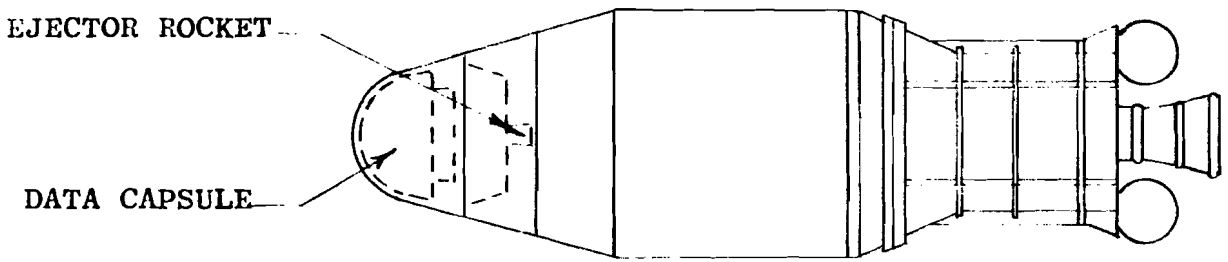

PRESENT RECOVERY SYSTEM

ROTOR DIA. - 8 FT.
PAYLOAD - 250 LBS.
IMPACT - 0-10 FPS

ROTOCHUTE RECOVERY SYSTEM

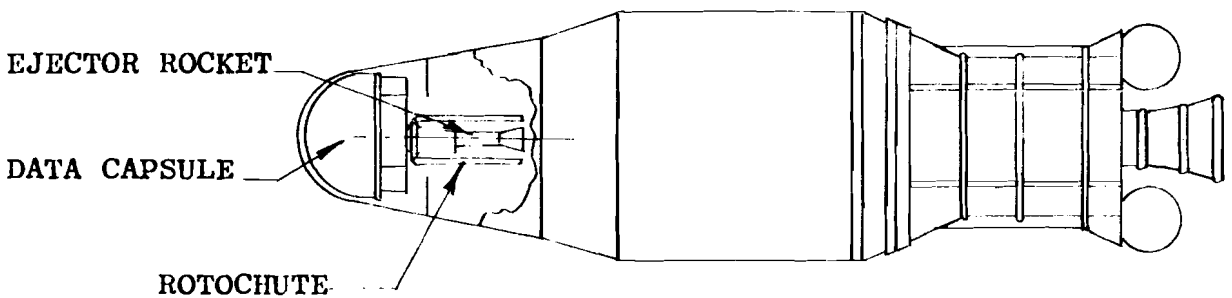

ROTOCHUTE INSTALLATION FOR A DATA CAPSULE

FIGURE 73

B. DELIVERY APPLICATIONS

Rotary-wing decelerators are particularly suited to delivery of arms, ammunition, supplies, and similar small cargo to isolated troops. Delivery may be made from low altitudes and high speeds, from modern fighter aircraft since the rotor system may be integrated into an aerodynamically clean package and deployed at high q's. The one-phase deployment, repetitive within close tolerances for a given system, makes possible more accurate prediction of trajectory.

Such deliveries may be performed without or with remote guidance. Without guidance, the system is relatively simple and inexpensive since no avionic equipment need be involved.

Another potential for accurate delivery of supplies is by means of a ground-to-groud missile boosted to a ballistic trajectory. The rotary-wing decelerator would be deployed in the terminal descent phase at low altitudes to reduce wind drift. Predictable, repetitive opening cycles make such deployment possible.

C. RETARDATION

Rotary-wing decerators may be used purely as a retarding device. Touchdown performance is of relatively little concern in this case. Rapid retardation may be provided to give maximum separation between the launch aircraft and the system being delivered.

Delivery of tactical weapons, anti-personnel weapons, flares, and similar systems are typical applications. Such weapons may be delivered from low altitudes at high or low speeds. The high rate of retardation will result in rapid separation between the weapon and the aircraft, providing an added margin of safety for the aircraft and personnel.

Rotary-wing devices may be programmed to provide a variety of trajectory characteristics. The opening may be governed for relatively constant deceleration. Deployment may be delayed as desired. Power augmentation could provide a short period hover capability, especially for flare delivery.

A rotary-wing decelerator with the capability of controlled opening and closing may be used as a drogue or air brake for fixed-wing aircraft. Such a device could be deployed and later retracted without repacking.

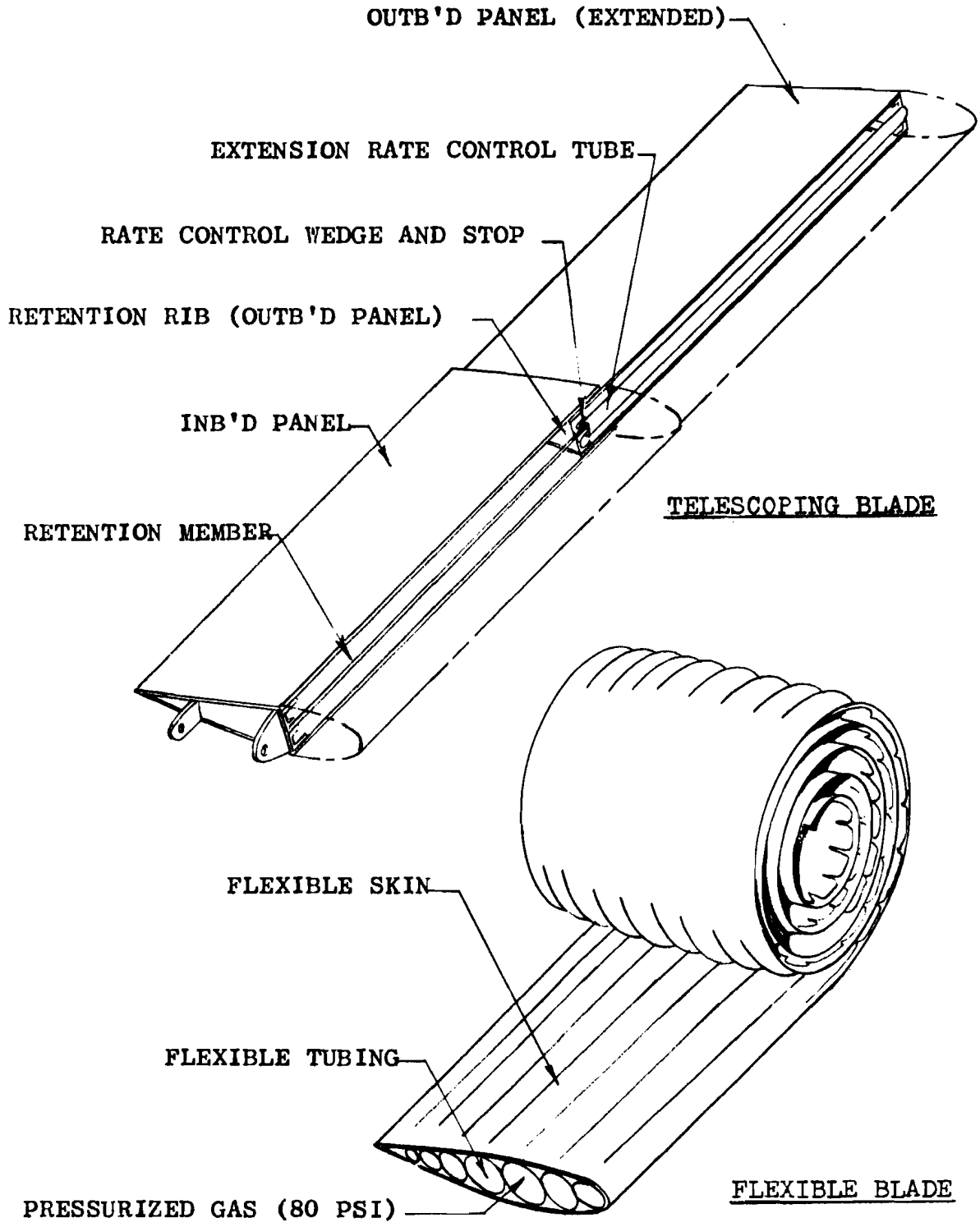
OUTB'D PANEL (EXTENDED)
EXTENSION RATE CONTROL TUBE
RATE CONTROL WEDGE AND STOP
RETENTION RIB (OUTB'D PANEL)
INB'D PANEL
RETENTION MEMBER
TELESCOPING BLADE
FLEXIBLE SKIN
FLEXIBLE TUBING
PRESSURIZED GAS (80 PSI)
FLEXIBLE BLADE

FIGURE 74

D. FUTURE POTENTIAL

Many of the above applications have already been demonstrated in actual tests with rigid, fixed-span blade rotor systems. Telescoping blade rotors have also been used for applications where stowage space prior to deployment was a problem. A typical telescoping blade configuration is shown in Figure 74.

The potential use of rotary-wing decelerators will be enhanced when a practical, stowable blade concept is developed. An approach that appears to be promising is a flexible inflatable type blade. Prior to inflation, such blades can be packaged into a small volume of space. Inflation will provide a nearly true airfoil structure with torsional stiffness that will aid in control of such rotors.

Power augmentation of the rotor by tip jets, trailing edge jets, or other means will reduce the required rotor size (for a given touchdown performance), extend the glide range, or permit a short-period of hover. Initial study shows this to be feasible and research in this area is recommended.

6. CONCLUSIONS AND RECOMMENDATIONS

A. CONCLUSIONS

Analytical investigations and results from experimental tests conducted during the performance of the program have been instrumental in forming the following conclusions relative to rotary-wing decelerators in general, and the rigid blade rotor system in particular.

1. The basic concept of using a controlled autorotating rotary-wing decelerator system for the retardation and recovery of payloads is sound and feasible technically. Additional effort is required in some areas to fully demonstrate the full potential, particularly in the landing mode.

2. Performance and stability of rotary-wing decelerators can be predicted analytically. Agreement with actual performance and behavior will be dependent upon the detail and accuracy of inputs for over-all system characteristics. These can be established with detail analysis and/or experimental tests for a given system.

3. Use of the rotor for retardation is presently feasible in axial flow operation up to speeds where aerodynamic heating is below critical for developed materials and fabrication methods. Additional detailed study and development of blade structure is required for use at high speeds involving more severe aerodynamic heating.

4. Glide descent at L/D ratios of 2.5 or better is deemed feasible. The test vehicle, whose body equivalent flat plate area was large in relation to the rotor disc area, approached an L/D ratio of 2.0 in steady descent with a peak L/D ratio of 2.38. Helicopters with aerodynamically clean bodies glide at L/D ratios of 2.5 in unpowered descents.

5. Use of the rotor kinetic energy to retard touchdown velocities to 5 feet per second or less, although not fully demonstrated in tests, is still believed feasible. Limitations imposed by test vehicle control provisions handicapped demonstration of potential performance. Soft touchdowns are performed by helicopters in power-off landings.

6. The glide and control capability of rotary-wing decelerators coupled with potential touchdown at low or zero horizontal and vertical velocities should enable recovery in small confined sites.

7. The same characteristics would permit emergency landings in rough, unprepared areas with a minimum risk to human occupants or sensitive payloads.

8. Artificial stabilization can be effectively used to stabilize the spiral mode. The spiral mode can also be made inherently stable by operating the rotor at a lower tip speed.

9. Over-all weight for a rotary-wing decelerator system, including remote control and automatic stabilization provisions, is estimated to run from 10 per cent to 15 per cent of a recoverable system gross weight for payloads over 2000 pounds. Many of the remote control system components are normally found in recovery capsule systems and would be usable for the rotor control.

10. With development, rotary-wing decelerator systems have the potential for combining in one unit features for initial retardation and stabilization, drag modulation during re-entry, glide at useful L/D ratios, control and maneuverability in descent, and terminal flare with near-zero velocity touchdown. These characteristics are especially desirable and suitable in recovery of manned aerospace systems.

11. Development of flexible, stowable blades would enhance use in potential application systems where storage volume is limited or at a premium.

12. Rotary-wing decelerator systems appear feasible for manned aerospace system recovery. Use in other applications should be considered when limitations of established recovery systems limit the deployment speed or do not provide the desired trajectory control, delivery accuracy, glide capability, controllability, or potential for soft touchdown.

B. RECOMMENDATIONS

In view of the above conclusions, the following recommendations are submitted by Kaman Aircraft Corporation to advance the knowledge and state-of-the-art for rotary-wing decelerator systems and expand the scope for potential applications.

1. To provide more detailed information of behavior and control requirements for the landing phase, as a guide for programming control for the maneuver, it is recommended that additional studies and experimental tests relative to the landing

phase be conducted, using the present KRC-6 test vehicle. The vehicle aerodynamic and stability characteristics should be established in greater detail by wind tunnel and/or ground tests prior to flight.

2. Glide range of rotary-wing decelerator systems would be extended if glide at supersonic speeds were feasible. The scope of the present reported program did not permit determinating feasibility of such operation. It is, therefore, recommended that studies be initiated toward this regime of operation, and that the KRC-6M model be adapted for wind tunnel investigation in glide attitude at supersonic speeds.

3. To improve prediction of performance and behavior in the transonic and supersonic regime, data from 0 to 180 degrees angle of attack should be determined and made available for airfoils that may be potentially used for the rotor blades. Such data in the high speed spectrum is presently insufficient or lacking.

4. Although the ROTOCHUTE concept can be made inherently stable in vertical descent with present knowledge and without the use of automatic stabilization, an understanding in greater depth of the effects of various parameters such as rotor disc loading, rotor inertia, vehicle center of gravity location, etc. is desirable for more accurate prediction and achievement of inherent stability. It is suggested that detailed parametric studies in this respect be initiated and corroborated by experimental tests. Such knowledge is essential for manned recovery applications.

5. With a view to improving stowage of rotor systems and reducing weight, studies should be initiated and directed toward investigating various flexible blade concepts. Development of such concepts would particularly enhance potential use in space systems where stowage volume and weight of installed systems are at a premium. It is possible that costs of rotor systems for more conventional applications would also be reduced with flexible blades.

LIST OF REFERENCES

1. Joy, D. P., and Simmonds, R. M., "Transport Helicopter Design Analysis Methods", Hiller Aircraft Corporation, Report No. 473.6, 1955

2. Gessow, A., and Tapscott, R., Charts for Estimating Performance of High Performance Helicopters, NACA Report No. 1266, 1956

3. Allen, H. Julian, and Eggers, A. J., Jr., A Study of the Motion and Aerodynamic Heating of Missiles Entering the Earth's Atmosphere at High Supersonic Speeds, NACA TN-4047, 1957

4. Chapman, R. Dean, An Approximate Analytical Method for Studying Entry Into Planetary Atmospheres, NASA TR-R-11, 1959

5. Horner, S. F., "Fluid-Dynamic Drag" (Published by the author, 148 Busteed Drive, Midland Park, New Jersey, 1958)

6. Arnold Center Test Facilities Handbook, Volume I, Arnold Air Force Station, 1961

7. Pitts, W. C., Force, Moment, and Pressure Distribution Characteristics of Rectangular Wings at High Angles of Attack and Supersonic Speeds, NACA RM-A55-K-09, 1956 (CONFIDENTIAL)

8. Joint Parachute Test Facility, USAF 6511th Test Group (Parachute) and U. S. Naval Parachute Facility, El Centro, California

9. Nikolsky, Helicopter Analysis

10. Haig, C. R., "Vertical Landing and Glide Characteristics of Rotor Landing Systems", Bell Helicopter Corporation, Report No. 8008-099-009, 1960

11. Castles, W., and Gray, R. B., Empirical Relation Between Induced Velocity, Thrust, and Rate of Descent of a Helicopter Rotor As Determined By Wind Tunnel Tests on Four Model Rotors, NACA TN-2474, 1951

12. Crabtree, J. A., and Amer, K. B., Helicopter Configuration and Propulsion System Study: Part I - Statistical Weight Analysis, WADC TR-57-583, Part I, 1957

13. Gessow, A., and Meyers, G. L., Jr., Aerodynamics of the Helicopter, Macmillan, 1952

14. Feldman, S., Hypersonic Gas Dynamic Charts for Equilibrium Air, AVCO Corporation, 1957

15. Finstron, M., and Barron, J. R., "Notes - Investigation of Rotor Aerodynamic Heating for KAC", Massachusetts Institute of Technology, Unpublished, 1961

16. Herron, R. D., and Binion, T. W., Jr., Tests of the Kaman KRC-6M ROTOCHUTE at Transonic Speeds, AEDC-TN-61-60, May 1961

17. Galigher, L. L., Wind Tunnel Tests of the Kaman KRC-6M ROTOCHUTE at Supersonic Speeds, AEDC-TDR-63-128, July 1963

18. Schlicting, H., Boundary Layer Theory, McGraw-Hill, 1955

APPENDICES I THROUGH V

APPENDIX I. ANALYTICAL STUDIES

A. AXIAL FLIGHT - "STRIP ANALYSIS"

Introduction

In autorotative axial flight at the moderate flight speeds being considered, the relatively low inboard and high outboard rotor tangential velocities mean that stall conditions prevail towards the rotor hub, while the blades are unstalled towards the tip. It follows that ordinary helicopter rotor theory for forward flight based on a modest amount of stall on the retreating blade is thus inapplicable.

For this reason, a "strip" analysis is carried out. For different descent velocities, the aerodynamic force and torque are expressed parametrically for an assumed blade pitch angle (θ). The correct value of θ must satisfy the requirement that the net shaft torque in autorotative flight must be zero.

Strip Analysis

Consider an element of rotor blade of length, Δr as shown in cross-section in Figure 75.

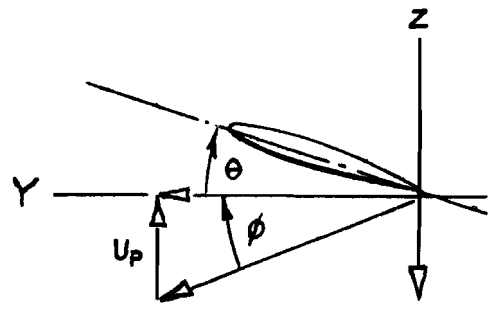

FIGURE 75

The aerodynamic lift (ΔL) and drag (ΔD) are expressible as follows:

$$\Delta L = \frac{b}{2} \rho c \, U^2 \, C_L \, \Delta r$$

$$\Delta D = \frac{b}{2} \rho c \, U^2 \, C_D \, \Delta r$$

Also,

$$U = \sqrt{U_p^2 + U_T^2}$$

$$U_p = (V - v) \cos \beta_o$$

$$U_T = \Omega r \cos \beta_o$$

Next:

$$(L \cos \phi + D \sin \phi) \cos \beta_o = \sum_e^R \frac{b}{2} \rho c \, U^2 \, (C_L \cos \phi + C_D \sin \phi) \times (\Delta r \cos \beta_o)$$

$$= \text{Thrust, } T$$

where

$$\cos \phi = \frac{U_T}{U}, \quad \sin \phi = \frac{U_p}{U}, \text{ at blade element}$$

Thus,

$$T \cong \frac{b}{2} \rho c \sum_1^m (U_{T_n} C_{L_n} + U_{p_n} C_{D_n}) U_n \, \Delta r, \text{ since } \cos \beta_o \cong 1$$

where n identifies the blade element

$$\text{or } \frac{Dt}{dr} = \frac{b}{2} \rho c \, (U_T C_L + U_p C_D) \, U$$

From Reference 9, Page 21,

$$f = \frac{1}{4\pi r V^2} \cdot \frac{Dt}{dr}$$

$$= \frac{\frac{b}{2} \rho c \, (U_T C_L + U_p C_D) \, U}{4\pi r \phi V^2}$$

Let

$$\bar{r} = \frac{r}{R};\ \lambda_r = \frac{U_p}{\Omega R}, \text{and } \lambda_d = \frac{V}{\Omega R}, \text{and } \sigma = \frac{bc}{\pi R}$$

$$\therefore f = \frac{\rho bc\ (\Omega R\ \bar{r}\ C_L + \lambda_r\ \Omega R\ C_D) \sqrt{\lambda_r^2\ \Omega^2 R^2 + \Omega^2 R^2\ \bar{r}^2}}{8\ \pi\ \bar{r}\ R\ \lambda_d^2\ \Omega^2\ R^2}$$

$$= \frac{\sigma\ \rho\ (F\ C_L + \lambda_r\ C_D) \sqrt{\lambda^2_r + \bar{r}^2}}{8\ \bar{r}\ \lambda^2_d}$$

For a particular rotor, σ and R are established quantities. C_L and C_D are fixed for a particular airfoil section once the angle of attack is known. The angle of attack is established when θ and ϕ are known ($\alpha = \theta + \phi$). ϕ is determined when λ_r is assigned a value. θ is decided by torque considerations to be considered below.

$$\text{Torque } Q = (L \sin \phi - D \cos \phi)\ r \cos \beta_o \qquad \cos \beta_o \approx 1$$

$$= \sum_{r=c}^{r=k} \frac{b}{2}\ \rho c\ U^2_r\ (C_L \sin \phi - C_D \cos \phi)\ \Delta r$$

$$= \frac{b}{2}\ \rho c \sum_{1}^{m} r_n\ (U_{p_n}\ C_{L_n} - U_{T_n}\ C_{D_n})\ U_n\ \Delta r$$

$$= 1/2\ \pi\ \rho\ \sigma\ R^5\ \Omega^2 \sum_{1}^{m} \bar{r}_n\ (\lambda_{r_n}\ C_{L_{\bar{n}}}\ \bar{r}_n\ C_D) \times \sqrt{\lambda^2_{r_n} + \bar{r}_n^2}\ .\ (\Delta \bar{r}_n)$$

$$C_Q = \frac{Q}{\pi\ \rho\ R^5 \Omega^2}$$

$$\frac{C_Q}{\sigma} = 1/2 \sum_{1}^{m} \bar{r}_n\ (\lambda_{r_n}\ C_L - \bar{r}_n\ C_{D_n}) \times \sqrt{\lambda^2_{r_n} + \bar{r}^2_n}\ .\ (\bar{r}_n)$$

In autorotative flight Q, and therefore C_Q/σ , = 0

Determination of λ_r

Since $\lambda_r = U_p/\Omega R$, the determination of λ_r for a particular rotor configuration at a given speed, Ω, fixed U_p, the component of air velocity perpendicular to an element of the rotor cone. As an approximation, since $\cos \beta_o = 1$, U may be taken as perpendicular to the plane of no feathering (PNF).

λ_r is determined by using the following formulae and chart:

(1) $$f = \frac{\sigma \varrho}{8 \bar{r} \lambda_d^2} (\bar{r} C_L + \lambda_r C_D) \sqrt{\lambda_r^2 + \bar{r}^2}$$

(2) $$\lambda_r = \lambda_d \sqrt{\frac{f}{F}}$$

(3) $$\frac{C_Q}{\sigma} = 1/2 \sum (\bar{r}_n \lambda_{r_n} - \bar{r}_n C_{D_n}) \sqrt{\lambda^2_{r_n} + \bar{r}^2_n} (\Delta \bar{r}_n) = 0$$

(4) Glauert-Lock Experimental Curve 1/f versus 1/F (Reference 9, Page 23)

In Equation (1), λ_d and $\bar{r}$ are assumed known. That is to say, the descent velocity, V, the rotor speed, Ω, the rotor radius, R, and the station radius, r, are known or assumed.

A value of λ_r is then assumed. This fixes ϕ and thus the angle of attack $\alpha = \theta + \phi$ and, in turn, C_L and C_D. Thus, f can be calculated. This yields a value of F from the curve, 1/f versus 1/F (4). Then Formula (2) is used to calculate λ_r, and comparison is made with the assumed λ_r. If agreement is not within one per cent, a new value of λ_r is assumed, and the process is repeated.

This procedure is carried out at each station along the rotor blade until each station has a value of λ_r associated with it.

Formula (3) is then used to calculate the torque acting about the rotor axis of rotation from aerodynamic forces on the rotor blades. For autorotative flight, this torque must be zero.

If the torque thus calculated does not sum to zero, a new assumption must be made for θ, and the whole process repeated until finally the torque sums to zero.

Lastly, the values used to sum torque to zero are inserted in the following formula to determine the thrust:

$$T = 1/2\ \pi\ \rho\ \sigma\ \Omega^2\ R^4 \sum_{1}^{m} (\bar{r}\ C_L + \lambda_r\ C_D) \sqrt{\lambda_r^2 + \bar{r}^2} \cdot \Delta r_n$$

NOTE:

Tip loss factor can be accounted for by subtracting three per cent of the blade radius from the length of element or station at the blade tip. Thus, has been calculated for a particular rotor in autorotation at a given speed, the axial component (U_p) of air relative to the rotor at each blade element, and the total thrust corresponding to this velocity distribution.

Gliding Flight Analysis

The ROTOCHUTE equations of motion are:

$$mV\dot{\gamma} = T \cos \alpha_R - H \sin \alpha_R - W \cos \gamma - 1/2\ \rho\ V^2 f \sin \alpha_F + 1/2\ \rho\ V^2\ C_{L_\alpha}\ (\alpha_F + \delta_t)\ S_t$$

$$m\dot{V} = -W \sin \gamma - T \sin \alpha_R - H \cos \alpha_R - 1/2\ \rho\ V^2\ f \cos \alpha_F - 1/2\ V^2\ C_{L_\alpha}\ (\alpha_F + \delta_t)\ S_t \sin (\alpha_F + \delta_t)$$

$$I\dot{q} = -Th \sin B_{1Z} + Hh \cos B_{1S} + E_y \sin a_1 + 1/2\ \rho\ V^2 f + (\partial M_t / \partial \alpha)\ (\alpha_F + \delta_t)$$

These equations are written in terms of forces and moments which lie in a wind axis system. Use of Euler's equations permits moments of inertia to be evaluated relative to the vehicle body axes. Since these are steady-state equations, velocities perpendicular to the direction of motion along the wind (X) axis are zero. Likewise, it is assumed that only pitching moments exist - that there are no rolling and yawing motions.

The tail effects are included in these equations. In practice, the drag term in the X-direction is ignored.

Using data from NACA Report No. 1266, and simultaneously solving the equations for stalled and unstalled tail configurations (see "Special Derivations"), the angular attitudes of the ROTOCHUTE are found for various assumed values of flat plate area; for different values of advance ratio; and for 8- and 10-foot rotors.

The various steps in the procedure are given below. Because the charts found in Report No. 1266 were on too small a scale to be used accurately in the range of interest, it was necessary to program the relevant formula for the IBM computer and plot the results in carpet-plot form. Thereafter, the iterative process of solving the simultaneous equations was carried out on the Burroughs computer. The graphs B_{1Z}, γ, and θ plotted separately against μ are the results.

Optimum glide ($\gamma = -0.5$ radians; i.e. 28.5°) is indicated at about $\mu = 0.14$.

Specific Derivations

Forward Flight - Steady-State Analysis

In the Steady-State Analysis, the following relations are developed from the three steady-state equations above. The acceleration terms on the left-hand side have been omitted, since the analysis is for steady-state.

$$C_H = -\left(C_W \frac{\sin\gamma}{\cos\gamma} + C_T \tan\alpha_R + 1/2\,\mu^2 C_f \frac{\cos\alpha_F}{\cos^2\alpha_R} \right)$$

B_{1Z} (for stalled tail angles)

$$= \frac{\frac{h}{R}C_H + \frac{E_\gamma}{\pi\rho\Omega^2R^5}a_1 + \frac{1}{2}\mu^2 C_F \frac{\ell}{R}\frac{1}{\cos^2\alpha_R} + \frac{1}{2}\frac{\rho\mu^2(\Omega R)^2 C_{l_\alpha}\alpha_t S_t \ell_t}{\cos^2\alpha_R \pi\rho\Omega^2R^5}}{\frac{h}{R}C_T}$$

B_{1Z} (for unstalled tail angles)

$$= \frac{\frac{h}{R} C_H + \frac{E_Y}{\pi \rho \Omega^2 R^5} a_1 + \frac{1}{2}\mu^2 C_F \frac{\ell}{R} \frac{1}{\cos^2 \alpha_R} + \frac{\mu^2 C_{l_\alpha} S_t \ell_{S_t}}{2\pi R^3} \frac{\delta_t + \alpha_R}{\cos^2 \alpha_R}}{\frac{h}{R} C_T - \frac{\mu^2 C_{l_\alpha} S_t \ell_{S_t}}{2\pi R^3} \cdot \frac{1}{\cos^2 \alpha_R}}$$

C_T (for stalled angels)

$$= C_H \tan \alpha_R + C_W \frac{\cos \gamma}{\cos \alpha_R} + \frac{1}{2}\mu^2 C_F \frac{\sin \alpha_F}{\cos^3 \alpha_R} \; * \; \frac{1}{2} \frac{\mu^2 C_{l_\alpha} S_t}{\pi R^2}$$

C_T (for unstalled angles)

$$= C_H \tan \alpha_R + C_W \frac{\cos \gamma}{\cos \alpha_R} + \frac{1}{2}\mu^2 C_F \frac{\sin \alpha_F}{\cos^3 \alpha_R} - \frac{\mu^2 C_{l_\alpha} S_t}{2\pi R^2} (\alpha_f + \delta_t)$$

(* Change sign for negative stall)

Collective Flare Study

This following study was performed to investigate the comparative merits of performing a collective flare maneuver after glide and cyclic flare versus performing the collective flare from vertical descent. Results indicate that if flare is performed from vertical descent, the rotor must be larger and heavier.

The minimum vertical rate of descent of a rotor-supported vehicle at sea level has been determined experimentally in a variety of tests to be:

$$V_V \cong 25 \sqrt{W/A}$$

The rotor kinetic energy required to decelerate the vehicle from the descent speed given by the above to zero ground contact velocity can be estimated by a modified form of the simple analysis given in Reference 10.

Following this analysis, the power required by the rotor at sea level is given by:

$$P = \frac{14.5}{M} \cdot nW \sqrt{n\ (W/A)}$$

Step-by-step calculations indicate that rotor stall occurs if an attempt is made to maintain a constant flare load factory by increasing blade collective pitch while rotor rotational speed is decreasing. The calculations indicate that a more reasonable assumption is that rotor thrust coefficient remains constant, as indicated in Reference 11, while rotor load factor decreases linearly to a value of unity at the end of flare as rotational speed decreases, at which point the decleration becomes zero.

The load factor is expressed by:

$$n = n_o - (n_o - 1)\ \ t/t_f$$

and deceleration is: $a = g\ (n - 1)$

Then: $$V_f - V_o = \int_o^{t_f} a\ dt = 1/2\ (n_o - 1)\ g\ t_f$$

taking $V_f = 0$

$$t_f = -\frac{V_o}{1/2\ (n_o - 1)\ g} \approx -\frac{1.56}{n_o - 1}\sqrt{W/A}$$

where downward initial velocity V_o is considered negative.

The rotor kinetic energy (KE) required for flare per pound of vehicle weight is:

$$\frac{KE}{W}_{req} = \int_o^{t_f} \frac{P}{W} \cdot dt$$

$$= \int_o^{t_f} \frac{14.5}{M}\sqrt{\frac{W}{A}}\ n^{3/2}\ dt$$

$$= \frac{9.05}{M}\ \frac{W}{A}\ \frac{n_o^{5/2} - 1}{(n_o - 1)^2}$$

Increasing rotor initial load factor decreases the kinetic energy required for flare. However, the rotor stall considerations place an upper limit on initial load factor. It is assumed that an initial load factor of two can be achieved in the present case. Assuming a rotor figure of merit of 0.70, the required kinetic energy becomes:

$$\frac{KE\ req}{W} = 60\ \frac{W}{A} \tag{5}$$

Rotor kinetic energy is expressed by:

$$KE = 1/2\ I_p\Omega^2$$

$$= 1/6\ m_b\ (\Omega R)^2 \text{ for a uniform blade}$$

It is assumed that two-thirds of the rotor kinetic energy can be used before rotor stalling occurs.

$$\therefore\ \frac{KE}{W}\ \text{available} = 1/9\ .\ \frac{W_b}{W}\ .\ \frac{1}{g}\ (\Omega R)^2 \tag{6}$$

The ratio (W_b/W) is expressed in Reference 12:

$$\frac{W_b}{W} = \frac{.00132}{W^{1.89}}\left[\sigma\ \frac{W}{A}\ R^4(\Omega R)^2\ (c\ \frac{t}{c} + .21)\right]^{.89} \tag{7}$$

for $15 \leq$ blade aspect ratio ≤ 20. The rotor blade weight is assumed to be one-half rotor group weight.

A rotor weight comparison between gliding and vertical autorotative descents may now be made on the following basis. It is assumed that a zero contact velocity landing can be made from a gliding descent with a rotor having a disc loading of five. This assumption is justified by helicopter experience and by analytical investigations. Then the required rotor weight increase to permit a zero contact velocity landing from a vertical descent is calculated using Equations (5), (6), and (7). Vehicles of 100, 1000, and 10,000 pounds gross weight are considered.

The gliding rotor is assumed to have a disc loading of 5.0, four blades, a solidity σ of .080, and a thickness-chord ratio t/c of 0.12. The vertical descent rotors are assumed to have disc loadings of 5.0, 3.0, 2.0, and 1.0, two blades, a solidity of .032, and a thickness-chord ratio of 0.12.

All rotors in the comparison satisfy the following conditions:

a. Blade aspect ratio ≤ 20: Satisfies Equation (7)

b. Before flare, C_T/σ max ≤ 0.10: Insures that rotor stall does not occur during flare.

c. Rotor solidity is a minimum within the limits set by Conditions (a) and (b): Corresponds to minimum rotor weight for a given disc loading and tip speed, since (W_b/W) is proportional to $\sigma^{.89}$.

d. Rotor tip speed is less than 900 feet/second to avoid serious compressibility effects.

NOTE

The number of blades is determined by Conditions (a), (b), and (c). Since the vertical descent rotors in general operate at higher tip speeds than the gliding rotor, their thrust coefficients are less, and they can use a lower solidity, as indicated by Condition (b). Then Condition (a) requires the minimum number of blades, i.e. two.

Solidity and tip speed can be chosen on the above basis, since vertical descent velocity is relatively independent of C_T/σ, as shown by Figure 6-11, Page 136, of Reference 13. For values of C_T/σ between .06 and .10, the corresponding values of C_{D_R} are comparable to the value of 1.16 for C_{D_R} implied in the equation of the present analysis. Torque Equilibrium is satisfied by an appropriate choice of collective pitch angle, as shown by Equations (71) and (72), Page 208, Reference 13.

The results of the calculations are as follows:

Disc Loading 5 Pounds/Sq Ft

			Gliding (σ = .080)		Vertical (σ = .032)	
W	A	R	c	$(W_b/W)(\Omega R)^{-1.78}$	c	$(W_b/W)(\Omega R)^{-1.78}$
100	20	2.5	.156	$.69 \times 10^{-6}$	.125	$.29 \times 10^{-6}$
10,000	200	8.0	.5	.65	.40	.27
10,000	2,000	25	1.56	1.05	1.25	.42

The rotor rotational speed required for flare is found by substituting W_b/W in Equation (6) and equating to Equation (5), e.g., for W = 100 pounds,

$$1/9 \times .29 \times 10^{-6} \quad (\Omega R)_{req}^{3.78} \quad \frac{1}{g} = 60 \times 5$$

$$(\Omega R)_{req} = 1090 \text{ ft/sec}$$

This value is impractical aerodynamically, but will be used to establish a weight comparison curve. At this tip speed, for the vertical case,

$$W_{b_V}/W = .29 \times 10^{-6} \quad (\Omega R)^{1.78}$$

$$= .074$$

$$\therefore \quad W_{R_V}/W = .148$$

For the gliding case, the tip speed can be taken as 500 ft/sec and,

$$W_{b_G}/W = .044$$

$$W_{R_G}/W = .088$$

Results are as follows:

		Vertical		Gliding		
W	$(\Omega R)_{req}$	W_{b_V}/W	W_{R_V}/W	W_{b_G}/W	W_{R_G}/W	W_{R_V}/W_{R_G}
100	1090	.074	.148	.044	.088	1.68
1,000	1110	.071	.142	.042	.084	1.69
10,000	986	.090	.180	.067	.134	1.34

The iteration required to include the increase in gross weight is not performed in this first approximation.

Disc Loading 3 Pounds/Sq Ft, σ = .032

W	A	R	c	$(W_b/W)(\Omega R)^{-1.78}$	R_V/R_G
100	33.3	3.26	.163	.50 x 10^{-6}	1.30
1,000	333	10.3	.52	.44	1.29
10,000	3333	32.6	1.63	.76	1.30

W	$(\Omega R)_{req}$	W_{bV}/W	W_{RV}/W	W_{RV}/W_{RG}
100	820	.077	.154	1.75
1,000	850	.072	.144	1.71
10,000	740	.097	.194	1.45

Disc Loading 2 Pounds/Sq Ft, σ = .032

W	A	R	c	$(W_b/W)(\Omega R)^{-1.78}$	R_V/R_G
100	50	4.0	.2	.715 x 10^{-6}	1.6
1,000	500	12.6	.63	.675	1.58
10,000	5,000	40	2.0	1.20	1.6

W	$(\Omega R)_{req}$	W_{bV}/W	W_{RV}/W	W_{RV}/W_{RG}
100	672	.077	.154	1.75
1,000	682	.075	.150	1.79
10,000	586	.101	.202	1.51

Disc Loading 1 Pound/Sq Ft, σ = .032

W	A	R	c	$(W_b/W)(\Omega R)^{-1.78}$	R_V/R_G
100	100	5.65	.282	1.36 x 10^{-6}	2.26
1,000	1,000	17.8	.89	1.36	2.23
10,000	10,000	56.5	2.82	2.62	2.26

W	$(\Omega R)_{req}$	W_{b_V}/W	W_{R_V}/W	W_{R_V}/W_{R_G}
100	470	.078	.156	1.77
1,000	470	.078	.156	1.86
10,000	396	.110	.220	1.64

The results are plotted in Figure 13.

B. STABILITY AND CONTROL - SUBSONIC AXIAL FLIGHT

Section II, ANALYTICAL INVESTIGATIONS, outlines the methods used to determine the conditions for steady-state equilibrium. Because of non-uniform inflow in axial subsonic flight, a strip analysis was necessary. In forward subsonic flight, the equivalent condition was derived from NACA Report TR 1266 and equilibrium equations.

With these steady-state conditions as background information, it is now possible to investigate dynamic stability. Fundamental to this investigation are the perturbation equations of the system, written in terms of force and moment derivatives which are, in turn, written in terms of flapping derivatives.

The first step is to determine the flapping derivatives for axial flight. The derivation, by co-ordinate transformations and Lagrangian methods, is presented below under "Flapping Derivatives".

Next, the force and moment derivatives, as indicated in "Force and Moment Derivatives", are found from elementary considerations, using the method of Bryan, and are finally expressed terms of the flapping derivatives. Certain of these derivatives are with respect to control variables, i.e. A_{1Z} and B_{1Z}, the harmonic coefficients of β_S and express the contribution to the forces and moments of control input.

When a tail is added to the ROTOCHUTE, the assumption is made that it does not materially influence the ROTOCHUTE forces when a change in a variable takes place. However, its effect on the ROTOCHUTE moment is taken to be significant, and a derivation for this derivative is included.

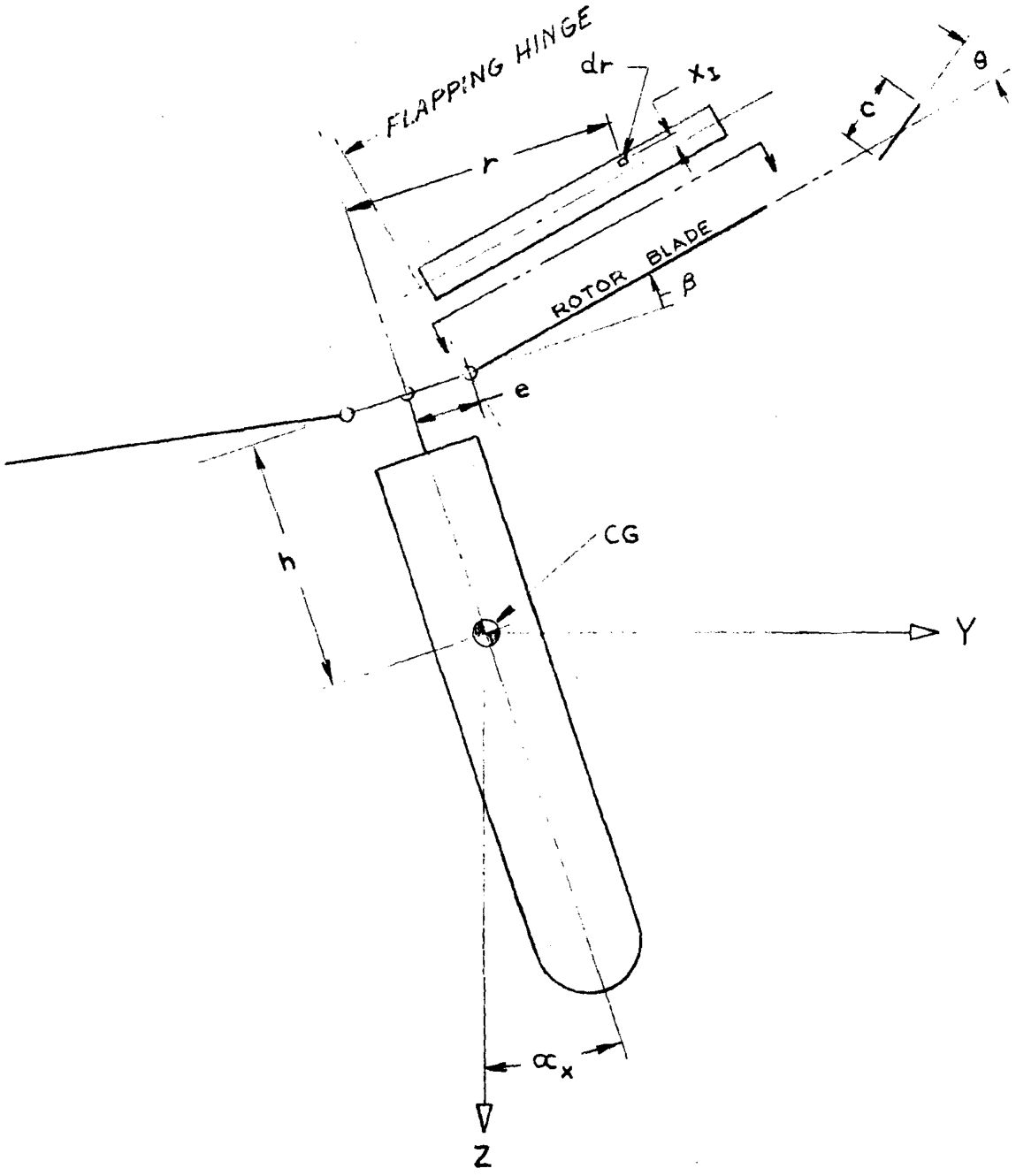

ROTOCHUTE PARAMETERS

FIGURE 76

NOTE OF INTEREST:

With the successful derivation of Forces and Moment Derivatives, the axial flight analysis, for the purposes of analyzing the ROTOCHUTE stability through the total flight spectrum, is complete.

However, with these derivations, it is now possible to perform an analysis for axial flight alone. The perturbation equations for axial flight can be written and solved, by assuming solutions of the form m = exp (pt), where p is complex. The perturbation equations, in terms of the number of variables of interest, can be reduced to a characteristic equation soluble by numerical methods. Finally, the modes of motion can be identified, this being the last step necessary for a parametric study.

Flapping Derivatives (Reference, Figure 76)

By suitable co-ordinate transformations and Lagrangian methods, the equilibrium of the ROTOCHUTE rotor about the flapping axis is expressed by:

$$I_1\ddot{\beta} + \left\{\Omega^2(I_1 + e S_b) + K_\beta\right\}\beta + \Omega(I_1 + e S_b)\dot{\theta} + \Omega^2(I_R + S_\theta)\theta$$
$$+ I_R\ddot{\zeta} + \Omega^2 I_R \zeta + (I_1 + e S_b)\ddot{n} + \Omega^2(I_1 + e S_b)n$$
$$= \frac{1}{b}(r - e)\left[\Delta L \cos(\phi + \Delta\phi) + \Delta D \sin(\phi + \Delta\phi)\right]$$

Making a harmonic substitution for β; using the definition of ζ and n; remembering that the ROTOCHUTE blades do not feather, ($\theta = A_0$); and substituting for the right-hand side of this equation as indicated in "Special Derivations", three equations may be derived from this single equation. That is, steady terms and the coefficients of sin Ψ and cos Ψ are equated to give the following equations:

$$\Omega^2(I_R + e S_\theta)A_0 + \left[\Omega^2(I_1 + e S_b) + K_\beta\right] a_0 = \frac{1}{2b}\pi\rho\sigma\Omega^2 R^5\left\{H_2 - H_1\zeta + \Delta A_0(M_2 - M_1\zeta)\right\}$$

$$K_1 a_1 + K_2 b_1 - q\left\{\frac{2I_R}{\frac{1}{2}b\pi\rho\sigma\Omega R^5} - \frac{1}{\Omega}(A_3 - A_2\zeta)\right\} + P\left\{\frac{2(I_1 + e S_b)b}{\frac{1}{2}\pi\rho\sigma\Omega R^5} + \frac{n}{\Omega}(B_2 - B_1\zeta)\right\}$$
$$+ \frac{\dot{y}}{\Omega R}(B_2 - B_1\zeta) + \alpha_x\frac{V}{\Omega R}(B_2 - B_1\zeta) - \dot{x}\frac{a_0}{\Omega R}(A_2 - A_1\zeta)$$
$$+ a_0\lambda_d\alpha_y(A_2 - A_1\zeta) = 0$$

$$-K_2 a_1 + K_1 b_1 - q\left\{\frac{2\Omega(I_1+eS_b)b}{\frac{1}{2}\pi\rho\sigma\Omega^2R^5} + \frac{n}{\Omega}(B_2 - B_1\bar{\xi})\right\} - \left\{\frac{2I_R\Omega b}{\frac{1}{2}\pi\rho\sigma\Omega^2R^5} - \frac{1}{\Omega}(A_3 - A_2\bar{\xi})\right\}p$$

$$+\dot{y}\frac{a_0}{\Omega R}(A_2 - A_1\bar{\xi}) + a_0\lambda_d\alpha_x(A_2 - A_1\bar{\xi}) + \frac{1}{\Omega R}(B_2 - B_1\bar{\xi})\dot{x} - \frac{V}{\Omega R}(B_2 - B_1\bar{\xi})\alpha_y = 0$$

$$a_1(K_1^2 + K_2^2) = q\left[-\left\{\frac{2\Omega b(I_1+eS_b)}{\frac{1}{2}\pi\rho\sigma\Omega^2R^5} + \frac{n}{\Omega}(B_2 - B_1\bar{\xi})\right\}K_2\right.$$

$$\left.+\left\{\frac{2I_R\Omega b}{\frac{1}{2}\pi\rho\sigma\Omega^2R^5} - \frac{1}{\Omega}(A_3 - A_2\bar{\xi})\right\}K_1\right]$$

$$+p\left[-\left\{\frac{2I_R\Omega b}{\frac{1}{2}\pi\rho\sigma\Omega^2R^5} - \frac{1}{\Omega}(A_3 - A_2\bar{\xi})\right\}K_2\right.$$

$$\left.-\left\{\frac{2\Omega b(I_1+eS_b)}{\frac{1}{2}\pi\rho\sigma\Omega^2R^5} + \frac{n}{\Omega}(B_2 - B_1\bar{\xi})\right\}K_1\right]$$

$$+\dot{x}\left\{(B_2 - B_1\bar{\xi})\frac{K_2}{\Omega R} + (A_2 - A_1\bar{\xi})\frac{a_0K_1}{\Omega R}\right\}$$

$$+\dot{y}\left\{(A_2 - A_1\bar{\xi})\frac{a_0K_2}{\Omega R} - (B_2 - B_1\bar{\xi})\frac{K_1}{\Omega R}\right\}$$

$$+\alpha_x\left\{(A_2 - A_1\bar{\xi})K_2a_0\lambda_d - (B_2 - B_1\bar{\xi})K_1\lambda_d\right\}$$

$$-\alpha_y\left\{(B_2 - B_1\bar{\xi})K_2\lambda_d + (A_2 - A_1\bar{\xi})K_1a_0\lambda_d\right\}$$

$$+A_{1s}\left\{-K_2K_1 + K_1\left[M_2 - M_1\bar{\xi} - \bar{\xi}(A_2 - A_1\bar{\xi})\right]\right\}$$

$$+B_{1s}\left\{-K_2\left[M_2 - M_1\bar{\xi} - \bar{\xi}(A_2 - A_1\bar{\xi})\right] - K_1^2\right\}$$

from which are available immediately the flapping derivatives:

$$\frac{\partial a_1}{\partial \Delta}$$

where:

$$\Delta = q, p, \dot{x}, \dot{y}, \alpha_x, \alpha_y$$

Lateral derivatives can be found from the relationships below which follow from symmetry:

$$\frac{\partial b_1}{\partial p} = \frac{\partial a_1}{\partial q} \qquad \frac{\partial b_1}{\partial q} = -\frac{\partial a_1}{\partial p}$$

$$\frac{\partial b_1}{\partial \alpha_y} = \frac{\partial a_1}{\partial \alpha_y} \qquad \frac{\partial b_1}{\partial \alpha_y} = -\frac{\partial a_1}{\partial \alpha_x}$$

$$\frac{\partial b_1}{\partial \dot{x}} = \frac{\partial a_1}{\partial \dot{y}} \qquad \frac{\partial b_1}{\partial \dot{y}} = -\frac{\partial a_1}{\partial \dot{x}}$$

Special Derivations

Lift and Torque Forces - Axial Flight

The steady-state lift force is expressed by $(L \cos \phi + D \sin \phi)$ and the torque force by $(L \sin \phi - D \cos \phi)$ where L is the lift on a blade element. It is necessary to express parametrically the incremented lift and torque forces.

$$(L + \Delta L) \cos (\phi + \Delta \phi) + (D + \Delta D) \sin (\phi + \Delta \phi)$$

and $(L + \Delta L) \sin (\phi + \Delta \phi) - (D + \Delta D) \cos (\phi + \Delta \phi)$

From: $L = \frac{b}{2} \rho c C_L U^2 dr$

is developed:

$$L + \Delta L = \frac{b}{2} \rho c (C_L + \Delta C_L) (U + \Delta U)^2 dr$$

Also, $\Delta C_L = C_{L_\alpha} (\Delta \alpha)$

$$\Delta \alpha = \Delta \phi + \Delta \theta = \Delta \tan^{-1} \frac{U_P}{U_T} + \Delta \theta = \frac{U_T (\Delta U_P) - U_P (\Delta U_T)}{U_P^2 + U_T^2}$$

Finally:

$$U + \Delta U = \sqrt{(U_p + \Delta U_p)^2 + (U_T + \Delta U_T)^2}$$

Thus,

$$\cos(\phi + \Delta\phi) \cong \cos\phi - \Delta\phi \sin\phi; \ \Delta\phi \text{ small}$$

$$\cong \frac{U_T}{\sqrt{U_p^2 + U_T^2}} - \frac{U_p[U_T(\Delta U_p) - U_p(\Delta U_T)]}{(U_p^2 + U_T^2)^{3/2}}$$

Similarly:

$$\sin(\phi + \Delta\phi) \cong \frac{U_p}{\sqrt{U_p^2 + U_T^2}} + \frac{U_T[U_T(\Delta U_p) - U_p(\Delta U_T)]}{(U_p^2 + U_T^2)^{3/2}}$$

Substituting in $(L + \Delta L)$ for ΔC_L (i.e. for $\Delta\alpha$) and for $(U + \Delta U)$, and for $\cos(\phi + \Delta\phi)$ and $\sin(\phi + \Delta\phi)$; multiplying out and ignoring non-linearities, the following is derived.

$$(L + \Delta L)\cos(\phi + \Delta\phi) + (D + \Delta D)\sin(\phi + \Delta\phi)$$

$$= \frac{\frac{1}{2}\rho bc}{\sqrt{U_p^2 + U_T^2}} \Big\{ (C_L U_T + C_D U_p)(U_p^2 + U_T^2)$$

$$+ (\Delta U_p)\left[C_L U_p U_T + C_D U_T^2 + 2C_D U_p^2 + C_{L_\alpha} U_T^2 + C_{D_\alpha} U_p U_T\right]$$

$$+ (\Delta U_T)\left[C_D U_p U_T + C_L U_p^2 + 2 C_L U_T^2 - C_{L_\alpha} U_p U_T - C_{D_\alpha} U_p^2\right]$$

$$+ \Delta\theta \ (U_p^2 + U_T^2)\left[U_T C_{L_\alpha} - U_p C_{D_\alpha}\right] \Big\} \ dr$$

$$(L + \Delta L)\sin(\phi + \Delta\phi) - (D + \Delta D)\cos(\phi + \Delta\phi)$$

$$= \frac{\frac{1}{2}\rho bc}{\sqrt{U_p^2 + U_T^2}} \Big\{ (C_L U_p - C_D U_T) \ (U_p^2 + U_T^2)$$

$$+ (\Delta U_p)\left[C_L U_T^2 + 2 C_L U_p^2 - C_D U_p U_T + C_{L_\alpha} U_p U_T - C_{D_\alpha} U_T^2\right]$$

$$+ (\Delta U_T)\left[C_L U_p U_T - C_D U_p^2 - 2 C_D U_T^2 - C_{L_\alpha} U_p^2 + C_{D_\alpha} U_p U_T\right]$$

$$+ \Delta\theta \ (U_p^2 + U_T^2)\left[U_p \ C_{L_\alpha} - U_T C_{D_\alpha}\right]\Big\} \ dr$$

The final step is to non-dimensionalize the results.

Thus,

$$\text{Lift Force } (L + \Delta L)\cos(\phi + \Delta\phi) + (D + \Delta D)\sin(\phi + \Delta\phi)$$
$$= 1/2\ \pi\rho\sigma\ \Omega R^3\left\{H\Omega R + A(\Delta U_p) + B(\Delta U_T) + M\Omega R(\Delta\theta)\right\}\Delta\bar{r}$$

$$\text{Torque Force } (L + \Delta L)\sin(\phi + \Delta\phi) - (D + \Delta D)\cos(\phi + \Delta\phi)$$
$$= 1/2\ \pi\rho\sigma\ \Omega R^3\left\{J\Omega R + C(\Delta U_p) + D(\Delta U_T) + N\Omega R(\Delta\theta)\right\}\Delta\bar{r}$$

where the coefficients A, B, C, D, H, J, M, and N are as defined under "Force and Moment Derivatives".

Axial Flight

ΔU_p and ΔU_T - Lift and Drag on a Blade Element

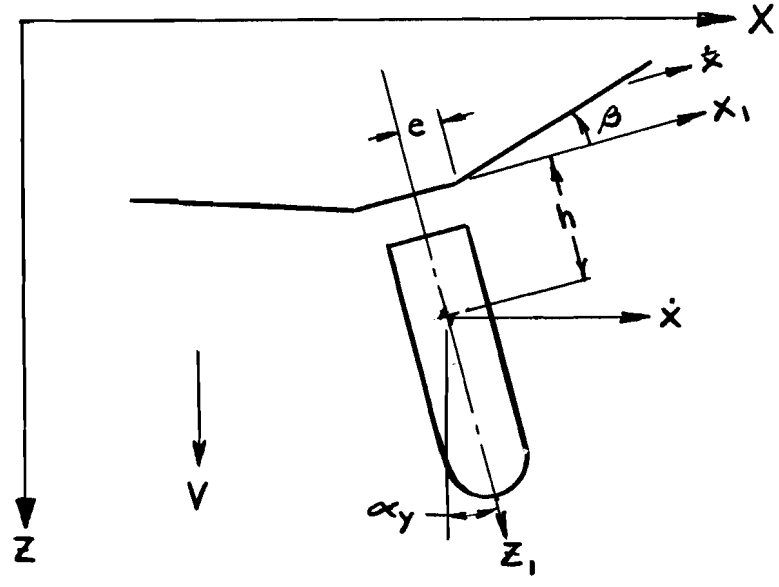

FIGURE 77

Perturbation Velocities (Reference, Figure 77)

The velocity of an element of rotor blade, relative to axes (x, y, and z) fixed in space, when the body dimensions h, r, and e and the angular motions (including associated velocities) β, α_x, α_y, and Ψ are accounted for, are (after small angle assumptions):

$$\dot{\bar{X}} = \dot{X} - V\alpha_y - h_q - r\,\beta_q + \Omega r \sin\Psi$$

$$\dot{\bar{y}} = \dot{y} + V\alpha_x + h_p + r_1\,\beta_p + \Omega r \cos\Psi$$

$$\dot{\bar{Z}} = V_v - r_1\,\dot{\beta} - \Omega r\left\{\alpha_y \sin\Psi - \phi\cos\Psi\right\} + r\left\{q\cos\Psi + p\sin\Psi\right\} + \dot{Z}$$

These velocities, except for a sign change, are also the orthogonal components of fluid relative to the blade element. Interest is mainly directed towards the fluid velocity components normal and tangential to the rotor surface of motion, since it is from these components the lift and drag forces on the blade element are calculated.

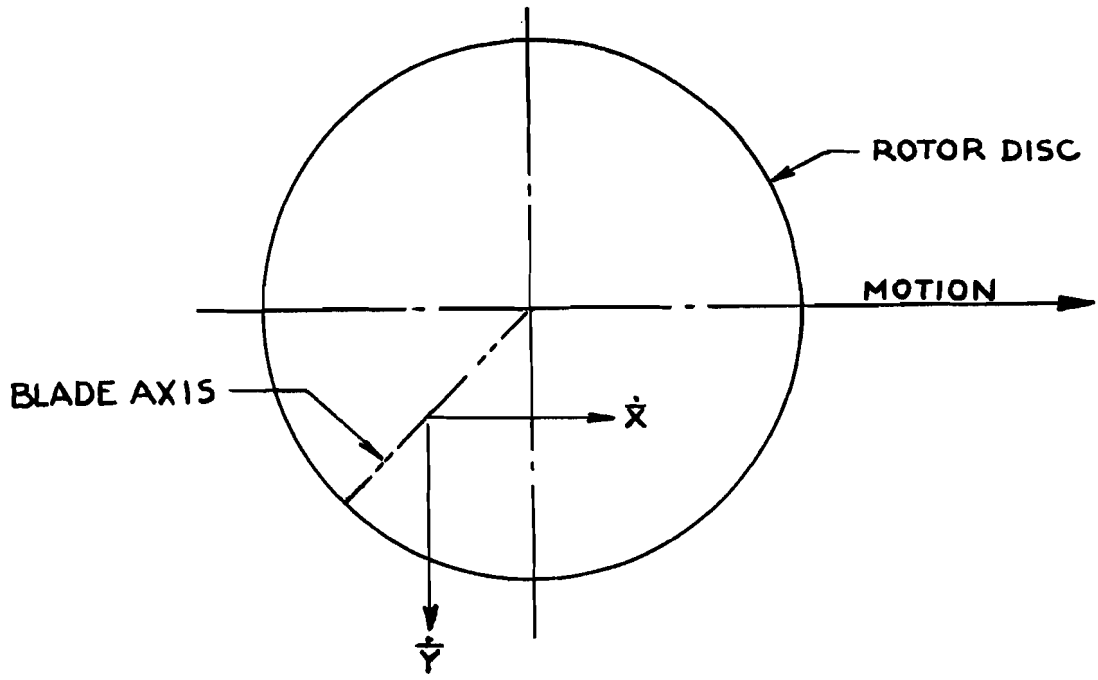

FIGURE 78

Therefore, (Reference Figure 78) taking components along and perpendicular to the rotor blade:

$$U_P + \Delta U_P = \dot{z} - v - (\dot{x}\cos\psi - \dot{y}\sin\psi)(\beta + \eta) + (\dot{x}\sin\psi + \dot{y}\cos\psi)\zeta$$

$$U_T + \Delta U_T = \dot{x}\sin\psi + \dot{y}\cos\psi$$

Substituting in the above for $\dot{x}$, $\dot{y}$, and $\dot{z}$, for β, η, and ζ, and ignoring non-linearities, the vertical increment of velocity, and the rate of control input, the following expressions are derived:

$$\Delta U_P = \cos\psi\,[\Omega b_1 (r-e) + q(r + h a_0) - \dot{x} a_0 + V a_0 \alpha_y + e\Omega A_{1s}]$$
$$+ \sin\psi\,[-\Omega a_1 (r-e) + p(r + h a_0) + \dot{y} a_0 + V a_1 \alpha_x + e\Omega B_{1s}]$$

$$\Delta U_T = \cos\psi\,[\dot{y} + V\alpha_x + \{h + (r-e)a_0\}p]$$
$$+ \sin\psi\,[\dot{x} - V\alpha_y - \{h + (r-e)a_0\}q]$$

Subsection 1: Force and Moment Derivatives - Axial Flight Analysis

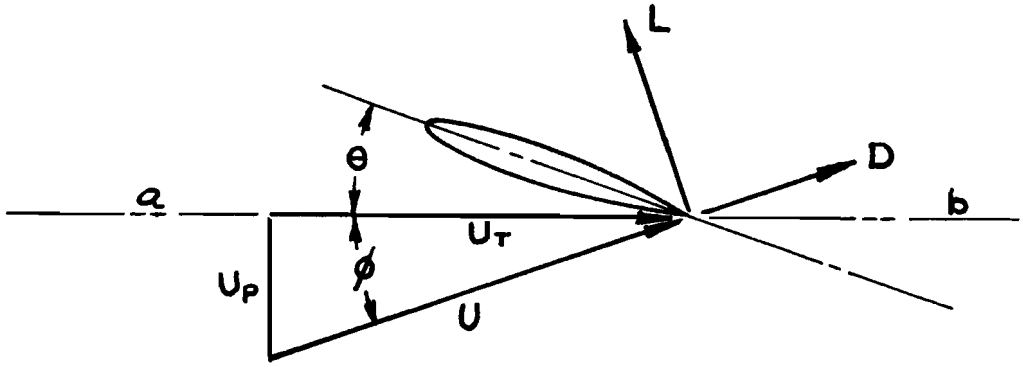

FIGURE 79

Steady State

Let L and D be the lift and drag forces on a blade element of area $c \cdot \Delta r$

Then $L = \frac{b}{2} \rho c C_L U^2$

and $D = \frac{b}{2} \rho c C_D U^2$

Let T = aerodynamic force on blade element normal to surface of motion (i.e. perpendicular to a and b in Figure 79).

and H = aerodynamic force in the surface of motion (i.e. along a and b)

then $T = L \cos \phi + D \sin \phi$

and $H = L \sin \phi - D \cos \phi$

$$T_x = T \sin \beta \cos \psi + H \sin \psi - T \alpha y$$

$$T_y = -T \sin \beta \sin \psi + H \cos \psi + T \alpha x$$

$$T_z = -T \cos \beta$$

Perturbation

$$T_x + \Delta T_x = (T + \Delta T) \sin \beta \cos \psi + (H + \Delta H) \sin \psi - (T + \Delta T) \alpha y$$

where

$$T + \Delta T = (L + \Delta L) \cos (\phi + \Delta \phi) + (D + \Delta D) \sin (\phi + \Delta \phi)$$

$$H + \Delta H = (L + \Delta L) \sin (\phi + \Delta \phi) - (D + \Delta D) \cos (\phi + \Delta \phi)$$

It can be shown (see "Special Derivations - Lift and Torque Forces") that:

$$(L + \Delta L) \cos (\phi + \Delta \phi) + (D + \Delta D) \sin (\phi + \Delta \phi)$$
$$= \tfrac{1}{2} \pi \rho \sigma \Omega R^3 \left\{ H \Omega R + A (\Delta U_P) + B (\Delta U_T) \Delta \bar{r} \right.$$

and

$$(L + \Delta L) \sin(\phi + \Delta\phi) - (D + \Delta D) \cos(\phi + \Delta\phi)$$
$$= \tfrac{1}{2} \pi \rho \sigma \Omega R^3 \left\{ J\Omega R + C(\Delta U_P) + D(\Delta U_T) \Delta \bar{r} \right.$$

Coefficients A, B, C, D, J, and H are defined at the end of this section. It can also be shown (see "Special Derivations") that:

$$\Delta U_P = \cos\psi \left\{ \Omega b_1 (r-e) + (r + h a_0) q - \dot{x} a_0 + V a_0 \alpha_y + e \Omega A_{1S} \right\}$$
$$+ \sin\psi \left\{ -\Omega a_1 (r-e) + (r + h a_0) p + \dot{y} a_0 + V a_0 \alpha_x + e \Omega B_{1S} \right\} - (r-e)\dot{a}_0$$

$$\Delta U_T = \cos\psi \left[\dot{y} + V\alpha_x + \{h + (r-e) a_0\} p \right]$$
$$+ \sin\psi \left[\dot{x} - V\alpha_y - \{h + (r-e) a_0\} q \right]$$

Also

$$\Delta T_X = (T + \Delta T) \sin\beta \cos\psi + (H + \Delta H) \sin\psi - (T + \Delta T)\ \alpha_y$$
$$- T \sin\beta \cos\psi - H \sin\psi + T\ \alpha_y$$

For small flapping angles: $\sin\beta \simeq \beta = a_0 - a_1 \cos\psi - b_1 \sin\psi$

Substitute for $(T + \Delta T)$ and $(H + \Delta H)$ and average around the azimuth to obtain $(\Delta T_X)_{AV.}$ using integrals

$$\int_0^{2\pi} \sin\psi\, d\psi = \int_0^{2\pi} \cos\psi\, d\psi = \int_0^{2\pi} \sin\psi \cos\psi\, d\psi = 0$$

$$\int_0^{2\pi} \sin^2\psi\, d\psi = \int_0^{2\pi} \cos^2\psi\, d\psi = \tfrac{1}{2}$$

etc.

$$(\Delta T_x)_{AV.} = \tfrac{1}{2}\pi\rho\sigma\Omega R^3\Big\{\tfrac{1}{2}a_0 A\left[\Omega b_1(r-e)+(r+ha_0)q-\dot{x}a_0+Va_0\alpha_y\right]$$
$$-H\Omega R\alpha_y+\tfrac{1}{2}a_0 B\left[\dot{y}+V\alpha_x+\left(h+(r-e)a_0\right)p-\tfrac{1}{2}a_1 H\Omega R\right.$$
$$+\tfrac{1}{2}C\left[-\Omega a_1(r-e)+(r+ha_0)p+\dot{y}a_0+Va_0\alpha_x\right]$$
$$+\tfrac{1}{2}D\left[\dot{x}-V\alpha_y-\left(h+(r-e)a_0\right)q\right]-\tfrac{1}{2}N\Omega R(\Delta B_{1s})\Big\}\Delta\bar{r}$$

This can be broken into partial derivatives by the method of Bryan.

$$\Delta T_x = \tfrac{1}{4}\pi\rho\sigma\Omega R^3\Big\{\dot{x}\left[-Aa_0^2+D+\Omega R(\bar{r}-\xi)a_0 A\frac{\partial b_1}{\partial\dot{x}}\right.$$
$$-H\Omega R\frac{\partial a_1}{\partial\dot{x}}-C\Omega R(\bar{r}-\xi)\frac{\partial a_1}{\partial\dot{x}}\Big]$$
$$+\dot{y}\left[a_0 B+a_0 A\Omega R(\bar{r}-\xi)\frac{\partial b_1}{\partial\dot{y}}-H\Omega R\frac{\partial a_1}{\partial\dot{y}}\right.$$
$$-C\Omega R(\bar{r}-\xi)\frac{\partial a_1}{\partial\dot{y}}+Ca_0\Big]$$
$$+q\left[RAa_0(\bar{r}-\eta a_0)+Aa_0\Omega R(\bar{r}-\xi)\frac{\partial b_1}{\partial q}\right.$$
$$-H\Omega R\frac{\partial a_1}{\partial q}-C\Omega R(\bar{r}-\xi)\frac{\partial a_1}{\partial q}-RD\left(\eta+(\bar{r}-\xi)a_0\right)\Big]$$
$$+p\left[a_0 A\Omega R(\bar{r}-\xi)\frac{\partial b_1}{\partial p}+a_0 BR\left(\eta+(\bar{r}-\xi)a_0\right)\right.$$
$$+CR(\bar{r}+\eta a_0)-CR\Omega(\bar{r}-\xi)\frac{\partial a_1}{\partial p}-H\Omega R\frac{\partial a_1}{\partial p}\Big]$$

$$+\alpha_x\left[a_0 A\Omega R(\bar{r}-\xi)\frac{\partial b_1}{\partial \alpha_x}+a_0 BV-H\Omega R\frac{\partial a_1}{\partial \alpha_x}\right.$$

$$\left.-C\Omega R(\bar{r}-\xi)\frac{\partial a_1}{\partial \alpha_x}+Ca_0V\right]$$

$$+\alpha_y\left[a_0 A\Omega R(\bar{r}-\xi)\frac{\partial b_1}{\partial \alpha_y}+Aa_0^2V-H\Omega R\frac{\partial a_1}{\partial \alpha_y}\right.$$

$$\left.-C\Omega R(\bar{r}-\xi)\frac{\partial a_1}{\partial \alpha_y}-DV-2H\Omega R\right]$$

$$+\Delta A_{1s}\left[a_0 A\Omega R(\bar{r}-\xi)\frac{\partial b_1}{\partial A_{1s}}+a_0\Omega R\xi-a_0 M\Omega R\right.$$

$$\left.-H\Omega R\frac{\partial a_1}{\partial A_{1s}}-C\Omega R(\bar{r}-\xi)\frac{\partial a_1}{\partial A_{1s}}\right]$$

$$+\Delta B_{1s}\left[a_0 A\Omega R(\bar{r}-\xi)\frac{\partial b_1}{\partial B_{1s}}+C\Omega R\xi-H\Omega R\frac{\partial a_1}{\partial B_{1s}}\right.$$

$$\left.\left.-C\Omega R(\bar{r}-\xi)\frac{\partial a_1}{\partial B_{1s}}-N\Omega R\right]\right\}$$

From this can be derived immediately non-dimensional force derivatives as follows:

$$\frac{1}{\frac{1}{4}\pi\rho\sigma\Omega^2R^4}\frac{\partial T_x}{\partial\left(\frac{\dot{x}}{\Omega R}\right)}=D_1-A_1a_0^2+\frac{\partial a_1}{\partial\left(\frac{\dot{x}}{\Omega R}\right)}(-H_1-C_2+C_1\xi)$$

$$+\frac{\partial a_1}{\partial\left(\frac{\dot{y}}{\Omega R}\right)}(-A_1\xi a_0+A_2a_0)$$

$$\frac{1}{\frac{1}{4}\pi\rho\sigma\Omega^2R^4}\frac{\partial T_x}{\partial\left(\frac{\dot{y}}{\Omega R}\right)}=a_0(B_1+C_1)+\frac{\partial a_1}{\partial\left(\frac{\dot{y}}{\Omega R}\right)}(-H_1-C_2+C_1\xi)$$

$$-\frac{\partial a_1}{\partial\left(\frac{\dot{x}}{\Omega R}\right)}(A_2a_0-A_1\xi a_0)$$

$$\frac{1}{\frac{1}{4}\pi\rho\sigma\Omega^2R^4}\frac{\partial T_x}{\partial\left(\frac{p}{\Omega}\right)}=\left[A_1\eta a_0^2+A_2a_0-D_1(\eta-\xi a_0)+D_2a_0\right]$$

$$+\frac{\partial a_1}{\partial\left(\frac{\dot{\xi}}{\Omega}\right)}\left(C_1\xi - H_1 - C_2\right) + \frac{\partial a_1}{\partial\left(\frac{\dot{\eta}}{\Omega}\right)}\left(-A_1\xi a_0 + A_2 a_0\right)$$

$$\frac{1}{\frac{1}{4}\pi\rho\sigma\Omega^2R^4}\frac{\partial T_x}{\partial \alpha_x} = \lambda_d \frac{\partial T_x}{\partial\left(\frac{\dot{x}}{\Omega R}\right)}\frac{1}{\frac{1}{4}\pi\rho\sigma\Omega^2R^4}$$

$$\frac{1}{\frac{1}{4}\pi\rho\sigma\Omega^2R^4}\frac{\partial T_x}{\partial \alpha_y} = -\lambda_d \frac{\partial T_x}{\partial\left(\frac{\dot{x}}{\Omega R}\right)}\cdot\frac{1}{\frac{1}{4}\pi\rho\sigma\Omega^2R^4} - 2H_1$$

In a similar fashion, the Moment Derivatives are derived from:

$$\Delta M_x = -F\left(e\cos\beta + h\sin\beta\right)\sin\psi + G\left[h + (r-e)\sin\beta\right]\cos\psi$$
$$-ebS_b\Omega^2\sin\beta\sin\psi + I_{z_{HUB}}\Omega q$$

and, in non-dimensional form they are:

$$\frac{1}{\frac{1}{4}\pi\rho\sigma\Omega^2R^5}\frac{\partial M_x}{\partial\left(\frac{\dot{x}}{\Omega R}\right)} = \left[-B_1\left(\xi + a_0\eta\right) - C_1a_0\left(\eta - \xi a_0\right) - C_2a_0^2\right]$$
$$+\frac{\partial a_1}{\partial\left(\frac{\dot{x}}{\Omega R}\right)}\left[-A_1\xi\left(\xi + a_0\eta\right) + A_2\left(\xi + a_0\eta\right)\right]$$
$$+\frac{\partial a_1}{\partial\left(\frac{\dot{y}}{\Omega R}\right)}\left[H_1\eta + K_1 - C_1\xi\left(\eta - \xi a_0\right)\right.$$
$$\left.+C_2\left(\eta - 2\xi a_0\right) + C_3 a_0\right]$$

$$\frac{1}{\frac{1}{4}\pi\rho\sigma\Omega^2R^5}\frac{\partial M_x}{\partial\left(\frac{\dot{y}}{\Omega R}\right)} = \left[-A_1a_0(\xi+a_0\eta)+D_1(\eta-\xi a_0)+D_2a_0\right]$$
$$+\frac{\partial a_1}{\partial\left(\frac{\dot{y}}{\Omega R}\right)}\left[-A_1\xi(\xi+a_0\eta)+A_2(\xi+a_0\eta)\right]$$
$$-\frac{\partial a_1}{\partial\left(\frac{\dot{x}}{\Omega R}\right)}\left[H_1\eta+K_1-C_1\xi(\eta-\xi a_0)\right.$$
$$\left.+C_2(\eta-2\xi a_0)+C_3a_0\right]$$

$$\frac{1}{\frac{1}{4}\pi\rho\sigma\Omega^2R^5}\frac{\partial M_x}{\partial\left(\frac{q}{\Omega}\right)} = B_1(\xi+a_0\eta)(\eta-\xi a_0)+B_2a_0(\xi+a_0\eta)$$
$$+C_1a_0\eta(\eta-\xi a_0)+C_2(\eta-\xi a_0+a_0^2\eta)$$
$$+C_3a_0+\frac{I_{2_{HUB}}\Omega^2}{\frac{1}{4}\pi\rho\sigma\Omega^2R^5}$$
$$+\frac{\partial a_1}{\partial\left(\frac{q}{\Omega}\right)}\left[-A_1\xi(\xi+a_0\eta)+A_2(\xi+a_0\eta)\right]$$
$$-\frac{\partial a_1}{\partial\left(\frac{p}{\Omega}\right)}\left[H_1\eta+K_1-C_1\xi(\eta-\xi a_0)\right.$$
$$\left.+C_2(\eta-2\xi a_0)+C_3a_0\right]$$

Force and Moment Derivatives

$$\frac{1}{\frac{1}{4}\pi\rho\sigma\Omega^2R^5}\frac{\partial M_x}{\partial\left(\frac{p}{\Omega}\right)} = -A_1a_0\eta(\xi+a_0\eta)-A_2(\xi+a_0\eta)$$
$$+D_1(\eta-\xi a_0)^2+2D_2a_0(\eta-\xi a_0)+D_3a_0^2$$

$$+\frac{\partial a_1}{\partial\left(\frac{p}{\Omega}\right)}\left[-A_1\xi(\xi+a_0\eta)+A_2(\xi+a_0\eta)\right]$$

$$+\frac{\partial a_1}{\partial\left(\frac{q}{\Omega}\right)}\left[H_1\eta+K_1-C_1\xi(\eta-\xi a_0)\right.$$
$$\left.+C_2(\eta-2\xi a_0)+C_3 a_0\right]$$

$$\frac{\partial M_x}{\partial \alpha_x}=\lambda_d\,\Omega R\,\frac{\partial M_x}{\partial \dot{y}}\quad;\quad\frac{\partial M_x}{\partial \alpha_y}=-\lambda_d\,\Omega R\,\frac{\partial M_x}{\partial \dot{x}}$$

$$\frac{1}{\frac{1}{4}\pi\rho\sigma\Omega^2R^5}\frac{\partial M_x}{\partial B_{1s}}=M_1(\xi+a_0\eta)-A_1\xi(\xi+a_0\eta)$$
$$+\frac{\partial a_1}{\partial B_{1s}}\left[-A_1\xi(\xi+a_0\eta)+A_2(\xi+a_0\eta)\right]$$
$$+\frac{\partial a_1}{\partial A_{1s}}\left[H_1\eta+K_1-C_1\xi(\eta-\xi a_0)\right.$$
$$\left.+C_2(\eta-2\xi a_0)+C_3 a_0\right]$$

$$\frac{1}{\frac{1}{4}\pi\rho\sigma\Omega^2R^5}\frac{\partial M_x}{\partial A_{1s}}=-N_1(\eta-\xi a_0)-N_2 a_0-K_1+C_1\xi(\eta-\xi a_0)$$
$$+C_2\xi a_0+\frac{\partial a_1}{\partial A_{1s}}\left[-A_1\xi(\xi+a_0\eta)+A_2(\xi+a_0\eta)\right]$$
$$-\frac{\partial a_1}{\partial B_{1s}}\left[H_1\eta+K_1-C_1\xi(\eta-\xi a_0)\right.$$
$$\left.+C_2(\eta-2\xi a_0)+C_3 a_0\right]$$

a_1 is the longitudinal harmonic coefficient of flapping. Thus, the Force and Moment Derivatives are written in terms of flapping derivatives.

Where:

$$A_1 = \int_{\xi}^{1.0} A\, d\bar{r} \qquad A_2 = \int_{\xi}^{1.0} A\bar{r}\, d\bar{r} \qquad A_3 = \int_{\xi}^{1.0} A\bar{r}^2 d\bar{r}$$

$$B_1 = \int_{\xi}^{1.0} B\, d\bar{r} \qquad B_2 = \int_{\xi}^{1.0} B\bar{r}\, d\bar{r} \qquad B_3 = \int_{\xi}^{1.0} B\bar{r}^2 d\bar{r}$$

$$H_1 = \int_{\xi}^{1.0} H\, d\bar{r} \qquad H_2 = \int_{\xi}^{1.0} H\bar{r}\, d\bar{r} \qquad H_3 = \int_{\xi}^{1.0} H\bar{r}^2 d\bar{r}$$

and (see "Lift and Torque Forces")

$$A = \frac{1}{\sqrt{\lambda_r^2 + \bar{r}^2}} \left\{ \bar{r}^2 (C_{L\alpha} + C_D) + \lambda_r \bar{r} (C_L + C_{D\alpha}) + 2 C_D \lambda_r^2 \right\}$$

$$B = \frac{1}{\sqrt{\lambda_r^2 + \bar{r}^2}} \left\{ 2\bar{r}^2 C_L + \lambda_r \bar{r} (C_D - C_{L\alpha}) + \lambda_r^2 (C_L - C_{D\alpha}) \right\}$$

$$H \cos\beta = \sqrt{\lambda_r^2 + \bar{r}^2} \left\{ \bar{r} (1 - \tfrac{3}{2}\beta^2) C_L + \lambda_r (1 - \tfrac{3}{2}\beta^2) C_D \right\}$$

$$J \cos\beta = \sqrt{\lambda_r^2 + \bar{r}^2} \left\{ \lambda_r (1 - \tfrac{3}{2}\beta^2) C_L - \bar{r} (1 - \tfrac{3}{2}\beta^2) C_D \right\}$$

$$C = \frac{1}{\sqrt{\lambda_r^2 + \bar{r}^2}} \left\{ \bar{r}^2 (C_L - C_{D\alpha}) + \lambda_r \bar{r} (C_{L\alpha} - C_D) + 2 C_L \lambda_r^2 \right\}$$

$$D = \frac{1}{\sqrt{\lambda_r^2 + \bar{r}^2}} \left\{ -2\bar{r}^2 C_D + \lambda_r \bar{r} (C_L + C_{D\alpha}) - \lambda_r^2 (C_D + C_{L\alpha}) \right\}$$

$$M = \sqrt{\lambda_r^2 \cos^2\beta + \left[\xi + (\bar{r} - \xi)\cos\beta\right]^2} \left[C_{L\alpha} \left\{ \xi + (\bar{r} - \xi)\cos\beta \right\} + C_{D\alpha} \lambda_r \cos\beta \right]$$

$$N = \sqrt{\lambda_r^2 \cos^2\beta + \left[\bar{\zeta} + (\bar{r} - \bar{\zeta})\cos\beta\right]^2}\left[C_L \lambda_r \cos\beta - C_{D\alpha}\left\{\bar{\zeta} + (\bar{r} - \bar{\zeta})\cos\beta\right\}\right]$$

The obvious symmetry of the ROTOCHUTE in axial flight, from a perturbation viewpoint, renders it unnecessary to derive ΔTy and ΔMy in terms of the independent variables and their derivatives. Instead, use can be made of the relationships (which follow from symmetry).

$$\frac{\partial Tx}{\partial \Delta_x} = \frac{\partial Ty}{\partial \Delta_y} \qquad \frac{\partial Tx}{\partial \Delta_y} = \frac{\partial Ty}{\partial \Delta_x}$$

where Δ = variable of interest.

Force and Moment Derivatives for Forward Flight

$$\frac{\partial x}{\partial \alpha} = \frac{1}{m}\left(B_{1z}\frac{\partial T}{\partial \alpha} - \frac{\partial H}{\partial \alpha}\right)$$

$$\frac{\partial x}{\partial \mu} = \frac{1}{m}\left(B_{1z}\frac{\partial T}{\partial \mu} - \frac{\partial H}{\partial \alpha}\right)$$

$$\frac{\partial x}{\partial q} = \frac{1}{m}\left(-\frac{\partial H}{\partial q}\right)$$

$$\frac{\partial x}{\partial B_{1z}} = \frac{1}{m}\left(-B_{1z}\frac{\partial T}{\partial \alpha} + \frac{\partial H}{\partial \alpha} + T\right)$$

$$\frac{\partial x}{\partial \theta} = \frac{1}{m}\left(B_{1z}\frac{\partial T}{\partial \theta} - \frac{\partial H}{\partial \theta}\right)$$

$$\frac{\partial z}{\partial \alpha} = \frac{1}{m u_0}\left(-\frac{\partial T}{\partial \alpha} - B_{1z}\frac{\partial H}{\partial \alpha}\right)$$

$$\frac{\partial z}{\partial \mu} = \frac{1}{m u_0}\left(-\frac{\partial T}{\partial \mu} - B_{1z}\frac{\partial H}{\partial \mu}\right)$$

$$\frac{\partial z}{\partial q} = \frac{1}{m u_o}\left(-B_{12}\frac{\partial H}{\partial q} + A_{12}\frac{\partial Y}{\partial q}\right)$$

$$\frac{\partial z}{\partial B_{12}} = \frac{1}{m u_o}\left(\frac{\partial T}{\partial \alpha} - H + B_{12}\frac{\partial H}{\partial \alpha}\right)$$

$$\frac{\partial z}{\partial \theta} = \frac{1}{m u_o}\left(-\frac{\partial T}{\partial \theta} - B_{12}\frac{\partial H}{\partial \theta}\right)$$

$$\frac{\partial M}{\partial \alpha} = \frac{1}{I_y}\left(-\bar{z}_r B_{12}\frac{\partial T}{\partial \alpha} + \bar{z}_r\frac{\partial H}{\partial \alpha} + \frac{\partial M_{n_1}}{\partial a_1}\frac{\partial a_1}{\partial \alpha}\right)$$

$$\frac{\partial M}{\partial \mu} = \frac{1}{I_y}\left(-\bar{z}_r B_{12}\frac{\partial T}{\partial \mu} + \bar{z}_r\frac{\partial H}{\partial \mu} + \frac{\partial M_{n_1}}{\partial a_1}\frac{\partial a_1}{\partial \mu} - .074\, f p \Omega^2 R^2 \mu\right)$$

$$\frac{\partial M}{\partial q} = \frac{1}{I_y}\left(\bar{z}_r\frac{\partial H}{\partial q} + \frac{\partial M_{n_1}}{\partial a_1}\frac{\partial a_1}{\partial q}\right)$$

$$\frac{\partial M}{\partial B_{12}} = \frac{1}{I_y}\left(\bar{z}_r B_{12}\frac{\partial T}{\partial \alpha} - \bar{z}_r\frac{\partial H}{\partial \alpha} - \bar{z}_r T - \frac{\partial M_{n_1}}{\partial a_1}\frac{\partial a_1}{\partial \alpha}\right)$$

$$\frac{\partial M}{\partial \theta} = \frac{1}{I_y}\left(-\bar{z}_r B_{1s}\frac{\partial T}{\partial \theta} + z_r\frac{\partial H}{\partial \theta} + \frac{\partial M_{n_1}}{\partial a_1}\frac{\partial a_1}{\partial \theta}\right)$$

Remarks of Appendix II regarding the derivation of angle of attack derivatives are apropos.

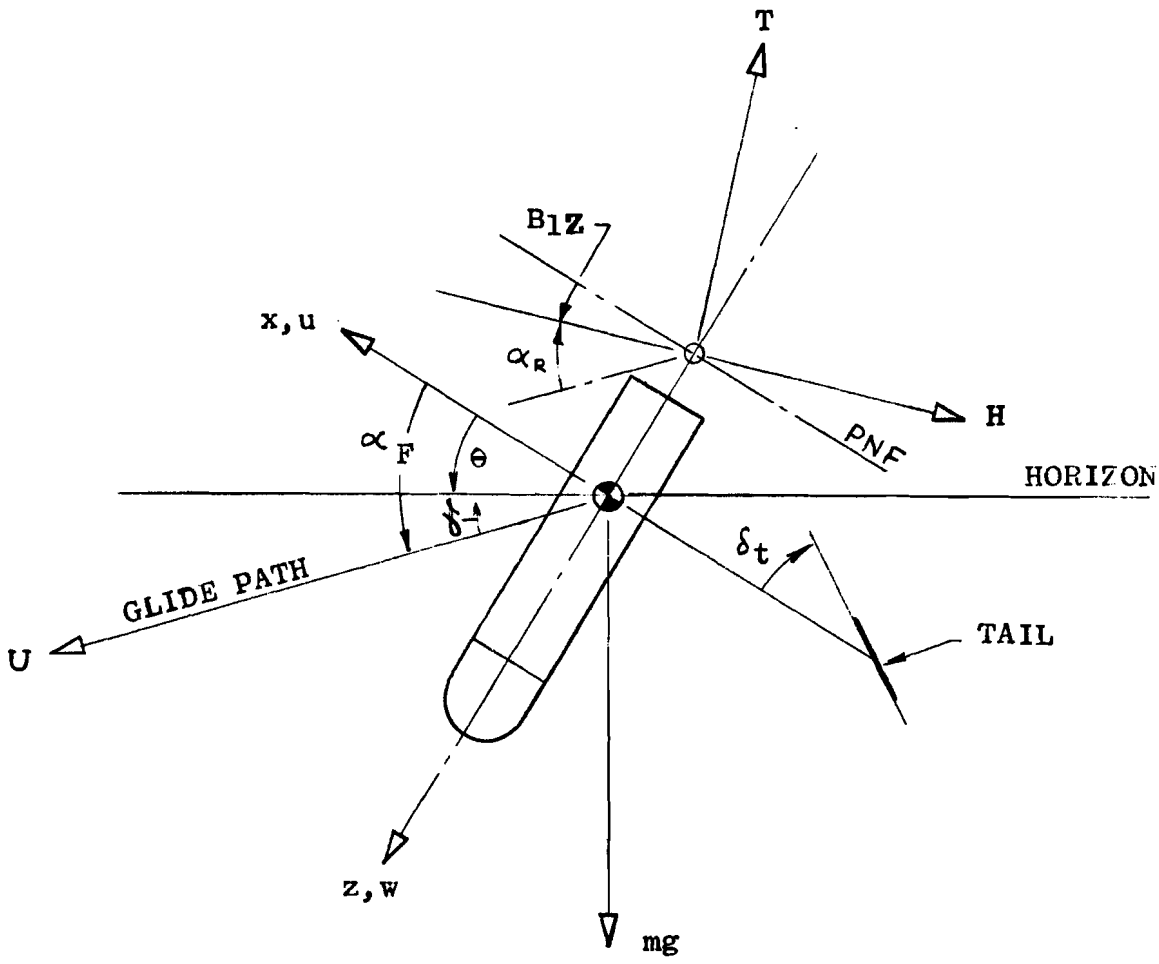

ROTOCHUTE (WITH TAIL) IN FLIGHT, SHOWING ANGLE RELATIONSHIPS

FIGURE 80

Automatic Stabilization Equipment

Longitudinal Equation of Motion

$$B_{1Z} = \frac{1}{1+\tau_z s}\left[\frac{\partial B_{1z}}{\partial \theta}(\theta - \theta_c) + \frac{\partial B_{1z}}{\partial q} q_L\right]$$

where :

$$\tau_z = 0.25 \text{ seconds}$$

$$\frac{\partial B_{1z}}{\partial \theta} = 0.4$$

$$\frac{\partial B_{1z}}{\partial q} = 0.25$$

The Total Flight Spectrum

Introduction

In this section, the dynamic stability of the ROTOCHUTE throughout the whole flight regime of interest, including both axial and forward flight is analyzed. The equations of motion are written (reference body axes) using Euler equations of motion. Tail moment effects are included in the analysis, but drag due to the tail is ignored (Reference Figure 80).

Analysis

Thus, the equations of motion are:

$$\sum F_x \xleftarrow{+}$$

$$m(\dot{u} + wq) = T \sin B_{12} - H \cos B_{12} - mg \sin\theta - \tfrac{1}{2} u^2 \rho f$$

$$\sum F_z \downarrow +$$

$$m(\dot{w} - uq) = -T \cos B_{12} - H \cos B_{12} + mg \cos\theta$$

$$\sum M_y \quad x \leftarrow \circlearrowright^{+} \; z$$

$$I_y \dot{q} = Hh \cos B_{12} - Th \sin B_{12} + M_f + \tfrac{1}{2} e b S_b \Omega^2 a_1 - M_t$$

Small angle assumptions can be made. Then small disturbance substitutions and the elimination of initial conditions result in the perturbation equations in terms of partial derivatives of Forces and Moments as follows:

$$F_x: \quad \dot{u} + w_0 q = \frac{\partial x}{\partial \alpha_f}\Delta\alpha_f + \frac{\partial x}{\partial B_{12}}\Delta B_{12} + \frac{\partial x}{\partial \mu}\Delta\mu + \frac{\partial x}{\partial q}\Delta q - (g\cos\theta_0)\Delta\theta - \frac{\rho f u_0}{m}\Delta u$$

$$F_z: \quad \dot{w} - u_0 q = \frac{\partial z}{\partial \alpha_f}\Delta\alpha_f + \frac{\partial z}{\partial B_{12}}\Delta B_{12} + \frac{\partial z}{\partial \mu}\Delta\mu + \frac{\partial z}{\partial q}\Delta q - (g\sin\theta_0)\Delta\theta$$

$$M_y: \quad \dot{q} = \frac{\partial M}{\partial \alpha_f}\Delta\alpha_f + \frac{\partial M}{\partial B_{1z}}\Delta B_{1z} + \frac{\partial M}{\partial \mu}\Delta\mu + \frac{\partial M}{\partial q}\Delta q + \frac{\partial M_f}{\partial U}\Delta U - \frac{\partial M_t}{\partial U}\Delta U$$

where $X = \sum Fx$; $Z = \sum Fz$; and $M = \sum My$. These are the right-hand side of the original equations of motion.

Typically:

$$\frac{\partial x}{\partial \alpha} = \frac{\partial}{\partial \alpha}\left\{T \sin B_{1z} - H\cos B_{1z} - mg \sin\theta - \tfrac{1}{2}u^2\rho f\right\}$$

$$\cong \frac{\partial}{\partial \alpha}\left\{T B_{1z} - H - mg\,\theta - \tfrac{1}{2}u^2\rho f\right\}$$

$$\cong B_{1z}\frac{\partial T}{\partial \alpha} - \frac{\partial H}{\partial \alpha}$$

The equations are now in terms of angular and speed variables with coefficients which are Force and Moment derivatives. The derivations of these derivatives were presented in detail for axial flight. For forward flight, standard helicopter methods apply.

Finally, by making the substitutions:

$$\Delta\alpha_f = \alpha_f - \alpha_{f_o} \qquad \Delta\Theta = \Theta - \Theta_o$$

$$\Delta B_{1z} = B_{1z} - B_{1z_o} \qquad \Delta\mu = \mu - \mu_o$$

The following are derived:

$$\dot{u} = \frac{\partial x}{\partial \alpha_f}\alpha_f + \frac{\partial x}{\partial B_{1z}}B_{1z} + \frac{\partial x}{\partial \mu}\mu + \frac{\partial x}{\partial q}q - w_0 q$$
$$- (g\cos\theta_0)\theta - \left(\frac{\rho u_0 f}{m}\right)u - Tu$$

$$\dot{w} = \frac{\partial z}{\partial \alpha_f}\alpha_f + \frac{\partial z}{\partial B_{1z}}B_{1z} + \frac{\partial z}{\partial \mu}\mu + \frac{\partial z}{\partial q}q - u_0 q$$
$$- (g\,\mathrm{SIN}\,\theta_0)\theta - Tw$$

$$q = \frac{\partial M}{\partial \alpha_f}\alpha_f + \frac{\partial M}{\partial B_{1z}}B_{1z} + \frac{\partial M}{\partial \mu}\mu + \frac{\partial M}{\partial q}q - T\theta$$

where the trim expressions are also expressible in terms of partial derivatives and initial conditions:

$$T_u = \frac{\partial x}{\partial \alpha_f}\alpha_{f_0} + \frac{\partial x}{\partial B_{1z}}B_{1z_0} + \frac{\partial x}{\partial \mu}\mu_0 - g\,\theta_0\cos\theta_0 - \frac{\rho U_0 f}{m}$$

$$T_w = \frac{\partial z}{\partial \alpha_f}\alpha_{f_0} + \frac{\partial z}{\partial B_{1z}}B_{1z_0} + \frac{\partial z}{\partial \mu}\mu_0 - g\,\theta_0\,\mathrm{SIN}\,\theta_0$$

$$T_\theta = \frac{\partial M}{\partial \alpha_f}\alpha_{f_0} + \frac{\partial M}{\partial B_{1z}}B_{1z_0} + \frac{\partial M}{\partial \mu}\mu_0 + \frac{\partial M_t}{\partial U}U_0$$

All force and moment derivatives, and the trim functions are calculated in terms of the advance ratio. The trim functions are derived from a static analysis of the ROTOCHUTE in which the tail configuration plays a prominent part (Reference Static Equilibrium Equations).

Special Note:

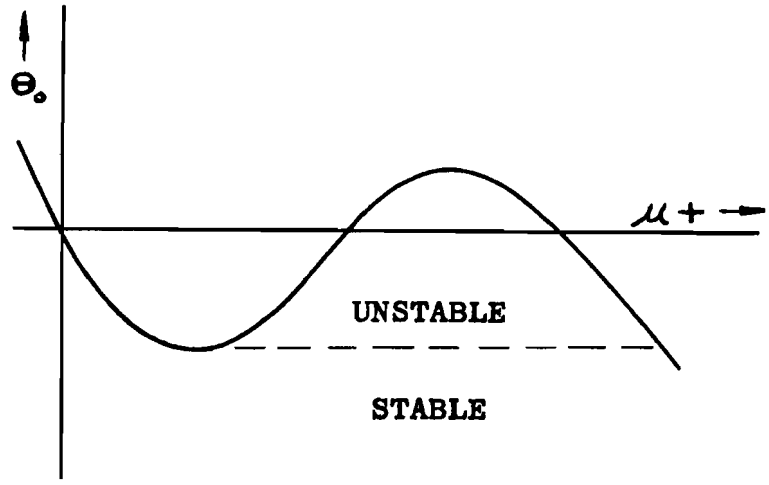

FIGURE 81

Of particular interest in analyzing the results is the fact that the ROTOCHUTE body pitch attitude (θ) is a feedback signal to the ASE. Since the problem was programmed on the computer as a function of advance ratio, then the feedback signal should be a single-valued function of advance ratio. It transpired that at $\mu < 0.15$ such is not the case, as Figure 81 illustrates. However, for $\mu > .15$, the advance ratio is satisfactory in this respect.

For this reason, sufficient control must be available, with the existing control system, to overcome the hump in the $\theta - \mu$ curve. Since the existing ROTOCHUTE lacked this amount of control, a tail was added to supplement the control with a forward pitching moment.

$$+\left(\text{Tail Moment, } M = -\frac{1}{2}\rho U^2 S_{st}\ l_{st}\ C_N\right.$$

$$= \rho U S_{st}\ l_{st}\ C_N$$

$$= \rho U_o S_{st}\ l_{st}\ C_N \quad \text{at the trim point}$$

APPENDIX II. STABILITY AND CONTROL ANALYSIS

SUMMARY

An analog computer program was performed for the purpose of investigating the stability and control characteristics of the KRC-6 ROTOCHUTE. Six rigid body equations of motion were considered in the analysis. It was found that the autopilot system was capable of stabilizing the ROTOCHUTE during the glide and flare maneuver. However, on the basis of trim considerations and autopilot gains, it was found essential that the synchronizing links be disconnected during this phase of operation. A satisfactory procedure for flaring the ROTOCHUTE has been demonstrated. During this phase of the analysis, the stability derivatives were programmed on the analog computer as a function of advance ratio. Conclusions are drawn relative to the dynamic characteristics of the ROTOCHUTE with free-flapping blades and a semi-rigid rotor.

INTRODUCTION

During a typical mission, the ROTOCHUTE will initially be traveling at high forward speeds during descent through the atmosphere. At a predetermined altitude, the rotor will be deployed and the ROTOCHUTE will decelerate with the longitudinal body axis essentially aligned with the flight path. Initially, the rotor is completely stalled, due to the high inflow, and acts as a drag device. As the ROTOCHUTE decelerates, the inflow decreases and the rotor becomes unstalled. This phase of operation is known as the axial flight mode. During this mode, no attempt is made to direct the flight path except through the controlled deployment of the rotor.

After the ROTOCHUTE has decelerated to a sufficiently low descent velocity, control is applied to the rotor and a horizontal velocity is developed. As the forward velocity of the ROTOCHUTE is increased to the nominal glide speed, the vertical descent velocity decreases further, since the rotor is aerodynamically more efficient in forward flight than in axial flight. During the glide mode, the ROTOCHUTE will be maneuvered into the desired landing area. A glide path of 22 degrees with relation to the horizontal can be expected from a configuration with an L/D of 2.5.

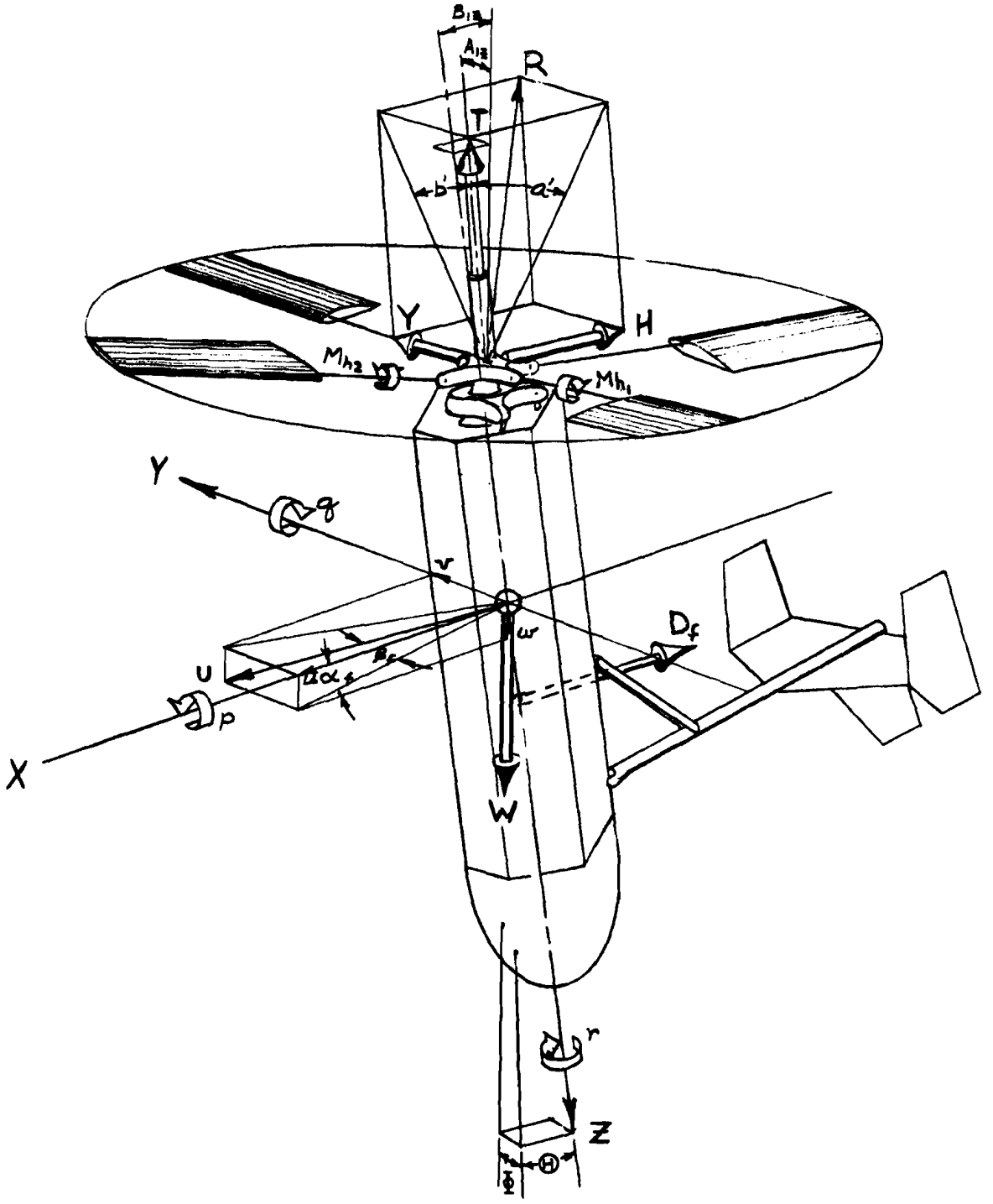

SCHEMATIC VIEW OF ROTOCHUTE AXIS SYSTEM

FIGURE 82

The final mode is the flare and landing maneuver. The flare maneuver is initiated by increasing the fuselage pitch attitude by the application of aft rotor tilt. An incremental increase in pitch attitude results in an approximate constant deceleration along the flight path. The forward speed should be arrested before ground contact and collective pitch control applied to result in near-zero vertical velocity at touchdown. The total time required for the flare and landing maneuver could be on the order of 5 to 10 seconds.

The mission profile of the KRC-6 will include the three flight modes previously discussed. The capability to maneuver during the glide and flare will be provided through an autopilot system. The autopilot commands will be transmitted by radio from a ground control station. The autopilot will provide the necessary stabilization of the ROTOCHUTE, with the ground control station closing the navigation loop.

A. DYNAMICS DURING GLIDE AND FLARE

The initial design concept for the KRC-6 rotor used synchronizing links to insure the uniform opening of the rotor blades during deployment. These links were attached to each of the four blades and restricted blade flapping relative to the hub or control axis (a_1 and b_1). However, the ability of the rotor to change coning angle (a_o) was not affected. The rotor flapping derivatives were calculated assuming the blade had a root hinge restraint equal to the effective blade flapping stiffness. Analog computer tests showed that the ASE system, with proper control coupling, was capable of stabilizing and controlling the ROTOCHUTE with this rotor configuration. However, the system was very sensitive to changes in gain and the system would become unstable if the advance ratio increased substantially above the nominal glide speed. Also, the longitudinal and lateral trim required at the nominal glide speed exceeded the design limits. With the semi-rigid rotor, it was essential that the effect of non-uniform inflow be included in the calculations. With a normal flapping rotor, considering the effect of non-uniform inflow results in increasing the lateral flapping angle (b_1). However, for the semi-rigid rotor, this effect results in a longitudinal hub moment which is much larger than that predicted if non-uniform inflow is neglected.

A second design studied was one in which the synchronizing links are released after the rotor is deployed. This system has smaller steady-state hub moments and hence required less control to trim. Also, while coupling is still present, due to the large offset of the flapping hinges, the coupling is much less than that experienced by the semi-rigid rotor. Hence, the autopilot doesn't require coupling and is less sensitive to changes in gain.

1. Equations of Motion

The motions of the ROTOCHUTE in space can be described by six equations of motion if one neglects the rotor dynamics. These equations define the force and moment equilibrium along and about the X, Y, and Z axes. The equations of motion used in the ROTOCHUTE analysis are referred to body axes, with the X and Y axes aligned with the principal axes. As a result, there exists a steady-state value for angle of attack. Also, since the ROTOCHUTE is in unpowered autorotation, the nominal flight path is inclined downward and a steady-state value for θ-α_f is considered. Figure 82 presents a schematic. of axes orientation.

The six-degree of freedom equations of motion and the auxiliary equations for transforming from body rates to space rates are as follows:

$$\dot{u} + u_o \alpha_{f_o} q = -\Theta g \cos\Theta_o + \frac{\partial X}{\partial \alpha}\Delta\alpha_f + \frac{\partial X}{\partial \mu}\mu + \frac{\partial X}{\partial q} q$$

$$+ \frac{\partial X}{\partial \rho}(\rho + \dot{A}_{Iz}) + \frac{\partial X}{\partial \beta_f}\beta_f + \frac{\partial X}{\partial \beta_{Iz}}\beta_{Iz} + \frac{\partial X}{\partial \theta}\theta \qquad (1)$$

$$\dot{\beta}_f + r = \frac{g}{u_o}(\Phi \cos\Theta_o \cos\Phi - \Theta \sin\Theta_o \sin\Phi_o) + \frac{\partial Y}{\partial \alpha}\Delta\alpha_f$$

$$+ \frac{\partial Y}{\partial \mu}\mu + \frac{\partial Y}{\partial q}(q - \dot{\beta}_{Iz}) + \frac{\partial Y}{\partial \rho}\rho + \frac{\partial Y}{\partial \beta_f}\beta_f$$

$$+ \frac{\partial Y}{\partial r} r + \frac{\partial Y}{\partial A_{Iz}} A_{Iz} + \frac{\partial Y}{\partial \theta}\theta \qquad (2)$$

$$\dot{\alpha}_f - q = \frac{g}{u_o}(-\Phi \sin\Phi_o \cos\Theta - \Theta \sin\Theta_o \cos\Phi_o) + \frac{\partial Z}{\partial \alpha}\Delta\alpha_f$$

$$+ \frac{\partial Z}{\partial \mu}\mu + \frac{\partial Z}{\partial q} q + \frac{\partial Z}{\partial \rho}(\rho + \Delta\dot{A}_{Iz}) + \frac{\partial Z}{\partial \beta_f}\beta_f$$

$$+ \frac{\partial Z}{\partial \beta_{Iz}}\beta_{Iz} + \frac{\partial Z}{\partial A_{Iz}} A_{Iz} + \frac{\partial Z}{\partial \theta}\theta \qquad (3)$$

$$\dot{\rho} = \frac{\partial L}{\partial \alpha}\Delta\alpha_f + \frac{\partial L}{\partial \mu}\mu + \frac{\partial L}{\partial q}(q - \dot{\beta}_{Iz}) + \frac{\partial L}{\partial \rho}\rho$$

$$+ \frac{\partial L}{\partial \beta_f}\beta_f + \frac{\partial L}{\partial r} r + \frac{\partial L}{\partial A_{Iz}} A_{Iz} + \frac{\partial L}{\partial \theta}\theta \qquad (4)$$

$$\dot{q} = \frac{\partial M}{\partial \alpha}\Delta\alpha_f + \frac{\partial M}{\partial \mu}\mu + \frac{\partial M}{\partial q} q + \frac{\partial M}{\partial \rho}(\rho + \dot{A}_{Iz})$$

$$+ \frac{\partial M}{\partial \beta_f}\beta_f + \frac{\partial M}{\partial \beta_{Iz}}\beta_{Iz} + \frac{\partial M}{\partial \theta}\theta \qquad (5)$$

$$\dot{r} = \frac{\partial N}{\partial \beta_f}\beta_f + \frac{\partial N}{\partial \rho}\rho + \frac{\partial N}{\partial r} r \qquad (6)$$

$$\dot{\Theta} = q \cos\Phi_o - r \sin\Phi_o \qquad (7)$$

$$\dot{\Phi} = \rho + q \sin\Phi_o \tan\Theta_o + r \cos\Phi_o \tan\Theta_o \qquad (8)$$

Where :

$$\frac{\partial X}{\partial \alpha} = \frac{1}{m}\left(B_{1z}\frac{\partial T}{\partial \alpha} - \frac{\partial H}{\partial \alpha}\right)$$

$$\frac{\partial X}{\partial \mu} = \frac{1}{m}\left(B_{1z}\frac{\partial T}{\partial \mu} - \frac{\partial H}{\partial \mu} - \frac{\partial D_f}{\partial \mu}\right)$$

$$\frac{\partial X}{\partial q} = \frac{1}{m}\left(-\frac{\partial H}{\partial q}\right)$$

$$\frac{\partial X}{\partial \rho} = \frac{1}{m}\left(-\frac{\partial H}{\partial \rho}\right)$$

$$\frac{\partial X}{\partial \beta_f} = \frac{1}{m}\left(-\frac{\partial H}{\partial \beta_f}\right)$$

$$\frac{\partial X}{\partial B_{1z}} = \frac{1}{m}\left(-B_{1z}\frac{\partial T}{\partial \alpha} + \frac{\partial H}{\partial \alpha} + T\right)$$

$$\frac{\partial X}{\partial \theta} = \frac{1}{m}\left(B_{1z}\frac{\partial T}{\partial \theta} - \frac{\partial H}{\partial \theta}\right)$$

$$\frac{\partial Y}{\partial \alpha} = \frac{1}{mu_o}\left(A_{1z}\frac{\partial T}{\partial \alpha}\right)$$

$$\frac{\partial Y}{\partial \mu} = \frac{1}{mu_o}\left(A_{1z}\frac{\partial T}{\partial \mu}\right)$$

$$\frac{\partial Y}{\partial q} = \frac{1}{mu_o}\frac{\partial Y}{\partial q}$$

$$\frac{\partial Y}{\partial \rho} = \frac{1}{mu_o}\left(\frac{\partial Y}{\partial \rho} + a_t\frac{\rho}{2}\mu\Omega R S_t \bar{z}_t\right)$$

$$\frac{\partial Y}{\partial \beta_f} = \frac{1}{mu_o}\left(\frac{\partial Y}{\partial \beta} - a_t\frac{\rho}{2}\mu^2\Omega^2 R^2 S_t\right)$$

$$\frac{\partial Y}{\partial r} = \frac{1}{mu_o}\left(a_t\frac{\rho}{2}\mu\Omega R S_t \ell_t\right)$$

$$\frac{\partial Y}{\partial A_{1z}} = \frac{1}{mu_o}T$$

$$\frac{\partial Y}{\partial \theta} = \frac{1}{mu_o}A_{1z}\frac{\partial T}{\partial \theta}$$

$$\frac{\partial z}{\partial \alpha} = \frac{1}{mu_o}\left(-\frac{\partial T}{\partial \alpha} - B_{1z}\frac{\partial H}{\partial \alpha}\right)$$

$$\frac{\partial z}{\partial \mu} = \frac{1}{mu_o}\left(-\frac{\partial T}{\partial \mu} - B_{1z}\ \frac{\partial H}{\partial \mu}\right)$$

$$\frac{\partial z}{\partial q} = \frac{1}{mu_o}\left(-B_{1z}\frac{\partial H}{\partial q} + A_{1z}\frac{\partial Y}{\partial q}\right)$$

$$\frac{\partial z}{\partial \rho} = \frac{1}{mu_o}\left(-B_{1z}\frac{\partial H}{\partial \rho} + A_{1z}\frac{\partial Y}{\partial \rho}\right)$$

$$\frac{\partial z}{\partial B_f} = \frac{1}{mu_o}\left(-B_{1z}\frac{\partial H}{\partial \beta} + A_{1z}\frac{\partial Y}{\partial \beta}\right)$$

$$\frac{\partial z}{\partial B_{1z}} = \frac{1}{mu_o}\left(\frac{\partial T}{\partial \alpha} - H + B_{1z}\ \frac{\partial H}{\partial \alpha}\right)$$

$$\frac{\partial z}{\partial A_{1z}} = \frac{1}{mu_o}\ Y$$

$$\frac{\partial z}{\partial \theta} = \frac{1}{mu_o}\left(-\frac{\partial T}{\partial \theta} - B_{1z}\ \frac{\partial H}{\partial \theta}\right)$$

$$\frac{\partial L}{\partial \alpha} = \frac{1}{Ix}\left(\bar{z}\ A_{1z}\frac{\partial T}{\partial \alpha} + \frac{\partial M_{h2}}{\partial b_1}\ \frac{\partial b_1}{\partial \alpha}\right)$$

$$\frac{\partial L}{\partial \mu} = \frac{1}{Ix}\left(\bar{z}\ A_{1z}\frac{\partial T}{\partial \mu} + \frac{\partial M_{h2}}{\partial b_1}\ \frac{\partial b_1}{\partial \mu}\right)$$

$$\frac{\partial L}{\partial q} = \frac{1}{Ix}\left(\bar{z}_r\frac{\partial Y}{\partial q} + \frac{\partial M_{h2}}{\partial b_1}\ \frac{\partial b_1}{\partial q}\right)$$

$$\frac{\partial L}{\partial \rho} = \frac{1}{Ix}\left(\bar{z}_r\frac{\partial Y}{\partial \rho} + \frac{\partial M_{h2}}{\partial b_1}\ \frac{\partial b_1}{\partial \rho} - l_t\ a_t\ \frac{\rho}{2}\mu\ \Omega\ A\ S_t\ \bar{z}_t\right)$$

$$\frac{\partial L}{\partial \beta} = \frac{1}{Ix}\left(\bar{z}_r\frac{\partial Y}{\partial \beta} + \frac{\partial M_{h2}}{\partial b_1}\frac{\partial b_1}{\partial \beta} + l_t\ a_t\ \frac{\rho}{2}\mu^2\Omega^2 A^2\ S_t\right)$$

$$\frac{\partial L}{\partial r} = \frac{1}{Ix}\left(-l_t^2\ a_t\ \frac{\rho}{2}\mu\ \Omega\ R\ S_t\right)$$

$$\frac{\partial L}{\partial A_{1s}} = \frac{1}{Ix}\ \bar{z}_r\ T$$

$$\frac{\partial L}{\partial \theta} = \frac{1}{Ix}\left(\bar{z}_r\ A_{1z}\ \frac{\partial T}{\partial \theta} + \frac{\partial M_{h2}}{\partial b_1}\ \frac{\partial b_1}{\partial \theta}\right)$$

$$\frac{\partial M}{\partial \alpha} = \frac{1}{I_y}\left(-\bar{z}_r\ B_{1s}\ \frac{\partial T}{\partial \alpha} + \bar{z}_r\ \frac{\partial H}{\partial \alpha} + \frac{\partial M_{h1}}{\partial a_1}\ \frac{\partial a_1}{\partial \alpha}\right)$$

$$\frac{\partial M}{\partial \mu} = \frac{1}{I_y}\left(-\bar{z}_r B_{1z}\frac{\partial T}{\partial \mu} + \bar{z}_r \frac{\partial H}{\partial \mu} + \frac{\partial M h_1}{\partial a_1}\frac{\partial a_1}{\partial \mu} - 0.74 f \rho \Omega^2 R^2 \mu\right)$$

$$\frac{\partial M}{\partial q} = \frac{1}{I_y}\left(\bar{z}_r \frac{\partial H}{\partial q} + \frac{\partial M h_1}{\partial a_1}\frac{\partial a_1}{\partial q}\right)$$

$$\frac{\partial M}{\partial p} = \frac{1}{I_y}\left(\bar{z}_r \frac{\partial H}{\partial p} + \frac{\partial M h_1}{\partial a_1}\frac{\partial a_1}{\partial p}\right)$$

$$\frac{\partial M}{\partial B_f} = \frac{1}{I_y}\left(\bar{z}_r \frac{\partial H}{\partial B} + \frac{\partial M h_1}{\partial a_1}\frac{\partial a_1}{\partial B}\right)$$

$$\frac{\partial M}{\partial B_{1z}} = \frac{1}{I_y}\left(\bar{z}_r B_{1z}\frac{\partial T}{\partial \alpha} - \bar{z}_r \frac{\partial H}{\partial \alpha} - \bar{z}_r T - \frac{\partial M h_1}{\partial a_1}\frac{\partial a_1}{\partial \alpha}\right)$$

$$\frac{\partial M}{\partial \theta} = \frac{1}{I_y}\left(-\bar{z}_r B_{1s}\frac{\partial T}{\partial \theta} + \bar{z}_r \frac{\partial H}{\partial \theta} + \frac{\partial M h_1}{\partial a_1}\frac{\partial a_1}{\partial \theta}\right)$$

$$\frac{\partial N}{\partial \beta} = \frac{1}{I_z}\left(\bar{z}_t a_t \frac{\rho}{2}\mu^2 \Omega^2 R^2 S_t\right)$$

$$\frac{\partial N}{\partial p} = \frac{1}{I_z}\left(-z_t^2 a_t \frac{\rho}{2}\mu \Omega R S_t\right)$$

$$\frac{\partial N}{\partial r} = \frac{1}{I_z}\left(-z_t a_t \frac{\rho}{2}\mu \Omega R S_t \ell_t\right)$$

The above equations of motion assume constant rotor speed. At advance ratios below approximately $\mu = 0.20$, the collective pitch governor designed for axial flight should prove effective in maintaining constant rotor speed. An increase in rotor angle of attack results in a rotor torque tending to increase rotor angular velocity. The governor senses this speed increase and increases collective pitch which reduces the incremental driving torque to near zero. The rotor speed will vary through small limits, since an error signal is necessary for any closed-loop governing system. At higher advance ratios, this governing system becomes ineffective due to a reversal in the slope of rotor driving torque versus collective pitch. A quasi-static approach was used to incorporate the effect of the rotor governor into the equations of motion. The rate of change of collective pitch versus angle of attack was calculated for constant angular velocity. This ratio was then used to modify the angle of attack derivatives. For example, the derivative with the governing system operating was calculated as follows:

$$\frac{\partial M}{\partial \alpha} = \left(\frac{\partial M}{\partial \alpha}\right)_{\theta} + \frac{\partial M}{\partial \theta} \cdot \frac{\partial \theta}{\partial \alpha} \qquad (9)$$

2. Derivatives and Constants

In order to solve the equation of motion, it first is necessary to evaluate the various stability derivatives and constants. Table 5 presents a summary of the various derivatives calculated for both the semi-rigid and free-flapping rotors. The Burroughs E102 digital computer was used for performing the calculations.

After investigating the dynamic characteristics of the ROTOCHUTE with the semi-rigid rotor, the importance of each of the various derivatives was evaluated. The results of this investigation showed that only the inertia and gravitation terms were of primary importance in the drag and side force equations. Therefore, in the analysis of the free-flapping rotor, a number of small derivatives were dropped.

TABLE 5

STABILITY DERIVATIVES FOR KRC-6

(WITH AND WITHOUT FREE-FLAPPING HINGES)

		Semi-Rigid Rotor					Free-Flapping Rotor		
Derivative	Units	μ= 0.20	μ= 0.16	μ= 0.13	μ= 0.08	μ= 0.02	μ= 0.15	μ= 0.10	μ= 0.05
$g \cos \theta_o$	ft/sec^2	31.87	32.16	32.07	31.49	30.94	32.16	31.49	30.94
$\partial x/\partial \alpha$	ft/sec^2	-8.388	-5.433	-5.320	-2.767	-1.469	-5.433	-2.767	-1.469
$\partial x/\partial \mu$	ft/sec^2	-81.93	-68.04	-62.49	-57.12	-19.14	-31.02	-28.56	-9.56
$\partial x/\partial q$	ft/sec	0.718	0.901	0.914	0.884	0.769	-1.552	-2.554	-0.650
$u_o \alpha_{f_o}$	ft/sec	3.001	2.453	2.652	3.438	1.419			
$\partial x/\partial p$	ft/sec	0.779	1.037	1.098	1.138	1.348	----	----	----
$\partial x/\partial \beta$	ft/sec^2	0.002	0.012	0.028	0.037	0.542	----	----	----
$\partial x/\partial B_{1z}$	ft/sec^2	40.64	37.68	37.57	35.02	33.72	37.68	35.02	33.72
$\partial x/\partial \theta$	ft/sec^2	-4.158	-11.39	-14.81	-13.16	-9.708	----	----	----
$\frac{g}{u_o} \cos \theta_o \cos \Phi_o$	1/sec	0.325	0.422	0.518	0.828	2.599	0.452	0.677	1.350
$\frac{g}{u_o} \sin \theta_o \sin \Phi_o$	1/sec	-0.001	-0.0007	+0.003	0.000	+0.023	----	----	----
$\partial Y/\partial \alpha$	1/sec	-0.103	-0.160	-0.089	+0.013	-0.118	----	----	----
$\partial Y/\partial \mu$	1/sec	-0.025	-0.220	-0.225	+0.180	0.000	----	----	----
$\partial Y/\partial q$	Rad	0.0082	0.014	0.020	0.029	0.112	----	----	----
$\partial Y/\partial p$	Rad	-0.0039	-0.0083	-0.012	-0.019	-0.061	----	----	----
$\partial Y/\partial \beta$	1/sec	-0.057	-0.049	-0.048	-0.030	-0.014	-0.049	-0.030	-0.014
$\partial Y/\partial r$	Rad	0.0020	0.0020	0.0023	0.0020	0.0020	----	----	----
$\partial Y/\partial A_{1z}$	1/sec	0.330	0.422	0.593	0.844	2.700	0.422	0.593	0.844
$\partial Y/\partial \theta$	1/sec	-0.055	-0.321	-0.247	+0.064	-0.635	----	----	----
$\frac{g}{u_o} \sin \Phi_o \cos \theta_o$	1/sec	0.010	0.041	0.034	0.000	0.081	----	----	----
$\frac{g}{u_o} \sin \theta_o \cos \Phi_o$	1/sec	-0.045	-0.007	+0.045	+0.176	+0.751	----	----	----

TABLE 5 (Continued)

Derivative	Units	Semi-Rigid Rotor μ= 0.20	μ= 0.16	μ= 0.13	μ= 0.08	μ= 0.02	Free-Flapping Rotor μ= 0.15	μ= 0.10	μ= 0.05
$\partial z/\partial \alpha$	1/sec	-7.156	-2.091	-1.897	-1.064	-4.454	-4.505	-2.054	-0.720
$\partial z/\partial \mu$	1/sec	-1.742	-2.878	-4.767	-14.556	+0.027	-2.262	-5.938	-18.25
$\partial z/\partial q$	Rad	+0.0000	-0.0009	-0.0009	0.000	-0.0043	----	----	----
$\partial z/\partial p$	Rad	+0.0002	+0.0009	+0.0006	-0.0006	-0.0007	----	----	----
$\partial z/\partial \beta$	1/sec	+0.0001	+0.0007	+0.0005	-0.0001	-0.0007	----	----	----
$\partial z/\partial B_{1z}$	1/sec	7.149	2.083	1.884	1.048	4.441	4.490	2.024	0.684
$\partial z/\partial A_{1z}$	1/sec	-0.0054	-0.0093	-0.0110	-0.0104	-0.0132	----	----	----
$\partial z/\partial \theta$	1/sec	-3.750	-4.196	-5.247	-5.196	-23.942	----	----	----
$\partial L/\partial \alpha$	1/sec^2	-56.79	-10.94	-3.532	+1.219	-0.750	-6.176	-0.958	+0.391
$\partial L/\partial \mu$	1/sec^2	-21.69	-32.34	-28.62	-24.01	0.000	-0.492	-2.842	-0.041
$\partial L/\partial q$	1/sec	4.558	4.684	4.705	4.711	4.810	+0.0969	0.1156	0.1230
$\partial L/\partial p$	1/sec	-2.882	-2.992	-2.997	-3.013	-2.966	-0.9639	-1.1109	-1.1725
$\partial L/\partial \beta$	1/sec^2	+0.648	-0.664	-0.910	-0.864	-0.313	+0.499	-0.223	-0.350
$\partial L/\partial r$	1/sec	-0.034	-0.027	-0.0221	-0.0136	-0.0042	----	----	----
$\partial L/\partial A_{1Z}$	1/sec^2	15.00	15.00	15.00	15.00	15.00	+15.106	19.097	21.037
$\partial L/\partial \theta$	1/sec^2	-33.35	-30.79	-17.95	+1.225	-5.184	----	----	----
$\partial M/\partial \alpha$	1/sec^2	89.41	22.19	16.30	7.796	1.495	-1.324	-0.473	+0.085
$\partial M/\partial \mu$	1/sec^2	9.024	10.923	19.866	24.717	3.287	-1.769	-0.855	+2.726
$\partial M/\partial q$	1/sec	-2.985	-3.048	-3.054	-3.024	-2.957	-0.896	-1.061	-1.143
$\partial M/\partial p$	1/sec	-4.503	-4.644	-4.672	-4.691	-4.789	-0.037	-0.055	-0.0629
$\partial M/\partial \beta$	1/sec^2	-4.009	-3.655	-3.058	-1.846	-0.875	----	----	----
$\partial M/\partial B_{1z}$	1/sec^2	-104.3	-37.12	-31.23	-22.72	-16.42	-11.44	-18.44	-20.92
$\partial M/\partial \theta$	1/sec^2	47.60	48.26	49.39	45.72	14.25	----	----	----
$\partial N/\partial \rho_f$	1/sec^2	14.36	8.731	5.775	2.194	0.212	8.731	2.194	0.212
$\partial N/\partial p$	1/sec	-0.352	-0.275	-0.224	-0.137	-0.043	-0.275	-0.137	-0.043
$\partial N/\partial r$	1/sec	-0.590	-0.460	-0.374	-0.231	-0.0718	-0.460	-0.231	-0.0718

The trim conditions for the free-flapping rotor are presented in Table 6. The control trim required for the semi-rigid rotor was much greater than that shown in Table 6. For example, at an advance ratio of $\mu = 0.15$, the control required to trim the semi-rigid rotor was $B_{1Z} = 18.2$ degrees and $A_{1Z} = 7.0$ degrees.

TABLE 6

TRIM CONDITIONS FOR THE KRC-6

WITH FREE-FLAPPING ROTOR

		Advance Ratio		
Variable	Units	$\mu = 0.15$	$\mu = 0.10$	$\mu = 0.05$
a_1	Rad	0.0293	0.0311	0.0174
b_1	Rad	0.0283	0.0403	0.0179
a_o	Rad	0.0242	0.0320	0.0359
B_{1Z}	Rad	0.0919	0.0946	0.0515
A_{1Z}	Rad	-0.105	-0.126	-0.0526
θ	Rad	0.0384	0.0558	0.0698
λ	Rad	0.018	0.020	0.017
α_r	Rad	0.317	0.660	1.225
C_T	---	0.0093	0.0118	0.0130

The physical parameters which do not change as a function of advance ratio are presented in Table 7.

TABLE 7

KRC-6 PHYSICAL PARAMETERS

Parameter	Units	Magnitude
W	Lbs	256.3
m	$\frac{\text{Lbs-Sec}^2}{\text{Ft}}$	7.97
I_x	Slug-Ft^2	46.0
I_y	Slug-Ft^2	46.3
I_z	Slug-Ft^2	6.5
l_t	Ft	4.0
z_t	Ft	2.4
z_r	Ft	2.7
R	Ft	4.0
a	1/Rad	5.73
σ	---	0.159
e	---	0.113
ΩR	Ft/Sec	475

B. AUTOPILOT SYSTEM

The autopilot system in the KRC-6 consists of an attitude gyro, a differentiation circuit for determining angular rates, and electrical actuator for controlling the position of the tilt hub. The pitch and roll commands will be transmitted from the ground control station to a radio receiver

mounted in the KRC-6. A schematic of the stabilization system is presented in Figure 83.

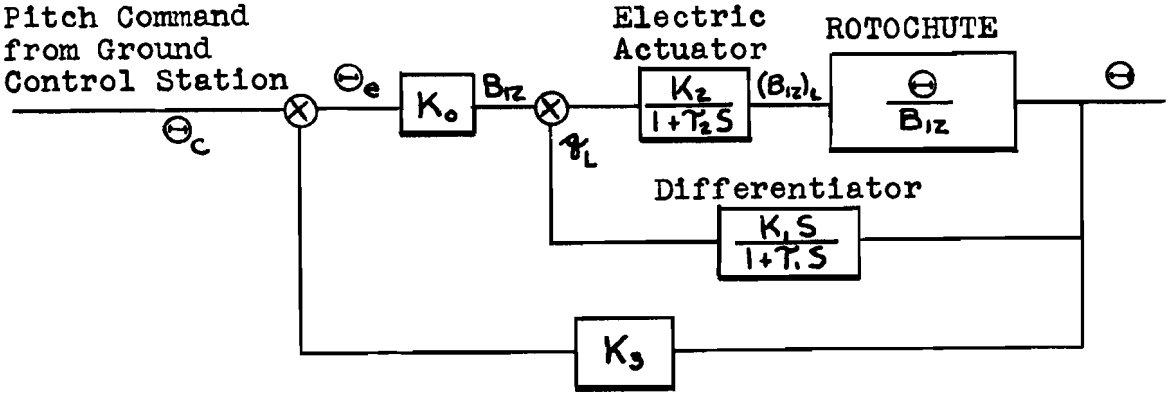

(a) Pitch Stabilization

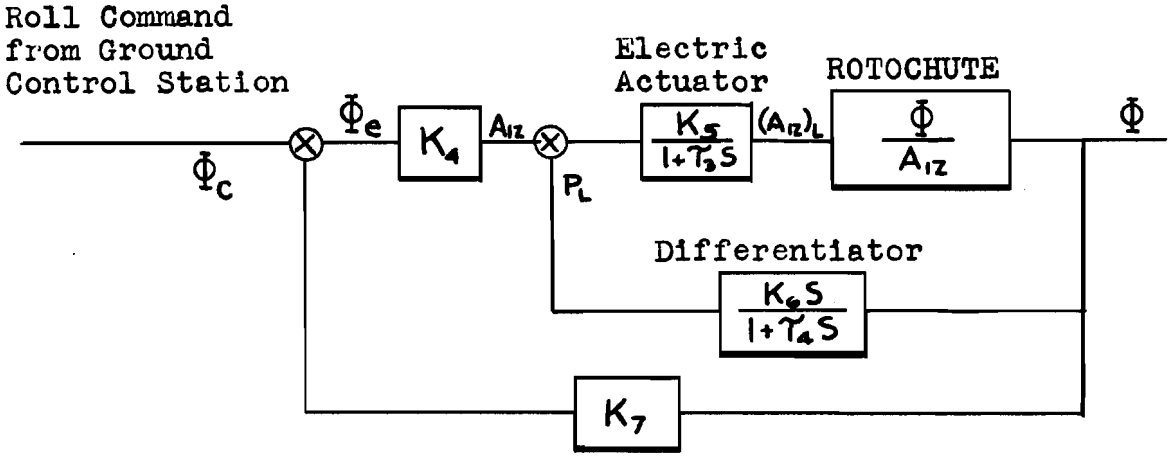

(b) Roll Stabilization

SCHEMATIC DIAGRAM OF AUTO-PILOT SYSTEM

FIGURE 83

Since the ROTOCHUTE is inherently unstable, the auto-pilot system is used for stabilization as well as for maneuvering. As discussed later, the six-degree of freedom equations of motion were set up on the 40-amplifier PACE electronic type analog computer. Simulation of the ROTO-CHUTE with both the semi-rigid and free-flapping rotor was performed. It was necessary during the simulation program to always have the auto-pilot system functioning due to the dynamic instability of the ROTOCHUTE.

From Figure 83, it can be seen that the command variables are pitch and roll attitudes and not control displacements. The equations which determine the longitudinal control displacement are as follows:

$$B_{1Z} = \frac{\partial B_{1Z}}{\partial \Theta} \Theta_e + \frac{\partial B_{1Z}}{\partial q} q_L \tag{10}$$

$$\Theta_e = \Theta - \Theta_C \tag{11}$$

$$(B_{1Z})_L = \frac{B_{1Z}}{1 + \tau_2 S} \tag{12}$$

The above equations can be combined to yield the following:

$$(B_{1Z})_L = \frac{1}{1+\tau_2 S}\left[\frac{\partial B_{1Z}}{\partial \Theta}(\Theta - \Theta_C) + \frac{\partial B_{1Z}}{\partial q} q_L\right] \tag{13}$$

$$= \frac{1}{\tau_2}\int\left[\frac{\partial B_{1Z}}{\partial \Theta}(\Theta - \Theta_C) + \frac{\partial B_{1Z}}{\partial q} q_L - (B_{1Z})_L\right] dt \tag{14}$$

A similar equation exists for defining the lateral control displacement. From the available components, it was estimated that the following system time lags would be encountered.

$\tau_1 = \tau_4 =$ 0.05 sec = differentiation lag

$\tau_2 = \tau_3 =$ 0.25 sec = electric actuator lag

The ROTOCHUTE with the semi-rigid rotor was simulated first on the analog computer. With this rotor, strong aerodynamic and gyroscopic coupling was found to exist. At low advance ratios (below $\mu = 0.10$), a positive pitch rate caused the ROTOCHUTE to roll to the right due to gyroscopic coupling. However, at high advance ratios (above $\mu = 0.10$), the aerodynamic coupling became predominant through the $\partial L / \partial \alpha$ derivative. As a result, a positive pitch rate, which increased angle of attack, caused the ROTOCHUTE to roll to the left. Cross coupling the controls at high advance ratios to reduce aerodynamic coupling tended to re-inforce the gyroscopic coupling at the low advance ratios. Through considerable experimentation, an optimum system of control coupling and system gains was found. The coupling derivatives and optimum gains are presented in Table 8. These gains are compared with those required for the free-flapping rotor.

TABLE 8

AUTO-PILOT COUPLING DERIVATIVES AND OPTIMUM GAINS

Derivatives	Units	Semi-Rigid Rotor Gains	Free-Flapping Rotor Gains
$\frac{\partial B_{1z}}{\partial \Theta}$	deg/deg	+0.75	+0.40
$\frac{\partial B_{1z}}{\partial q}$	$\frac{\text{deg}}{\text{deg/sec}}$	+0.25	+0.25
$\frac{\partial B_{1z}}{\partial A^{\circ}_{1z}}$	$\frac{\text{deg}}{\text{deg/sec}}$	-0.03	----
$\frac{\partial A_{1z}}{\partial \Phi}$	deg/deg	-0.75	-0.40
$\frac{\partial A_{1z}}{\partial P}$	$\frac{\text{deg}}{\text{deg/sec}}$	-0.25	-0.25
$\frac{\partial A_{1z}}{\partial B^{\circ}_{1z}}$	$\frac{\text{deg}}{\text{deg/sec}}$	+0.03	----
$\frac{\partial A_{1z}}{\partial \Theta_e}$	$\frac{\text{deg}}{\text{deg}}$	+2.25	----
$\frac{\partial A_{1z}}{\partial q}$	$\frac{\text{deg}}{\text{deg/sec}}$	+0.75	----

It will be noted in Table 8 that the auto-pilot is less complex for the free-flapping rotor configuration. Also, the attitude feedback gain for the free-flapping rotor was reduced by 47 per cent which improved the auto-pilot stability boundaries.

As a result of the decision to automatically disconnect the synchronizing links after rotor deployment, the analog computer simulation of the auto-pilot was concentrated on the free-flapping rotor system. The effect of varying the auto-pilot gains above and below the nominal values is presented in Figures 84 and 85. The response to a step command in pitch is shown in Figure 84. It will be noted that the ROTOCHUTE is stable over a wide region of rate and attitude gains. The forward speed response (not shown in Figure 84) to a step Θ_c command shows a linear decrease as a function of time. As a result, a control input as a function of time is required to maintain trim conditions due to the change in forward speed. With a constant Θ command, an increase in error signal is required to increase the cyclic pitch control. This is evident from the following expression.

$$B_{1Z} = \frac{\partial B_{1Z}}{\partial \Theta}(\Theta - \Theta_c) + \frac{\partial B_{1Z}}{\partial q} q_L \qquad (15)$$

For a constant Θ_c command and no pitch rate, the incremental change in cyclic pitch with respect to pitch attitude change is as follows.

$$\Delta B_{1Z} = \frac{\partial B_{1Z}}{\partial \Theta} \Delta \Theta \qquad (16)$$

Thus, as the forward speed changes, a change in pitch attitude is required for the auto-pilot to generate a trim control signal. An increase in gain will reduce the steady-state error.

During the roll command maneuver shown in Figure 85, a negligible speed change is incurred. As a result, the roll attitude response reaches a steady-state value. The roll response is stable for the complete range of gains considered in Figure 85.

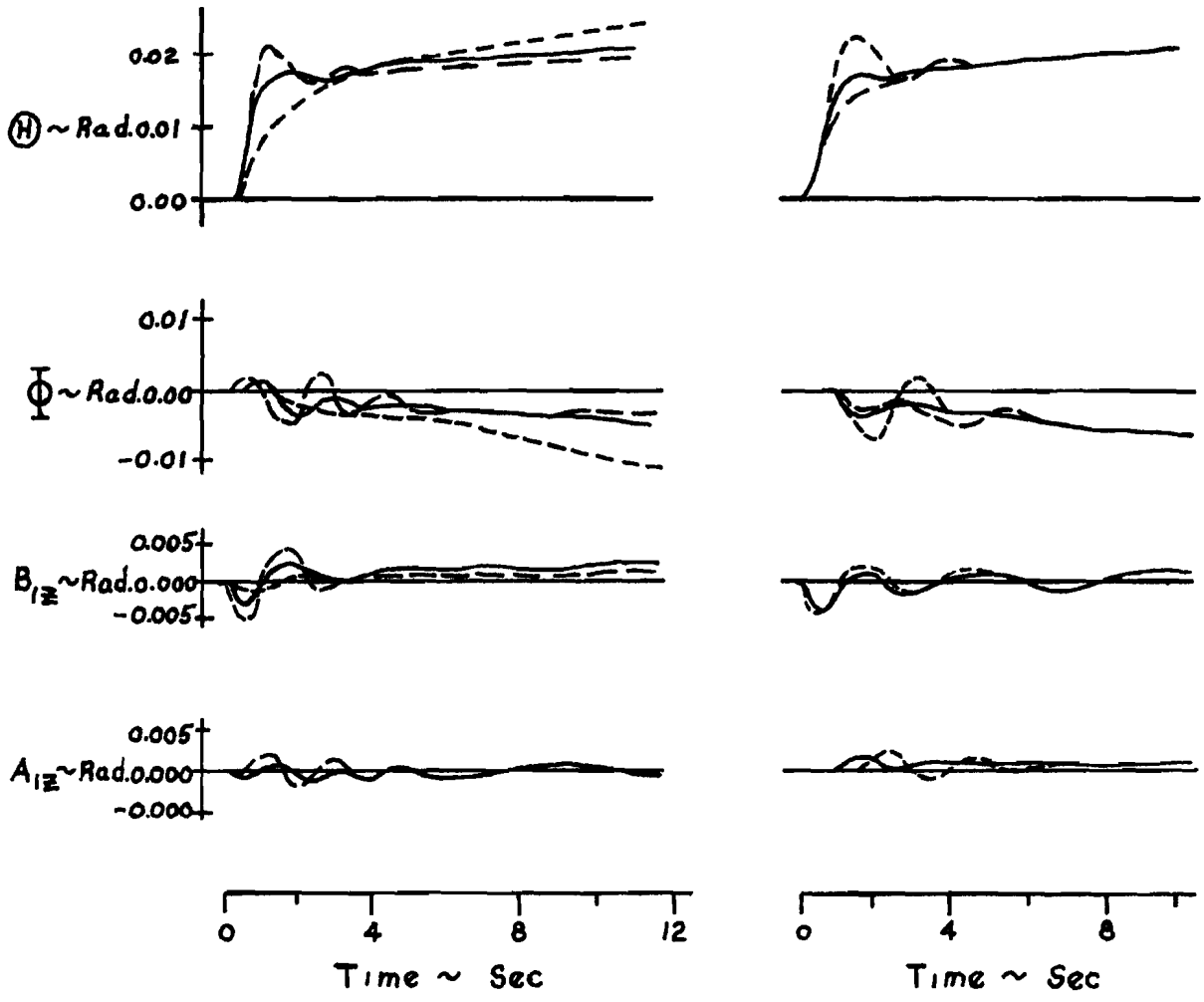

(a) Effect of Varying Attitude Gains

$\frac{\partial B_{1z}}{\partial q} = \frac{\partial A_{1z}}{\partial P} = 0.25 \frac{\text{deg.}}{\text{deg./sec.}}$

—— $\frac{\partial B_{1z}}{\partial \Theta} \quad \frac{\partial A_{1z}}{\partial \Phi} = 0.40 \frac{\text{deg.}}{\text{deg.}}$

— — $\frac{\partial B_{1z}}{\partial \Theta} \quad \frac{\partial A_{1z}}{\partial \Phi} = 0.60 \frac{\text{deg.}}{\text{deg.}}$

— — — $\frac{\partial B_{1z}}{\partial \Theta} \quad \frac{\partial A_{1z}}{\partial \Phi} = 0.20 \frac{\text{deg.}}{\text{deg.}}$

(b) Effect of Varying Rate Gains

$\frac{\partial B_{1z}}{\partial \Theta} = \frac{\partial A_{1z}}{\partial \Phi} = 0.40 \frac{\text{deg.}}{\text{deg.}}$

—— $\frac{\partial B_{1z}}{\partial q} \quad \frac{\partial A_{1z}}{\partial P} = 0.25 \frac{\text{deg.}}{\text{deg./sec.}}$

— — $\frac{\partial B_{1z}}{\partial q} \quad \frac{\partial A_{1z}}{\partial P} = 0.35 \frac{\text{deg.}}{\text{deg./sec.}}$

— — — $\frac{\partial B_{1z}}{\partial q} \quad \frac{\partial A_{1z}}{\partial P} = 0.15 \frac{\text{deg.}}{\text{deg./sec.}}$

EFFECT OF VARYING AUTOPILOT GAINS
(Θ_c = .0175 rad, μ = .15)

FIGURE 84

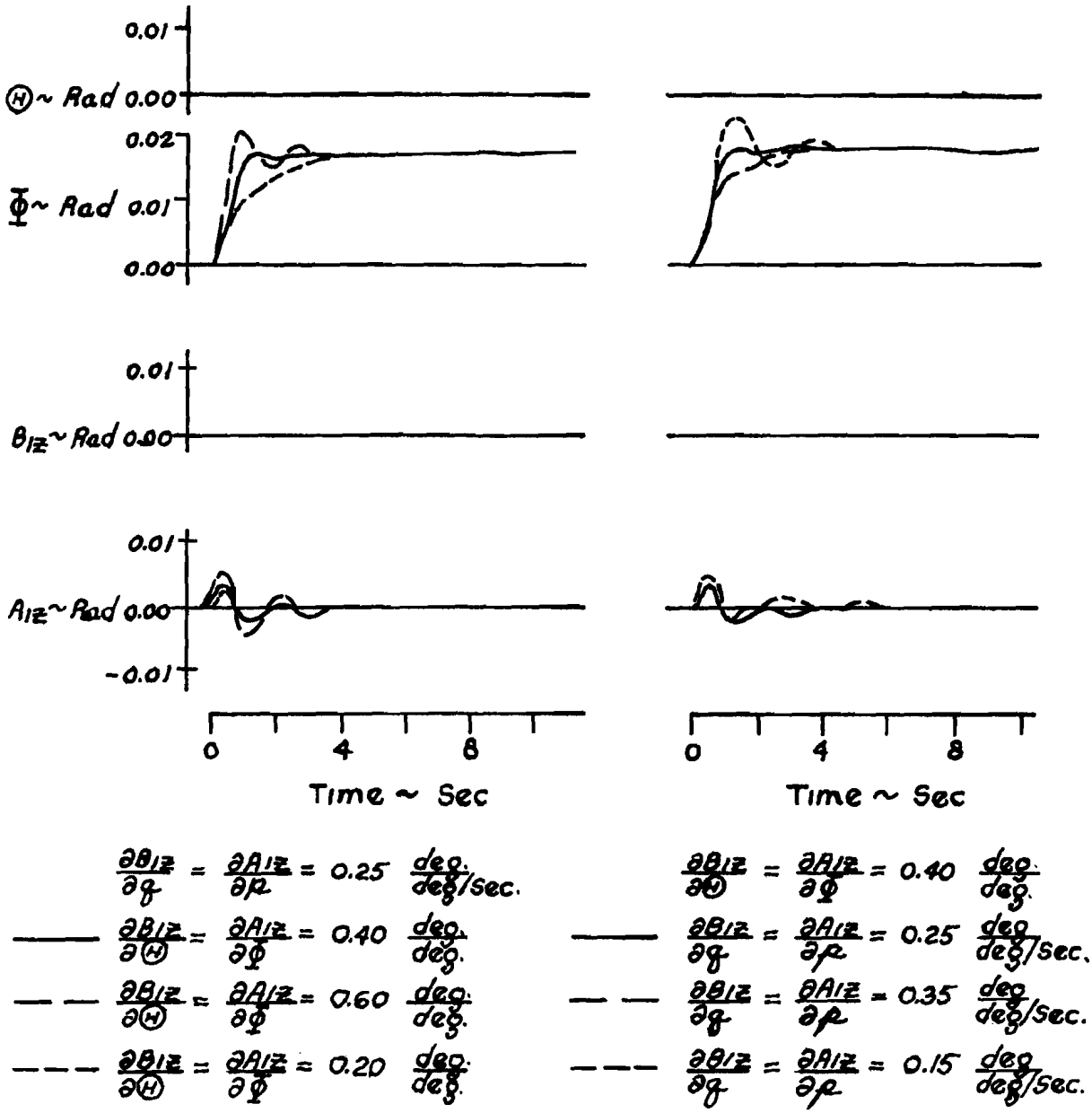

(a) Effect of Varying Attitude Gains (b) Effect of Varying Rate Gains

EFFECT OF VARYING AUTOPILOT GAINS
(Φ_c = .0175 rad, μ = .15)

FIGURE 85

C. ANALOG COMPUTER SIMULATION

The analog computer program was performed in three parts. The first part considered the dynamics of the ROTOCHUTE with free-flapping rotor blades. For the rigid body configuration of six degrees of freedom, constant coefficients were used during the analysis. The second area of this study was concerned with the semi-rigid rotor. This case involved a high degree of coupling between the lateral and longitudinal equations. The third part of the study concerned maneuvering the ROTOCHUTE during a simulated flare maneuver. Six-degree of freedom equations of motion with non-linear coefficients were used on the analog computer during the maneuver simulation. A successful technique for flaring the ROTOCHUTE during the landing maneuver was developed.

1. Simulation With Free-Flapping Blades

The PACE electronic type analog computer was used during the simulation studies of the ROTOCHUTE. Equations (1) through (8) were solved for the highest order derivatives and then each equation was integrated. The stability derivatives in Table 5 were converted to machine variables. This involved transforming the real variables in terms of physical units into machine voltages. It was necessary to estimate the maximum expected range of the variables and these values were used to calculate the scaling factor.

Perturbation responses were obtained at advance ratios of $\mu = 0.15$, 0.10, and 0.05. The ROTOCHUTE responses to both pitch and roll attitude commands are shown in Figures 86 through 91. As discussed in the preceding section, a step pitch attitude command results in a linear drop off in forward speed. Due to the speed derivatives, a change in longitudinal control is required as the forward speed is reduced. The only steady-state input to the longitudinal control is through the attitude error signal θ_e. From Equation (10) it can be seen that if B_{1Z} is a function of forward speed, then θ_e must also be a function of forward speed. It therefore follows from Equation (11) that for θ_c equal to a constant, θ must also vary with forward speed. The fact that θ does not stay constant through the speed range is not considered a serious problem, since in actual practice the command can also be changed as a function of speed if desired. In a simulated landing maneuver discussed later, the ability to hold constant attitude is not critical.

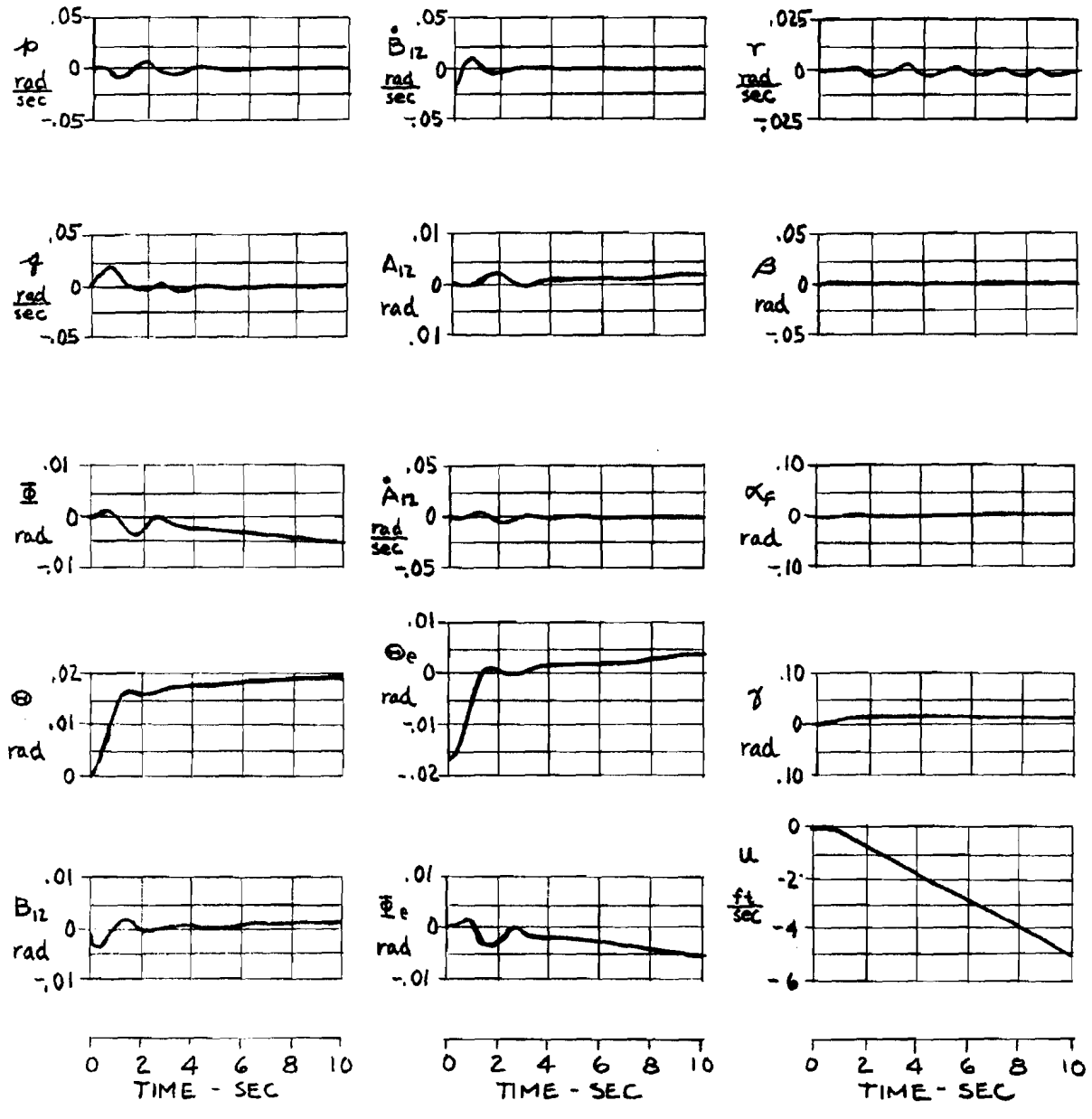

KRC-6 RESPONSE TO A ONE-DEGREE θ COMMAND

(μ = .15)

FIGURE 86

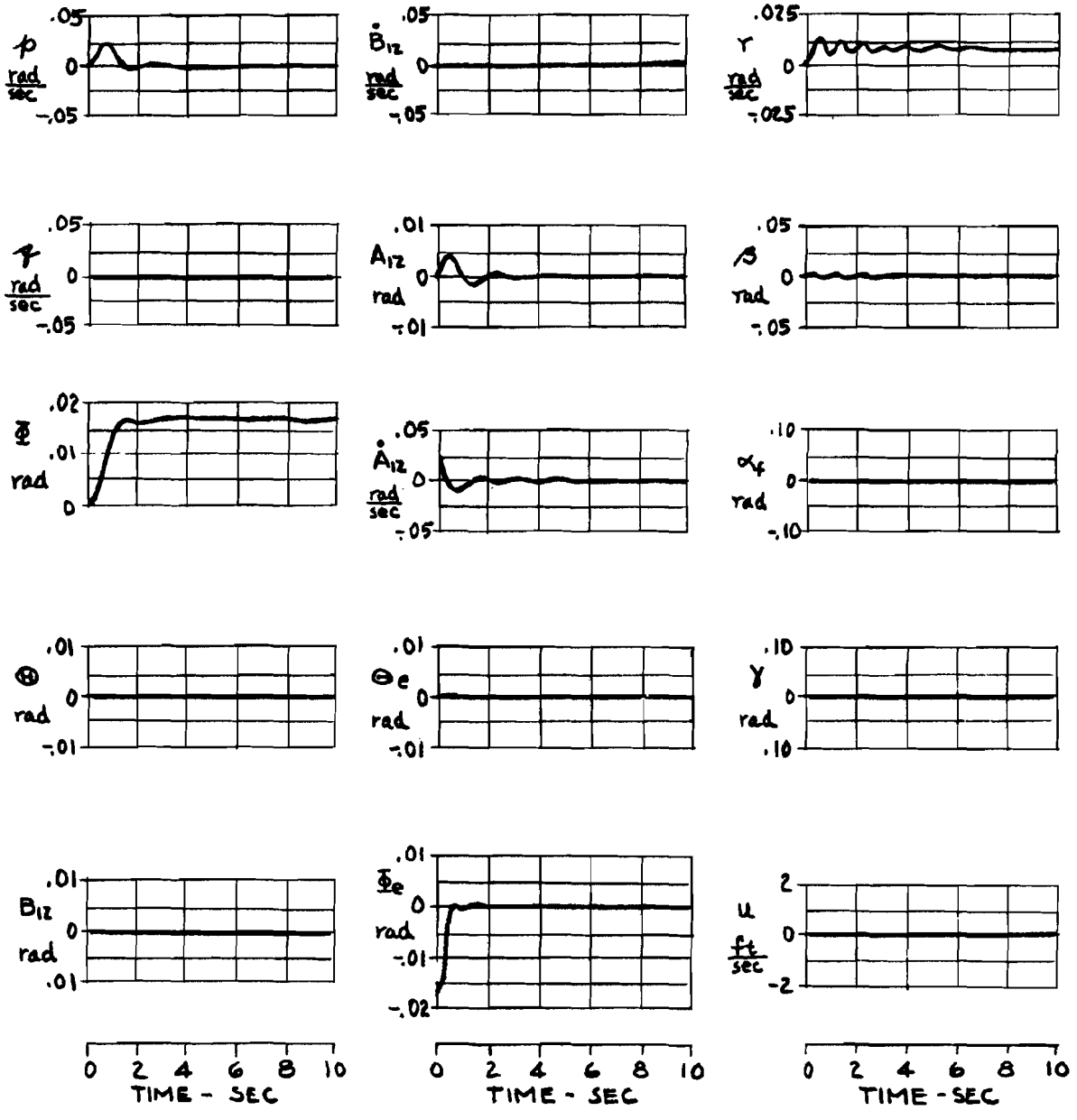

KRC-6 RESPONSE TO A ONE-DEGREE $\bar{\Phi}$ COMMAND

(μ = .15)

FIGURE 87

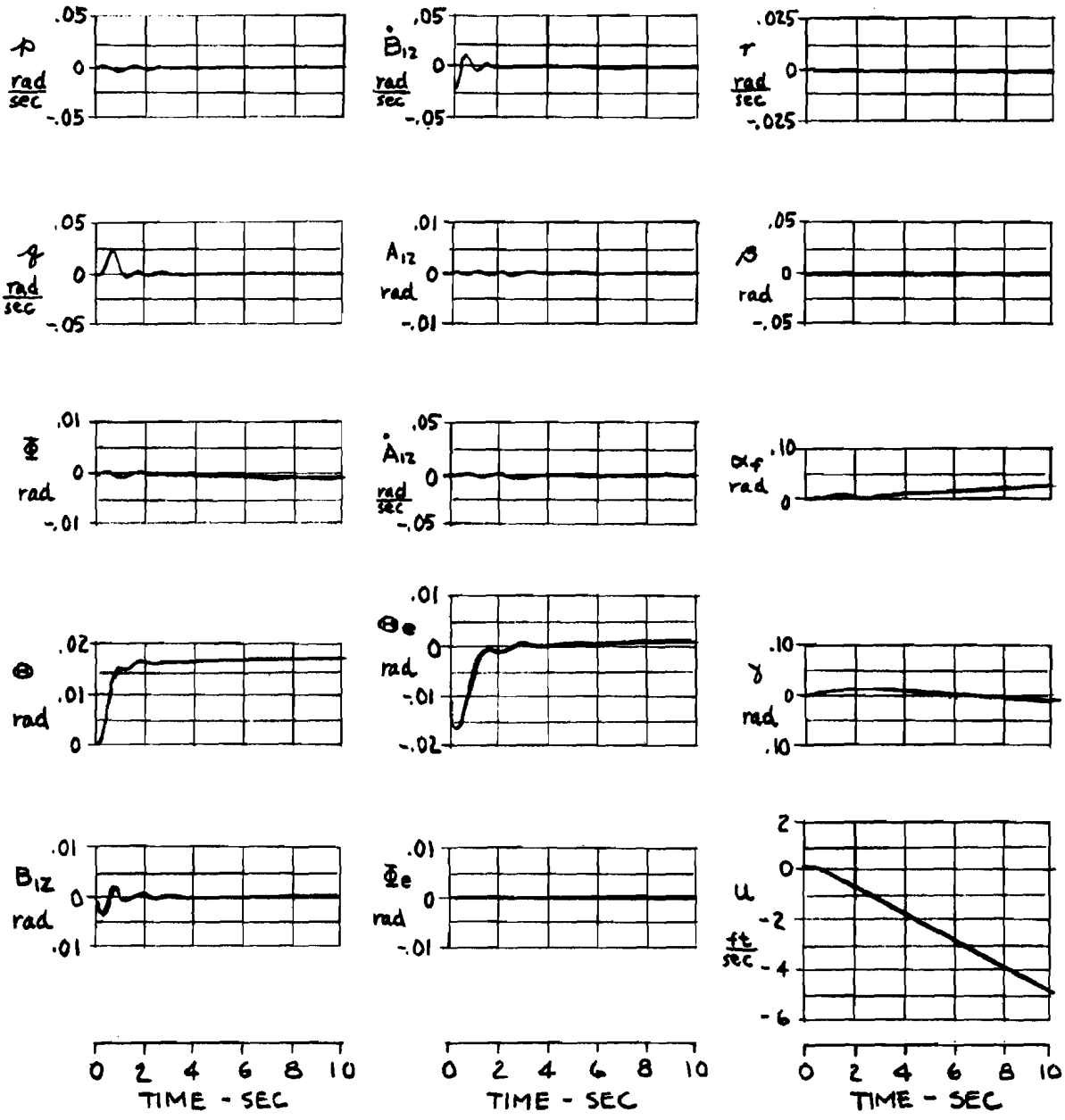

KRC-6 RESPONSE TO A ONE-DEGREE θ COMMAND

(μ = .10)

FIGURE 88

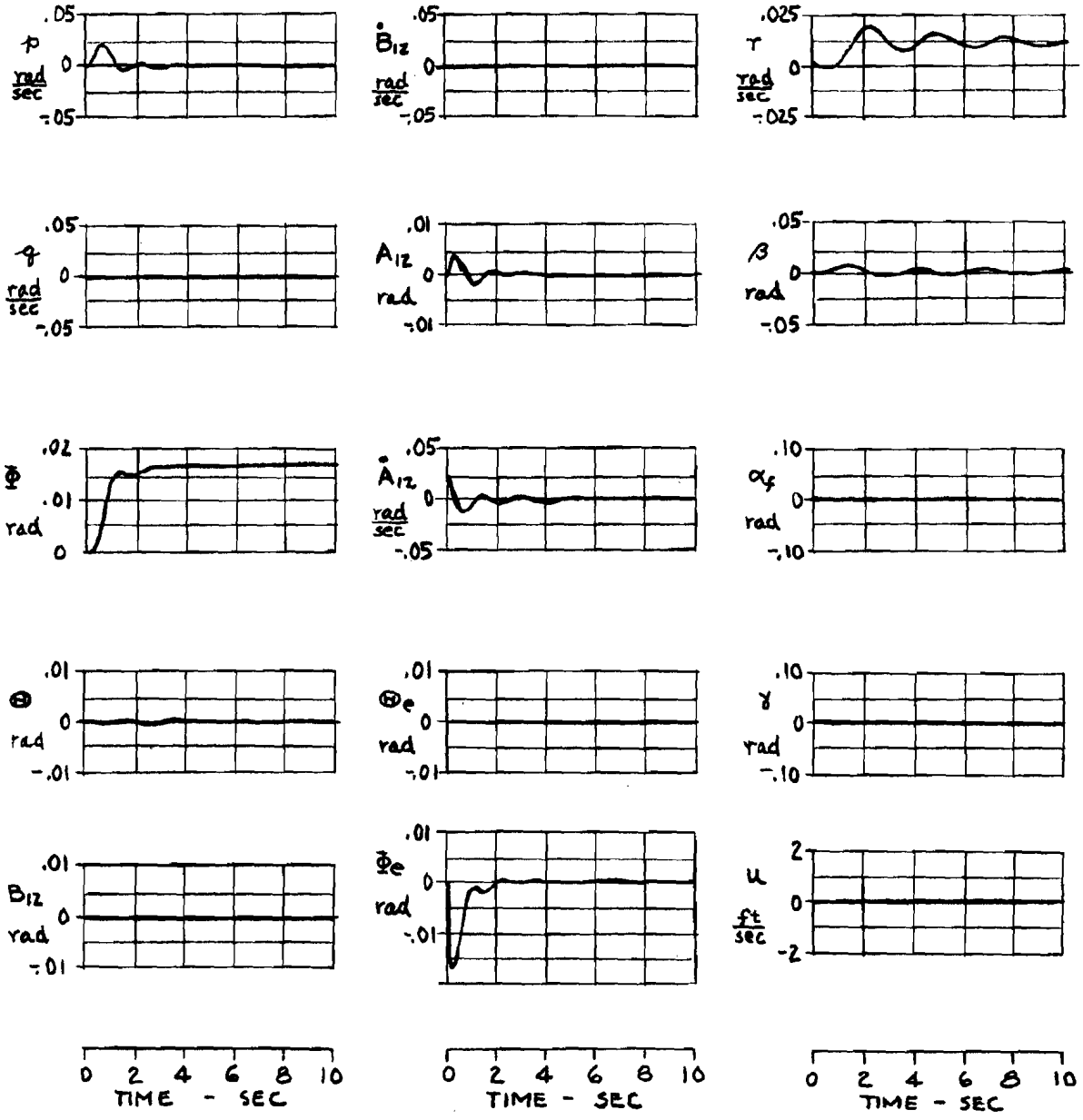

KRC-6 RESPONSE TO A ONE-DEGREE Φ COMMAND

(μ = .10)

FIGURE 89

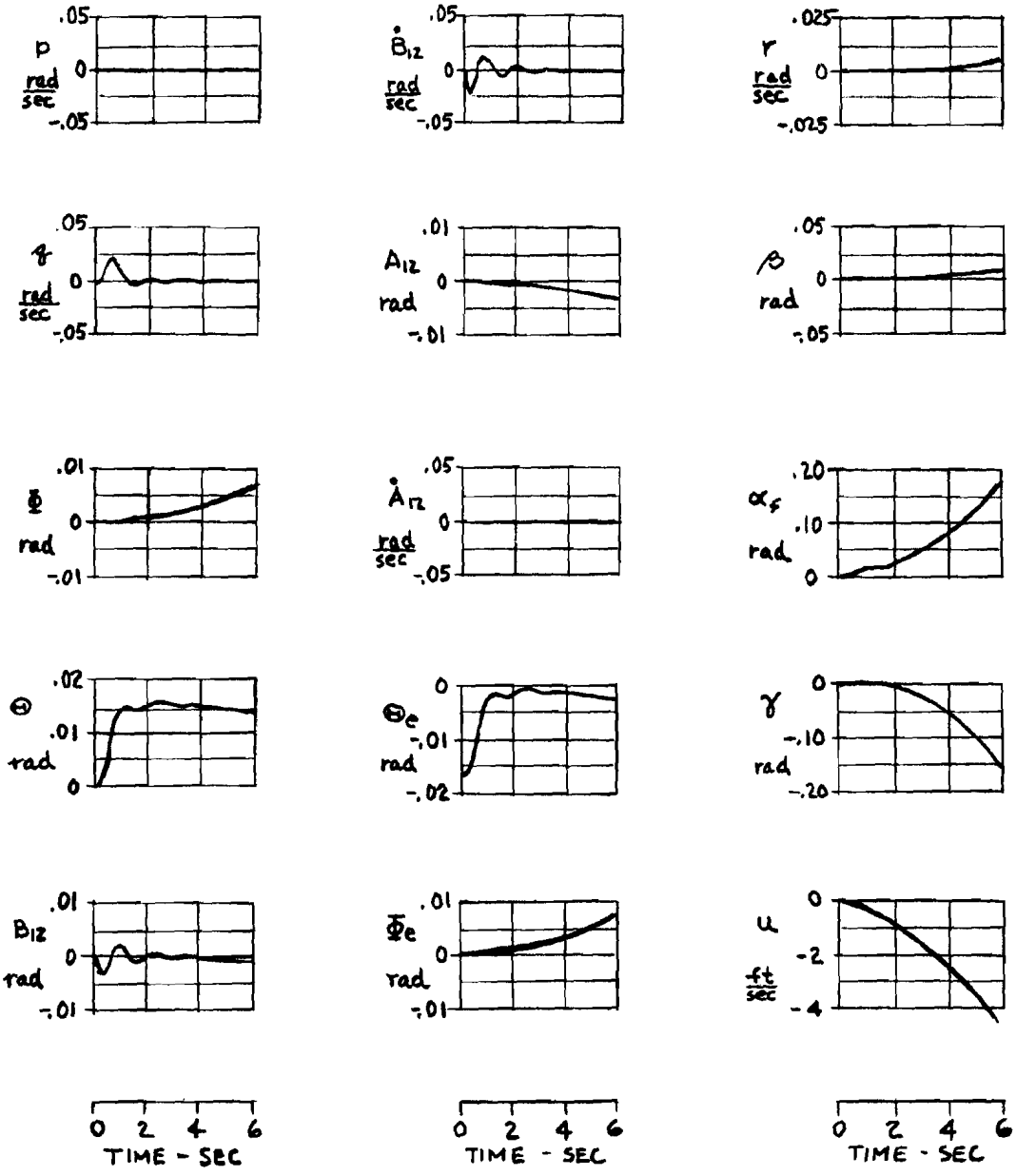

KRC-6 RESPONSE TO A ONE-DEGREE Θ COMMAND

(μ = .05)

FIGURE 90

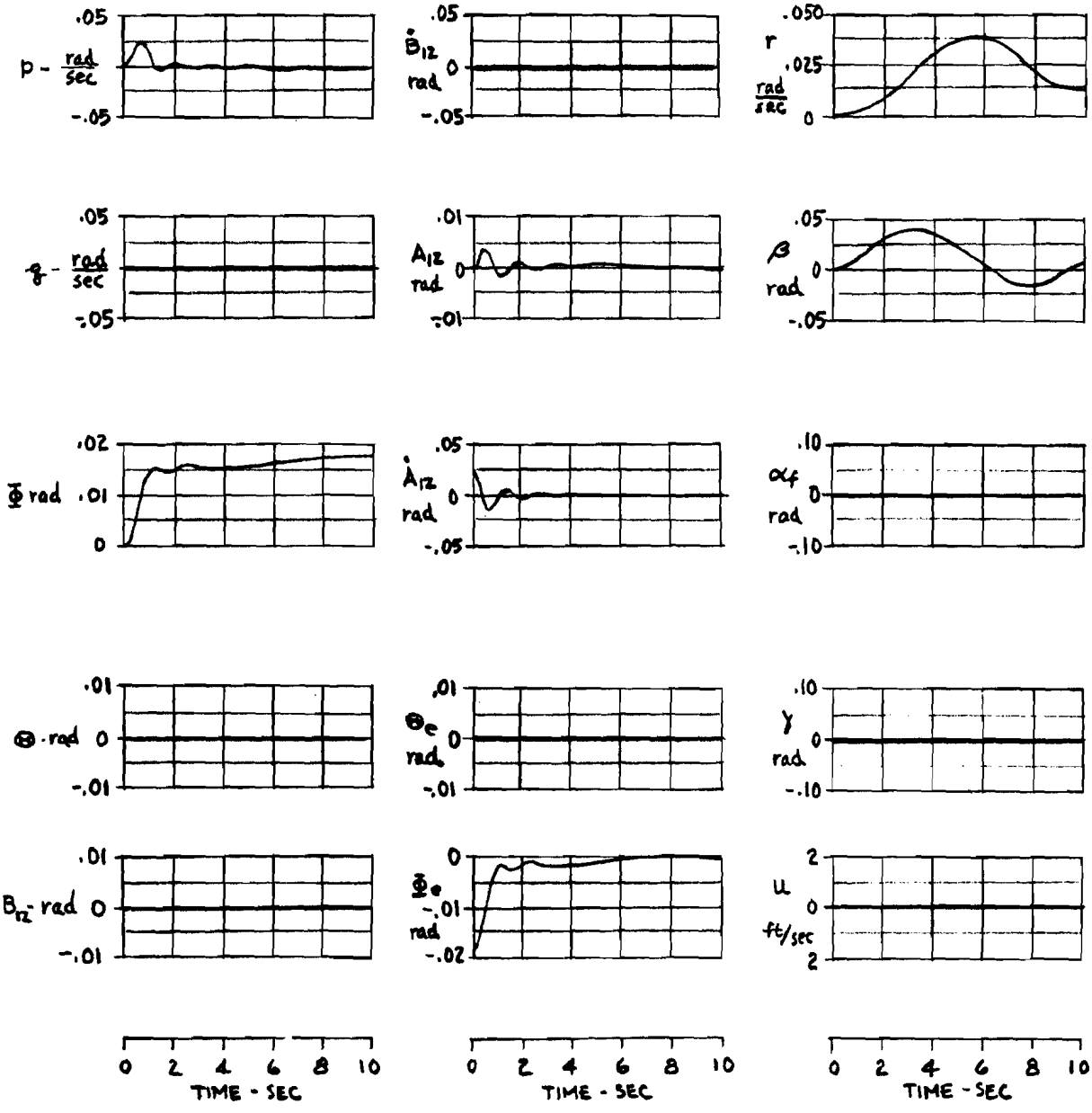

KRC-6 RESPONSE TO A ONE-DEGREE Φ COMMAND

(μ = .05)

FIGURE 91

At advance ratios of $\mu = 0.15$ and 0.10, the ROTOCHUTE with the auto-pilot functioning is stable in all modes. As previously shown, wide changes in auto-pilot gains do not result in any instabilities. However, at an advance ratio of $\mu = 0.05$, an instability in forward speed and angle of attack is encountered with the six-degree of freedom linear equations. This can be seen in Figure 90. This is a basic instability that cannot be controlled with attitude and rate feedbacks. The origin of this instability can be seen by examining the uncoupled longitudinal equations of motion. If a perfect auto-pilot is assumed, then $\dot{q} = q = \Delta\theta = 0$. For this case described, Equations (1), (3), and (5) can be written as follows:

$$\dot{u} = \frac{\partial x}{\partial \mu}\mu + \frac{\partial x}{\partial \alpha}\Delta\alpha_f + \frac{\partial x}{\partial B_{12}}B_{12} \qquad (17)$$

$$\dot{\alpha}_f = \frac{\partial z}{\partial \mu}\mu + \frac{\partial z}{\partial \alpha}\Delta\alpha_f + \frac{\partial z}{\partial B_{12}}B_{12} \qquad (18)$$

The determinant of the characteristic equation can now be written.

$$\Delta = \begin{vmatrix} \frac{\partial x}{\partial \mu} - S & \frac{\partial x}{\partial \alpha} \\ \frac{\partial z}{\partial \mu} & \frac{\partial z}{\partial \alpha} - S \end{vmatrix} = 0 \qquad (19)$$

An expansion of (19) results in a quadratic of the following form.

$$S^2 - \left(\frac{\partial z}{\partial \alpha} + \frac{\partial x}{\partial \mu}\right)S + \left(\frac{\partial z}{\partial \alpha}\frac{\partial x}{\partial \mu} - \frac{\partial z}{\partial \mu}\frac{\partial x}{\partial \alpha}\right) = 0 \qquad (20)$$

Equation (20) is a second-order equation with a spring constant equal to $(\partial z/\partial \alpha)(\partial x/\partial \mu) - (\partial z/\partial \mu)(\partial x/\partial \alpha)$. In order for Equation (19) to be stable it is necessary that the spring term be positive, i.e. $(\partial z/\partial \alpha)(\partial x/\partial \mu) > (\partial z/\partial \mu)(\partial x/\partial \alpha)$. However, at low advance ratios ($\mu = 0.05$), the $(\partial z/\partial \mu)$ derivative becomes large (see Table 5) and the spring becomes negative. For the free-flapping rotor at an advance ratio of $\mu = 0.05$, the roots of Equations (20) are $\lambda_1 = +1.65$ and $\lambda_2 = -11.95$. The positive real root results as a divergence in angle of attack and speed. This instability in speed and angle of attack, with fixed pitch attitude, is not serious in terms of physically landing the ROTOCHUTE. As the ROTOCHUTE forward speed drops off, the large $(\partial z/\partial \mu)$ derivative causes the lift to decrease rapidly. The loss in lift requires an increase in sink speed and a resulting increase in angle of attack. The increase angle of attack causes more drag which further slows the ROTOCHUTE and the divergence continues. During the simulated non-linear flare maneuver, discussed later, this divergence results in speeding up the flare near-zero airspeed before the application of collective pitch (see Figure 94). This instability may well be a characteristic of autorotating helicopters at low airspeeds with fixed collective pitch.

2. Simulation With Semi-Rigid Blades

Considerable lateral-longitudinal coupling was evident with the semi-rigid rotor configuration. With reference to Table 5, it can be shown that the important coupling derivatives are $(\partial L/\partial \alpha)$, $(\partial L/\partial \mu)$, $(\partial L/\partial q)$, and $(\partial M/\partial p)$. At the highest advance ratio considered during the simulation ($\mu = 0.205$), the influence of the $(\partial L/\partial \alpha)$ was particularly important. A nose-up pitch command caused an increase in rotor angle of attack. An increase in angle of attack then generated a strong negative rolling moment. By cross-coupling the auto-pilot commands, it was possible to apply the proper lateral control to balance this moment at $\mu = 0.205$. However, since it was desired not to change the auto-pilot gains as a function of advance ratio, the same control coupling existed at the lower advance ratios. This coupling was in the direction to increase the roll excursions during the speed drop off assoicated with the flare maneuver. However, the system was stable in pitch and roll throughout the speed range.

Figure 92 presents the ROTOCHUTE response to a one-degree step pitch attitude command at two different advance ratios. The auto-pilot gains used during these simulations are presented in Table 8. The gains were adjusted to favor the higher ratio, since this corresponds to the advance ratio used during the glide phase. The lower advance ratio would be encountered during the flare transient before landing. The flare maneuver is discussed in the following paragraphs.

3. Non-Linear Simulated Flare Maneuver

During the non-linear simulation of the ROTOCHUTE, the derivatives with significant variations with respect to advance ratio were programmed on function multipliers. The servo-motors associated with the function multipliers were driven by the advance ratio (μ) voltage. With this setup, it was possible to simulate flare maneuvers where large speed variations were encountered. The semi-rigid rotor derivatives were used during this analysis. With the exception of the ASE control inputs, the general characteristics of this maneuver should also be true for the free-flapping rotor.

Figure 93 presents a simulated flare maneuver. The initial trim forward speed was 76 feet per second ($\mu = 0.16$). The technique used in performing the flare was to command 23-degree nose-up θ command. Following this command, the forward speed dropped off in a linear manner. At a forward speed of about 8 feet per second, the attitude command was removed. At this point, collective pitch should be applied prior to touchdown. The complete maneuver was performed in about nine seconds. The lateral ASE appears capable of satisfactorily controlling roll attitude and heading during this maneuver. Lateral commands could be applied, if desired, to further reduce the roll excursion.

Figure 94 presents a plot of the trajectory profile during the flare maneuver. The divergence in flight path angle is apparent for $t > 6$ seconds. The initiation of the flare maneuver was at an altitude of 85 feet and required a ground distance of 330 feet to arrest forward speed. Again, the attitude command was for a 23-degree nose-up pitch attitude.

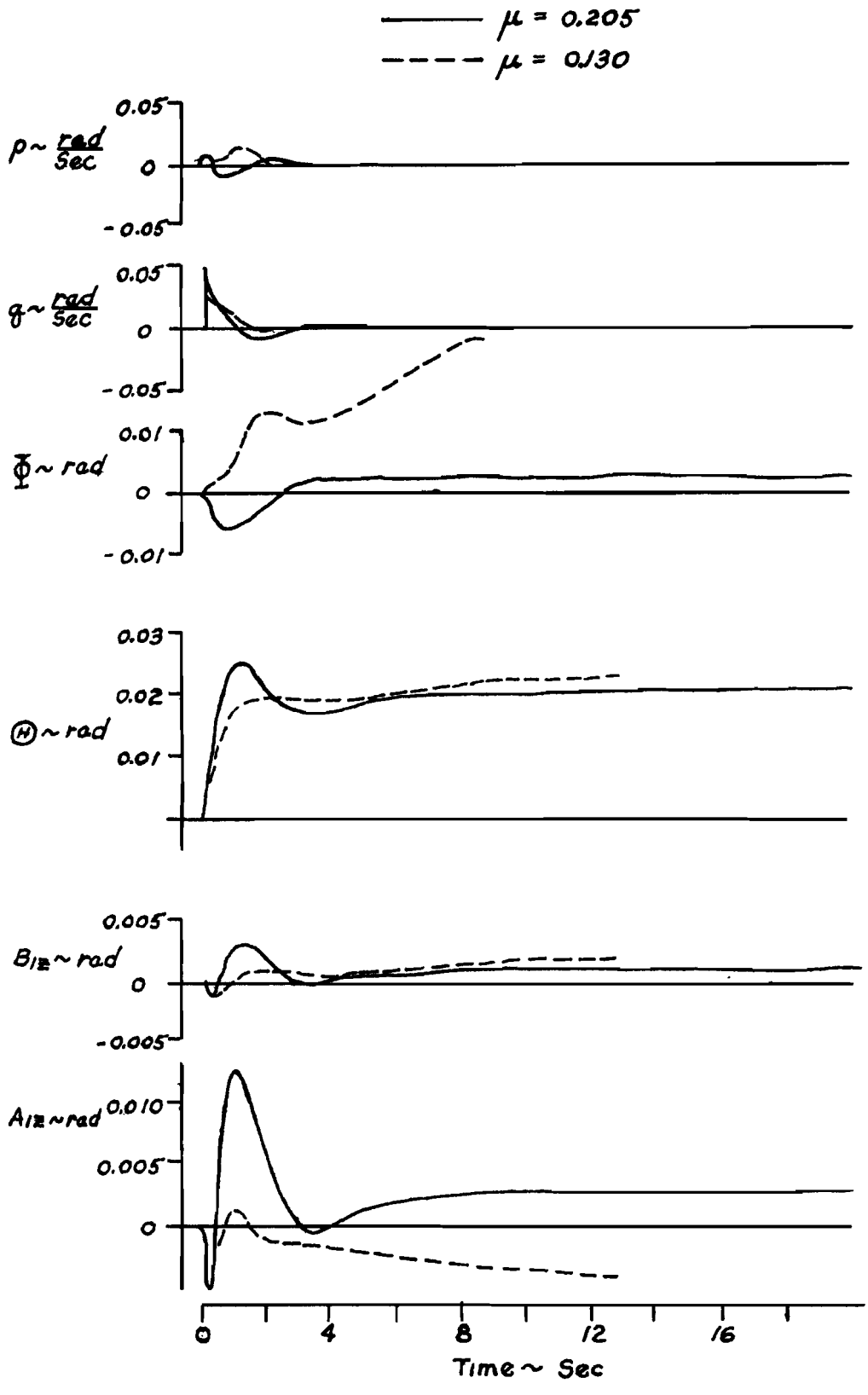

RESPONSE TO A ONE DEGREE ATTITUDE COMMAND
(SEMI-RIGID ROTOR)

FIGURE 92

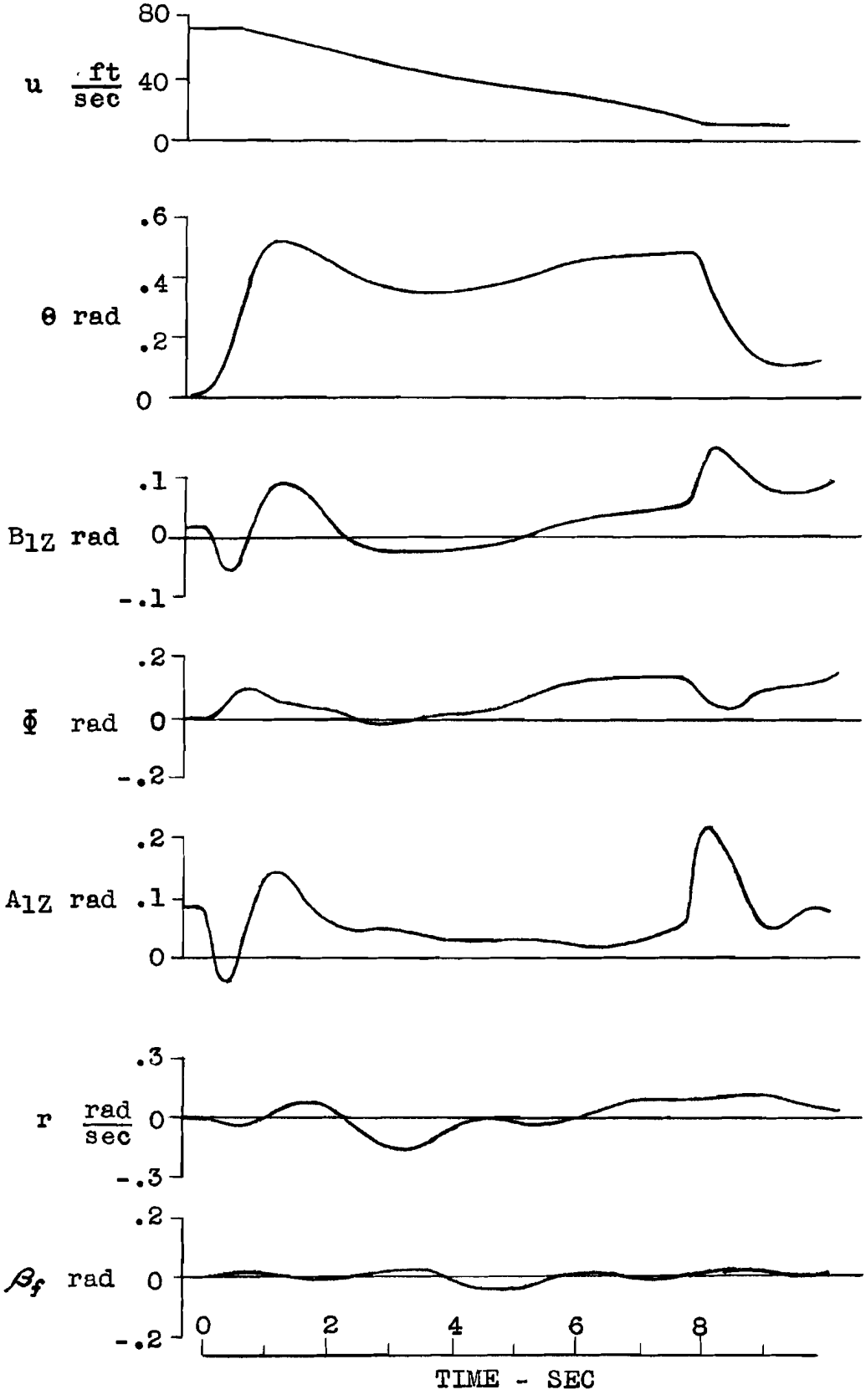

NON-LINEAR RESPONSE TO A 23 DEGREE θ_c COMMAND
(FLARE SIMULATION)

FIGURE 93

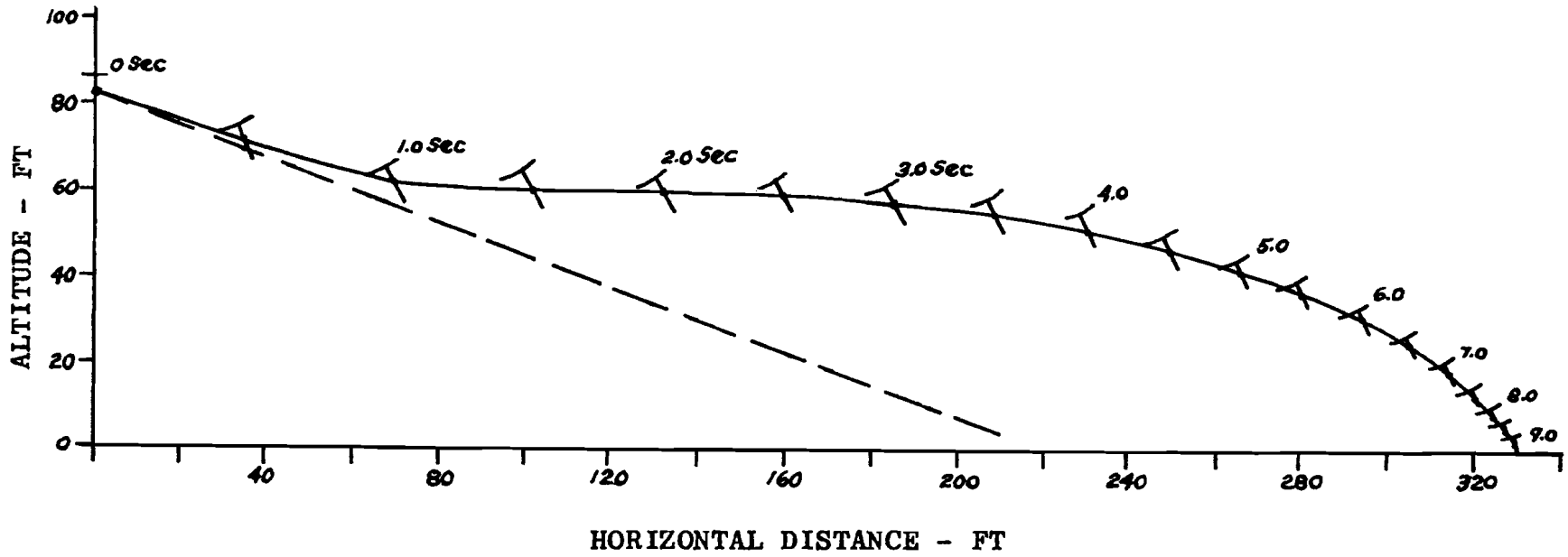

TRAJECTORY PROFILE DURING FLARE MANEUVER

FIGURE 94

The ROTOCHUTE response to a 23-degree roll command is shown in Figure 95. The directional control of the ROTOCHUTE is obtained by means of roll control. The steady-state yaw rate per roll attitude amounts to about $(r/\Phi)_{ss} \cong 0.5$ deg/sec/deg at $\mu = 0.16$. For the roll command shown in Figure 95, it would require about 16 seconds to perform 180 degree turn maneuver. With a rate of descent of 32 feet per second, the total altitude lost during a 180-degree turn would be about 510 feet or roughly 1000 feet per 360 degree turn.

4. Comparison Between Free-Flapping and Restrained Flapping Blades

In a valid comparison between the free-flapping rotor and the semi-rigid blade rotor, both the static trim and dynamic characteristics must be considered. Due to the large longitudinal hub moment and relatively low control power with the tilt hub, the control for trim is excessively high for the semi-rigid rotor. A comparison between the control required for trim for the free-flapping and semi-rigid rotors is shown in Table 9.

TABLE 9

COMPARISON OF CONTROL REQUIRED FOR TRIM AT $\mu = 0.15$

Configuration	B_{1Z}	A_{1Z}
Free-Flapping Rotor	+5.3 degrees	-6.0 degrees
Semi-Rigid Blade Rotor	+18.2 degrees	+7.0 degrees

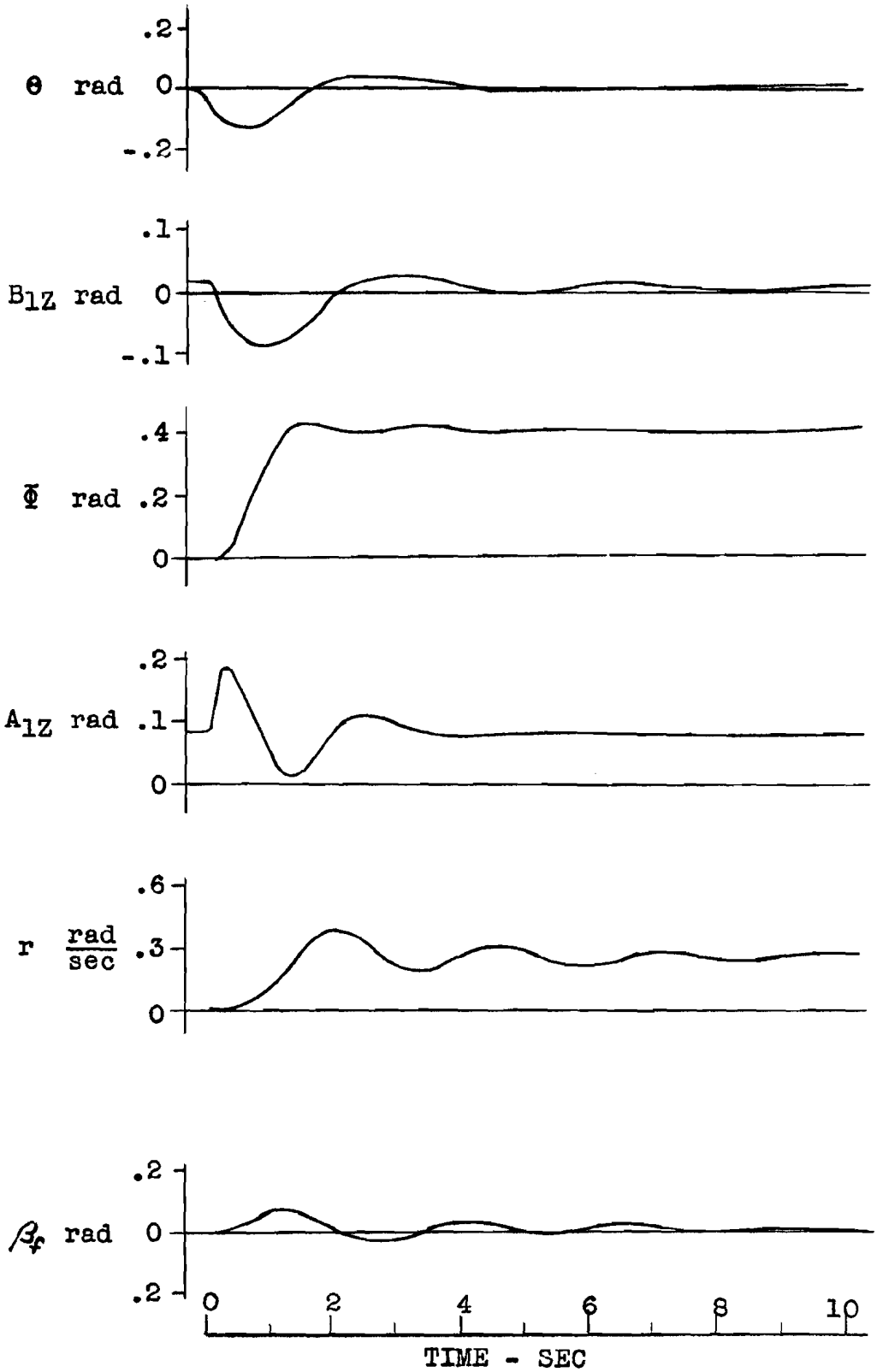

NON-LINEAR RESPONSE TO A 23 DEGREE Φ COMMAND
(u = .16)

FIGURE 95

Due to clearance restrictions, the hub of the KRC-6 does not have sufficient travel for trim using the semi-rigid rotor.

The response of the KRC-6 to a one-degree pitch command for both rotor systems at $\mu = 0.15$ is shown in Figure 96. It will be noted that with the free-flapping rotor the roll couples to the left. However, the roll coupling reverses sign with the semi-rigid rotor. The reason for this can be seen by examining the $(\partial L/\partial \alpha)$ and $(\partial L/\partial \mu)$ derivatives in Table 5. For the semi-rigid rotor, the following inequality exists.

$$\left|\left(-\frac{\partial L}{\partial \mu}\right)(-\mu)\right| > \left|\left(-\frac{\partial L}{\partial \alpha}\right)(+\Delta\alpha_f)\right| \qquad (21)$$

Therefore, a steady-state positive rolling moment exists which causes a positive roll altitude.

For the free-flapping rotor, the following is true.

$$\left|\left(-\frac{\partial L}{\partial \mu}\right)(-\mu)\right| < \left|\left(-\frac{\partial L}{\partial \alpha}\right)(+\Delta\alpha_f)\right| \qquad (22)$$

From Equation (22), it can be seen that the steady-state rolling moment with the free-flapping rotor is negative. This results in a negative roll attitude. The key derivative which experiences the largest change is the $(\partial L/\partial \mu)$ derivative.

The magnitude of lateral control required to laterally stabilize the ROTOCHUTE is much greater with the semi-rigid blades.

CONCLUSIONS

Based on the analog computer studies discussed in the preceding paragraphs, certain conclusions can be drawn.

First, the ROTOCHUTE is dynamically unstable during the glide and flare modes without ASE. However, since an auto-pilot is required for maneuvering the KRC-6, the feedback loops can be made to provide satisfactory artificial stabilization.

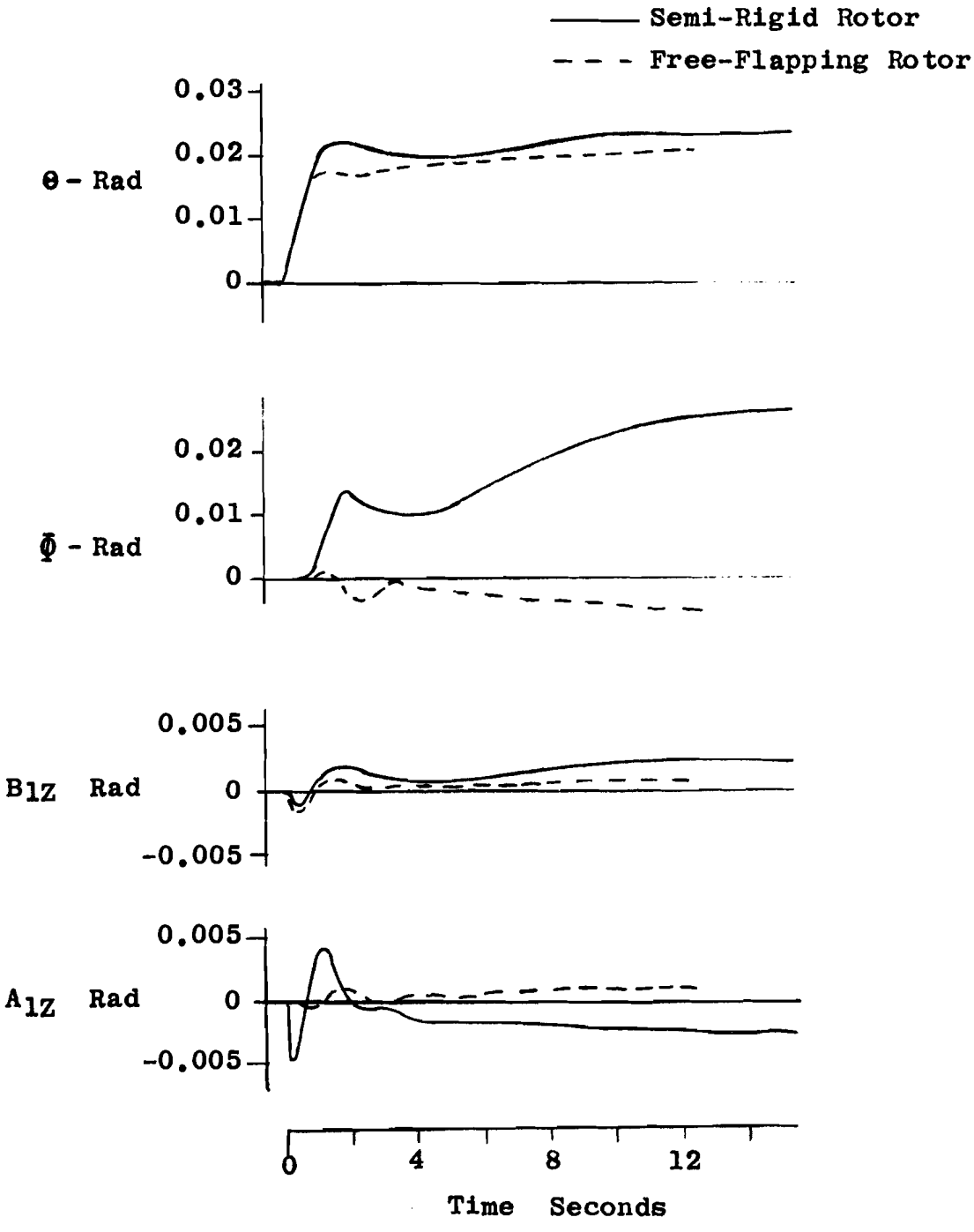

COMPARISON BETWEEN RESPONSE OF ROTOCHUTE WITH SEMI-RIGID ROTOR AND FREE-FLAPPING ROTOR

(μ = 0.15)

FIGURE 96

Second, it is highly desirable to have the blades free-flapping during the glide and flare modes of operation. This conclusion is based on both static trim and dynamic stability considerations.

Third, a reasonable flare maneuver was performed by holding anose-up pitch command of 23 degrees for nine seconds. This maneuver was initiated at an altitude of 85 feet. The ROTOCHUTE was laterally stabilized with the ASE within acceptable limits.

Fourth, during the aerodynamic analysis, it was essential that non-uniform inflow be considered. This conclusion is particularly applicable to the semi-rigid rotor configuration.

Fifth, with the free-flapping blades, the auto-pilot constants can be varied through wide limits without encountering gain instabilities.

APPENDIX III. ELECTRONIC EQUIPMENT DESIGN

A. AUTO-PILOT CONTROL SYSTEM

The stabilization and command input system for the KRC-6 ROTOCHUTE was designed to incorporate electronic hardware purchased for this purpose under Contract Number AF33(616)-7544. A brief description of the electrical characteristics of this equipment is presented in Table 10.

The optimum transfer function for the over-all auto-pilot system was determined by an analog computer study (Reference, Appendix II). In addition to providing the anticipated response characteristics of a ROTOCHUTE employing the optimum characteristics specified below, the report also assures acceptable operation for variations in attitude gain of ±50 per cent and variations in rate gain of ±40 per cent.

TABLE 10

ELECTRONIC EQUIPMENT GAINS

Component	Maximum Transfer Ratio	Limits
Vertical Gyro Pitch or Roll Attitude	0.206 $\frac{\text{Volts RMS}}{\text{deg } \theta}$	$\pm 85^{\circ}$ travel of inner gimbals
Learsyn (Servo Position Feedback)	0.043 $\frac{\text{Volts RMS}}{\text{deg } \alpha}$	$\pm 30^{\circ}$ pitch and roll
Tachometer (Servo Rate Feedback)	0.00067 $\frac{\text{Volts RMS}}{\text{deg } \alpha/\text{sec}}$	
Lear Servo Amplifier Derivative Channel $\frac{KmS}{TS+1}$	$\frac{800S}{(0.1S+1)}$ $\frac{\text{Volts DC}}{\text{Volt RMS}}$	0.218 volts RMS input
Kn - Proportional	340 $\frac{\text{Volts DC}}{\text{Volt RMS}}$	
Kz - Common Amplifier	0.13 $\frac{\text{Milliamps}}{\text{Volt DC}}$	
Command Input Directional Gyro Resolver Output	2.5 VRMS + A ϕ -2.5 VRMS -A ϕ	Maximum proportional signal

Pitch Stabilization (Free-flapping Rotor)

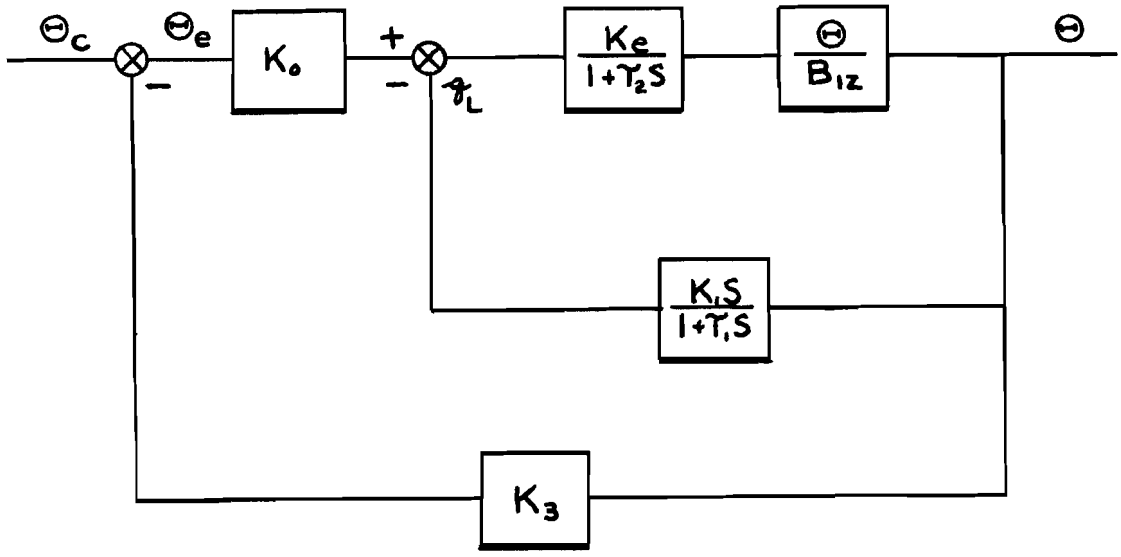

AUTO-PILOT CONTROL SYSTEM BLOCK DIAGRAM

FIGURE 97

SYMBOLS

Θ	Fuselage attitude angle; angle between longitudinal (pitch) axis and horizontal plane
B_{1Z}	Longitudinal tilt of no-feather axis (pitch axis hub tilt) with respect to the y-z plane
$q-\frac{d}{dt}$	Incremental rate change in angular position about the lateral (roll) axis
C	Servo command signal
e	Servo error signal
L	Response with first-order time lag

Optimum Gains and Time Constants

$$\frac{\partial B_{1Z}}{\partial \Theta} = +0.40 \ \frac{\text{deg}}{\text{deg}}$$

$$\frac{\partial B_{1Z}}{\partial q} = +0.25 \ \frac{\text{deg}}{\text{deg/sec}}$$

τ_1 = 0.05 sec - differentiation lag

τ_2 = 0.25 sec - selectric actuator lag

The report further indicates that the same transfer function applies to the roll stabilization channel and that no cross-coupling of channels is required with a free-flapping rotor system.

For simplicity, the subsequent discussion will utilize only pitch attitude parameters, although the results are equally applicable to roll attitude control (except as noted herein).

The system incorporated is shown in Figure 98.

Optimization of the system is limited primarily by the relationship:

$$\frac{B_{1Z}}{\Theta \text{ max}} = \text{constant.}$$ Where:

ΔB_{1Z} = minimum droop of control hub caused by glide load force

Θ max = maximum pitch allowable prior to derivative amplifier saturation

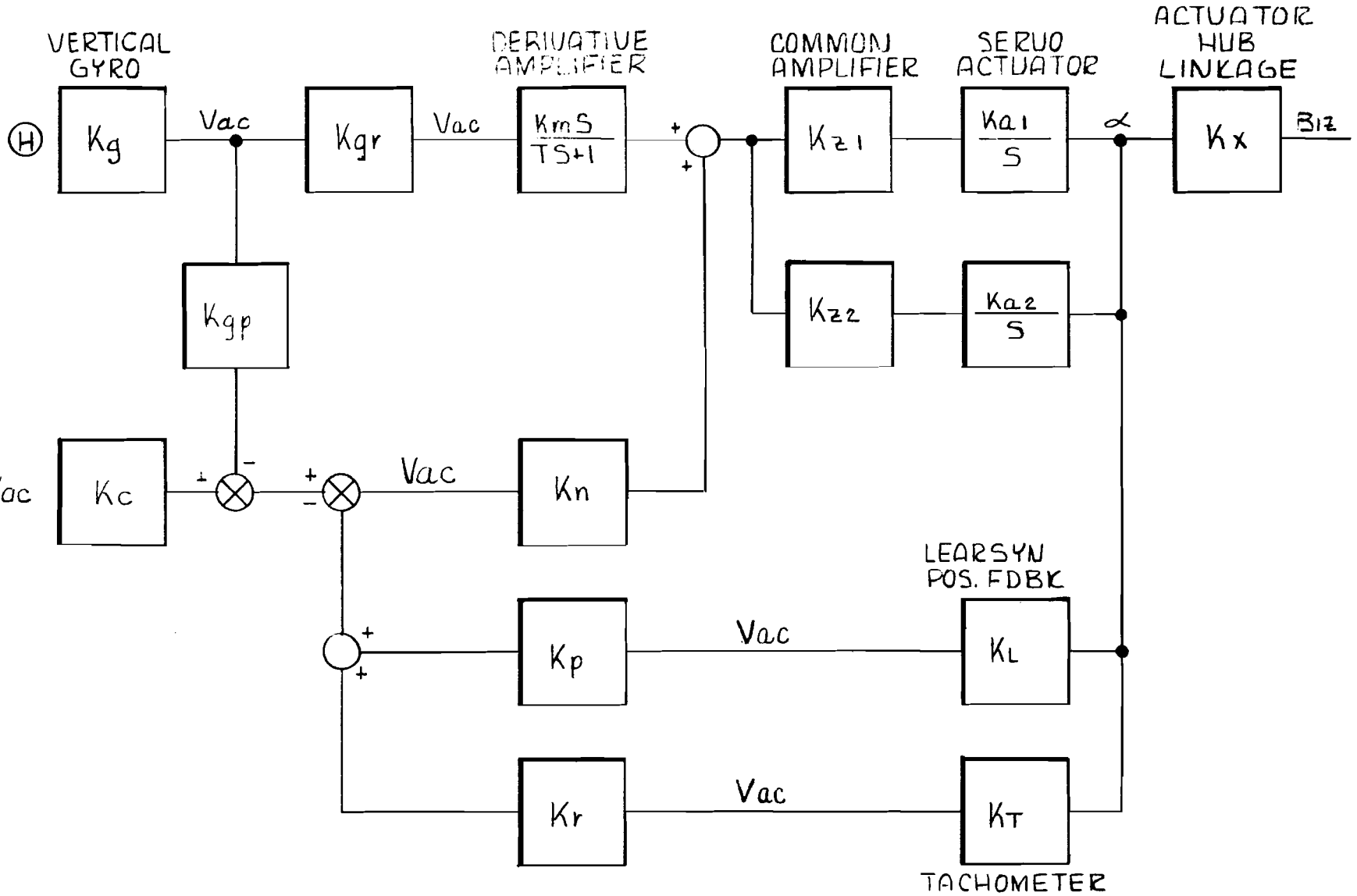

PITCH ATTITUDE BLOCK DIAGRAM

FIGURE 98

The above relationship may be derived as follows. From Table 10 :

$$(1) \quad \Theta_{max} (K_g) (K_{gr}) = 0.218 \text{ VRMS}$$

$$\frac{\Delta B_{1Z}}{q} = \frac{\Delta B_{1Z}}{S\,\theta} = 0.25$$

$$\frac{\Delta B_{1Z}}{S\,\theta} \quad \omega \to 0 \quad \approx \quad \frac{K_g\ K_{gr}\ K_m\ K_x}{K_L\ K_p\ K_n}$$

$$(2) \quad \frac{K_g\ K_{gr}\ K_m\ K_x}{K_L\ K_p\ K_n} = 0.25$$

From actuator characteristics:

at 1 m.a. quiescent clutch current:

$$\frac{\text{Output Torque}}{\text{Milliamp Input}} = \frac{T_{1Z}}{\text{m.a.}} = 4.2\ (13.2) = 55.5\ \frac{\text{in/lbs}}{\text{m.a.}}$$

$$\frac{T_{1Z_a}}{T\alpha} = \frac{^{o}\alpha}{^{o}B_{1Z}} = \frac{1}{K_x} = 5.5$$

The original KRC-6 hub provided a total available travel of ± 5.50 B_{1Z} corresponding to a total actuator travel of $\pm 30^{o}\ \alpha$. Kx then defined as the ratio: $5.50\ B_{1Z}/30^{o}\ \alpha$ = 0.182 deg/deg. Prior to actual vehicle tests, the nominal hub moment anticipated during glide was 33 foot-pounds. Thus:

$$T\alpha = \frac{(33)\ (12)}{5.5} = 72 \text{ inch-pounds}$$

$$\Delta i = \frac{72}{55.5} = 1.3 \text{ m.a.}$$

$$(3) \quad \Delta B_{1Z} = \frac{1.3\ K_x}{K_1\ K_p\ K_n\ K_z}$$

From (1) and (2):

$$(4) \quad \Theta \text{ Max} = \frac{0.218\ K_g\ K_m\ K_x}{0.25\ K_g\ K_1\ K_p\ K_n} = \frac{0.87\ K_m\ K_x}{K_1\ K_p\ K_n}$$

From (3) and (4):

$$\frac{\Delta B_{1Z}}{\Theta \text{ Max}} = \frac{.1.3\ K_x\ K_1\ K_p\ K_n}{0.87\ K_z\ K_m\ K_x\ K_1\ K_p\ K_n}$$

$$\frac{\Delta B_{1Z}}{\Theta \text{ Max}} = \frac{1.5}{K_z\ K_m}$$

The maximum $K_z\ K_m$ product obtainable in the Lear Servo Amplifiers is approximately (800) (.13) or 104 at low input frequencies, thus:

$$\frac{\Delta B_{1Z}}{\Theta \text{Max}} = 0.0145$$

Setting Θ max at 50^o, the droop resulting from anticipated glide conditions was 0.72 degrees, or approximately 13 per cent of the total hub control available. The original ASE gains were based upon a Θ max of 50^o and a glide hub moment of 33 foot-pounds.

In flight data obtained from the first series of drop tests indicated that a greater range of hub tilt was advisable. Rework of the hub resulted in a new K_x of .33 deg/deg, corresponding to a total hub travel of $\pm 10^o$ B_{1Z}.

In addition, hub moments approaching 200 foot-pounds were recorded in the pitch channel during glide maneuvers. The problem of redesign was compounded by the fact that the maximum rated torque output of the actuator corresponded to 125 foot-pounds of hub moment. Consequently, a second servo actuator was placed in tandem in the pitch channel. The latter actuator is controlled by a slave amplifier (K_{Z2}) connected in parallel with K_{Z1}. The final configuration is reflected in Figure 99.

The system droop corresponding to a maximum hub moment of 200 foot-pounds may now be calculated as follows:

$$T\alpha = \frac{(200)\ (12)}{3} = 800 \text{ inch-pounds}$$

$$\Delta i = 1/2\ \frac{800}{55.5} = 7.2 \text{ m.a. per actuator}$$

$$(5)\quad \Delta B_{1Z} = \frac{7.2\ K_x}{K_1\ K_p\ K_n\ K_z}$$

From (4) and (5):

$$\frac{\Delta B_{1Z}}{\theta \text{ Max}} = \frac{7.2\ (K_x)\ (K_1\ K_p\ K_n)}{0.87\ K_z\ K_m\ (K_x)\ (K_1\ K_p\ K_n)}$$

$$\frac{\Delta B_{1Z}}{\theta \text{ Max}} = \frac{8.3}{K_z\ K_m}$$

Since $K_z\ K_m = 104$:

$$\frac{\Delta B_{1Z}}{\theta \text{ Max}} = 0.08$$

Maintaining θ max = 50°, the resulting droop corresponding to a 200-foot-pound hub moment equals 4.0 degrees, or 20 per cent of the total available hub travel.

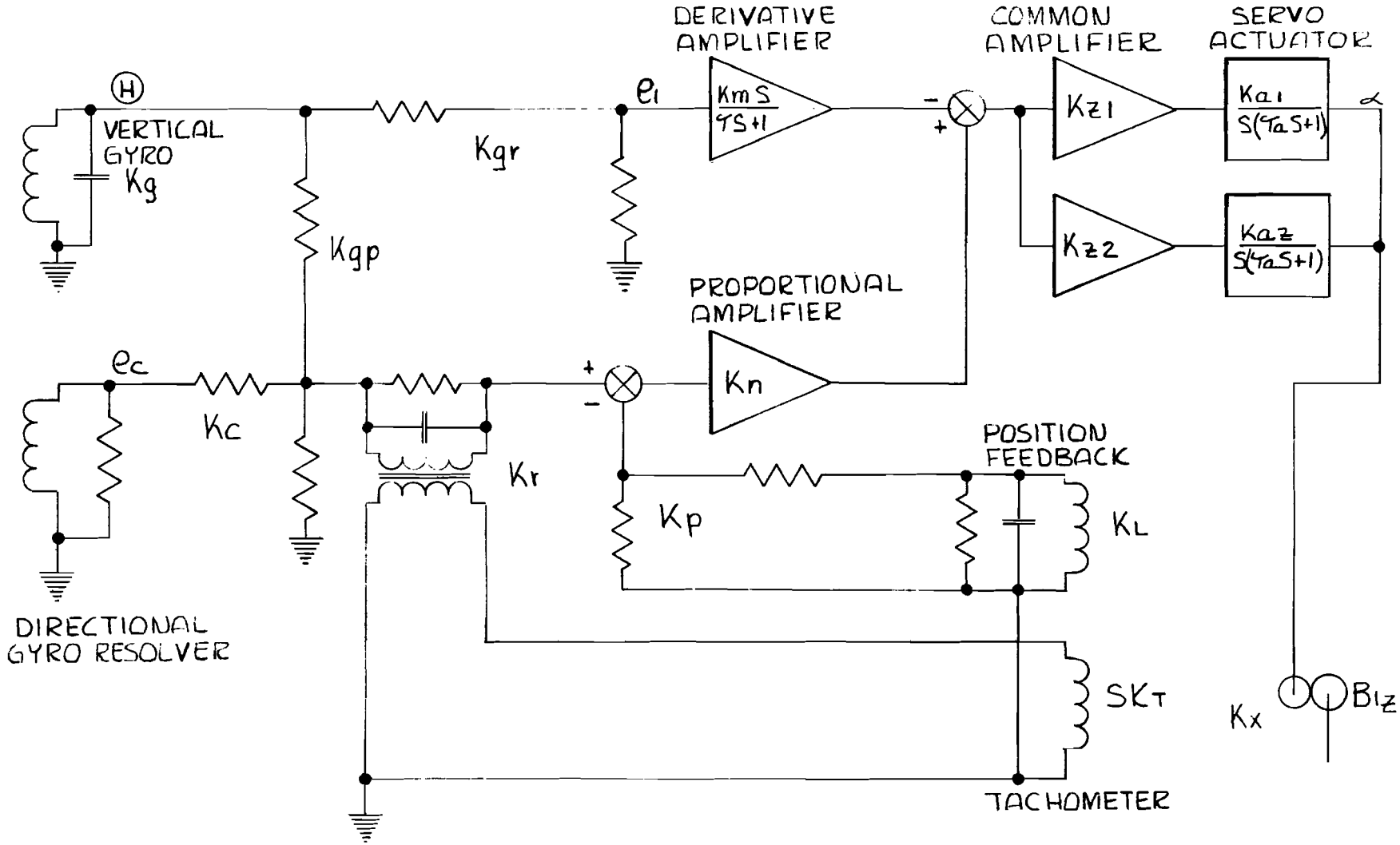

PITCH CHANNEL AUTOPILOT

FIGURE 99

The following system analysis reflects the incorporation of the $\pm 10^{o}$ hub and tandem servo drive.

Attitude Rate of Change Input

Assume θ max = 50^{o}

e_1 max = 0.218 volts

then: $50\ (K_g)\ (K_{gr}) = 0.218 \quad K_{gr} = 0.0212$

$$\left(\frac{K_m}{K_n}\right)_{w \to 0} = \left(\frac{800S}{340\ (T_m\ S+1)}\right) \quad T\ mS \to 0 \quad = \quad 2.358$$

$$\frac{\partial B_{1Z}}{\partial q} = \frac{\partial B_{1Z}}{\partial S\theta} = 0.25; \alpha = \frac{B_{1Z}}{K_x} = \frac{B_{1Z}}{.33}$$

$$\frac{\partial \alpha}{\partial S\ \theta} = 0.75 \quad \text{Therefore:} \quad \frac{\partial \alpha}{\partial \theta} = 0.75S$$

or $K_g\ K_{gr}\ K_m = 0.75S\ K_1\ K_p\ K_n$

$$K_p = \frac{K_g\ K_{gr}}{0.75\ K_1 S} \cdot \frac{K_m}{K_n} = \frac{0.206\ (0.0212)}{0.75\ (0.043)S} \cdot 2.35S$$

$$K_p = 0.318\ \frac{\text{volt}}{\text{volt}}$$

Attitude Position Input

$$\frac{\partial B_{1Z}}{\partial \theta} = 0.4 \quad \text{or} \quad \frac{\partial \alpha}{\partial \theta} = \frac{0.4}{K_x} = 1.2$$

$$K_g\ K_{gp} = K_1\ K_p\ (1.2)$$

$$K_{gp} = \frac{(1.2)\ (.043)\ (0.318)}{0.206} = 0.08\ \frac{\text{volts}}{\text{volt}}$$

Command Input Requirements

The directional heading command inputs were designed to meet two basic requirements. To provide adequate hub control, it is necessary that the command signal be capable of dictating stop to stop travel of pitch and roll servo actuators during normal glide maneuvers. During large displacements of the longitudinal axis, it is likewise necessary that the vertical gyro be capable of overriding existing servo commands and returning the hub to neutral. This requirement is necessary to prevent open-loop operation which might cause inadvertent diving of the vehicle during remotely-controlled flight. Consequently, the maximum command signal is set equal to 45 degrees of vertical gyro displacement or approximately 75 per cent of maximum gyro output. A command limiting circuit is incorporated in pitch and roll servo channels to assure that this limit remains constant regardless of gain variations in transmission, receiving and resolving stages.

Rate Feedback Stabilization

To insure stability of the inner servo loop, a minimum rate feedback gain of approximately 0.00135 volts/deg α /sec was required. Excessive feedback created an intolerable lag in the over-all control system. For best results, a feedback gain of 0.002 was incorporated.

From Table 10: $K_t = 0.00067$

$$K_r = 0.002/0.00067 = 3 \ \frac{\text{volts}}{\text{volt}}$$

A partial schematic of the preceding system for pitch attitude control is presented in Figure 99 . An identical system is incorporated for roll attitude control with the single exception that the over-all attitude rate of change transfer $A_1Z/\partial\varphi$ has been increased to 0.375 deg/deg. The latter gain increase resulted from the analysis of actual flight performance data. The tandem servo concept, initially added to the pitch control system is now likewise used in lateral axis control.

Control System Transfer Functions

The response of the control system to error signals q and θ are shown in Figures 100 and 101.

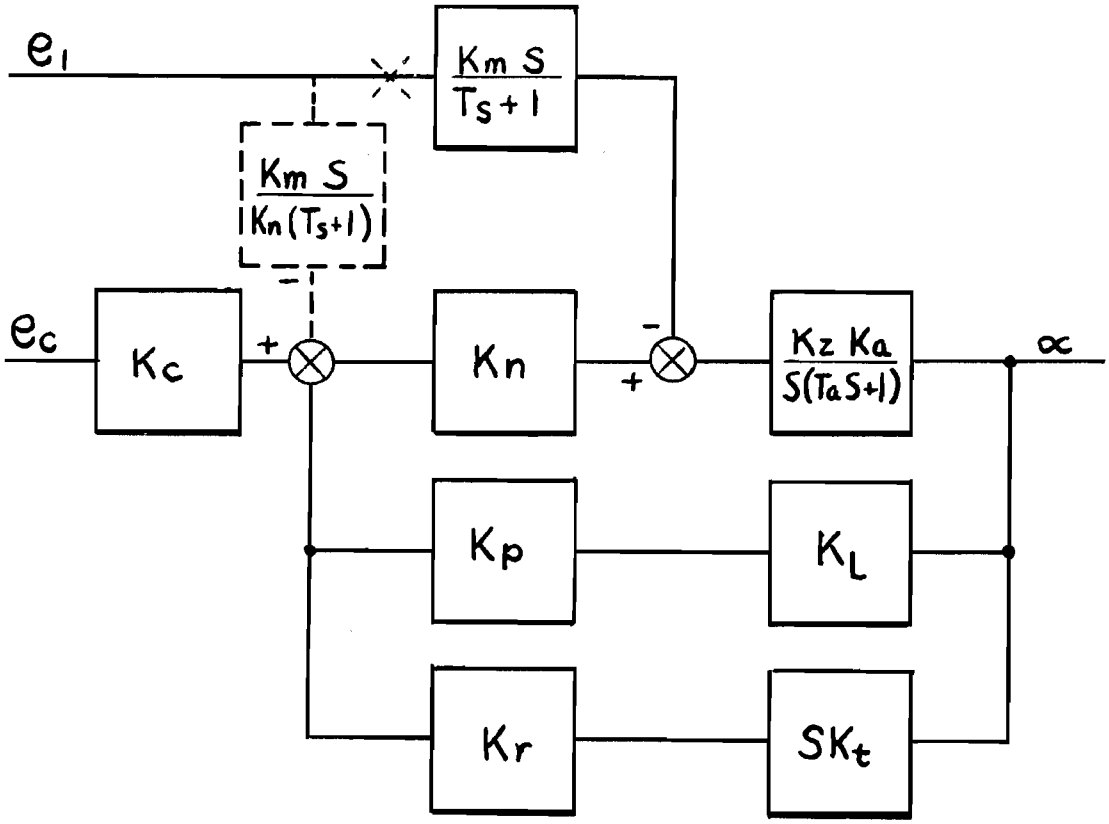

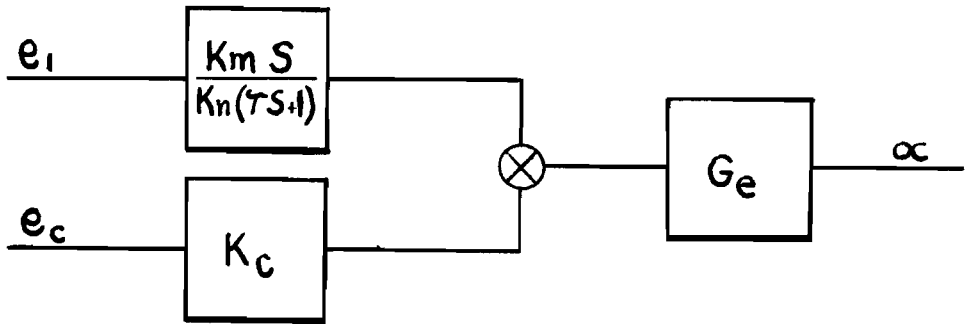

ASSUMING $K_n K_z K_a \gg K_L K_p$; AT LOW FREQUENCIES

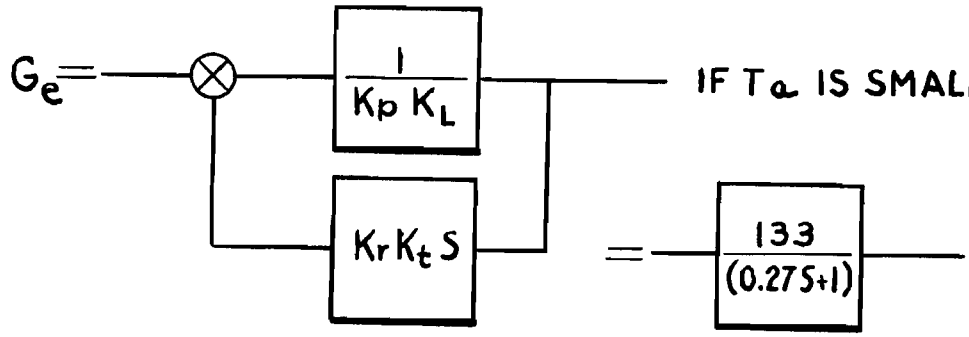

SERVO SYSTEM TRANSFER FUNCTION

FIGURE 100

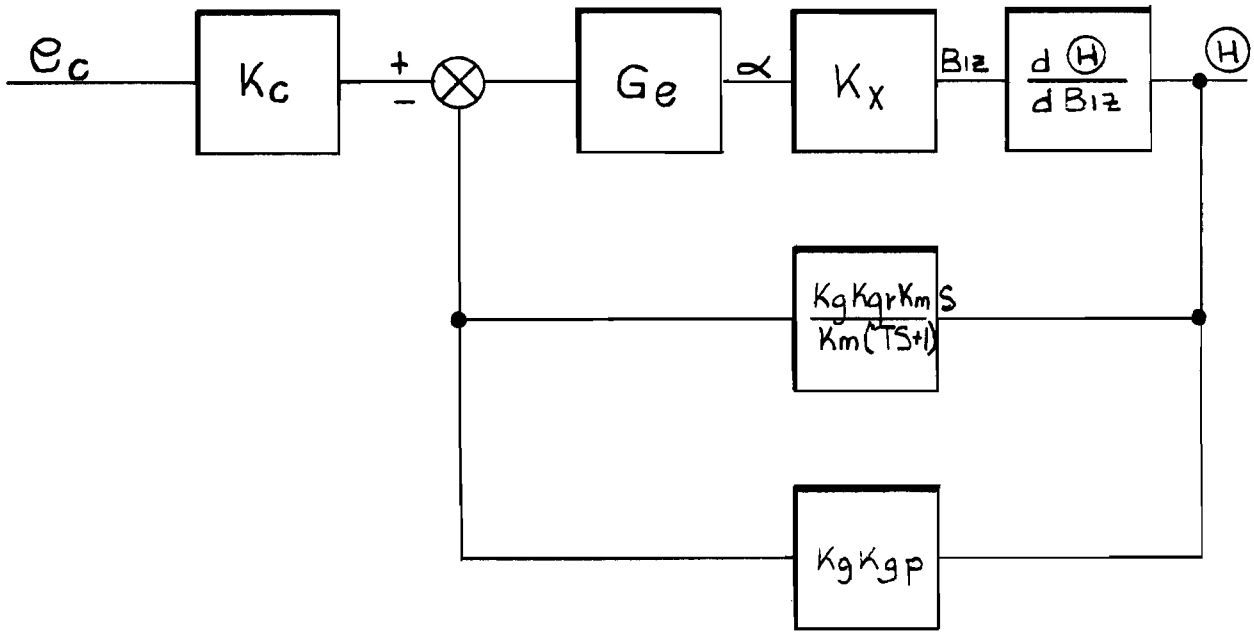

TRANSFER FUNCTIONS:

$$\frac{d\,B_{iz}}{d\,(H)} = \frac{K_g\,K_{gp}\,G_e\,K_x}{1} = \frac{0.4}{(0.27S+1)}$$

$$\frac{d\,B_{iz}}{d\,q} = \frac{K_g\,K_{gr}\,K_m\,G_e K_x}{K_n(TS+1)} = \frac{0.25}{(0.1S+1)(0.27S+1)}$$

PITCH CHANNEL BLOCK DIAGRAM

FIGURE 101

B. ROTOR RPM TELEMETRY

Maximum accuracy in the rotor speed telemetry system was achieved through the transmission of a bi-stable signal activated by a pulse-type magnetic pickup assembly. Such a signal is essentially independent of gain variations in the coding, transmission, and decoding systems; consequently, the read-out accuracy is only a function of the input pulse frequency and the period over which the output is averaged. Thus,

$$E = \frac{K}{f_p T} \qquad \text{Where:}$$

E = Per cent error in average speed read-out

f_p = Pulse frequency

T = Period of averaging

K = System constant

To minimize the error over a fixed averaging period the pulse frequency must be maintained as high as possible for any given rotor speed. A standard telemetry channel has a cutoff frequency of 20 c.p.s., due primarily to capacitors in the ground station emitter followers. In normal operation, the emitter followers are supplied with input pulses of 50 micro-second width and appropriate amplitudes at a rate of 250 samples per second. The average level of the input pulses is stored in each emitter follower to provide a semi-continuous output. Thus, at information fequencies approaching 20 c.p.s., the filtering action of the emitter follower becomes appreciable. The box-car detector output, however, consists of short periodic samples, and is capable of providing a theoretical accuracy of 100 per cent when employed to count square wave frequencies up to 250/2 or 125 c.p.s.

The ROTOCHUTE design employs a four-tooth gear in the rotor assembly to provide four pickup pulses per revolution of the rotor. This arrangement provides accurate telemetry up to speeds of:

$$\frac{(125)(60)}{2} \quad \text{or} \quad 3750 \text{ RPM}$$

As described above, the pickup output is utilized to trigger a bi-stable flip-flop, the state of which is sampled by the data system (Each gear tooth provides a positive and negative input pulse. The negative pulses are suppressed, whereas positive pulses are amplified to trigger the output flip-flop.) By employing a high gain pulse amplifier, and clipping the resulting output pulses, the flip-flop has been found to function properly for any rotor speed above 20-30 RPM The circuitry employed is shown in Figure 102.

The ground station receiver is shown in Figure 103. The input from the box car detector (the emitter follower output has been deleted from this channel) consists of positive and negative pulses. The number of similar pulses occurring in each block is:

$$N = \frac{250}{S\ n}$$

where S = rotor speed in revolutions per second

n = number of teeth on rotor gear

As in the transmitter amplifier, the pulses are utilized to trigger a flip-flop, but only a change in pulse polarity will provide the necessary triggering. The square wave output is differentiated by transformer action, and resulting positive pulses are routed to an oscillograph and the RPM display circuitry shown in Figure 104.

The function of the rotor RPM display circuitry is to provide square wave output pulses of constant amplitude and width when triggered by the signal described above. A highly damped microammeter monitors the average loop current generated by these pulses to provide an indication directly proportional to rotor speed. Unlike circuits employed to transmit and record the rotor speed signal, the read-out circuitry is relatively sensitive to gain variations and has been temperature-compensated from 50°F to 160°F. Periodic calibration is advisable.

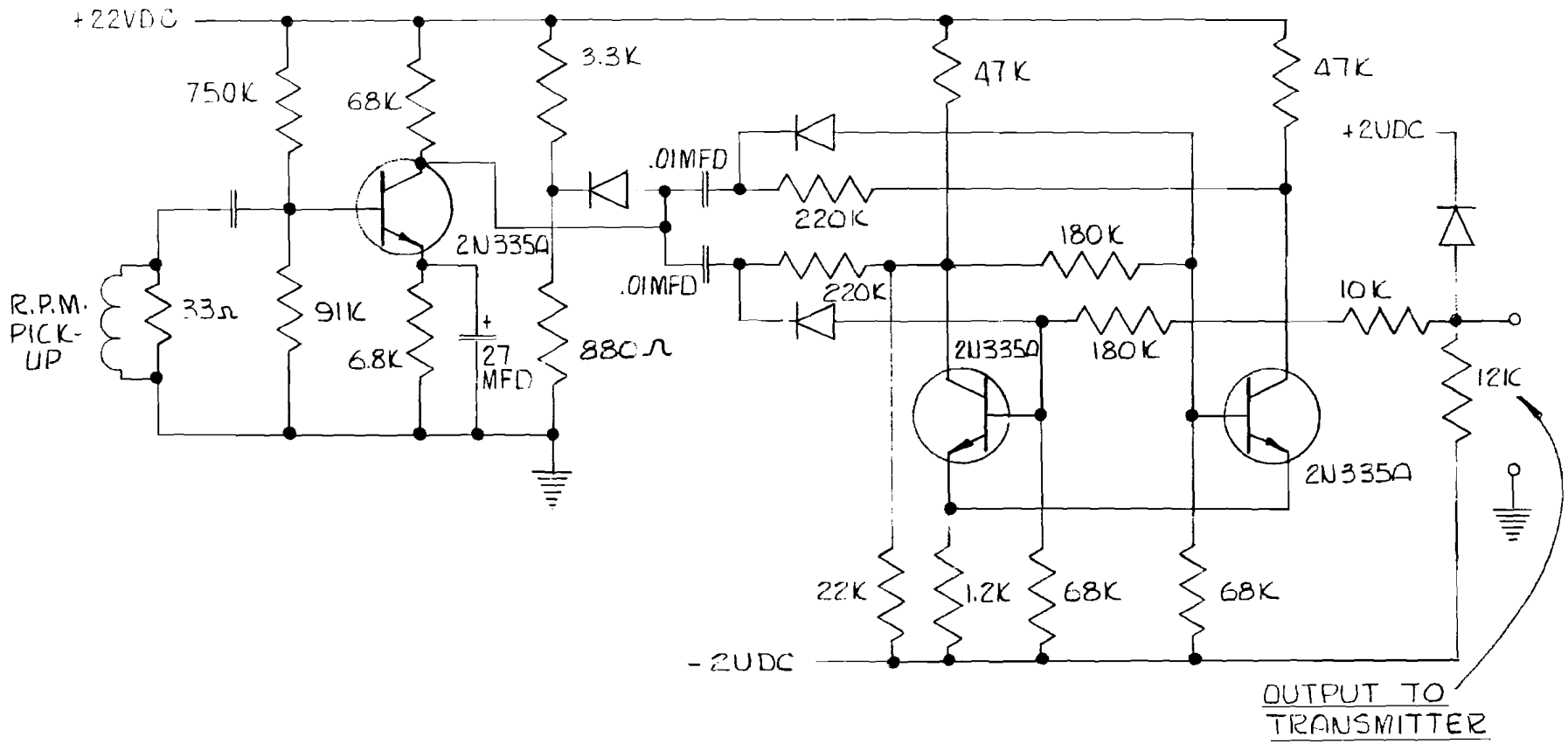

AIRBORNE ROTOR SPEED AMPLIFIER AND SHAPER

FIGURE 102

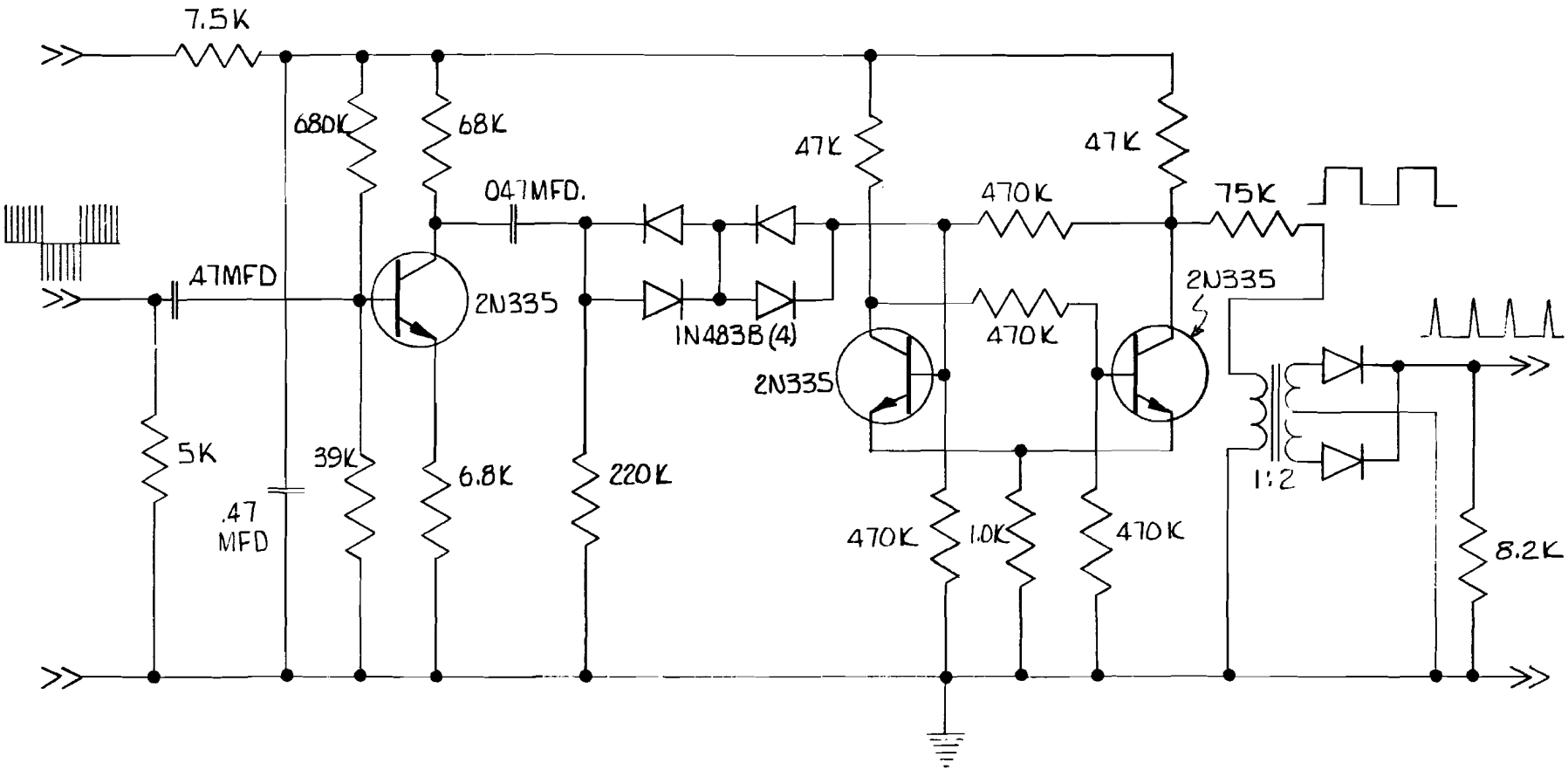

KRC-6 ROTOCHUTE ROTOR SPEED AMPLIFIER & SHAPER: GROUND STATION

FIGURE 103

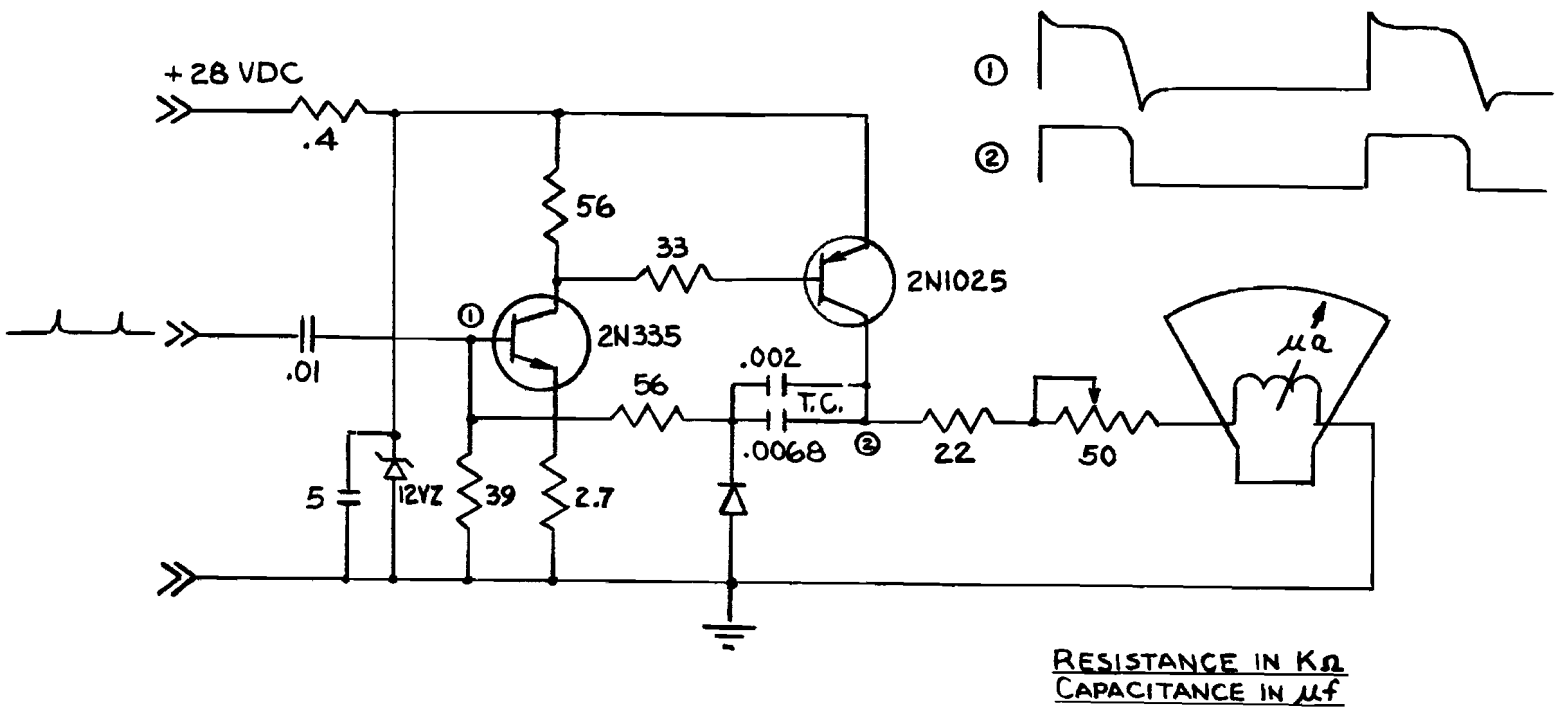

ROTOR SPEED READOUT

FIGURE 104

C. SEQUENCING LOGIC

The ROTOCHUTE sequencing logic is presented in Figures 105 and 106. Figure 105 represents the logic arrangement utilized in aircraft bomb rack installations and is designed for use in conjunction with 28-volt DC aircraft power during vehicle delivery. Figure 106 is modified for use with 24-volt DC external supplies during vehicle delivery by helicopter. In this case, the directional gyro is set on the ground and left uncaged; gyro reference is thereby maintained as the ROTOCHUTE rotates on the winch cable below the helicopter prior to release. Due to the similarity between the two logic diagrams, only the bomb rack installation circuitry will be discussed further.

Switch 1 is a handling switch which permits a fully assembled ROTOCHUTE to be de-energized for storage. Switch 2 prevents activation of fin deployment and collective flare circuitry during system tests. Fuses F1, F2, and F3 provide necessary electrical overload protection during system check-out. All except F1 are bypassed prior to take-off.

During the flight to the drop area, aircraft 28-volt DC power serves three (3) functions:

(a) Provides primary power to ROTOCHUTE electronics
(b) Maintains sequencing circuitry in the de-energized state through K-20
(c) Provides charging current to the ROTOCHUTE battery

At the time of drop, the following sequence, described in order of occurrence, is initiated:

1. ROTOCHUTE is released from bomb rack

    (a) Aircraft power disconnected
    (b) Battery power utilized

2. Drop lanyard detaches from ROTOCHUTE

    (a) Firing pin on rotor deployment squib pulled, initiating two or three second firing delay

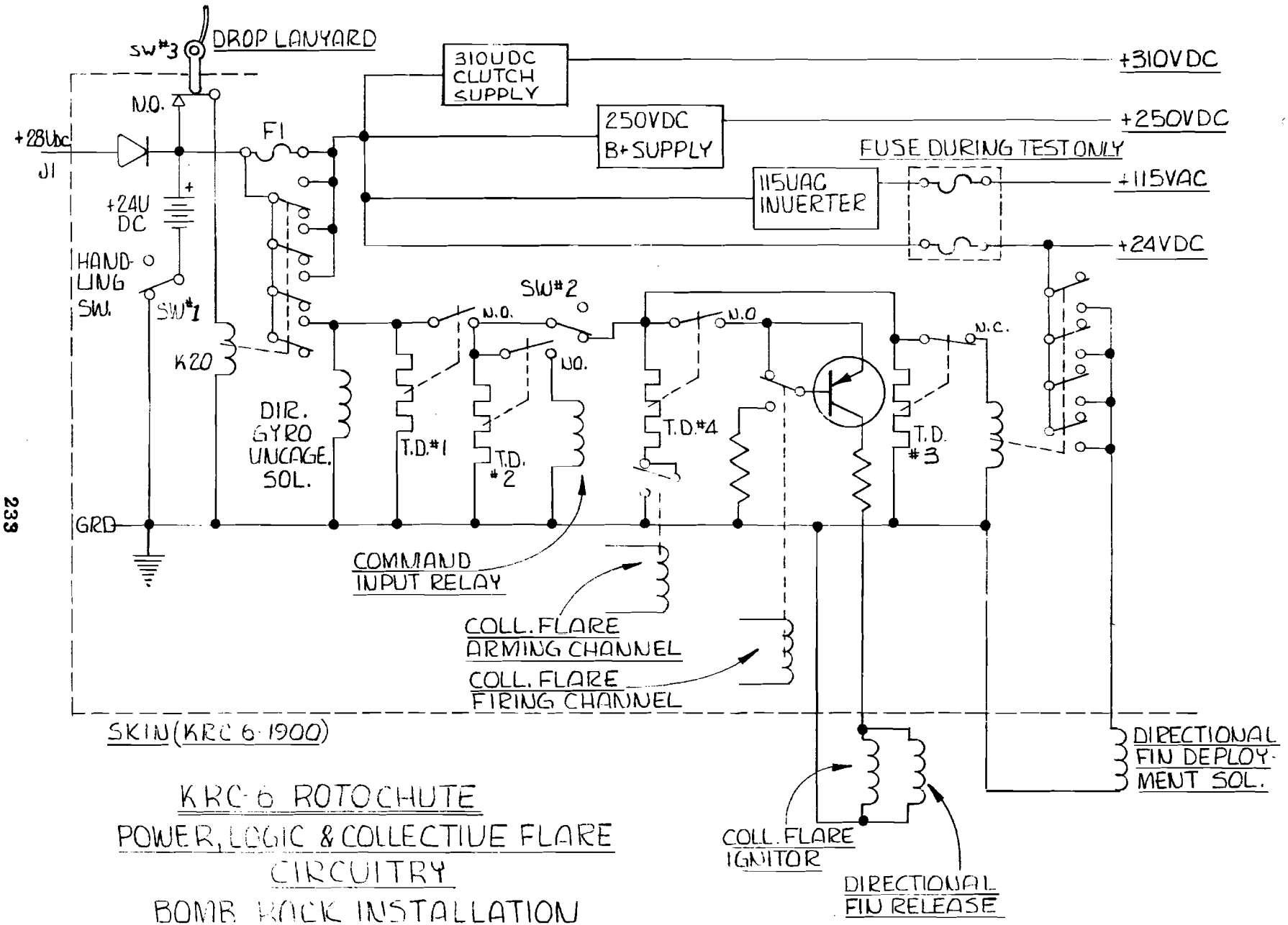

KRC-6 ROTOCHUTE
POWER, LOGIC & COLLECTIVE FLARE
CIRCUITRY
BOMB RACK INSTALLATION

FIGURE 105

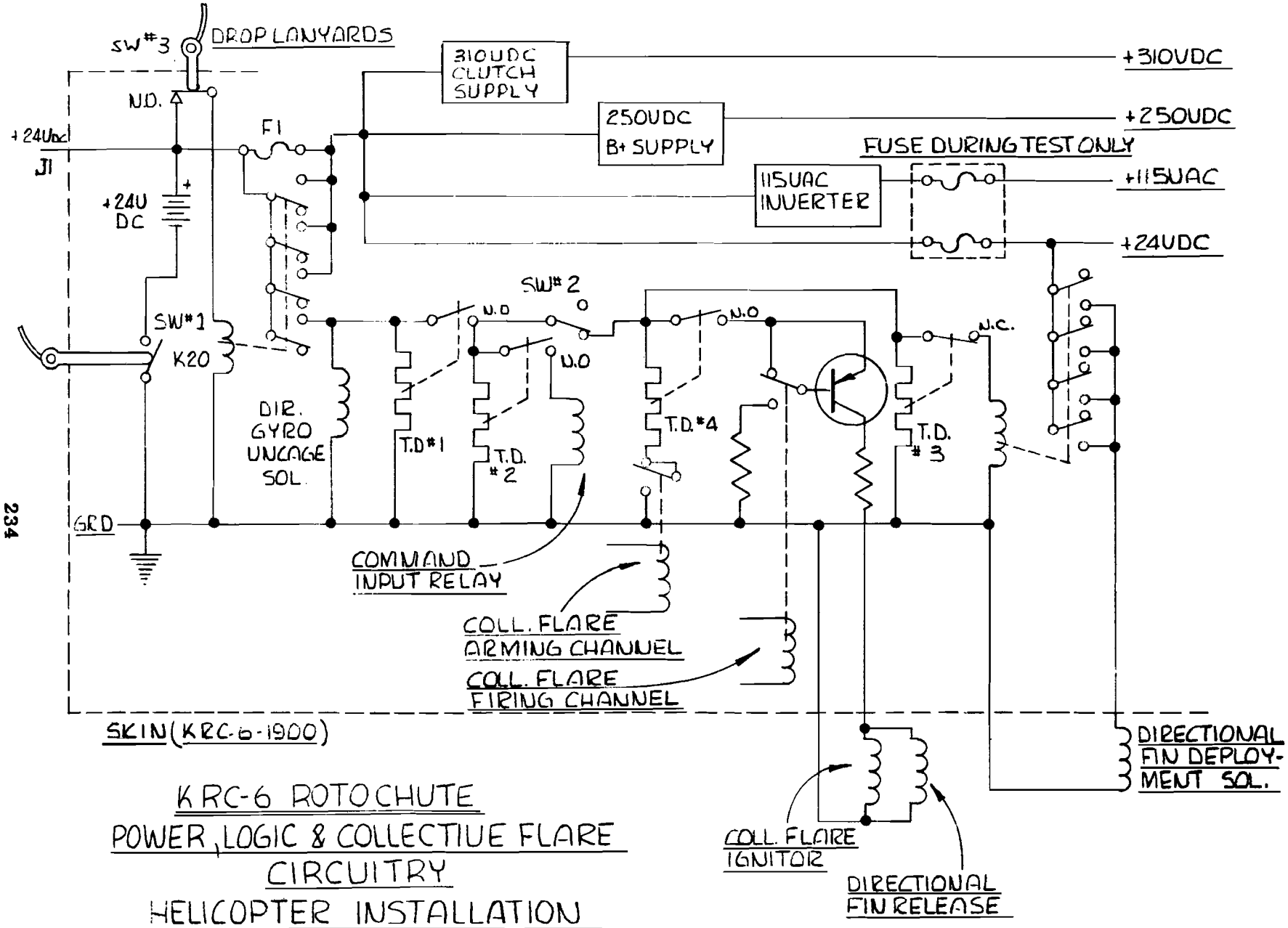

KRC-6 ROTOCHUTE
POWER, LOGIC & COLLECTIVE FLARE
CIRCUITRY
HELICOPTER INSTALLATION

FIGURE 106

(b) Microswitch activated de-energizing K-20

1. F1 shorted out
2. Sequencing circuitry energized
3. Directional gyro uncaging solenoid energized

3. ROTOCHUTE clears aircraft

(a) Squib fires - rotors begin to deploy

4. Rotor drag causes ROTOCHUTE to assume normal nose-down descent attitude

1. Directional fins deployed through K-6
2. Collective flare circuitry armed
3. Directional gyro uncaging solenoid de-energized

(b) Time Delay No. 2 closes ungrounding ASE inputs

5. Time delay relay No. 3 opens, removing power to K-6 and fin deployment solenoid

Upon recovery, the entire system is de-energized by the external handling switch.

D. COLLECTIVE FLARE CONTROL

The collective flare capability of the ROTOCHUTE is controlled remotely from the ground station. Since the collective flare can only be employed once during the flight, the electronics involved must be protected from erroneous firing signals. Such signals may appear in the data system as a result of faulty FM reception, due either to range or interference. The system employed is illustrated in the logic diagrams, Figures 101 and 102. During the initial phases of transportation and drop sequencing, the firing circuitry is de-energized. Activation occurs when the ASE command circuitry is ungrounded. Two command channels are required to complete the firing logic. The first input, an arming command, energizes a 3-second time delay relay. Following the latter interval, and if the arming command is still present, the firing channel may be

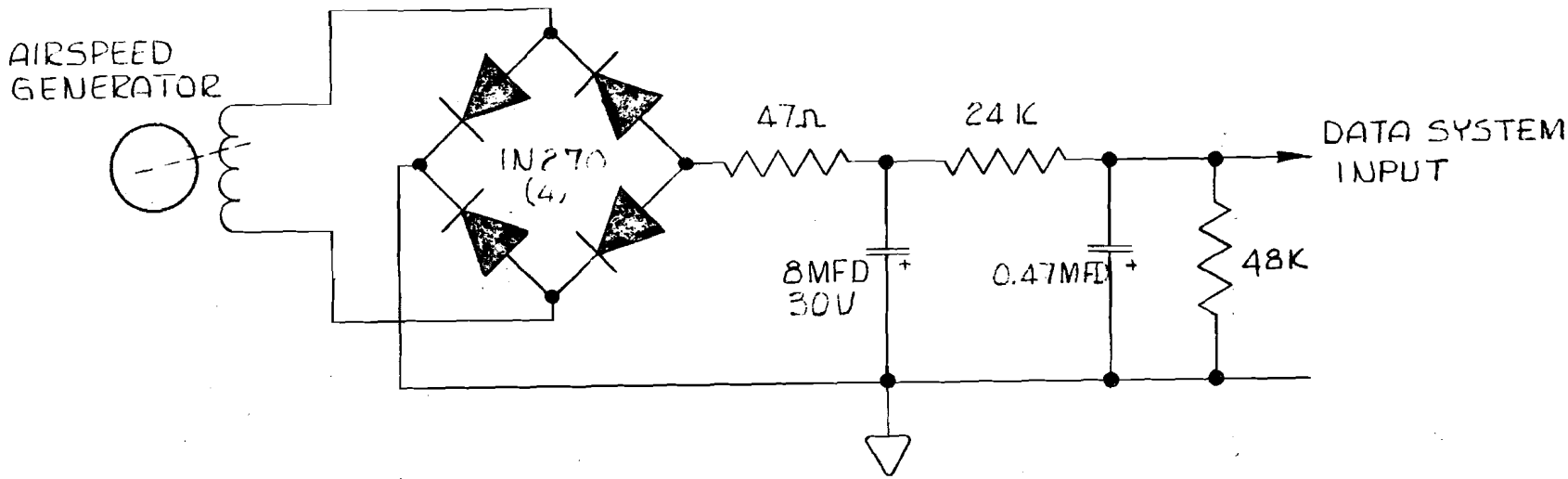

KRC-6 ROTOCHUTE AIRSPEED TELEMETRY

FIGURE 107

activated to instantaneously fire the collective thruster. Immediately following the thruster discharge, the horizontal tail bolt cutter is fired, allowing the tail to release and swing upward. This precautionary measure prevents the tail from pitching the ROTOCHUTE forward once the rotor has stalled.

E. AIRSPEED READ-OUT

During advanced vehicle flight tests, it proved advantageous to transmit flight path airspeed to the ground control station as a visual control aid. A Science Associates Wind Speed Detector (anemometer) Model 417 was boom-mounted on the front of the flight vehicle. Airspeed is sensed by an air-powered alternating current generator working into a rectifier and filter to provide the necessary proportional direct current input to the airborne telemetry system. The applicable circuitry is shown in Figure 107.

APPENDIX IV. RE-ENTRY AND AERODYNAMIC HEATING STUDIES

A. RE-ENTRY

Two distinctive types of re-entry were considered: unmodulated and modulated. In the first case, drag was held constant while drag was varied in the second case.

1. Unmodulated Re-Entry

Expressions for unmodulated re-entry were developed from the following basic expressions from Reference 3.

$$-\frac{dV/dt}{g} = \frac{C_D \rho_o A V_E^2}{2mg} e^{-\beta Y} e^{-\frac{C_D \rho_o A}{\beta m \sin\theta_E} e^{-\beta Y}}$$

$$V = V_E e^{-\frac{C_D \rho_o A}{2\beta m \sin\theta_E} e^{-\beta Y}}$$

The first equation may be re-arranged so as to yield an expression for time.

$$dt = \frac{-2m}{C_D \rho_o A V_E^2} e^{\beta Y} e^{\frac{C_D \rho_o A}{\beta m \sin\theta_E} e^{-\beta Y}} dV$$

Differentiation of the second equation with respect to Y results in the following:

$$dV = V_E \frac{C_D \rho_o A}{2m \sin\theta_E} e^{-\beta Y} e^{-\frac{C_D \rho_o A}{2\beta m \sin\theta_E} e^{-\beta Y}} dY$$

Substituting this expression into the preceding expression and re-arranging terms produce the following expression:

$$t = \frac{-1}{V_E \sin\theta_E} \int_{Y_E}^{Y} e^{\frac{C_D \rho_o A}{2\beta m \sin\theta_E} e^{-\beta Y}} dY$$

It was found that generalized plots could be achieved and simplified if the following parameters are used:

$$\frac{V}{V_E}, \frac{Y}{Y_E}, \frac{t V_E \sin\theta_E}{Y_E}, \frac{W \sin\theta_E}{C_D A}$$

In terms of these parameters, the previously obtained equations may be rewritten as follows:

$$\frac{V}{V_E} = e^{-\frac{\rho_0 g}{2\beta}\frac{1}{\left(\frac{W \sin\theta_E}{C_D A}\right)}e^{-\beta Y\left(\frac{Y}{Y_E}\right)}}$$

$$-\frac{t V_E \sin\theta_E}{Y_E} = \int_1^{\frac{Y}{Y_E}} e^{\frac{\rho_0 g}{2\beta}\frac{1}{\left(\frac{W \sin\theta_E}{C_D A}\right)}e^{-\beta Y\left(\frac{Y}{Y_E}\right)}} d\left(\frac{V}{Y_E}\right) = \int_1^{\frac{Y}{Y_E}} \left(\frac{V}{V_E}\right)^{-1} d\left(\frac{Y}{Y_E}\right)$$

In terms of these equations, the $C_D A$ of the vehicle remains constant during unmodulated entry into the atmosphere. Consequently, the parameter $W \sin\theta_E / C_D A$ also remains constant for a given entry.

The last equation may be integrated graphically to yield altitude time histories for an entry vehicle with assumed $W \sin\theta_E / C_D A$ ratios.

The deceleration history may be calculated from the first basic equation. The presentation is simplified if it is made in terms of a load factor in the parametric form $n/V_E^2 \sin\theta_E$.

The basic equation may be rewritten as follows:

$$\frac{n}{V_E^2 \sin\theta_E} = -\frac{\rho_0}{2\left(\frac{W \sin\theta_E}{C_D A}\right)} e^{-\beta Y_E\left(\frac{Y}{Y_E}\right)} e^{-\frac{\rho_0 g}{\beta\left(\frac{W \sin\theta_E}{C_D A}\right)}e^{-\beta Y_E\left(\frac{Y}{Y_E}\right)}}$$

The expression is simplified if both sides of the equation are squared, if logarithms for both sides of the equation for V/V_E are taken, and the results are re-arranged and substituted into the expression being simplified.

$$\left(\frac{V}{V_E}\right)^2 = e^{-\frac{\rho_0 g}{\beta}\frac{1}{\left(\frac{W \sin\theta_E}{C_D A}\right)}e^{-\beta Y_E\left(\frac{Y}{Y_E}\right)}}$$

$$\ln\frac{V}{V_E} = -\frac{\rho_0 g}{2\beta}\frac{1}{\left(\frac{W \sin\theta_E}{C_D A}\right)} e^{-\beta Y_E\left(\frac{Y}{Y_E}\right)}$$

$$\frac{n}{V_E^2 \sin\theta_E} = \frac{\beta}{g}\left(\frac{V}{V_E}\right)\ln\frac{V}{V_E}$$

The equation implies that the deceleration is a function only of speed and flight path angle for unmodulated entry.

2. Modulated Entry

The initial phase of modulated entry is identical to the unmodulated case up to the point where a desired maximum deceleration is reached.

Then the rotor disc area is varied so as to yield constant deceleration of an arbitrarily chosen value. Initially, the disc area is decreased as the dynamic pressure increases with density until maximum dynamic pressure is reached. From there on, the disc area is increased until the rotor is fully opened. At this point, the vehicle continues along an unmodulated trajectory, decelerating at levels below maximum.

The velocity at which the modulation is terminated, i.e. rotor is fully opened, is of interest and is calculated as follows. From dynamic equilibrium: $Wn = 1/2\,\rho V^2 C_D A$. this may be rewritten:

$$\left(\frac{V}{V_E}\right)^2 = \frac{\left(\frac{n}{V_E^2 \sin\theta_E}\right)\left(\frac{W \sin\theta_E}{C_D A}\right)}{\frac{1}{2}\rho_0 e^{-\beta Y_E (Y/Y_E)}}$$

For constant deceleration:

$$\Delta S = \frac{\Delta Y}{\sin\theta_E} = \frac{V_1 + V_2}{2}\Delta t$$

where subscripts 1 and 2 denote conditions at the beginning and end of modulation. This may be rewritten in terms of previously chosen parameters.

$$\frac{Y_2}{Y_E} - \frac{Y_1}{Y_E} = \frac{1}{2}\frac{\Delta t\, V_E \sin\theta_E}{Y_E}\left(\frac{V_1}{V_E} + \frac{V_2}{V_E}\right)$$

The velocity is reduced as defined by the following expression:

$$ng\ \Delta t = V_2 - V_1$$

This, when rewritten, yields the following:

$$\frac{\Delta t V_E \sin\theta_E}{Y_E} = \frac{1}{Y_E g}\left(\frac{1}{V_E^2 \sin\theta_E}\right)^{-1}\left(\frac{V_2}{V_E} - \frac{V_1}{V_E}\right)$$

Combining equations gives the following expression for the initial and final points of modulation.

$$\frac{Y_2}{Y_E} - \frac{Y_1}{Y_E} = \frac{1}{2gY_E}\left(\frac{n}{V_E^2 \sin\theta_E}\right)^{-1}\left[\left(\frac{V_2}{V_E}\right)^2 - \left(\frac{V_1}{V_E}\right)^2\right]$$

The rotor is fully opened for both the initial and final conditions of modulated flight. Therefore, to satisfy dynamic equilibrium for both conditions, dynamic pressures must be equal.

$$\frac{1}{2}\rho_2 V_2^2 = \frac{1}{2}\rho_1 V_1^2$$

or

$$\left(\frac{V_2}{V_E}\right)^2 = \left(\frac{V_1}{V_E}\right)^2 \frac{\rho_0 e^{-\beta Y_1}}{\rho_0 e^{-\beta Y_2}} = \left(\frac{V_1}{V_E}\right)^2 e^{-\beta(Y_1 - Y_2)}$$

or

$$\frac{V_2}{V_1} = \frac{V_1}{V_E} e^{-\frac{\beta Y_2}{2}\left(\frac{Y_1}{Y_E} - \frac{Y_2}{Y_E}\right)}$$

or

$$\ln \frac{V_2/V_E}{V_1/V_E} = -\frac{\beta Y_2}{2}\left(\frac{Y_1}{Y_E} - \frac{Y_2}{Y_E}\right)$$

The final equation for unmodulated re-entry also satisfies the starting condition (Condition 1). If this is substituted into the equation for initial and final points of modulation and the resulting substituted into the above derived equation, then the following results:

$$\ln \frac{V_2/V_E}{V_1/V_E} = -\frac{1}{4 \ln V_1/V_E}\left[\left(\frac{V_2/V_E}{V_1/V_E}\right)^2 - 1\right]$$

or

$$\ln \frac{V_1}{V_E} = \frac{\left(\frac{V_2/V_E}{V_1/V_E}\right)^2 - 1}{4 \ln \frac{V_2/V_E}{V_1/V_E}}$$

The expression may be be used to relate the final velocity of modulated flight to the initial velocity. The corresponding decelerations are given in Figure 19.

The required variation of C_D to produce constant deceleration may be calculed from the dynamic equilibrium relationship. The expression for the total C_D is:

$$C_D = \frac{Wn}{\frac{1}{2}\rho V^2 A} = \frac{\frac{n}{V_E^2 \sin\theta_E} \cdot \frac{W \sin\theta_E}{A}}{\left(\frac{V}{V_E}\right)^2 \frac{1}{2}\rho e^{-\beta(Y/Y_E)}}$$

Inasmuch as the total C_D is the sum of the rotor C_{D_R} and body C_D, the coning angles must be based on:

$$C_{D_R} = C_{D\ \text{Total}} - C_{D\ \text{Body}}$$

The expression for the coning angle is:

$$\beta = \arccos \sqrt[3]{\frac{C_{D_R}}{\sigma C_N}}$$

B. AERODYNAMIC HEATING

The gross problem is specified by the geometry of the re-entrant body (ROTOCHUTE) and some initial conditions (velocity and altitude) at re-entry into the earth's atmosphere. The ROTOCHUTE is assumed to be in axial flight. The geometry is virtually that of a flat plate (or plates) as shown in Figure 108. For simplicity, we can identify the rotor blade with a flat plate rotating at an angular speed Ω. The coning angle is expressed by β, and rotor blade span by ℓ. A length ℓ_s is influenced by the presence of a central body of radius r. The axis of the vehicle is assumed to be always aligned with the flight path such that axisymmetric flow fields are of interest.

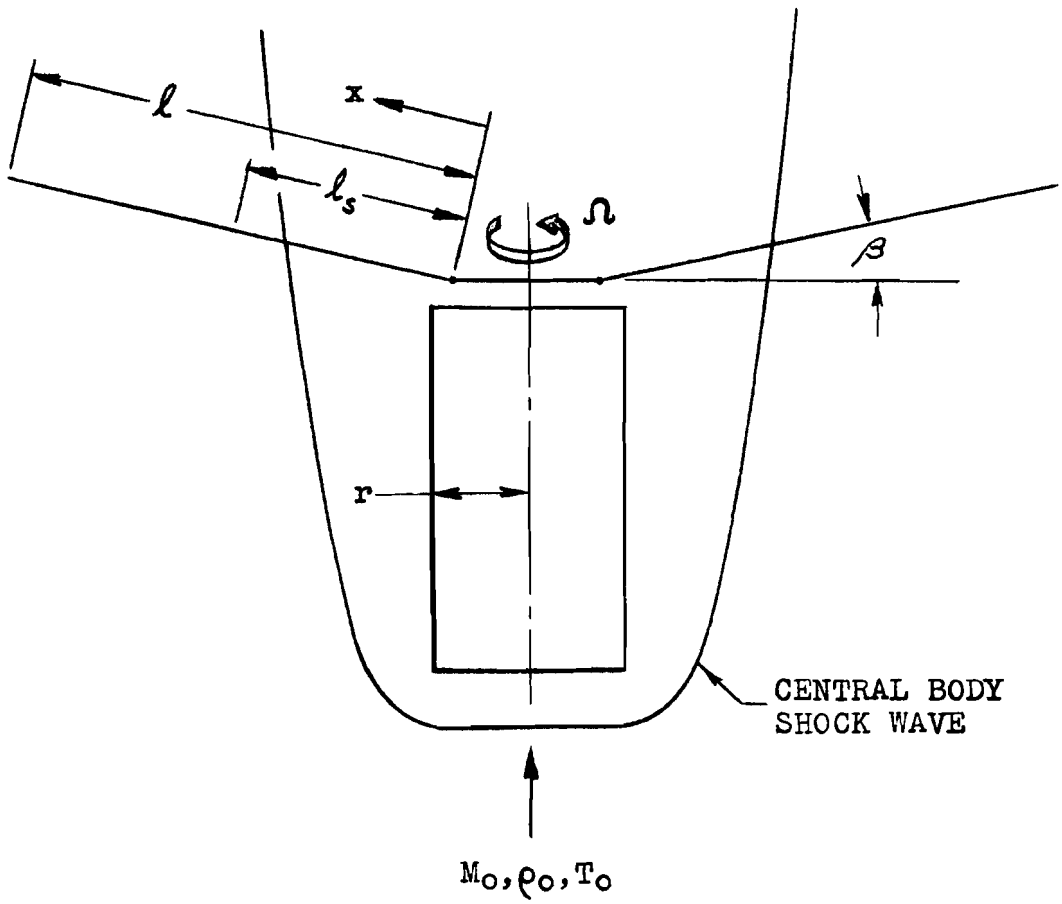

RE-ENTRY PARAMETRIC RELATIONSHIPS

FIGURE 108

Over a major portion of the re-entry trajectory, the flight Mach number will be quite large (4→15), and we can expect ($\ell_s \cos \beta$) to be of the order of $(M^2 - 1)^{-1/2} [\approx M^{-1}]$ times the length of the central body. Customary re-entering bodies have "slenderess" ratios of order unity. However, even relatively slender central bodies, in view of the above, imply that $\ell_s / \ell < 1$ for moderate coning angles. Thus, we may reflect the disturbances induced by the central body. It should be noted that such disturbances are appreciable for perhaps only one-half the shock layer extent in any case.

The rotor blade "sees" a stream in accord with its inclination, rotational speed, and coning angle. Velocities along and normal to the span direction are the components $V_o \sin \beta$ and $V_o \cos \beta$, respectively, due to descent through the atmosphere. If β is small, interest is in the resultant of $V_o \cos \beta$ and $V_R = \Omega(r + x \cos \beta)$, the rotational component. That is:

$$\frac{V_R}{V_o} = \cos^2\beta \left\{1 + \left(\frac{\Omega x}{V_o}\right)^2\right\} + \left(\frac{\Omega x}{V_o}\right)^2 \left\{2\frac{r}{x}\cos\beta + \left(\frac{r}{x}\right)^2\right\}$$

At an outboard section $(r/x) < 1$ and the second term may be omitted. But, $(\Omega x/V_o) \sim 0.1$ for $\Omega \cong 10^2$ RPM, $\ell \cong 50$ feet, and $V_o \approx 5 \times 10^3$ FPS. Therefore, for small β, $V_R/V_o \approx 1$.

At an inboard section, the above reduces to $(r/x) > 1$

$$\left(\frac{V_R}{V_o}\right)^2 = \cos^2\beta + \left(\frac{\Omega R}{V_o}\right)^2$$

and even with r = 10 feet, the second term is small and $V_R/V_o \approx 1$.

It is, therefore, reasonable to restrict considerations to that of a simple flat plate as representative of a general section of a rotor blade as shown in Figure 109. A shock will stand off in front of the blade for expected re-entry velocities.

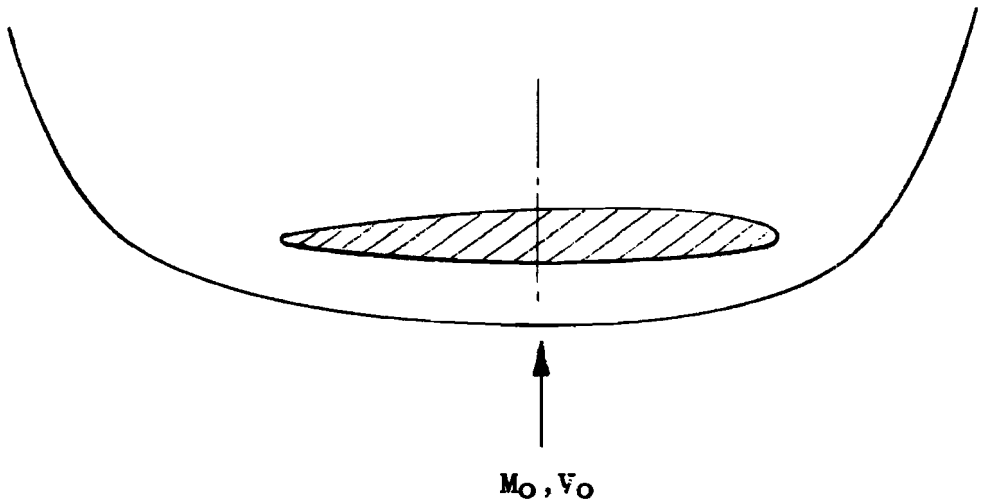

RE-ENTRY BLADE FLOW

FIGURE 109

Allen and Eggers have shown that the over-all heat transfer to re-entry bodies may be evaluated in terms of a skin friction parameter (Γ) representative of the specific geometry involved. Their approach is used initially and refined later as necessary. Let H be the heat transfer per unit area so that:

$$\dot{H} = h\,(Taw - Tw) \qquad \text{is energy/area/time}$$

$$\dot{H} = -\dot{H}/V_o \sin\theta_E \qquad \text{is energy/area/length along trajectory}$$

since $dY/dt = -V_o \sin\theta_E$, if Y is altitude and θ_E is the re-entry angle. For large decelerations, gravity is negligible and $\theta = \theta_E$ throughout the trajectory.

The heat transfer coefficient, h, adiabatic wall temperature, Taw, and surface temperature, Tw, are all functions of position along the trajectory insofar as they depend upon M_o, Reynolds number, and heat capacity (or cooling system) of structure. For simplicity, however, assume Reynolds analogy

$$S_x = \frac{h}{g\rho U C_p} = \frac{C_f}{2}$$

for the Stanton number, S_x, and skin friction coefficient, C_f. Further, in terms of a recovery factor, $\bar{r}$,

$$Taw = T_o \left(1 + \frac{\gamma-1}{2}\,\bar{r}\,M_o^2\right)$$

so that

$$Taw - Tw = T_o - Tw + \frac{\gamma-1}{2}\,\bar{r}\,M_o^2\,T_o \approx \frac{\gamma-1}{2}\,\bar{r}\,M_o^2\,T_o \left(\text{for large } M_o\right)$$

$$\approx \frac{\bar{r}}{2}\,\frac{V_o^2}{C_p}$$

If Q is the over-all heat transfer to the geometry, then the rate of over-all heat transfer to the vehicle per length along the trajectory is:

$$\frac{dQ}{dY} = \iint \dot{H} d\bar{A} = -\iint \frac{h(T_{aw} - T_w)}{V_o \sin\theta_E} d\bar{A}$$

$$= \frac{\bar{r}\rho_o V_o^2 \bar{A}}{4 \sin\theta_E} \left\{ \frac{1}{\bar{A}} \iint C_f \frac{\rho}{\rho_o} \frac{\mu}{V_o} d\bar{A} \right\} = -\frac{\bar{r}\rho_o V_o^2 \bar{A}}{4 \sin\theta_E} \{F\}$$

where $\bar{A}$ is the surface area and F represents the details of the local flow field for the vehicle as it affects the heat transfer.

In order to eliminate the local influence implied by ρ_o and V_o, the Allen and Eggers assumption of an isothermal atmosphere is used. If the drag coefficient is constant, then:

$$V_o = V_E \exp\left\{ -\frac{C_D \rho_o A}{2\beta \sin\theta_E} e^{-\beta Y} \right\} = V_E \left\{ \frac{2m e^{\beta Y}\left(-\frac{dV_o}{dt}\right)}{C_D \rho V_E^2 A} \right\}^{1/2}$$

m being the mass in slugs and A the reference area for C_D .

Thus,

$$\frac{dQ}{dY} = \left(\frac{\bar{r}\bar{A}F}{2 \sin\theta_E}\right)\left(\frac{W}{C_D A}\right)\left(\frac{\frac{dV_o}{dt}}{g}\right)$$

An important consequence is that maximum dQ/dY is equivalent to maximum deceleration, which (if $Y > 0$) occurs at:

$$Y = \frac{1}{\beta} \ln \frac{C_D \rho_o A}{\beta m \sin\theta_E}$$

and is

$$V_o = \frac{V_E}{e^{1/2}} \qquad \frac{\frac{dV_o}{dt}}{g} = -\frac{\beta V_E^2 \sin\theta_E}{2ge}$$

In fact:

$$\left(\frac{dQ}{dY}\right)_{MAX} = -\frac{\beta V_E^2}{4ge}(\bar{r}\bar{A}F)\left(\frac{W}{C_D A}\right)$$

Total heat transfer requires integration over the flight path from entry to impact, or:

$$\int_{\infty}^{0} \frac{dQ}{dY}\, dY = -D_1 \int_{\infty}^{0} e^{-\beta Y} e^{D_1 e^{-\beta Y}}\, dY = -\frac{D_1}{\beta}\int_{0}^{1} e^{D_2 Z}\, dZ = -\frac{D_1}{\beta D_2}\int_{1}^{e^{D_2}} dZ$$

where

$$D_1 = -\frac{\rho_0 V_E^2}{4 \sin\theta_E}\left(\bar{r}\bar{A}F\right)$$

$$D_2 = -\left(\frac{C_D A}{W}\right)\left(\frac{\rho_0 g}{\beta \sin\theta_E}\right)$$

Thus:

$$\int_{\infty}^{0} \frac{dQ}{dY}\, dY = \frac{V_E^2}{4g}\left(\frac{W}{C_D A}\right)\left(\bar{r}\bar{A}F\right)\left(1 - e^{D_2}\right)$$

Or finally:

$$Q = \left(\frac{\bar{r}\bar{A}F}{2C_D A}\right)\left\{\frac{m}{2}\left(V_E^2 - V_o^2\right)\right\}$$

$$= \left(\bar{r}\bar{A}F\right)\left(\frac{W}{C_D A}\right)\frac{1}{4g}\left(V_E^2 - V_o^2\right)$$

is the total heat input during the descent. The results of this equation are shown graphically in Figure 110. Clearly, the energy exchange represents the change in kinetic energy of the vehicle from entry to "impact" (note that $V_o = V_E\, e^{D_2/2}$ for $Y = 0$) weighted by a proportionality constant:

$$\frac{\bar{r}\ \bar{A}\ F}{2C_D A}$$

The heat transfer may be reduced (for a given kinetic energy change) by reducing the recovery factor, $\bar{r}$, and thus the temperature potential (Taw -Tw), or by reducing the "skin friction", $F\bar{A}$, relative to the drag, $C_D A$, forces. If $W/C_D A$ is assumed to be 15 pounds per square foot, and $2\beta/\rho_0 g = 0.00119$ 1/psf, then for the extremes of re-entry angles:

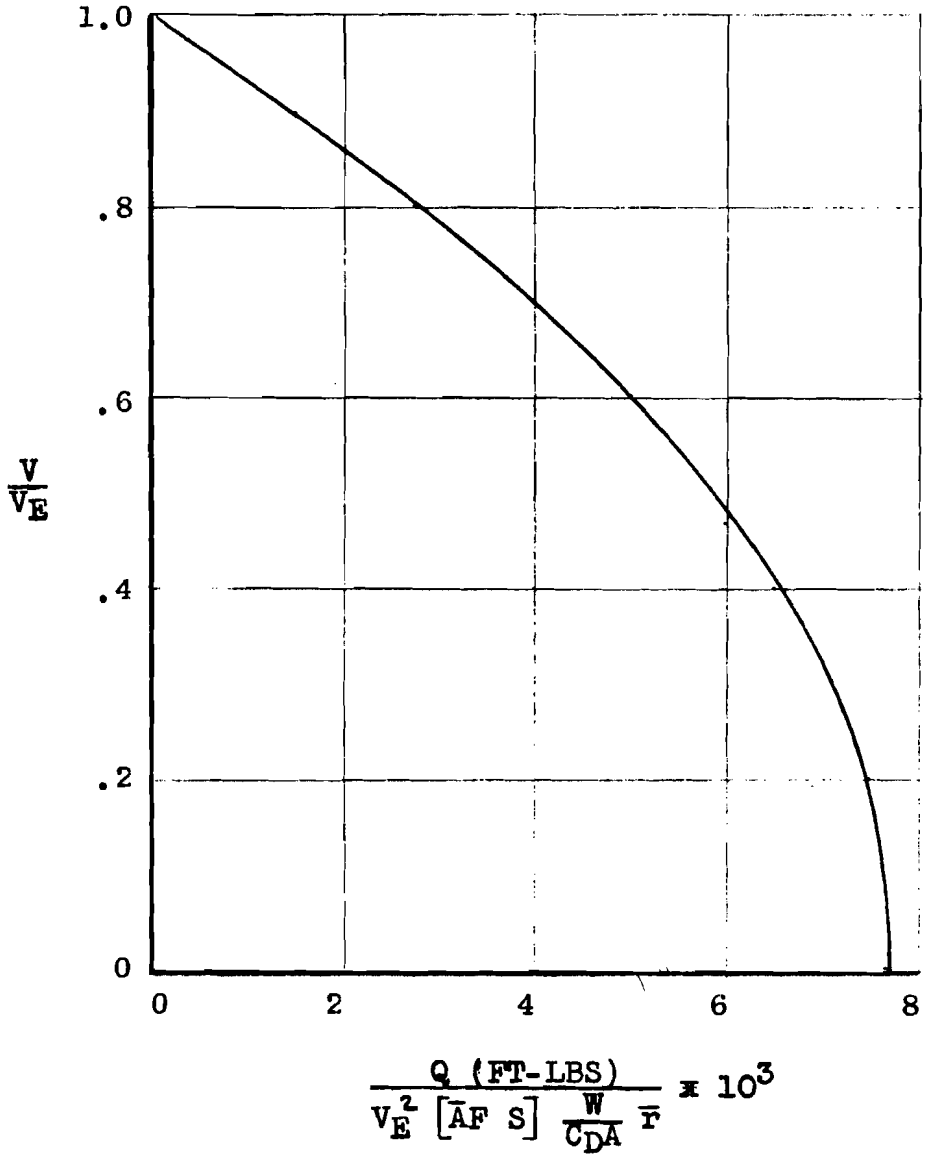

TOTAL HEAT INPUT DURING RE-ENTRY

FIGURE 110

$$\frac{V_o}{V_e} = \exp\left\{-\frac{1}{0.01788 \sin \theta_E}\right\} = (0.00370)^{\frac{1}{\sin \theta_E}}$$

$$= \begin{cases} 0.000\ 00 & (\theta_E = 10^o) \\ 0.003\ 70 & (\theta_E = 90^o) \end{cases}$$

In either case:

$$\frac{m}{2}(V_E^2 - V_o^2) = \frac{mV_E^2}{2}\left[1 - \left(\frac{V_o}{V_E}\right)^2\right] \approx \frac{mV_E^2}{2}$$

i.e. the final (impact) kinetic energy is negligible relative to the entry value.

On the basis of preliminary design considerations, the above can be used to indicate the severity of the thermal problem for assumed blade sections, dimensions, and materials. Clearly, step by step computations are necessary for a final design. In so doing, two other viewpoints are of special interest: (1) the average rate at which heat is transmitted to the entire surface, and (2) the most severe rate at which heat is transferred locally.

The first of these is:

$$\dot{H}_{avg} = \frac{1}{A}\iint \dot{H}\, d\bar{A} = \frac{1}{A}\iint e\mu\, \frac{C_f\, \bar{r} V^{o2}}{4}\, d\bar{A}$$

$$= 1/4\ \bar{r}\ F\ \rho_o\ V_o^3 = 1/4\ \bar{r}\ F\ \rho_o V_E^3\, e^{-\beta Y} e^{-\frac{3}{2}D_2 e^{-\beta Y}}$$

and has its maximum value of:

$$(\dot{H}_{avg})_{max} = \frac{\beta}{6eg}\ (\bar{r}\ F)\left(\frac{W}{C_D A}\right) V_E^3 \sin \theta_E$$

at the altitude $Y = \left[\begin{matrix}\text{Y max over-all} \\ \text{heat transfer}\end{matrix}\right] + \frac{1}{\beta} \ln \frac{3}{2}$

and speed $V_o = \frac{V_E}{e^{1/3}} = \left[\begin{matrix}V_o \text{ max over-all} \\ \text{heat transfer}\end{matrix}\right] e^{1/6}$

The second rate of interest occurs at the stagnation point and can be written in terms of a Nusselt number

$$Nu = \frac{k\sigma}{k_2} \quad (\sigma = \text{some characteristic length})$$

$$= KR_e^{1/2}$$

Where K is to be specified for a given geometry (e.g. for a sphere, stagnation point, $K = 0.934\,\rho\,\bar{r}^{2/5}$ and $Re = \rho_0 V_0 \sigma/\mu_{aw}$.

Thus,

$$\dot{H} = -\frac{Nu\,k}{\sigma}(T_w - T_{aw}) = \left(K\frac{\bar{r}}{2}\right)\left(\frac{k}{\mu_{aw}}\right)\sqrt{\frac{\rho_0 V_0 \mu_{aw}}{\sigma}}\,V_0^2$$

If now,

$$\mu_{aw} = k_1 T_{aw}^{1/2}, \quad T_{aw} - T_w \approx T_{aw} = \frac{\bar{r} V_0^2}{2C_p}$$

$$V_0 \mu_{aw} = K_1 \left(\frac{\bar{r}}{2C_p}\right)^{1/2} V_0^2$$

and so

$$\dot{H} = K_3 \sqrt{\frac{\rho_0}{\sigma}}\,V_0^3$$

where

$$K_3 = \frac{1}{2} K \bar{r} K_1^{1/2} \left(\frac{k}{\mu_{aw} C_p}\right)\left(\frac{\bar{r}}{2C_p}\right)^{1/4}$$

This heat transfer rate has a maximum

$$\dot{H}_{MAX} = K_3 \frac{\beta}{3 e g \sigma}\left(\frac{W}{C_D A}\right) V_E^3 \sin\theta_E$$

at the altitude $Y = \left[\begin{matrix}\text{Y max over-all} \\ \text{heat transfer}\end{matrix}\right] + \frac{1}{\beta} + \ln 3$

and speed $V_0 = \frac{V_E}{e^{1/6}} = \left[\begin{matrix}V_0 \text{ max over-all} \\ \text{heat transfer}\end{matrix}\right] e^{1/3}$

In Figure 111, a plot of the trajectory appears in an altitude-velocity plane for two extreme entry angles with $(W/C_DA) = 15$. Superimposed are locii for:

1. Stagnation temperature (see e.g. NACA TN 4150)

2. Separation of real gas regimes according to presence of different air components behind shock

3. Maximum over-all heat transfer/ft.alt.

4. Maximum average heat transfer rate

5. Maximum local heat transfer rate (stag. pt.)

Descent times from entry are also noted, as well as molecules mean free path for the altitude.

It may be concluded that peak heating occurs well into the dissociated gas region. In this respect, the earlier discussion is conservative insofar as it neglects the natural heat sink implied by such processes. Rigorously, corrections for $V_o \gtrsim 10{,}000$ FPS should be considered.

The locii are primarily determined by the velocity V_o. Thus, the smaller entry angle implies peak heating at higher altitude where less dense air is present and the heat input is reduced (i.e., F is smaller). This is a consequence of the fact that the parameter $(W/C_DA) \sin \theta_E$ governs the fraction of kinetic energy absorbed in descent to a given altitude. Lesser values for the parameter imply faster decelerations (i.e. a relatively "light" body). An over-all conclusion must consider the descent time which is longer for the "light" body and may, thereby, result in greater heat transfer.

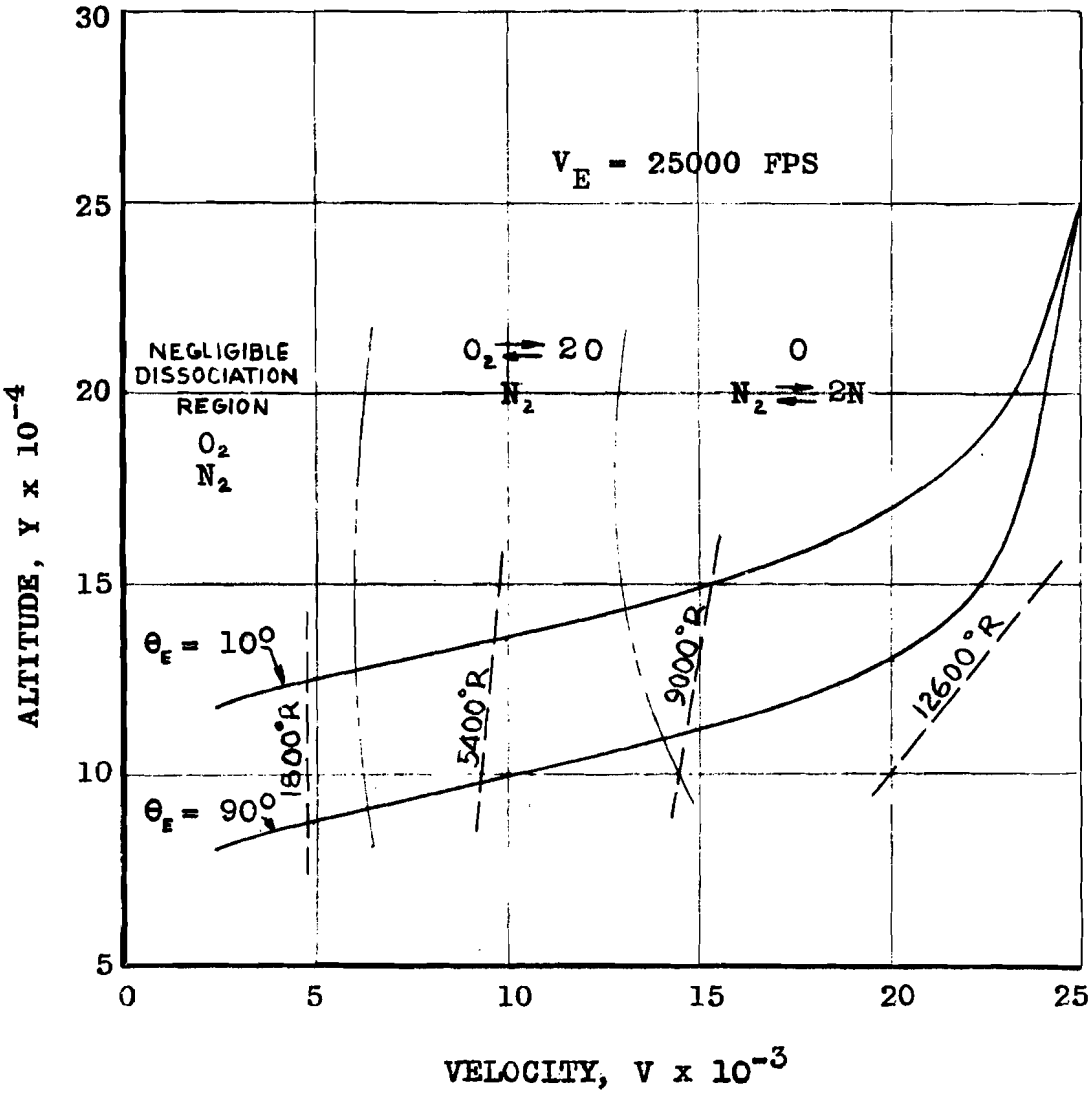

RE-ENTRY VELOCITY-ALTITUDE RELATIONSHIP

FIGURE 111

APPENDIX V. TEST VEHICLE DESIGN INFORMATION

A. CONFIGURATION

Figure 112 shows the original configuration and overall dimensions of the KRC-6 ROTOCHUTE Test Vehicle at the beginning of the air drop test series. The final modified configuration at the conclusion of the test series is presented in Figure 113. A general arrangement of the final configuration is shown in Figure 114.

The following summarizes the major differences between the initial configuration and the final modified version:

	Original	Final
Gross Weight, Pounds	275	315
Rotor Diameter, Feet	8	10
Disc Loading, Lbs/Sq.Ft.	5.5	4.0
Rotor Solidity	.159	.127
Governed Tip Speed, FPS	475	430
Hub Tilt, Degrees		
Forward	11	16
Aft	4	5
Right	4	10.5
Left	11	10.5
Vertical Fin Area, Sq.Ft.	.85	3.20
Horizontal Tail Area, Sq.Ft.	0	3.75
Rotor Disc Area, Sq.Ft.	50.2	78.5

B. STRUCTURAL DESIGN CRITERIA

1. Blades and Grips

The blades were designed for maximum flatwise bending which occurs during the opening cycle at approximately 400 RPM, and is maximum at a 22-inch radius. The inboard end of the blade, the grip, and the attachment to the hub were designed for centrifugal force at an overspeed condition of 1700 RPM.

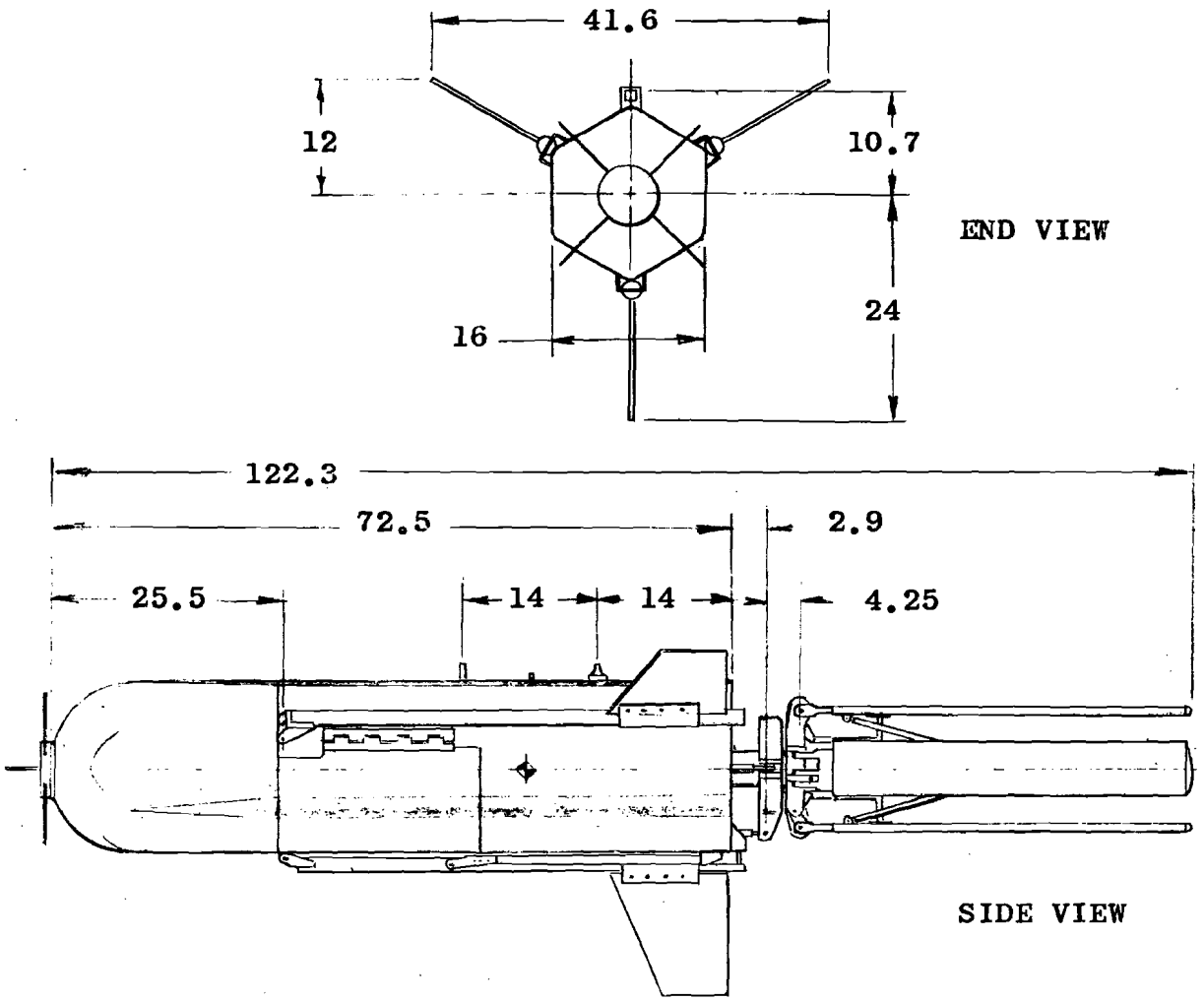

KRC-6 ROTOCHUTE DIMENSIONS (ORIGINAL CONFIGURATION)

FIGURE 112

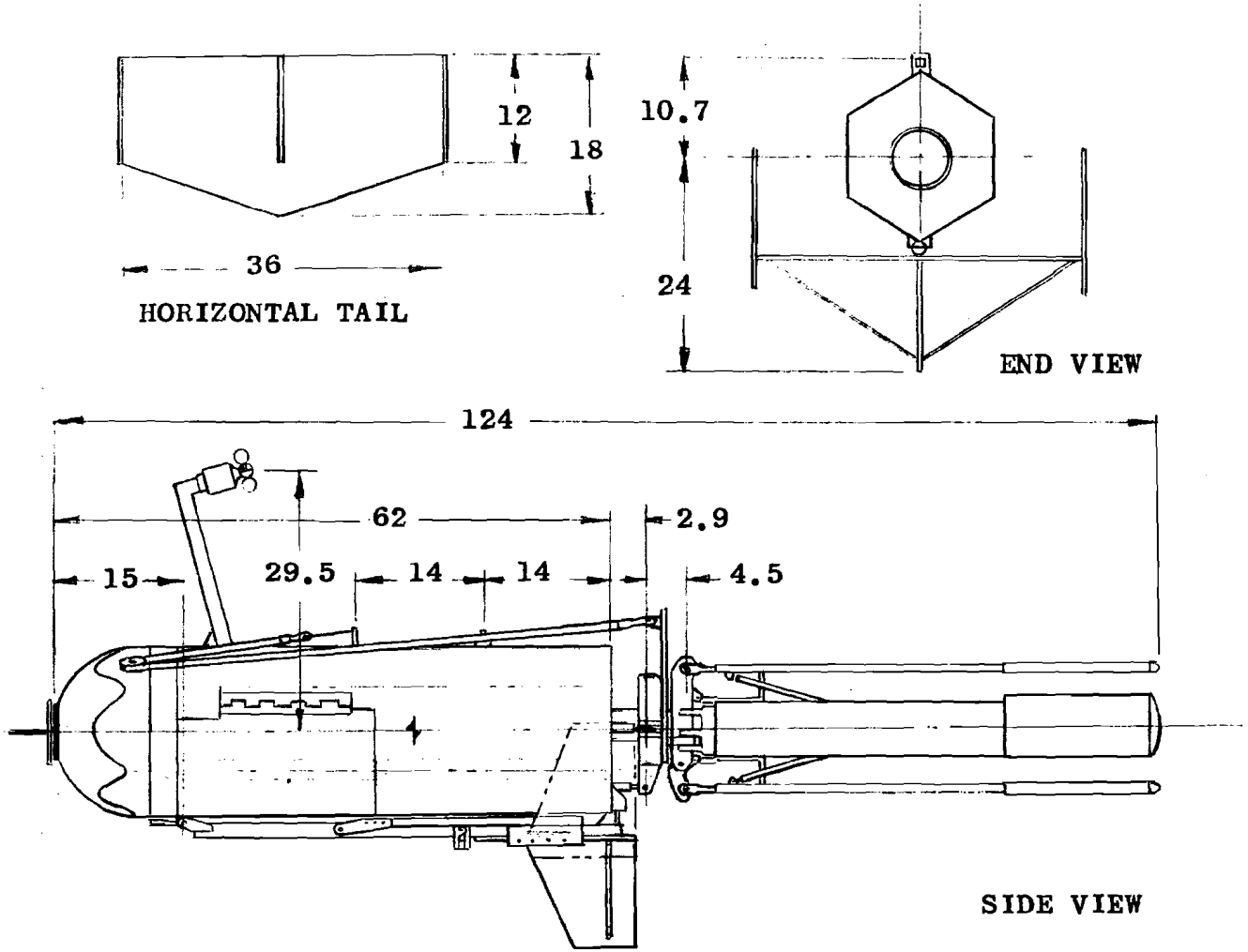

KRC-6 ROTOCHUTE DIMENSIONS (FINAL CONFIGURATION)

FIGURE 113

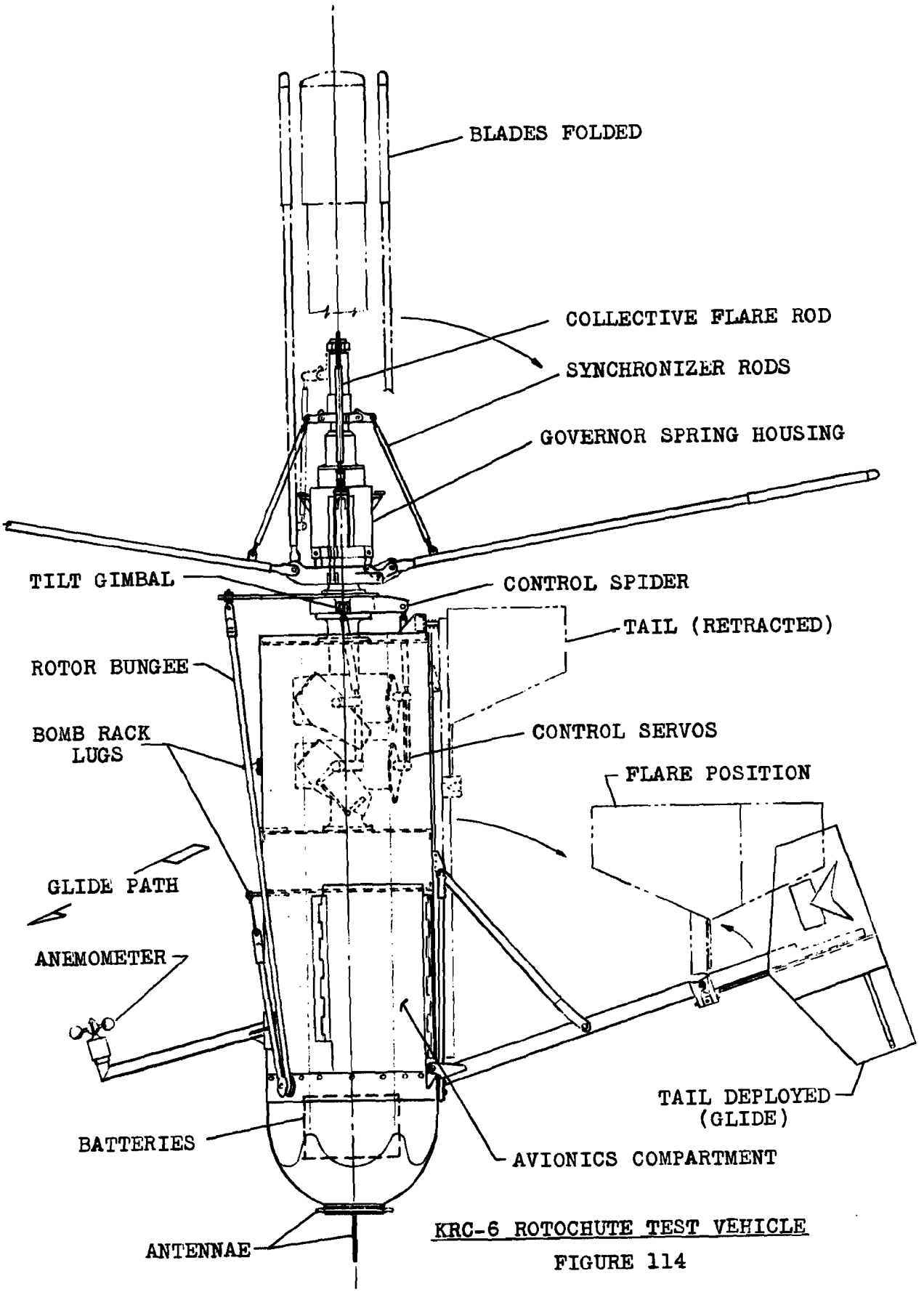

KRC-6 ROTOCHUTE TEST VEHICLE

FIGURE 114

2. The hub was designed as a ring with in-plane bending due to the centrifugal forces from the blades.

3. Controls

(a) The pitch control links were designed for the centrifugal forces at 1700 RPM.

(b) Hub tilt control rods were designed for maximum output torque of the control servos.

(c) Collective pitch flare controls were designed for the output of the thruster unit. Shock loading was given consideration, but accurate prediction was difficult. As a result, the system was re-inforced after ground firing tests.

4. The hub to body attachments were designed for a 30-G axial inertia force assumed during the opening cycle phase. Initial estimated vehicle gross weight of 256 pounds and a body weight of 172 pounds were used for the designs.

5. The body unit was designed for shear and bending for a 10-G force imposed by an estimated ejection force of 2600-pounds. A secondary design condition was considered - a 5-G side force with the vehicle suspended on the bomb shackle attachments.

6. The nose cone was originally designed as an energy absorption device to limit landing impact vertical accelerations to 30 G's.

The alighting gear struts were designed for a 4.0-G load perpendicular to the ground with the vehicle resting on the nose and any two struts.

C. WEIGHT DATA

The following tabulation shows calculated weights for the major groupings of the test vehicle in its original configurations.

TABULATION - CALCULATED WEIGHT

ITEM	WEIGHT - POUNDS	
GROSS WEIGHT		278.1
ROTOR GROUP	67.2	
Blades	14.6	
Hub	3.8	
Shafting	48.8	
BODY GROUP	55.0	
Basic	27.6	
Secondary	14.2	
Provision	13.2	
ALIGHTING GEAR	25.1	
CONTROLS	35.4	
AVIONICS AND BATTERIES	95.4	

D. SYSTEM DESIGN SPECIFICATIONS

The design specifications and ratings for the various units of the flight vehicle remote control and telemetry system are summarized in the following tabulation.

SYSTEM DESIGN SPECIFICATIONS
(KRC-6 TEST VEHICLE)

POWER REQUIREMENTS

Airborne System	-	Up to 30 amps, 28 volts DC
Ground Station	-	Up to 30 amps, 28 volts DC

RADIO LINK

Ground Transmitter	-	Power output up to 35 watts at frequency of 410 mc
Airborne Transmitter	-	Power output up to 4.5 watts at frequency of 232.9 mc

CONTROL COMMAND CHANNELS

Number	Type		
2	Proportional	-	Up to ± 2 volts DC
4	Switching	-	"On" +2 volts DC, "off" -2 volts DC

TELEMETRY CHANNELS

14 Channels	-	Will accept up to ± 2 volts DC input signals

AC input signal data may be transmitted by use of appropriate demodulators. Six channels presently are provisioned with such demodulators.

SERVO CONTROL OUTPUTS

Output Torque Rating (Max.)	675 pound-inches
Output Arm Angular Travel	60 degrees
Output Arm Length (Max.)	2.25 inches